

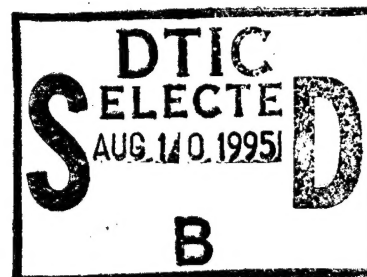
DOT/FAA/CT-95/25
DOT-VNTSC-FAA-95-10

FAA Technical Center
Atlantic City, NJ 08405

Strain Fields in Boeing 737 Fuselage Lap Splices: Field and Laboratory Measurements with Analytical Correlations

D. Y. Jeong
D. P. Roach
J. V. Canha
J. C. Brewer
T. H. Flournoy

②
Research and
Special Programs
Administration
Volpe National
Transportation Systems Center
Cambridge, MA 02142-1093



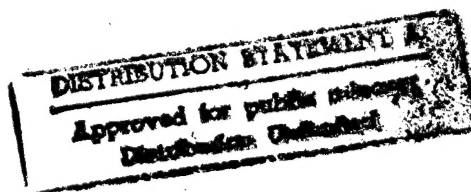
Final Report
June 1995

19950808 003

This document is available to the public
through the National Technical Information
Service, Springfield, VA 22161



U.S. Department of Transportation
Federal Aviation Administration



DTIC QUALITY INSPECTED 5

NOTICE

This document is disseminated under the sponsorship of the Department of Transportation in the interest of information exchange. The United States Government assumes no liability for its contents or use thereof.

NOTICE

The United States Government does not endorse products or manufacturers. Trade or manufacturers' names appear herein solely because they are considered essential to the objective of this report.

REPORT DOCUMENTATION PAGE

Form Approved
OMB No. 0704-0188

Public reporting burden for this collection of information is estimated to average 1 hour per response, including the time for reviewing instructions, searching existing data sources, gathering and maintaining the data needed, and completing and reviewing the collection of information. Send comments regarding this burden estimate or any other aspect of this collection of information, including suggestions for reducing this burden, to Washington Headquarters Services, Directorate for Information Operations and Reports, 1215 Jefferson Davis Highway, Suite 1204, Arlington, VA 22202-4302, and to the Office of Management and Budget, Paperwork Reduction Project (0704-0188), Washington, DC 20503.

1. AGENCY USE ONLY (Leave blank)		2. REPORT DATE June 1995	
		3. REPORT TYPE AND DATES COVERED Final Report January 1994 - March 1995	
4. TITLE AND SUBTITLE Strain Fields in Boeing 737 Fuselage Lap Splices: Field and Laboratory Measurements with Analytical Correlations			
5. FUNDING NUMBERS A5044/FA5H2			
6. AUTHOR(S) David Y. Jeong ¹ , Dennis P. Roach ² , Joseph V. Canha ¹ , John C. Brewer ¹ , and Thomas H. Flournoy ³			
7. PERFORMING ORGANIZATION NAME(S) AND ADDRESS(ES) ¹ U.S. Department of Transportation John A. Volpe National Transportation Systems Center Kendall Square Cambridge, MA 02142 ² Aging Aircraft NDI Validation Center Sandia National Laboratories Albuquerque, NM 87185 ³ U.S. Department of Transportation Federal Aviation Administration Technical Center Atlantic City, NJ 08405			
8. PERFORMING ORGANIZATION REPORT NUMBER DOT-VNTSC-FAA-95-10			
9. SPONSORING/MONITORING AGENCY NAME(S) AND ADDRESS(ES)			
10. SPONSORING/MONITORING AGENCY REPORT NUMBER DOT/FAA/CT-95/25			
11. SUPPLEMENTARY NOTES			
12a. DISTRIBUTION/AVAILABILITY STATEMENT This document is available to the public through the National Technical Information Service, Springfield, VA 22161			12b. DISTRIBUTION CODE
13. ABSTRACT (Maximum 200 words) In support of the Federal Aviation Administration Technical Center's (FAATC) National Aging Aircraft Research Program (NAARP), Sandia National Laboratories and the John A. Volpe National Transportation Systems Center (Volpe Center) are conducting research to determine if current rules for design, inspection, and maintenance are sufficient to ensure the safe operation of the aging fleet. Particular emphasis has been given to a phenomenon of multiple cracking that appears to be an attribute of airplanes that have been in service for some time. This phenomenon is commonly referred to as Widespread Fatigue Damage (WFD). Several experimental and analytical studies have been initiated by FAATC to understand the phenomenon of WFD. Some of these research activities include: (1) collection of strain gage data from a Boeing 737 airplane conducted by the Aging Aircraft Nondestructive Inspection Validation Center (AANC); (2) laboratory testing of full-scale curved panels conducted by Foster-Miller, Inc. (FMI); and (3) modeling of fuselage lap splices by the Volpe Center. This report documents the strain gage testing of the Boeing 737 airplane acquired by the AANC. Additionally, correlations among the three research activities mentioned above have been performed, and are described in this report.			
14. SUBJECT TERMS Lap Splice Joint, Strain Gage, Analytical Correlations			15. NUMBER OF PAGES 218
			16. PRICE CODE
17. SECURITY CLASSIFICATION OF REPORT Unclassified	18. SECURITY CLASSIFICATION OF THIS PAGE Unclassified	19. SECURITY CLASSIFICATION OF ABSTRACT Unclassified	20. LIMITATION OF ABSTRACT

PREFACE

In support of the Federal Aviation Administration Technical Center's (FAATC) National Aging Aircraft Research Program (NAARP), Sandia National Laboratories and the John A. Volpe National Transportation Systems Center (Volpe Center) are conducting research to determine if current rules for design, inspection, and maintenance are sufficient to ensure the safe operation of the aging fleet. Particular emphasis has been given to a phenomenon of multiple cracking that appears to be an attribute of airplanes that have been in service for some time. This phenomenon is commonly referred to as Widespread Fatigue Damage (WFD).

Several experimental and analytical studies have been initiated by FAATC to understand the phenomenon of WFD. Some of these research activities include: (1) collection of strain gage data from a Boeing 737 airplane conducted by the Aging Aircraft Nondestructive Inspection Validation Center (AANC); (2) laboratory testing of full-scale curved panels conducted by Foster-Miller, Inc. (FMI); and (3) modeling of fuselage lap splices by the Volpe Center.

This report documents the strain gage testing of the Boeing 737 airplane acquired by the AANC. Additionally, correlations among the three research activities mentioned above have been performed, and are described in this report.

The following individuals are acknowledged for their contributions to the work described in this report. Mr. Phil Walkington mounted the strain gages and worked on all aspects of the test instrumentation and support equipment. Mr. Ken Harmon prepared the Boeing 737 Test Bed for pressurization and ran the cockpit controls during the tests. Ms. Marlene Shields helped with data acquisition and with troubleshooting the strain gage and displacement transducer instrumentation. The authors also extend their gratitude to Kirtland Air Force Base for providing the ground power and pressurization units used during the B737 tests. Finally, the support of the FAA Technical Center and its staff is gratefully acknowledged.

Accession For	
NTIS GRA&I	<input checked="" type="checkbox"/>
DTIC TAB	<input type="checkbox"/>
Unannounced	<input type="checkbox"/>
Justification	
By _____	
Distribution/	
Availability Codes	
Distr	Avail and/or Special
A-1	

METRIC/ENGLISH CONVERSION FACTORS

ENGLISH TO METRIC

LENGTH (APPROXIMATE)
1 inch (in) = 2.5 centimeters (cm)
1 foot (ft) = 30 centimeters (cm)
1 yard (yd) = 0.9 meter (m)
1 mile (mi) = 1.6 kilometers (km)

METRIC TO ENGLISH

LENGTH (APPROXIMATE)
1 millimeter (mm) = 0.04 inch (in)
1 centimeter (cm) = 0.4 inch (in)
1 meter (m) = 3.3 feet (ft)
1 meter (m) = 1.1 yards (yd)
1 kilometer (k) = 0.6 mile (mi)

AREA (APPROXIMATE)
1 square inch (sq in, in ²) = 6.5 square centimeters (cm ²)
1 square foot (sq ft, ft ²) = 0.09 square meter (m ²)
1 square yard (sq yd, yd ²) = 0.8 square meter (m ²)
1 square mile (sq mi, mi ²) = 2.6 square kilometers (km ²)
1 acre = 0.4 hectare (he) = 4,000 square meters (m ²)

AREA (APPROXIMATE)
1 square centimeter (cm ²) = 0.16 square inch (sq in, in ²)
1 square meter (m ²) = 1.2 square yards (sq yd, yd ²)
1 square kilometer (km ²) = 0.4 square mile (sq mi, mi ²)
10,000 square meters (m ²) = 1 hectare (he) = 2.5 acres

MASS - WEIGHT (APPROXIMATE)
1 ounce (oz) = 28 grams (gm)
1 pound (lb) = 0.45 kilogram (kg)
1 short ton = 2,000 pounds (lb) = 0.9 tonne (t)

MASS - WEIGHT (APPROXIMATE)
1 gram (gm) = 0.036 ounce (oz)
1 kilogram (kg) = 2.2 pounds (lb)
1 tonne (t) = 1,000 kilograms (kg) = 1.1 short tons

VOLUME (APPROXIMATE)
1 teaspoon (tsp) = 5 milliliters (ml)
1 tablespoon (tbsp) = 15 milliliters (ml)
1 fluid ounce (fl oz) = 30 milliliters (ml)
1 cup (c) = 0.24 liter (l)
1 pint (pt) = 0.47 liter (l)
1 quart (qt) = 0.96 liter (l)
1 gallon (gal) = 3.8 liters (l)
1 cubic foot (cu ft, ft ³) = 0.03 cubic meter (m ³)
1 cubic yard (cu yd, yd ³) = 0.76 cubic meter (m ³)

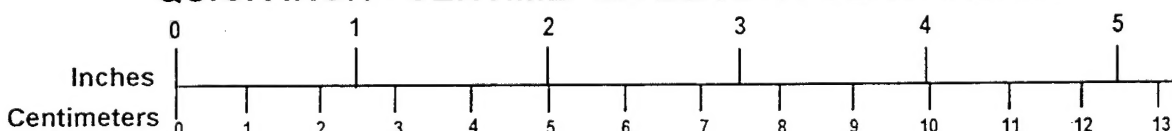
VOLUME (APPROXIMATE)
1 milliliter (ml) = 0.03 fluid ounce (fl oz)
1 liter (l) = 2.1 pints (pt)
1 liter (l) = 1.06 quarts (qt)
1 liter (l) = 0.26 gallon (gal)

1 cubic meter (m³) = 36 cubic feet (cu ft, ft³)
 1 cubic meter (m³) = 1.3 cubic yards (cu yd, yd³)

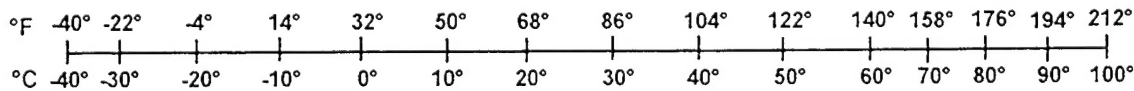
TEMPERATURE (EXACT)
$[(x-32)(5/9)]^{\circ}\text{F} = y^{\circ}\text{C}$

TEMPERATURE (EXACT)
$[(9/5)y + 32]^{\circ}\text{F} = x^{\circ}\text{C}$

QUICK INCH - CENTIMETER LENGTH CONVERSION



QUICK FAHRENHEIT - CELSIUS TEMPERATURE CONVERSION



For more exact and or other conversion factors, see NBS Miscellaneous Publication 286, Units of Weights and Measures.
 Price \$2.50 SD Catalog No. C13 10286

Updated 1/23/95

TABLE OF CONTENTS

<u>Section</u>	<u>Page</u>
1. BACKGROUND.....	1
2. TEST PLAN AND IMPLEMENTATION.....	7
2.1 Selection of Lap Splice Test Sections	9
2.1.1 Selection of Circumferential Positions on the Fuselage	9
2.1.2 Selection of Longitudinal Positions on the Fuselage	12
2.1.3 Locations within Selected Bays	12
2.1.4 Strain Gage Deployment.....	15
2.2 Instrumentation.....	21
2.2.1 Strain Gage Specifications	21
2.2.2 Measurement of Fuselage Radial Displacement	22
2.2.3 Data Acquisition System	22
2.3 Aircraft Ground Pressurization	24
3. EXPERIMENTAL STRAIN AND DISPLACEMENT DATA	29
3.1 External Strains in the Skin	29
3.1.1 Load Transfer Through the Lap Splice Joint.....	29
3.1.2 Hoop Strains at Reinforced Areas of the Lap Skin	38
3.1.3 Hoop Strains Along the Lap Splice Joint	38
3.1.4 Longitudinal Strain Levels.....	51
3.2 Bending Strains in the Skin	59
3.3 Load Transfer into Lower/Inner Skin of Lap Splice Joint.....	59
3.4 Strains in Substructure Elements	71
3.5 Compensation for Thermal and Ambient Noise Induced Strains	71
3.6 Strain Consistency Over Several Pressure Cycles.....	77
3.7 Stress Fields in Lap Splice Bays	77
3.7.1 Membrane Stresses	77
3.7.2 Principal Stresses	92
3.8 Fuselage Radial Growth.....	95

TABLE OF CONTENTS (continued)

<u>Section</u>	<u>Page</u>
4. STRAIN GAGE DATA CORRELATIONS	99
4.1 Correlations with Foster-Miller Data	99
4.1.1 FMI Strain Gage Designations.....	99
4.1.2 Structural and Procedural Considerations.....	102
4.1.3 Results of Correlations Between FMI and AANC Data.....	104
4.2 Correlations with NASA Boeing 737 Data	119
4.3 Correlations with Results from Finite Element Models	126
4.3.1 Description of Finite Element Models	126
4.3.2 Results of Correlations Between Finite Element Models and AANC Data.....	127
4.4 Comparisons Among Different Test Sections in the AANC Boeing 737.....	137
5. CONCLUSIONS	149
REFERENCES	153
APPENDICES	
A. Deployment of Strain Gages at Specific Lap Splice Bays	A-1
B. Tables of Measured Strain Data.....	B-1

LIST OF FIGURES

<u>Figure</u>	<u>Page</u>
1.1 Full-Scale Panel Test Facility.....	2
1.2 Fuselage Lap Splice Test Panels Used in Full-Scale Facility	3
1.3 Photograph of FAA/AANC Boeing 737 Airplane Test Bed	5
2.1 AANC B737 Strain Monitoring Test Set-Up.....	8
2.2 Forward and Aft Body Stations in AANC Boeing 737	10
2.3 Frame Configurations Above and Below Floor Level in AANC B737	11
2.4 Generic Shear and Moment Diagrams for Fuselage Supported by Two Sets of Landing Gear.....	13
2.5 Specific Strain Gage Locations Within Selected Lap Splice Bays	14
2.6 Locations of Lap Splice Test Sections on AANC Airplane	16
2.7 View of Instrumented Lap Splice Bays Above and Below the Window Between Body Stations 470 and 480	18
2.8 Photograph of External Skin Strain Gage Layout Between Body Stations 470 and 480 at Stringer S-14L	19
2.9 Strain Gage Installations on the Interior of AANC B737 Around Stringer S-10L	20
2.10 Portable Data Acquisition System	23
2.11 Two 26-Pin Electrical Connectors and Pressure Pass-Through Sealed Against the Nose Wheel Well Bulkhead	25
2.12 Photograph of AANC Boeing 737 with Airstart and Ground Pressurization Units	26
2.13 Typical Fuselage Pressure Profile	28
3.1 External Skin Hoop Strains Along Midline at S-4L, BS475	30
3.2 External Skin Hoop Strains Along Midline at S-10L, BS475	31
3.3 External Skin Hoop Strains Along Midline at S-14L, BS475	32
3.4 External Skin Hoop Strains Along Midline at S-4L, BS785	33
3.5 External Skin Hoop Strains Along Midline at S-10L, BS785	34
3.6 Deformation of Lap Splice Joint Due to Internal Pressurization.....	36
3.7 External Skin Hoop Strains Along Tear Strap at S-4L, BS470.....	39
3.8 External Skin Hoop Strains Along Frame at S-4L, BS480.....	40
3.9 External Skin Hoop Strains Along Tear Strap at S-10L, BS470.....	41
3.10 External Skin Hoop Strains Along Frame at S-10L, BS480.....	42
3.11 External Skin Hoop Strains Across Midbay at S-4L Lap Splice Bay Between BS470 and BS480	43
3.12 External Skin Hoop Strains 1 Inch Above Upper Rivet Row at S-4L Lap Splice Bay Between BS470 and BS480.....	44
3.13 External Skin Hoop Strains Across Middle Rivet Row at S-4L Lap Splice Bay Between BS470 and BS480.....	45

LIST OF FIGURES (continued)

<u>Figure</u>	<u>Page</u>
3.14 External Skin Hoop Strains 1 Inch Below Lower Rivet Row at S-4L Lap Splice Bay Between BS470 and BS480.....	46
3.15 External Skin Hoop Strains Across Midbay at S-10L Lap Splice Bay Between BS470 and BS480	47
3.16 External Skin Hoop Strains 1 Inch Above Upper Rivet Row at S-10L Lap Splice Bay Between BS470 and BS480.....	48
3.17 External Skin Hoop Strains Across Middle Rivet Row at S-10L Lap Splice Bay Between BS470 and BS480.....	49
3.18 External Skin Hoop Strains 1 Inch Below Lower Rivet Row at S-10L Lap Splice Bay Between BS470 and BS480.....	50
3.19 External Skin Longitudinal Strains at S-4L, BS475	54
3.20 External Skin Longitudinal Strains at S-10L, BS475	55
3.21 External Skin Longitudinal Strains at S-14L, BS475	56
3.22 External Skin Longitudinal Strains at S-4L, BS785	57
3.23 External Skin Longitudinal Strains at S-10L, BS785	58
3.24 Comparison of Internal and External Hoop Strains Measured at S-4L Lap Splice Joint, BS475.....	60
3.25 Comparison of Internal and External Hoop Strains Measured at S-10L Lap Splice Joint, BS475.....	61
3.26 Comparison of Internal and External Longitudinal Strains Measured at S-10L Lap Splice Joint, BS475.....	62
3.27 Bending Strains in the Longitudinal Direction at S-10L Lap Splice Joint, BS475	63
3.28 Bending Strains in Hoop Direction at S-4L, BS475	64
3.29 Bending Strains in Hoop Direction at S-10L, BS475	65
3.30 Hoop Strains in Lower Rivet Row on Inner and Outer Lap Skins at S-4L, BS475	66
3.31 Hoop Strains in Lower Rivet Row on Inner and Outer Lap Skins at S-10L, BS475	67
3.32 Hoop Strains in Lower Rivet Row on Inner and Outer Lap Skins at S-14L, BS475	68
3.33 Longitudinal Strains in Lower Rivet Row on Inner and Outer Lap Skins at S-4L, BS475	69
3.34 Longitudinal Strains in Lower Rivet Row on Inner and Outer Lap Skins at S-10L, BS475	70
3.35 Hoop Strains in BS480 Fuselage Frame at Stringers S-4L and S-10L	72
3.36 Radial Strains in BS480 Fuselage Frame at Stringers S-4L and S-10L	73

LIST OF FIGURES (continued)

<u>Figure</u>	<u>Page</u>
3.37 Longitudinal Strains in S-10L and S-4L Stringer Caps at BS475.....	74
3.38 Hoop Strains in S-10L and S-4L Stringer Caps at BS475.....	75
3.39 Strains Induced by Temperature and Signal Noise Effects.....	76
3.40 Hoop Strains Measured in Upper Rivet Row at S-4L, BS475 from Tests 1, 2, and 3.....	78
3.41 Hoop Strains Measured 1 Inch Above Upper Rivet Row at S-10L, BS480 from Tests 1 and 2	79
3.42 Hoop Strains Measured by Channels 60 and 96 from Tests 1 and 2.....	80
3.43 External Hoop Stresses at S-10L, BS475	83
3.44 External Longitudinal Stresses at S-10L, BS475	84
3.45 Internal Hoop Stresses at S-10L, BS475.....	85
3.46 Internal Longitudinal Stresses at S-10L, BS475.....	86
3.47 External Hoop Stresses at S-10L, BS785	87
3.48 External Longitudinal Stresses at S-10L, BS785	88
3.49 Longitudinal Stresses in Stringers S-4L and S-10L at BS475.....	89
3.50 Hoop Stresses in Fuselage Frames at BS480, Stringers S-4L and S-10L.....	91
3.51 Strain Components Measured by Rectangular Strain Gage Rosette	93
3.52 Maximum Principal Stresses One Inch Above Upper Rivet Row	94
3.53 Principal Stress Directions Measured by Rosettes One Inch Above Upper Rivet Row.....	96
3.54 Fuselage Diameter Growth Measured Forward and Aft of the Wing.....	98
4.1 Strain Gage Deployment for FMI Panel (Exterior Gages)	100
4.2 Strain Gage Deployment for FMI Panel (Interior Gages)	101
4.3 Cross-Section of Boeing 737 Airplane	103
4.4 Waffle Doubler Tear Strap Design in Boeing 737 Airplane.....	105
4.5 Comparison Between AANC Channel 18 and FMI Gage B3H	107
4.6 Comparison Between AANC Channel 20 and FMI Gage B2H	108
4.7 Comparison Between AANC Channel 21 and FMI Gage BNL	109
4.8 Comparison Between AANC Channel 22 and FMI Gage BNH.....	110
4.9 Comparison Between AANC Channel 25 and FMI Gage BRL	111
4.10 Comparison Between AANC Channel 26 and FMI Gage BRH.....	112
4.11 Comparison Between AANC Channel 29 and FMI Gage B1L.....	113
4.12 Comparison Between AANC Channel 30 and FMI Gage B1H	114
4.13 Comparison Between AANC Channel 69 and FMI Gage UB3L	115

LIST OF FIGURES (continued)

<u>Figure</u>	<u>Page</u>
4.14 Comparison Between AANC Channel 70 and FMI Gage UB3H.....	116
4.15 Comparison Between AANC Channel 71 and FMI Gage UB2L	117
4.16 Comparison Between AANC Channel 72 and FMI Gage UB2H.....	118
4.17 Strain Gage Deployment for NASA Boeing 737 Test.....	120
4.18 Comparison of Hoop Strains in Upper Rivet Row	121
4.19 Comparison of Longitudinal Strains in Upper Rivet Row	122
4.20 Comparison of Hoop Strains at Midbay/Midline Location.....	123
4.21 Comparison of Longitudinal Strains at Midbay/Midline Location.....	124
4.22 Comparison of Hoop Strains Near Top Edge of Lap Joint at Midbay.....	125
4.23 Finite Element Mesh Pattern for Pressurized Aircraft Section	128
4.24 Comparison of Strains Across Lap Splice at S-4L, BS475 (Riveted Lap Splice Model)	129
4.25 Comparison of Strains Across Lap Splice at S-4L, BS475 (Adhesively Bonded Lap Splice Model).....	130
4.26 Comparison of Strains in Upper Rivet Row of AANC and NASA B737 Lap Splices with Results from Finite Element Models	132
4.27 Comparison of Strains in Inner and Outer Skin at S-4L, BS475 (Riveted Lap Splice Model)	133
4.28 Comparison of Strains in Inner and Outer Skin at S-4L, BS475 (Adhesively Bonded Lap Splice Model).....	134
4.29 Comparison of Internal and External Strains on the Same Skin at S-4L, BS475 (Riveted Lap Splice Model).....	135
4.30 Comparison of Internal and External Strains on the Same Skin at S-4L, BS475 (Adhesively Bonded Lap Splice Model)	136
4.31 Common Strain Gage Locations in Each Bay of AANC Tests.....	138
4.32 Comparison of Longitudinal Strains at Midbay Locations in AANC Airplane	139
4.33 Comparison of Hoop Strains at Midbay Locations in AANC Airplane	140
4.34 Comparison of Longitudinal Strains Near Top Edge of Lap Joint in AANC Airplane.....	141
4.35 Comparison of Hoop Strains Near Top Edge of Lap Joint in AANC Airplane	142
4.36 Comparison of Longitudinal Strains in Upper Rivet Row in AANC Airplane	143
4.37 Comparison of Hoop Strains in Upper Rivet Row in AANC Airplane	144

LIST OF FIGURES (continued)

<u>Figure</u>	<u>Page</u>
4.38 Comparison of Longitudinal Strains Near Bottom Edge of Lap Joint in AANC Airplane.....	145
4.39 Comparison of Hoop Strains Near Bottom Edge of Lap Joint in AANC Airplane.....	146
A.1 Strain Gage Layout for Lap Joints Around Stringers S-4L and S-10L; Body Stations 470 - 480 (36 Gage Configuration).....	A-3
A.2 Strain Gage Layout for Lap Joint Around Stringer S-14L; Body Stations 470 - 480 (10 Gage Configuration)	A-4
A.3 Strain Gage Layout for Lap Joints Around Stringers S-4L and S-10L; Body Stations 780 - 790 (8 Gage Configuration).....	A-5
A.4 Strain Gage Numbers for Lap Joint at Stringer S-4L; Body Stations 470 - 480; External (30 Gages).....	A-6
A.5 Strain Gage Numbers for Lap Joint at Stringer S-10L; Body Stations 470 - 480; External (30 Gages).....	A-7
A.6 Strain Gage Numbers for Lap Joint at Stringer S-14L; Body Stations 470 - 480; External (8 Gages).....	A-8
A.7 Strain Gage Numbers for Lap Joint at Stringer S-4L; Body Stations 470 - 480; Internal (6 Gages).....	A-9
A.8 Strain Gage Numbers for Lap Joint at Stringer S-10L; Body Stations 470 - 480; Internal (6 Gages).....	A-10
A.9 Strain Gage Numbers for Lap Joint at Stringer S-14L; Body Stations 470 - 480; Internal (2 Gages).....	A-11
A.10 Strain Gage Numbers for Lap Joint at Stringer S-4L; Body Stations 780 - 790; External (8 Gages).....	A-12
A.11 Strain Gage Numbers for Lap Joint at Stringer S-10L; Body Stations 780 - 790; Internal (8 Gages).....	A-13
A.12 Other Data Channels for Pressure Tests 1 and 2	A-14
A.13 Other Data Channels for Pressure Tests 3 and 4	A-14
A.14 Strain Gage Numbers for Lap Joint at Stringer S-4L; Body Stations 470 - 480; Internal (6 Gages)	A-15
A.15 Strain Gage Numbers for Lap Joint at Stringer S-10L; Body Stations 470 - 480; Internal (6 Gages)	A-16

LIST OF TABLES

<u>Table</u>	<u>Page</u>
2.1 Summary of AANC Strain Gage Deployment	17
3.1 Load Transfer Through Different Lap Splice Joints at 6.5 psi.....	37
3.2 Peak External Skin Hoop Strains Across S-4L Lap Splice Bay at 6.5 psi.....	52
3.3 Peak External Skin Hoop Strains Across S-10L Lap Splice Bay at 6.5 psi.....	53
3.4 Comparison of Strains and Stresses at Midline/Midbay Location in Various Test Sections at 6.5 psi.....	81
4.1 Stringer Dimensions for Various Test Sections.....	102
4.2 Figure Numbers Corresponding to One-to-One Strain Gage Comparisons Between AANC and FMI Measurements.....	106
4.3 List of AANC Channels with Common Strain Gage Locations	137
4.4 Comparisons Among Test Sections in AANC Airplane	147

LIST OF ABBREVIATIONS AND SYMBOLS

<i>A</i>	cross-sectional area of stringer
AANC	Aging Aircraft NDI Validation Center
BS	body station location
B737	Boeing 737
FAATC	Federal Aviation Administration Technical Center
<i>E</i>	modulus of elasticity
FMI	Foster-Miller, Inc.
<i>L</i>	stringer spacing
MED	Multiple Element Damage
MSD	Multiple Site Damage
<i>N</i>	number of stringers
NAARP	National Aging Aircraft Research Program
NASA	National Aeronautics and Space Administration
NTSB	National Transportation Safety Board
<i>p</i>	differential pressure
PT	pressure test
<i>R</i>	radius of curvature
<i>S</i>	stringer location
<i>t</i>	skin thickness
WFD	Widespread Fatigue Damage
α	dimensionless parameter = $NA/2\pi Rt = A/Lt$
ΔR	change in radius
ε_b	bending strain
ε_e	external strain
ε_i	internal strain
ε_z	longitudinal strain
ε_θ	hoop strain
$\mu\varepsilon$	microstrain (10^{-6} inch/inch)
σ_L	longitudinal stress in stringer
σ_{max}	maximum principal stress
σ_{min}	minimum principal stress
σ_z	longitudinal stress
σ_θ	hoop stress
ν	Poisson's ratio
θ	orientation of principal direction

EXECUTIVE SUMMARY

This report documents the procedures and results of a series of ground pressurization tests that measured the strain fields in a Boeing 737 aircraft. These strain gage tests were conducted at Sandia National Laboratories, Aging Aircraft Nondestructive Inspection Validation Center (AANC) in Albuquerque, NM. The objectives of the tests were: (1) to monitor the strain field at the probable location of failure initiation in Aloha Airlines Flight 243, (2) to verify the accuracy of empirical results from laboratory aircraft panel tests, and (3) to validate results from finite element models of curved stiffened panels containing lap splices. For these purposes, five (5) lap splice bays on the AANC aircraft were instrumented with 98 strain gages.

Strains and displacements on a Boeing 737 aircraft were measured in a previous test conducted by NASA Langley Research Center. The NASA data, however, were obtained from a small area near a lap joint at the tail end of the fuselage. The AANC data provides more detailed information from which various research efforts can be validated. Data from a comparable lap splice bay in the AANC tests correlated well with the NASA strain data.

The AANC strain data were also correlated with data obtained from curved, stiffened panels tested by Foster-Miller, Inc. (FMI) on a unique fixture that uses water rather than air as a pressurization medium. The agreement between the AANC and laboratory data was reasonable. The results of this correlation suggest that the FMI curved, laboratory panels produce strains representative of those in an actual aircraft fuselage.

The AANC data were also correlated with results from computational models. These models were developed using a commercial finite element code ANSYS by the John A. Volpe National Transportation Systems Center (Volpe Center) in Cambridge, MA. Two finite element models were developed: one with a riveted lap splice, the other with an adhesively bonded lap joint. Finite element results from the riveted lap splice model agree reasonably well with the AANC strain gage data. This correlation implied that the adhesive bond in the tested lap splices of the AANC airplane may have degraded. Nondestructive inspections later confirmed that the lap splices of the AANC B737 airplane had debonded.

The structural effects of windows, floor beams, and fuselage bending on the strain fields were examined by comparing the data among the various lap splice test sections. These correlations revealed that the structural influence of windows and floor beams can increase strains from 4% to 46%. Furthermore, fuselage body bending can increase strains by approximately 30%. Since the AANC airplane was pressurized while it was on the ground, the magnitude of the bending at the tail would probably not be as severe if the airplane had been in flight.

1. BACKGROUND

The Federal Aviation Administration Technical Center (FAATC) has initiated several research projects to evaluate the structural integrity of the aging fleet. One area of research involves the understanding of a phenomenon known as "Widespread Fatigue Damage" or WFD, which refers to multiple cracking that degrades the damage tolerance capability of an aircraft structure. The terms "Multiple Site Damage" and "Multiple Element Damage" have been used to define sources of WFD characterized by the simultaneous presence of fatigue cracks in the same structural element (MSD), and in similar adjacent structural elements (MED). The formation and growth of multiple cracking along a longitudinal lap splice in the fuselage is believed to have contributed to the structural failure of Aloha Airlines Flight 243 in April 1988 [1].

Research concerning WFD has been performed both experimentally and analytically. Experimental research has primarily been conducted in the laboratory using specimens ranging from 1-inch wide flat coupons to 90-inch wide flat panels. Curved, stiffened, full-scale panels have also been tested by Foster-Miller, Inc. (FMI) using a fixture that employs water rather than air as a pressurization medium to create biaxial loading. Photographs of the FMI test fixture are shown in Figure 1.1. The dimensions of the test panel used in this fixture were: 120 inches in width, 68 inches along the circumference, and a 75-inch radius of curvature. Moreover, the panel construction resembled that of the early Boeing 737 airplanes (through production line number 291), particularly in the crown lap splice section. Figure 1.2 shows photographs of the FMI panels. Fatigue testing of one panel resulted in coalescence or linkup of multiple site damage which ultimately lead to structural failure¹ after 75,263 pressurization cycles [2]. This particular panel was initially undamaged, except for an intentionally debonded lap joint. Specific details of the full-scale fuselage panel tests conducted at the FMI facility can be found in References [2], [3], and [4]. A limited number of strain gage measurements were collected during the FMI tests to ensure accurate and realistic loading, and were found to be in reasonable agreement with other available data [4]. These measurements, however, were not sufficient to accurately characterize strains in areas experiencing large gradients. As such, further verification of whether the strains produced in these panels are representative of those in actual lap splice structures is needed. In addition, analytical modeling of the aircraft fuselage that also requires experimental validation has been performed by various researchers. In particular, the Volpe National Transportation System Center (Volpe Center) has developed two finite element models of the fuselage lap splice joint. One model emulates a perfect adhesive bond in the 3-inch skin overlap region. The second model assumes no bonding while the entire load transfer is carried through the rivets.

¹ "Failure" as used here means the size and density of multiple site damage was such that hydraulic pressure could not be maintained to continue testing.

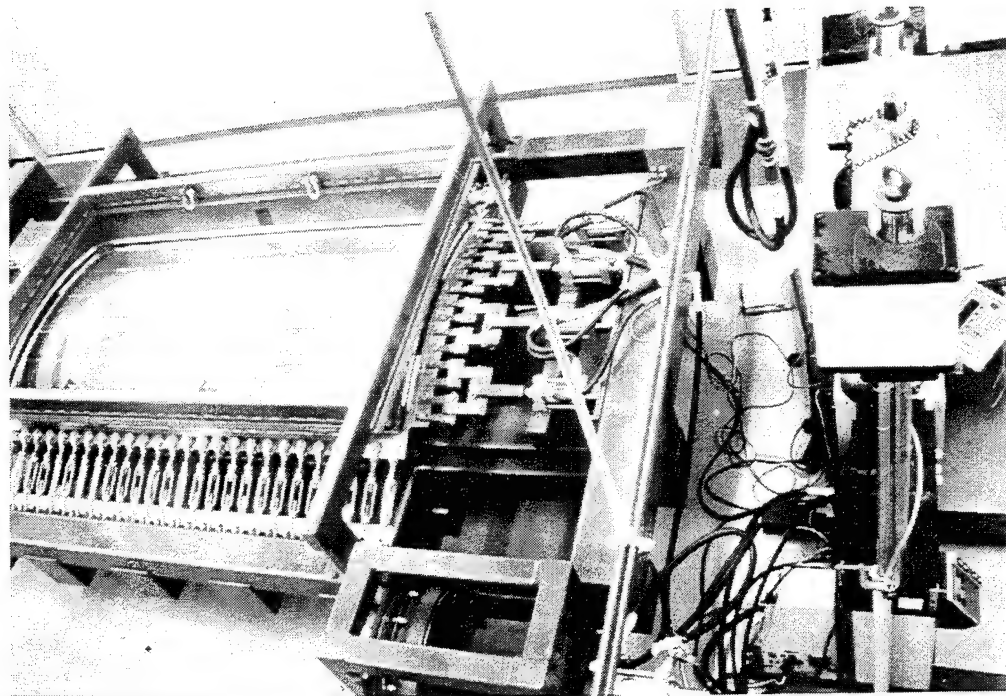
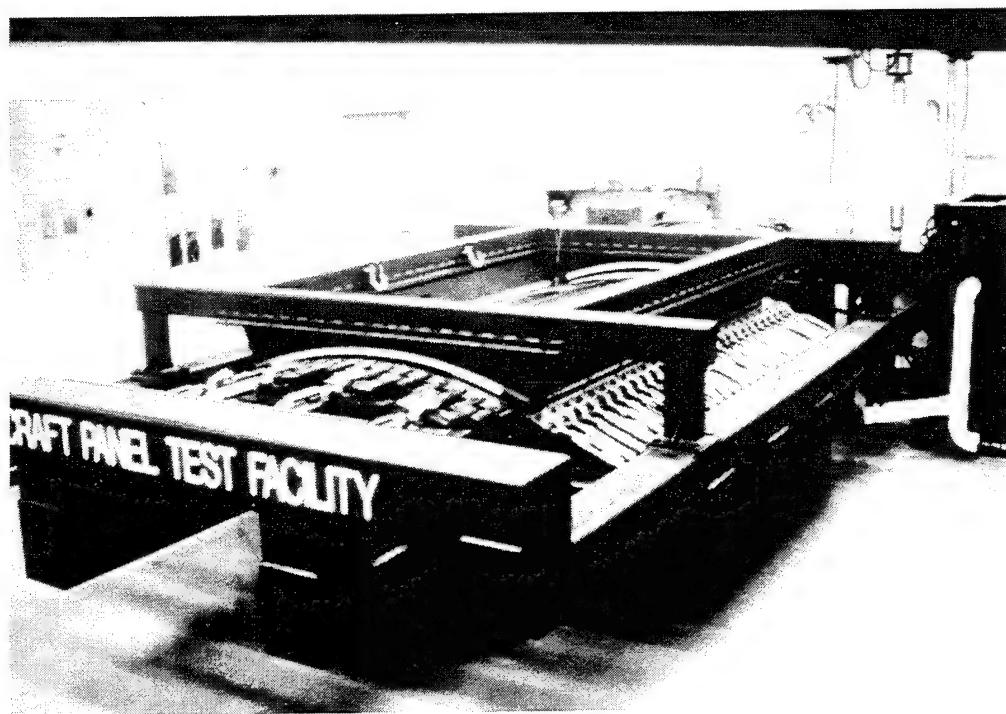
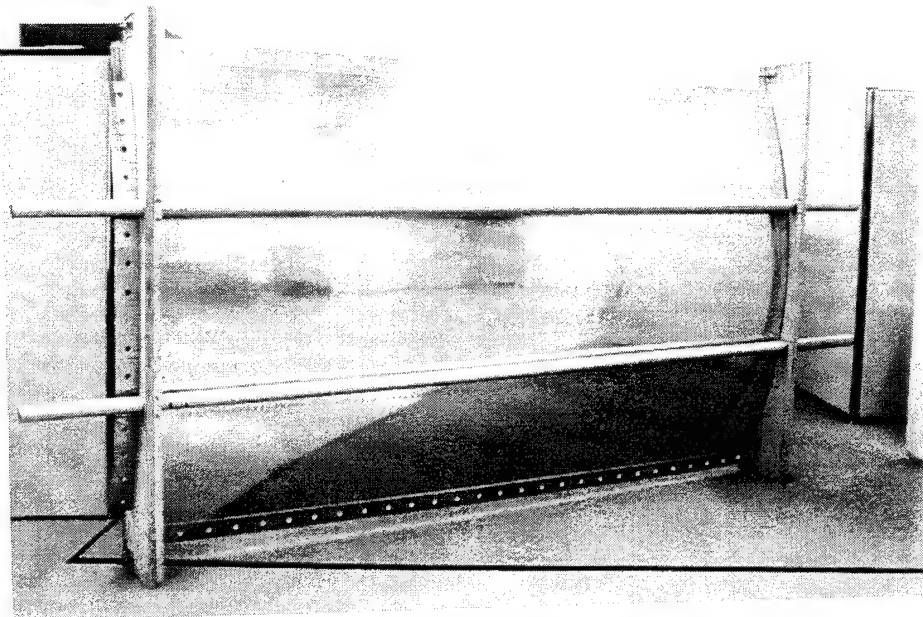


Figure 1.1. Full-Scale Panel Test Facility.



(a) *Exterior View.*



(b) *Interior View.*

Figure 1.2. Fuselage Lap Splice Test Panels Used in Full-Scale Facility.

In 1992, the Aging Aircraft Nondestructive Inspection Validation Center (AANC) at Sandia National Laboratories acquired a Boeing 737 airplane for use as a transport test bed. During January and February 1994, a series of ground pressurization tests was conducted on the AANC airplane with gages installed at critical areas on the fuselage to measure strains. The specific objectives of the AANC tests were:

- (1) to monitor the state of strain at the probable location of failure initiation in the Aloha Boeing 737 airplane; and
- (2) to validate results from other experimental and analytical research efforts supported by FAATC's National Aging Aircraft Research Program (NAARP). Particular attention was given to verify the Foster-Miller full-scale test results, and to evaluate the accuracy of the finite element models developed by the Volpe Center for aircraft fuselages.

In addition to the FAATC-supported research activities, an analytical and experimental program is underway at the NASA Langley Research Center to study multiple site fatigue cracking in fuselage skin joints. One of the goals of the NASA study is to develop and verify the methodology necessary to predict the fatigue crack growth behavior in such joints. In support of this effort, strains and displacements were measured in a small area near a lap joint at the tail end of a Boeing 737 fuselage. The results of the NASA tests were reported by Phillips and Britt [5]. The AANC tests provided an expansion of the NASA activity since 100 strain and two displacement channels were used to monitor 5 different lap splice bays compared to 36 channels and one lap splice bay monitored in the NASA test. In addition to strains in the fuselage skin (internal and external), the AANC tests also measured strains in the substructure elements such as stringers, tear straps, and frames.

The airplane acquired by the AANC is a Boeing 737-200, Serial Number 19058, Line Number 49. A photograph of the AANC B737 airplane is shown in Figure 1.3. According to the Aircraft Utilization Database [6], this airplane was in service between August 1968 and February 1992. During these dates, the airplane accumulated 46,358 cycles in 38,342 flight hours. The most important structural feature pertinent to this test was that the lap splice joints were not altered with the terminating action. The terminating action is a remedial repair which entails the replacement of shear head countersunk rivets with universal head rivets that have a larger shank diameter². In this context, the upper rivet rows on the lap joints on the AANC aircraft all contained shear head countersunk rivets.

² Boeing Service Bulletin 737-53A Revision 3 [7] describes this remedial action repair for fuselage lap splices.



Figure 1.3. Photograph of FAA/AANC Boeing 737 Airplane Test Bed.

The purposes of this report are: (1) to document the procedures and implementation of the strain gage tests conducted on the AANC Boeing 737 aircraft, (2) to present data characterizing strains near the lap splices of the AANC airplane, and (3) to correlate the AANC strain gage data with data obtained from other sources.

Section 2 is a description of the test plan for collecting strain data and its implementation. The process of selecting the various test sections for strain gage deployment is described in detail. Accordingly, five (5) lap splice bays were instrumented with a total of 98 strain gages. The specific strain gage layouts in each test section are included in Appendix A. The data acquisition system and the ground pressurization of the aircraft are also described in this part of the report.

In Section 3, data are presented to characterize the strain fields in the various test sections of the AANC airplane. Particular attention is given to the state of strain near the lap splices, and to the load transfer through the joints. Strains in both the skin and substructure elements (e.g., stringers, tear straps and frames) are presented. Bending strains, membrane stresses, and principal stresses are calculated from these data. Appendix B contains the strain gage data collected from two pressurization tests on the AANC airplane.

In Section 4, the AANC strain gage data are compared with data from the following sources:

- (1) Foster-Miller full-scale panel tests [4],
- (2) NASA Boeing 737 tests [5], and
- (3) results from finite element models developed by the Volpe Center.

Section 4 also includes comparisons among the different test sections in the AANC tests.

Finally, results and conclusions are summarized in Section 5.

2. TEST PLAN AND IMPLEMENTATION

The cabin of the AANC aircraft was pressurized to simulate in-flight loads experienced by the fuselage skin and its supporting structure. The equipment and methodology for this ground pressurization test are described in this part of the report (see Section 2.3). The most fundamental pre-test consideration in the AANC tests was the selection of the various lap splice bays for strain gage instrumentation. Ninety-eight (98) strain gages were mounted in 5 different lap splice bays on the fuselage of the aircraft. The process for selecting the instrumented areas is explained in the following text. Sections of the aircraft above and below the windows, and forward and aft of the wing were instrumented to study structural uniformity, effects of fuselage bending and effects of different frame configurations. The terms "interrupted" and "continuous" are used in this report to refer to two different frame configurations (see Section 2.1.1). Other information regarding the types of strain gages, data acquisition, and specialized test support equipment is also presented.

The selection of strain gage locations accommodated the following issues:

- instrumentation of several key lap splice joint bays, inside and out, with strain gages;
- instrumentation of similar bays forward and aft of the wing to assess variations due to bending;
- selection of strain gage locations to resemble the strain gage layouts in the Foster-Miller and NASA tests to allow for straightforward comparisons;
- determination of strain levels in high gradient areas on the skin as well as on substructure elements such as tear straps, stringers, and frames;
- configuration of gages in single arm bridges to measure uniaxial strains with some rosettes used to provide principal strain data;
- pressurization of the aircraft up to 6.5 psi with strain measured during increasing and decreasing pressure.

For reference during the following discussion, a schematic of the entire test set-up is shown in Figure 2.1.

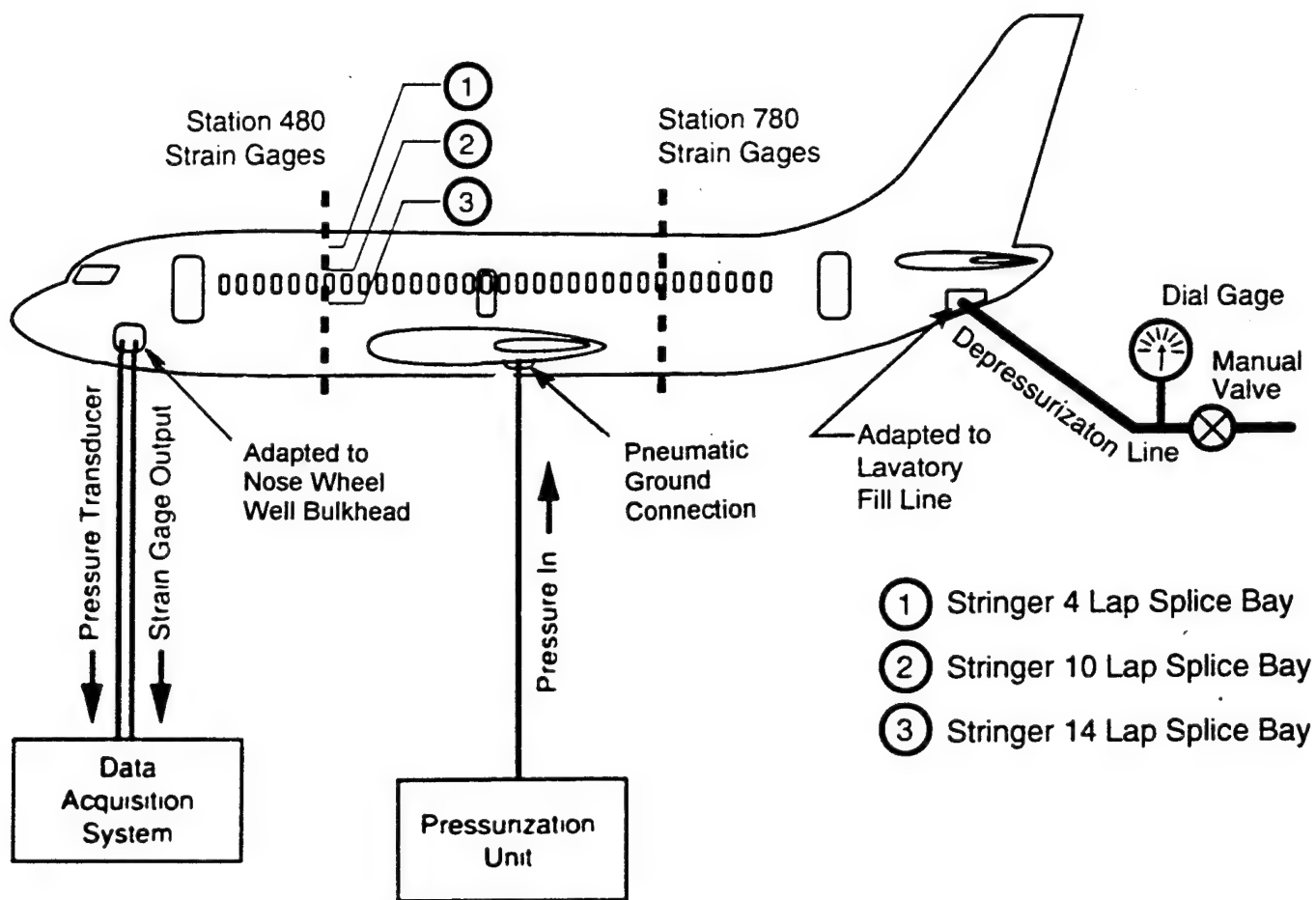


Figure 2.1. AANC 737 Strain Monitoring Test Set-Up.

2.1 SELECTION OF LAP SPLICE TEST SECTIONS

The process for selecting the exact locations on the fuselage to install strain gages was broken down into three steps:

- (1) selecting circumferential position of the bay (i.e., stringer location),
- (2) selecting longitudinal position of the bay (i.e., body station location), and
- (3) selecting specific locations within the selected bay.

2.1.1 Selection of Circumferential Positions on the Fuselage

Five (5) fuselage stringers with lap splice joints can be found on both the left and right side of the Boeing 737 airplane. These stringers are designated as S-4, S-10, S-14, S-19, and S-25. Stringers are numbered sequentially from the crown (S-1) to the keel (S-28). An additional designation, either "R" or "L", is generally used to refer to the left and right side of the aircraft when facing forward. For the purposes of this study, the aircraft is essentially symmetric.

The National Transportation Safety Board (NTSB) report [1] on the Aloha accident concluded that the most likely point of failure initiation was the fuselage lap splice at stringer S-10L in Section 43 (see Figure 2.2). The S-10 stringers are located just above the windows in the fuselage. Therefore, bays at the S-10 stringer locations were chosen as areas for strain gage instrumentation.

The lap joints at the S-4 stringers are located closer to the aircraft crown, and are more isolated from the structural effects of windows. Bays at these locations were considered to be ideal for comparisons with the Foster-Miller panels.

The lap joints at the S-14 stringer are located between the windows and the floor line. Both structural features have the potential to affect the strain field. The remaining lap joints, S-19 and S-25, are below the floor level of the aircraft. The structure in this region is significantly different from the region above the floor in that the circumferential frames are "interrupted" by the longitudinal stringers. Specifically, the frames extend radially between stringers and are riveted directly to the skin and stringers. Figure 2.3 shows the difference between the interrupted and continuous frame configurations. The additional stiffening provided to the skin by the interrupted frames may be necessary for the structure to support the load in the cargo bay. The interrupted frame configuration, however, is not representative of the Foster-Miller panel construction or the location where failure is believed to have initiated in the Aloha Airlines accident. In addition, much of the fuselage skin below the floor level may be influenced by the landing gear and their associated bays. For these reasons, the lap splices at stringers S-19 and S-25 were not chosen for strain gage instrumentation.

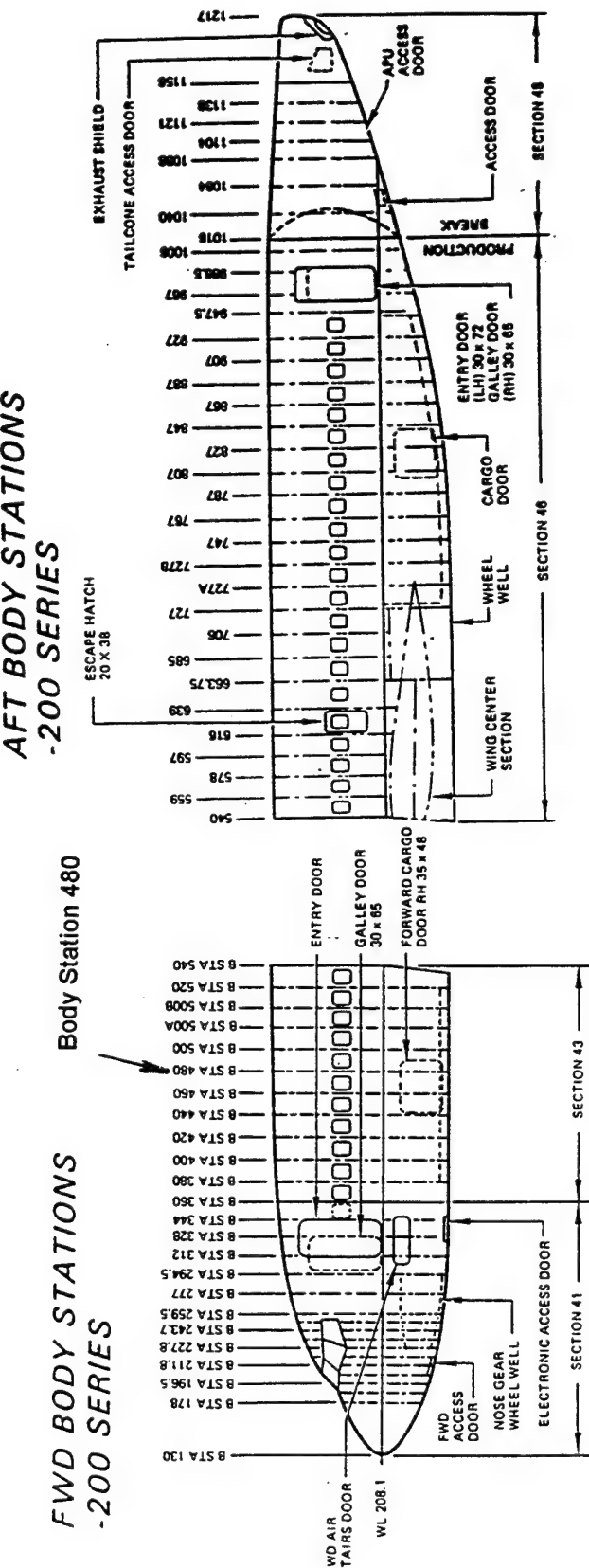
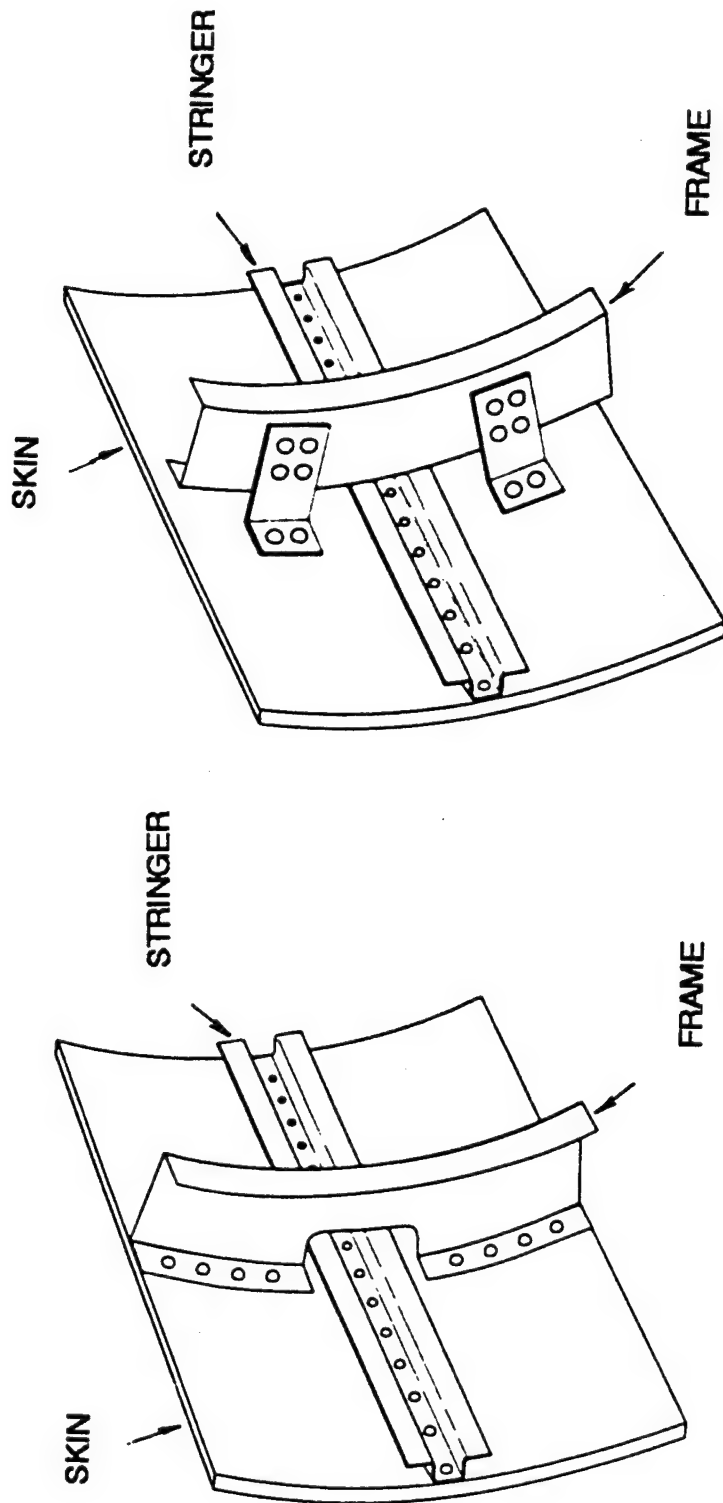


Figure 2.2. Forward and Aft Body Stations in AANC B737.



(a) Below Floor Level (Interrupted Configuration)

(b) Above Floor Level (Continuous Configuration)

Figure 2.3. Frame Configurations Above and Below Floor Level in AANC B737.

2.1.2 Selection of Longitudinal Positions on the Fuselage

One of the considerations in selecting bays to deploy strain gages was to minimize the effects of structural interaction. In the context of selecting longitudinal positions, this means avoiding proximity to major structural features such as wings, doors, vertical and horizontal stabilizers, repairs, and tapers in the fuselage radius. Another consideration was to select areas with minimal fuselage bending which produces longitudinal stresses. Longitudinal bending also affects the circumferential or hoop stress through Poisson's ratio.

An elementary beam analysis of a fuselage supported by two sets of landing gear suggests that the magnitude of the fuselage bending moment reaches a local minimum between the two landing gear. A generic sketch of this concept is shown in the shear and moment diagrams illustrated in Figure 2.4. The uniform weight distribution of the fuselage, as shown in the figure, is a simplification, but is useful to illustrate the concept. The exact location of the local minimum is not critical since other practical considerations govern. Specifically, the location of the instrumented bays at Body Station 480 (designated as BS480) were chosen to be as far forward relative to the wing as possible to minimize structural interaction. The longitudinal location of all bays was chosen to have a uniform cross section as opposed to locations where the diameter of the fuselage tapers. The lap splice at BS480 is considered to be the primary longitudinal position of interest because of its relatively low fuselage bending moment and its proximity to the probable failure initiation point on the Aloha aircraft.

A second longitudinal position was chosen near the tail end of the aircraft. The area near BS800 is relatively free of major structural interactions. It is, however, subject to the fuselage bending moment induced by the weight distribution of the empennage. Nonetheless, this location provides a useful comparison to the more forward location as well as to the strain characterization experiments performed by Phillips and Britt [5] which were conducted at BS862 on the NASA Boeing 737.

2.1.3 Locations within Selected Bays

Specific strain gage locations were selected within a given lap splice bay to resemble the strain gage layouts in the Foster-Miller [4] and NASA [5] tests which allowed for direct comparisons of strains. Seven (7) circumferential positions were identified (refer to Figure 2.5):

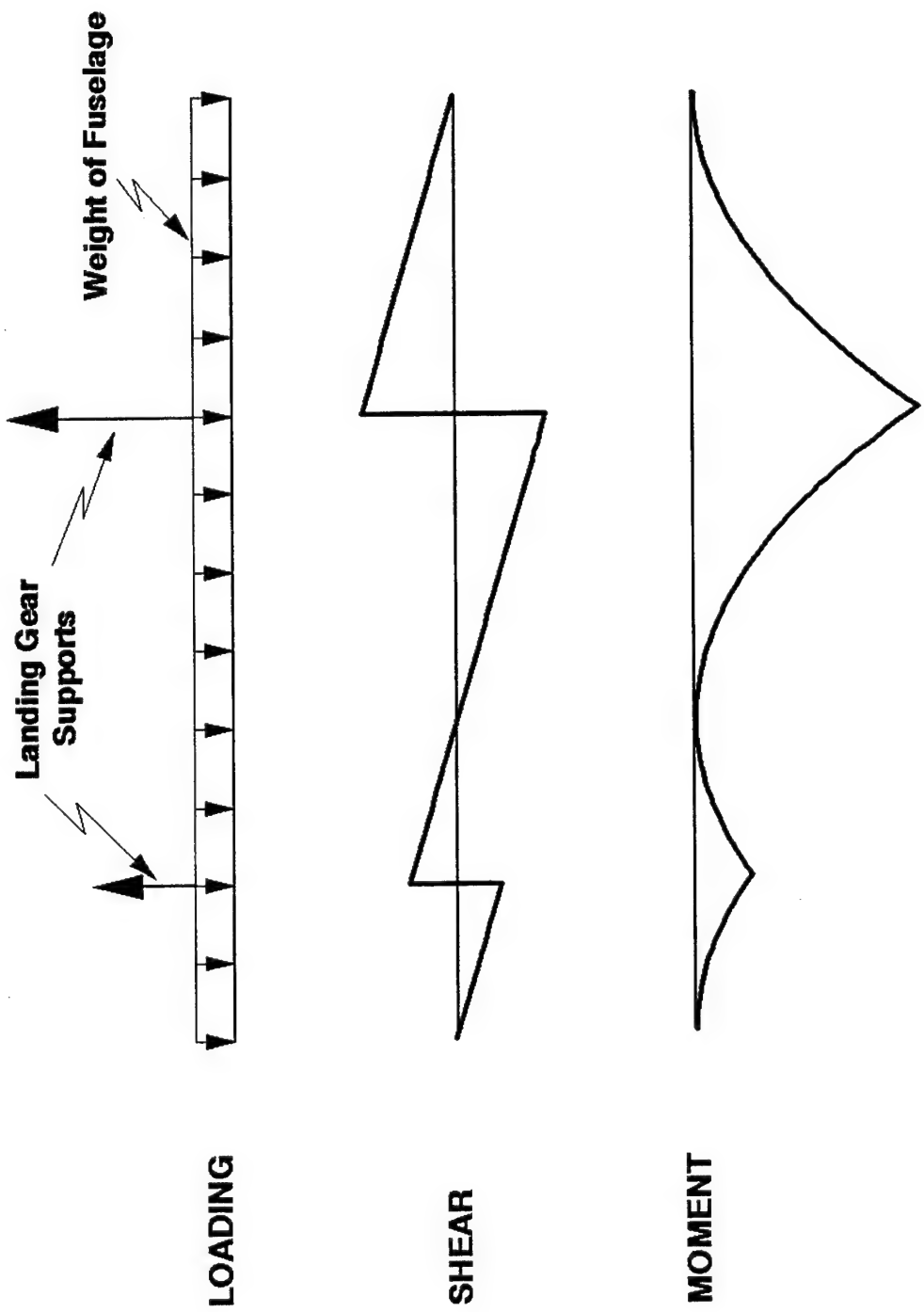


Figure 2.4. Generic Shear and Moment Diagrams for Fuselage Supported by Two Sets of Landing Gear.

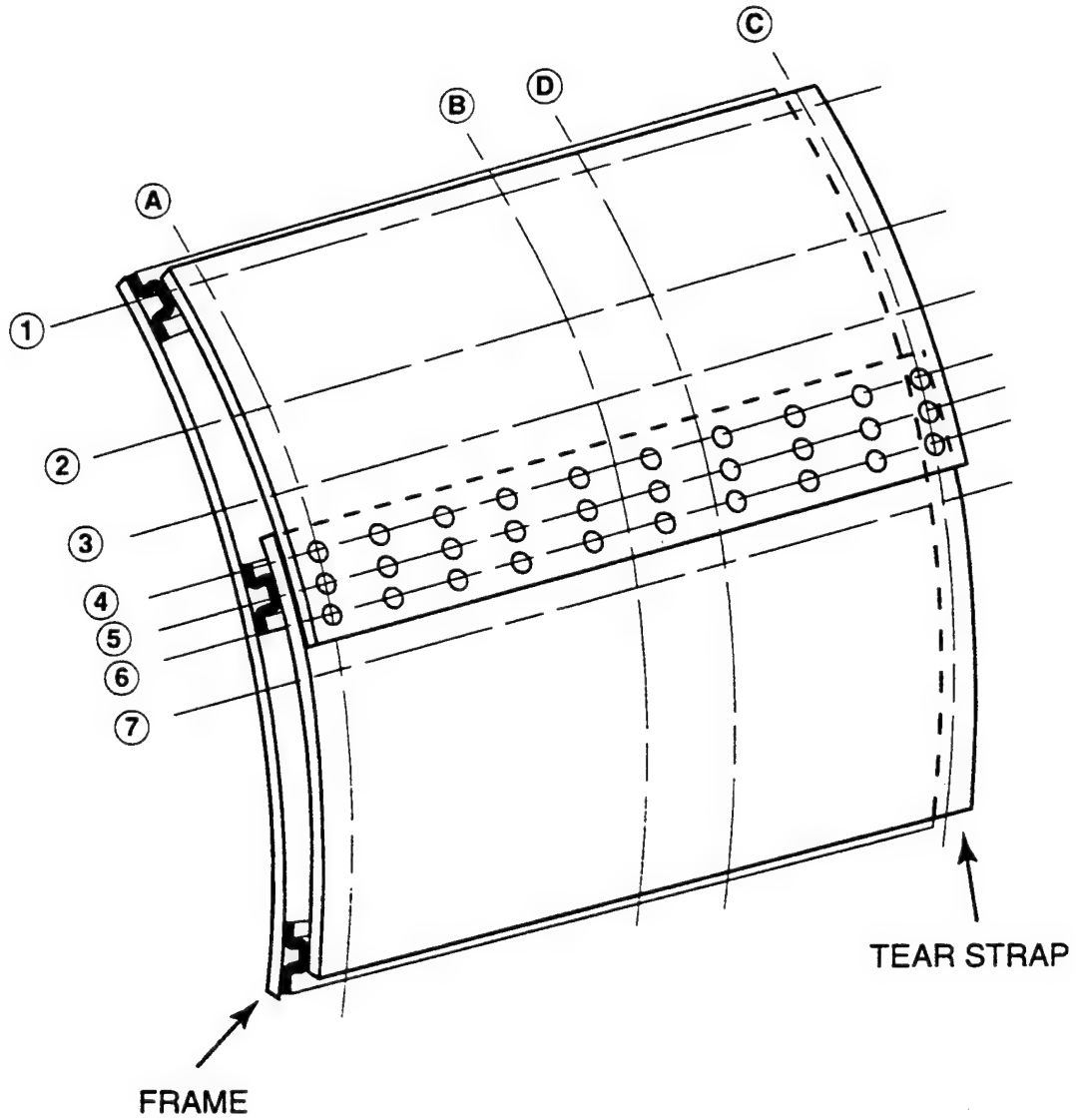


Figure 2.5. Specific Strain Gage Locations Within Selected Lap Splice Bays.

- (1) the stringer above the lap joint,
- (2) a "midbay" location: halfway between the lap joint stringer and the one above it,
- (3) a position just above the upper boundary of the lap joint, two inches above the lap joint stringer,
- (4) the upper row of rivets in the lap joint,
- (5) the middle row of rivets and the lap joint stringer,
- (6) the lower row of rivets, and
- (7) a position just below the lower boundary of the lap joint, two inches below the lap joint stringer.

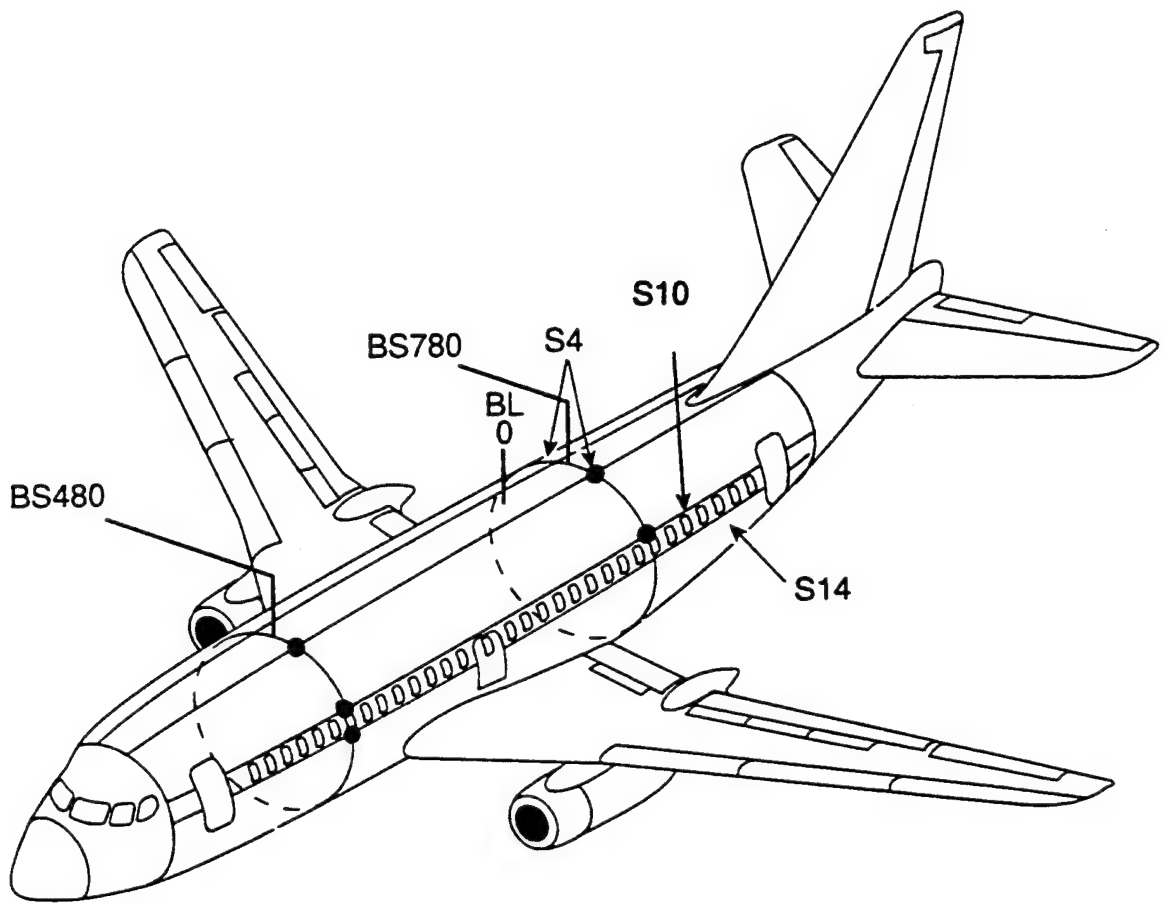
Four (4) longitudinal positions were also identified (see Figure 2.5):

- (1) along the frame,
- (2) a "midline" location: halfway between the tear strap and the frame, halfway between the two central rivets,
- (3) along the tear strap, and
- (4) one inch from the midline location, but closer to the tear strap than the frame.

In addition to comparisons with other strain data, characterization of the strain gradient across the lap splice was considered in the selection of strain gage locations. The effects of local bending were examined by installing gages on both the inside and outside surfaces of the fuselage skins at coincident locations. Substructure elements such as tear straps, stringers, and frames were also instrumented to assess load transfer into the fuselage structure.

2.1.4 Strain Gage Deployment

Based upon the aircraft structure selection process and the considerations mentioned previously, five (5) lap splice locations on the fuselage of the AANC Boeing 737 airplane were chosen for strain gage instrumentation. The relative locations of the instrumented lap splice bays on the AANC airplane are shown schematically in Figure 2.6. The gages monitored strain levels in high gradient areas on the skin as well as on substructure elements such as tear straps, stringers, and frames. Each strain gage monitored uniaxial strains with some gages arranged in rosette configurations to provide principal strain data. The distribution of strain gages in each test bay of the aircraft is summarized in Table 2.1. Figures A.1 to A.3 in Appendix A show the generic strain gage layouts for 36-gage, 10-gage, and 8-gage configurations, respectively. Longitudinal, biaxial, rosette, as well as interior and exterior designations are provided to clarify the structure being monitored. Figures A.4 to A.15 in Appendix A show the exact locations of the uniaxial, biaxial, and rosette gages in the various lap splice bays.



● – location of instrumented lap splice bay

Figure 2.6. Locations of Lap Splice Test Sections on AANC Airplane.

Table 2.1. Summary of AANC Strain Gage Deployment.

Stringer Number	Body Station Location	Number of Gages in Bay	Reference Figure	Remarks
S-4L	BS470-BS480	36	A-1,4,7,14	Compares with FMI full-scale panel [4].
S-10L	BS470-BS480	36	A-1,5,8,15	Compares with initiation site on Aloha B737 [1].
S-14L	BS470-BS480	10	A-2,6,9	Affected by windows and floor beams.
S-4L	BS780-BS790	8	A-3,10	Affected by fuselage bending. Also, compares with NASA test [5].
S-10L	BS780-BS790	8	A-3,11	Affected by fuselage bending.

The photograph in Figure 2.7 shows the exterior of the AANC Boeing 737 airplane between Body Stations 470 and 480 where three lap splice bays are instrumented. The gage installations around stringer S-10L (above the window) and stringer S-14L (below the window) are visible in the photograph. The gages mounted near the crown of the B737 (i.e., the lap splice bay at stringer S-4L) can also be seen in the background. A close-up view of the strain gage layout on the external skin between BS470 and BS480 at stringer S-14L is shown in Figure 2.8. A photograph of the strain gage array on the inside of the aircraft between the same body stations at stringer S-10L is shown in Figure 2.9. In this photograph, strain gages can be seen on the stringer, on the skin of the lap splice just above the window, and on the adjacent frame.

The lap joint bays around stringers S-4 (on crown) and S-10 (above window) were instrumented with the 36-gage array. Four gages in this array measured hoop strains along the circumference at the tear strap and frame locations. Most of the gages in this array were located along the midline of the bay; i.e., midway between the tear strap and the frame. Biaxial gages were used to measure strains in the longitudinal and hoop directions. Several of these gages were mounted on the interior to monitor the circumferential bending of the joint and load transfer across the rivets. Several triaxial (rosette) gages were mounted near structural reinforcements (tear strap and frame) to determine shearing strains in this area (i.e., orientation of the principal strains).



Figure 2.7. View of Instrumented Lap Splice Bays Above and Below the Window Between Body Stations 470 and 480.

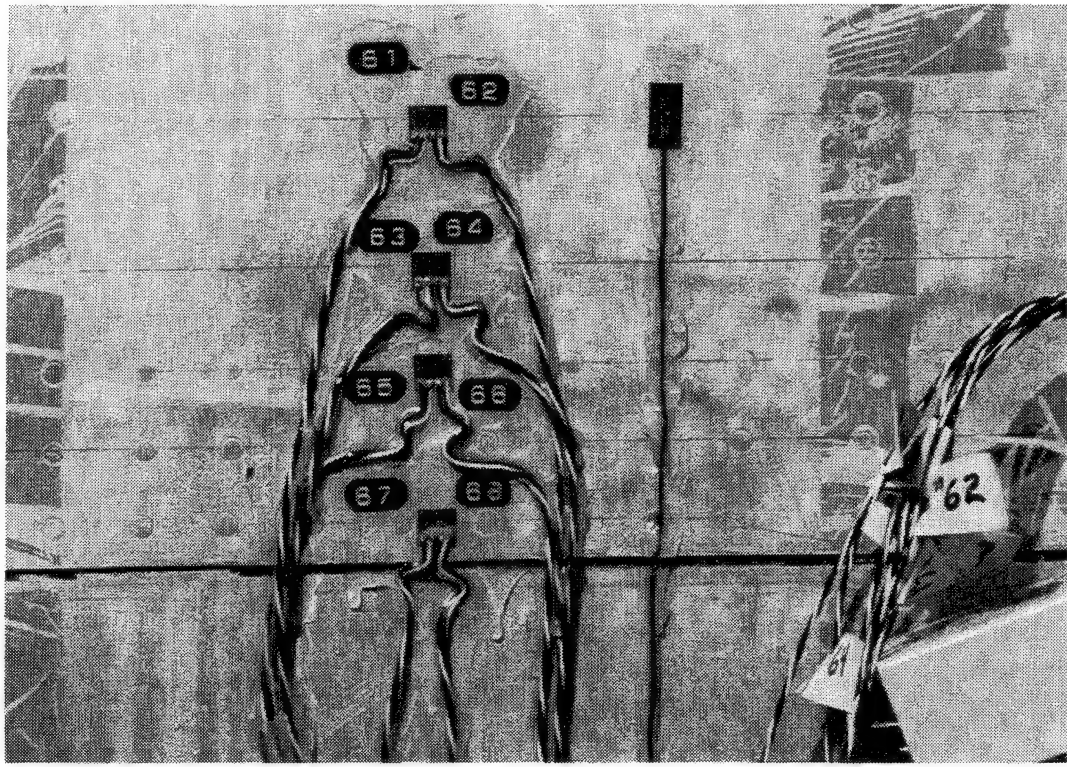


Figure 2.8. Photograph of External Skin Strain Gage Layout Between Body Stations 470 and 480 at Stringer S-14L.

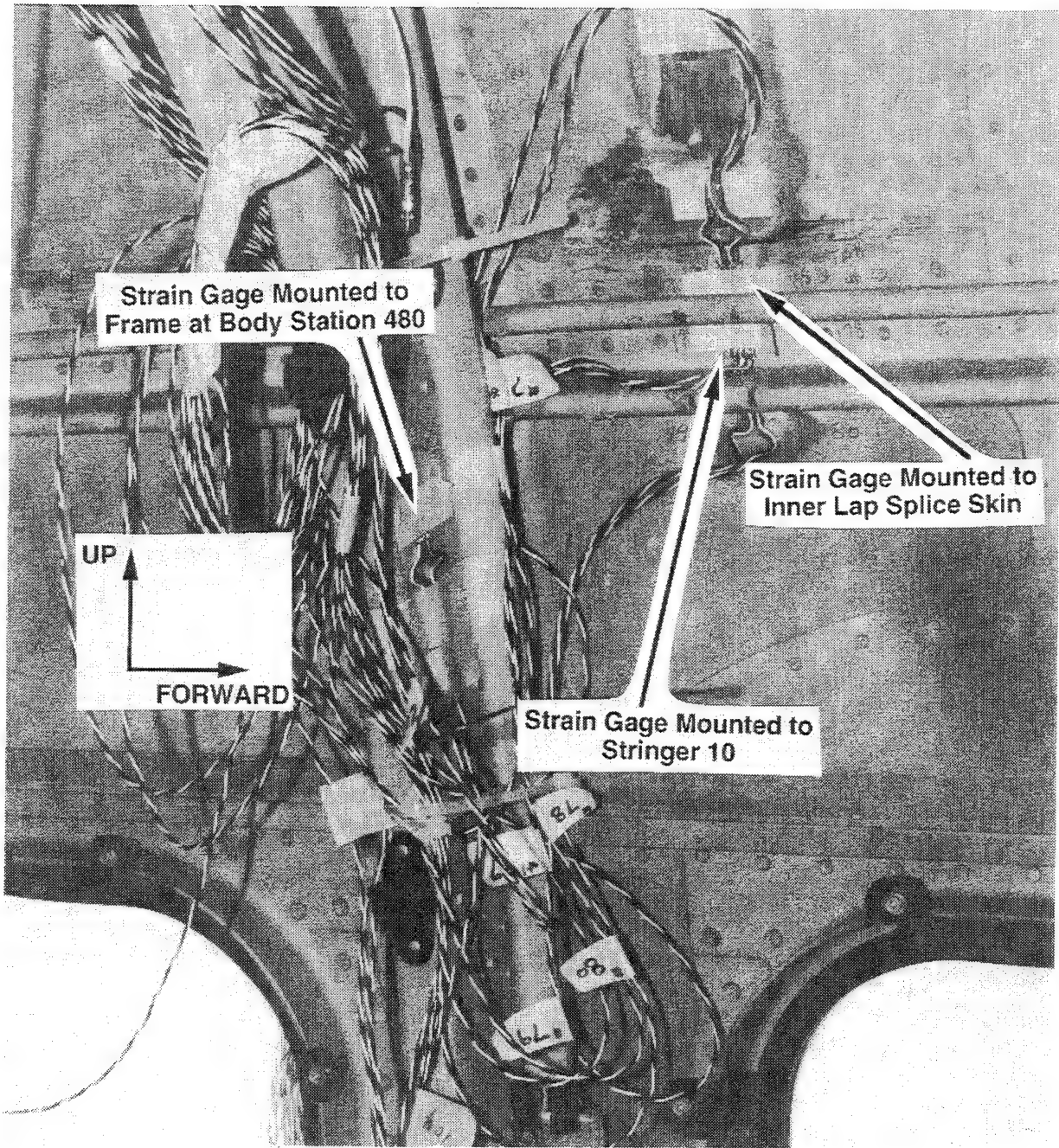


Figure 2.9. Strain Gage Installations on the Interior of AANC B737 Around Stringer S-10L.

Stringer S-14 is located between the windows and the floor line. A subset of the S-4 and S-10 strain gage configurations was installed at the S-14 test section to obtain data which may provide an understanding of how the various reinforcing structures interact. Biaxial gages were concentrated between the tear strap and frame because results from related studies have indicated that this area contains the highest strains.

The longitudinal position of the test sections on the AANC airplane were located forward and aft of the wing (see Figure 2.6). At these two longitudinal positions, the cross section of the fuselage was identical, and the strain singularities due to wing effects were negligible. Installation of similar strain gage configurations in bays forward and aft of the wing allowed for direct comparisons of strains between areas experiencing different fuselage bending loads. The lap splice bays between BS470 and BS480 were considered the primary test sections because fuselage bending effects were assumed to be negligible at those locations, and because of their direct relationship with the Aloha aircraft and the Foster-Miller test panels.

Gages were also mounted on unstrained plates of similar aluminum, and placed near the instrumented lap splice bays on both the inside and outside of the airplane. The data collected from these gages represented a reference state of strain from which thermal effects and strain signals due to spurious noise were determined (see Section 3.5).

2.2 INSTRUMENTATION

Strain gage specifications, the set-up to measure fuselage radial displacement, and the data acquisition system are described in this part of the report.

2.2.1 Strain Gage Specifications

The strain gages used for these tests were all encapsulated constantan foil gages with a nominal resistance of 350 ohms and a gage length of 0.125 inch. They were purchased from Micro-Measurements, Inc. and the designations for the gages are CEA-13-125UN-350, CEA-13-125UT-350, and CEA-13-125UR-350 for the uniaxial, biaxial, and rosette configurations, respectively. All of the biaxial and three element 45-degree rosette gages were in the single plane or unstacked configuration. These particular gages were manufactured to match the thermal coefficient of expansion of 2024-T3 aluminum so that this installation was considered a self-temperature-compensated (STC) set-up. The result was a flat thermal output (i.e. almost zero thermally induced strain) over a temperature range of 0 to 200 °F. The sensitivity or Gage Factor of the strain

gages, which relates change in resistivity to actual strain levels, is 2.05. The gage resistance of 350 ohms was chosen because it allows for higher excitation and a corresponding improvement in the signal-to-noise ratio. This resistance also reduces lead-wire effects.

The strain gage installation was performed using materials purchased from Micro-Measurements. First, the paint and primer was removed from the aircraft structure using fine grit sandpaper. Surface preparation was carried out with the following chemicals: CSM-1 degreaser, M-Prep Conditioner A, and M-Prep Neutralizer 5A. The gages were bonded using M-Bond 200 adhesive. Finally, a layer of RTV 3140 silicon rubber was placed over the entire installation to provide protection from moisture.

2.2.2 Measurement of Fuselage Radial Displacement

Since hoop strains are the primary strains associated with fuselage pressurization, the corresponding radial growth of the fuselage was also measured. Zero to five volt direct current (dc) linear voltage displacement transducers (LVDT's) were mounted circumferentially across the inside of the aircraft at both the BS475 and BS785 lap splice bay locations. In this test set-up, the total displacement between stringers S-14L and S-10R was measured during cabin pressurization. The LVDT's were connected to a data acquisition system located outside the aircraft using 80-foot lengths of wire.

2.2.3 Data Acquisition System

The hardware for data acquisition was controlled by a personal computer with Disk Operating System (DOS). The system provided power up to 100 strain gage channels - in quarter, full- or half-bridge configurations - and 20 full-bridge transducers. The system also contained a controller to provide logic and timing commands to the data scanner and to digitize the signal received from the scanner. The data acquisition system was capable of scanning 30 channels per second. Entry of all test data was automated using manufacturer supplied software. Figure 2.10 shows a photograph of the data acquisition system positioned next to the AANC B737 aircraft. The computer operator shown in the photograph is using an intercom system which linked the data acquisition personnel with the cockpit personnel (fuselage pressure control) and the test equipment personnel (Ground Power and Airstart Unit control).



Figure 2.10. Portable Data Acquisition System.

During pressurization of the AANC B737, the following data channels were monitored:

- (1) 98 channels of strain from aircraft structure
- (2) 2 strain gage control channels to measure temperature and noise effects
- (3) 1 digital pressure transducer accurate to ± 0.05 psig
- (4) 2 displacement transducers to measure fuselage radial growth
- (5) 2 thermocouples to measure internal and external air temperature.

The pressure transducer was connected to an existing auxiliary bulkhead port in the aft end of the aircraft. Each gage was prepared in a quarter-bridge arrangement to monitor all uniaxial strain levels. The data acquisition system was then programmed to calculate principal strains and directions from the rosettes according to strain gage sets specified by the user. A conventional three-wire system was used to eliminate any erroneous strain readings caused by resistance build-up in the lead wires (70 to 90-foot lengths). The computer provided a real-time display of strain and pressure data in graphical format. A strip chart plotted profiles of pressure versus time for each cycle. The wires from all internal instrumentation were transferred outside the aircraft through a series of sealed bulkhead pass-throughs installed in the nose wheel well. Figure 2.11 shows the two 26-pin electrical connectors sealed against the wheel well bulkhead. Also shown is a pressure fitting connected to an external pressure dial gage with 0.1 psig resolution. This dial gage was placed outside the cockpit window, and provided real-time feedback to the personnel controlling the cabin pressure.

2.3 AIRCRAFT GROUND PRESSURIZATION

The AANC airplane was pressurized using an Airstart Unit borrowed from Kirtland Air Force Base. Figure 2.12 shows a photograph of the Airstart Unit located next to the AANC Boeing 737. The unit was calibrated to provide the maximum allowable flow rate for the Boeing 737 duct work. The maximum differential pressure applied to the aircraft was dictated by flow restrictions and aircraft leakage. Leaks in the fuselage were sealed to minimize loss of pressure. These areas included door seals, drain hole seals, lavatory and galley vents, seals on dump valves, air inlet valves, and check valves. The Airstart Unit was connected to the aircraft packs so that the turbines could maximize the volume flow into the aircraft. The aircraft was equipped with pressure relief valves that were calibrated to prevent inadvertent pressurization beyond 8.5 psi. The maximum differential pressure in the AANC tests was 6.5 psi. This value, while less than the maximum pressure difference of 8.5 psi in the Foster-Miller tests, was sufficient to allow for accurate extrapolation of the strain data. Cabin pressure levels were regulated using the pressurization controls in the cockpit of the Boeing 737. The pressurization rates were chosen

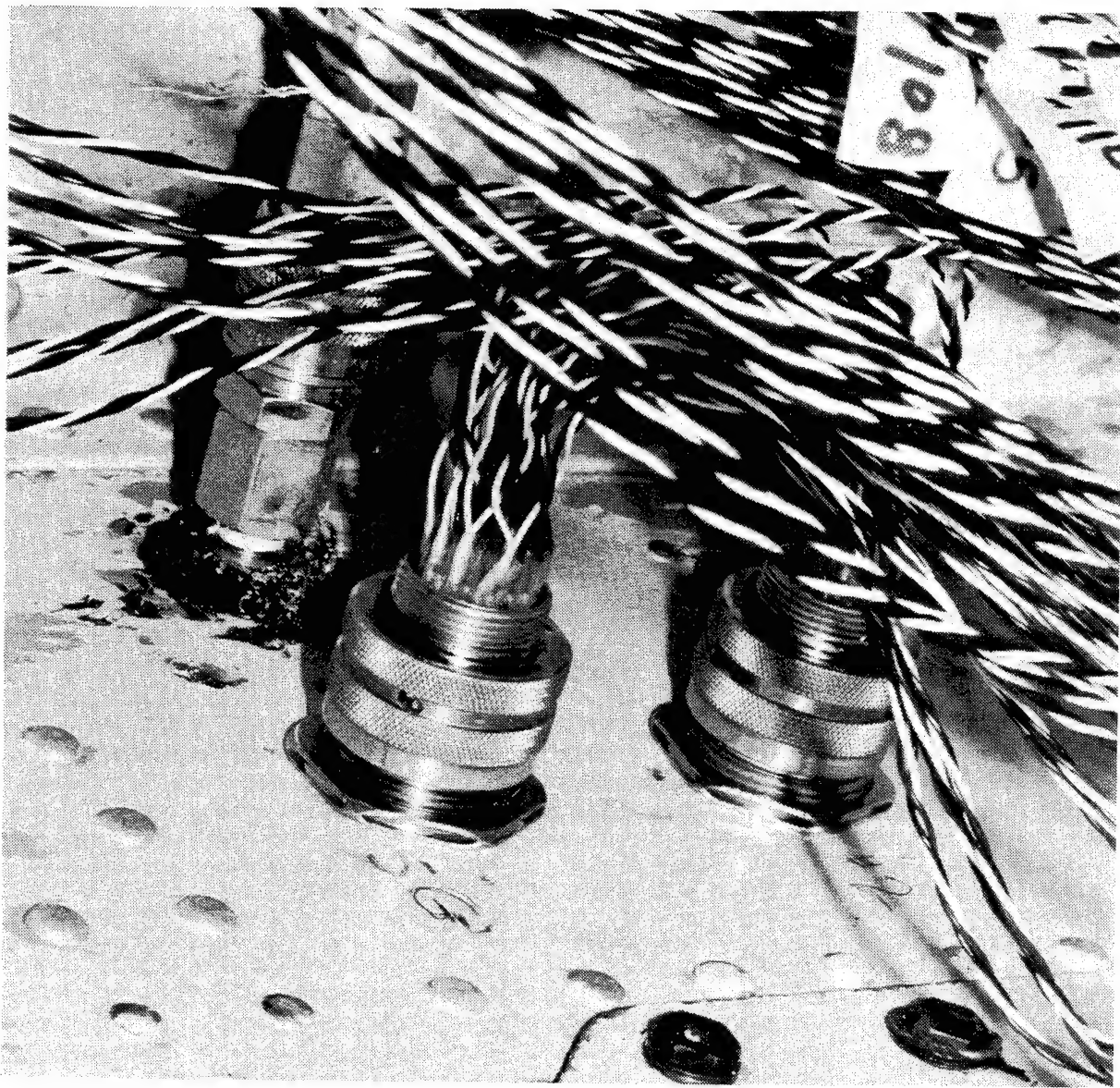


Figure 2.11. Two 26-Pin Electrical Connectors and Pressure Pass-Through Sealed Against the Nose Wheel Well Bulkhead.

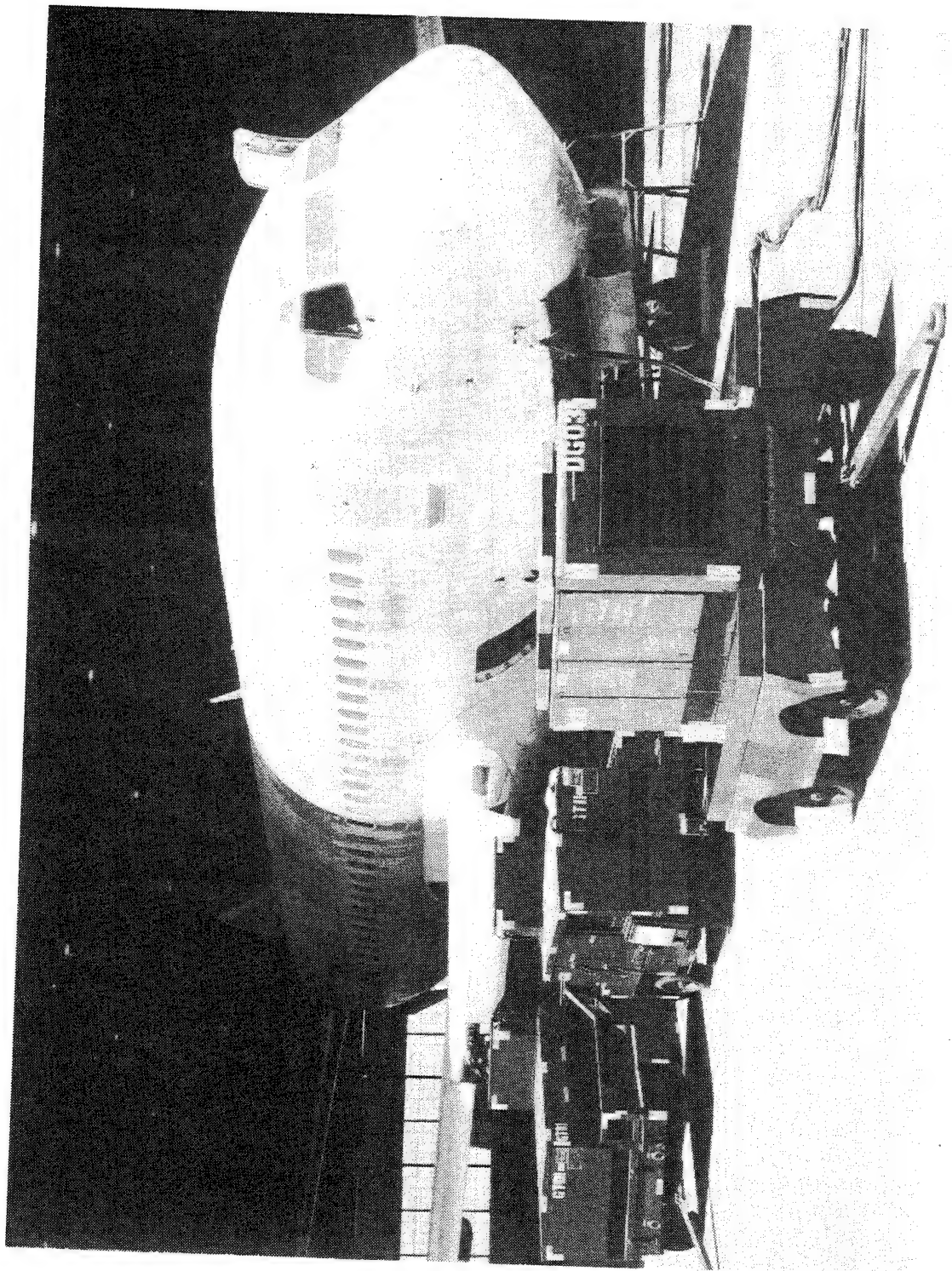


Figure 2.12. Photograph of AANC 737 with Airstart and Ground Pressurization Units.

to closely match those associated with normal aircraft climb rates.

In the AANC tests, data were recorded during loading and unloading of the fuselage to determine any hysteresis effects. Strain gage measurements were recorded for cabin pressures between 0 and 6.5 psi at 0.50 psi increments. A typical pressure profile is shown in Figure 2.13.

Prior to collecting strain gage data, several pre-test exercises were performed. These exercises were deemed necessary because the ability to control pressurization and depressurization rates and levels was essential to ensure accurate data. Discrete pressure levels had to be maintained because the data acquisition system required 3 to 4 seconds to record data. It was found that this test set-up could control pressures to within ± 0.05 psig and could maintain these pressures for the maximum required dwell time of 10 minutes. Additionally, the pre-test exercises allowed for verification of strain gage installations and for troubleshooting any instrumentation, wiring, data acquisition, and pressure-monitoring difficulties.

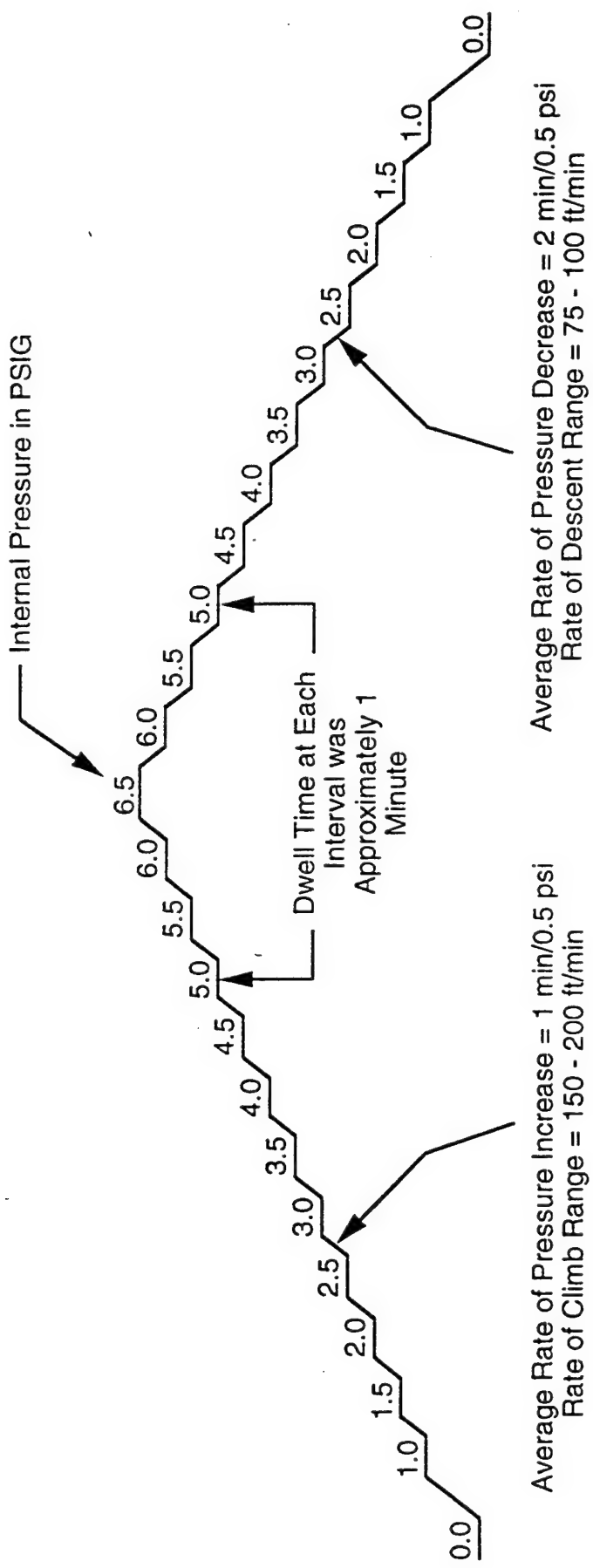


Figure 2.13. Typical Fuselage Pressure Profile.

3. EXPERIMENTAL STRAIN AND DISPLACEMENT DATA

Structural data were collected from 98 strain and 2 displacement channels during ground pressurization of the AANC aircraft. The data obtained from two of these pressurization tests are listed in Appendix B. In this section, some data are presented to characterize the strain fields in the different instrumented areas of the aircraft. These data are generally presented in the form of plots showing microstrain as a function of applied pressure. Particular attention is given to the state of strain near the lap splices and to the load transfer through the joints. Some consideration is also given to compensation for thermal and ambient noise-induced strains. Repeatability of strains over several pressure cycles is also discussed. Finally, stresses in the lap splice test sections and the radial displacement of the fuselage are examined.

3.1 EXTERNAL STRAINS IN THE SKIN

In this section, data collected from the exterior strain gages are used to examine the load transfer through the various lap splice joints. Strains at reinforced areas of the lap skin (e.g. near tear straps and frame), and strains across the lap splice joint are also examined. In general, the data presented are strains in the hoop or circumferential direction, but some data are also presented for strains in the longitudinal or axial direction.

3.1.1 Load Transfer Through the Lap Splice Joint

In each of the five (5) instrumented lap splice bays, gages were installed to monitor strain levels at locations above and below the joint as well as in the upper, middle, and lower rivet rows of the lap itself. Figures 3.1 through 3.5 show plots of hoop strains in the external skin as a function of pressure. The strain channels are grouped to show the load transfer in each lap splice joint. Furthermore, these grouped channels monitored strains along the midline¹ in each of the instrumented bays. The following observations can be made from these plots:

- (1) Most of the load in the skin above the lap splice joints is transferred into the skin around the upper rivet row. Strain levels above the lap joint (e.g., Channels 18 and 20) are approximately equal to those in the first row of rivets (e.g., Channel 24).

¹ The terms "midline" and "midbay" were defined in Section 2.1.3.

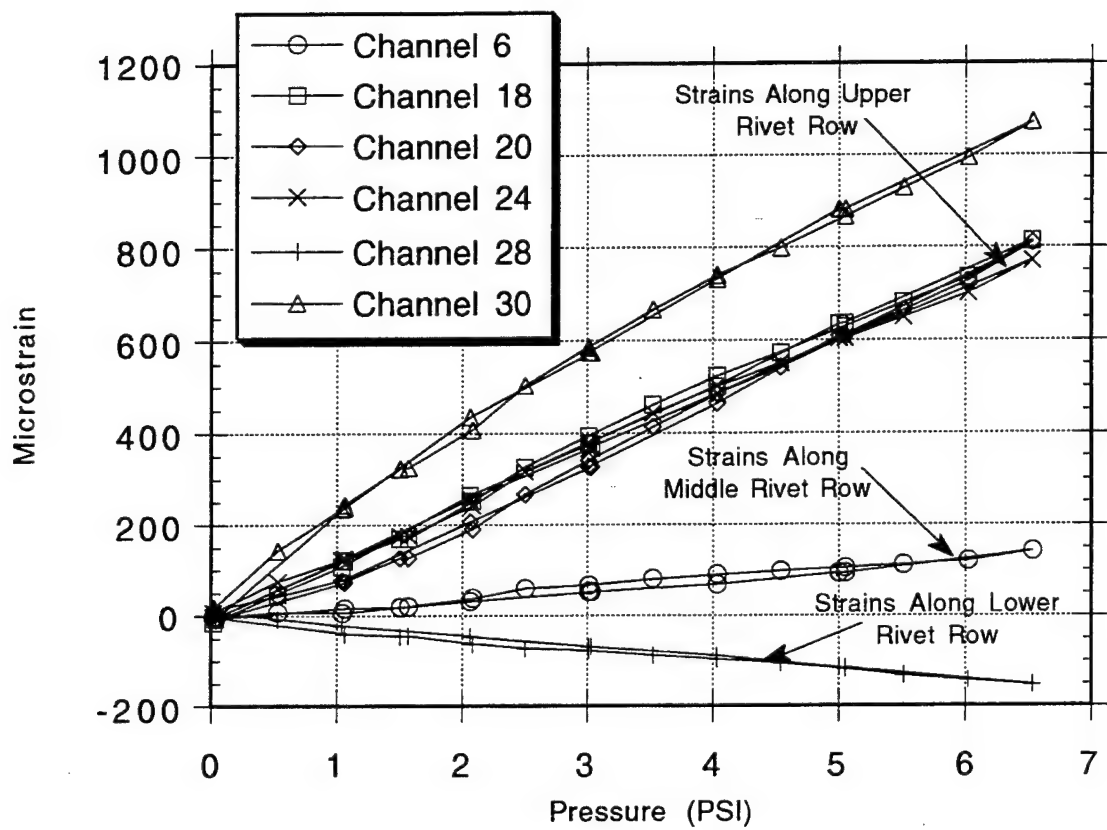


*Figure 3.1. External Skin Hoop Strains Along Midline at S-4L, BS475.
(Refer to Figure A.4 for specific location of channels.)*

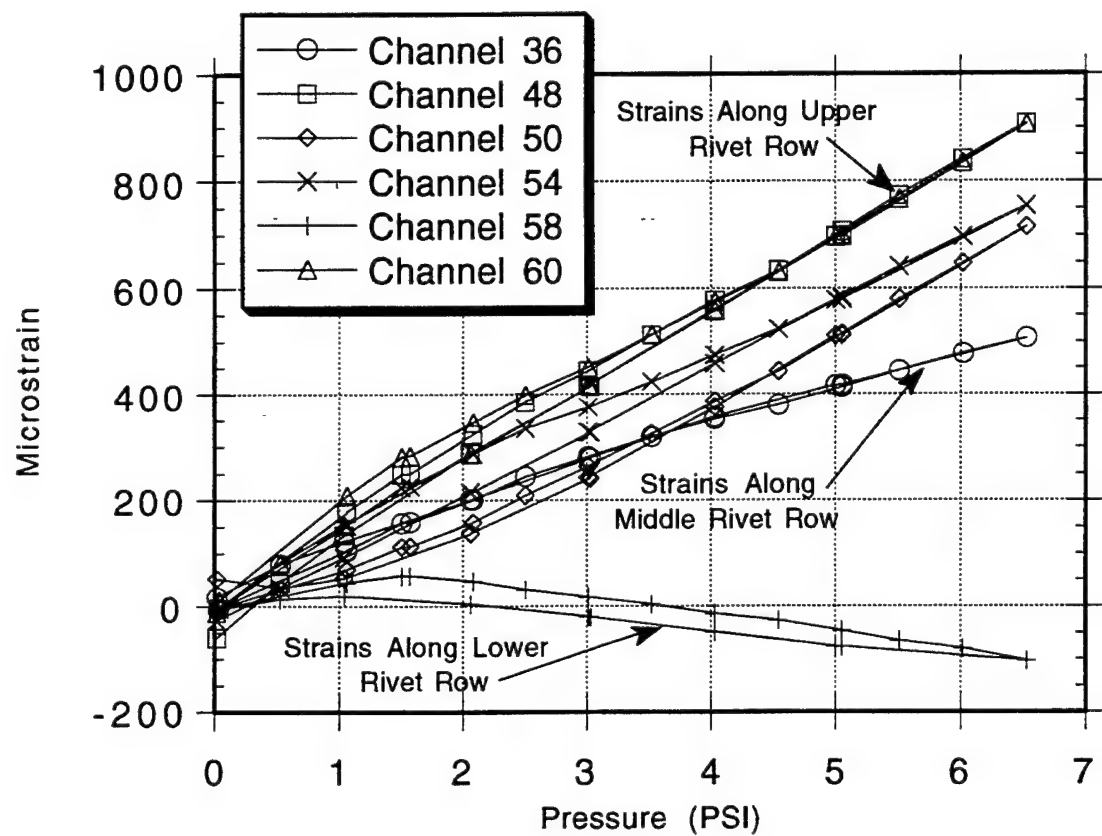


*Figure 3.2. External Skin Hoop Strains Along Midline at S-10L, BS475.
(Refer to Figure A.5.)*

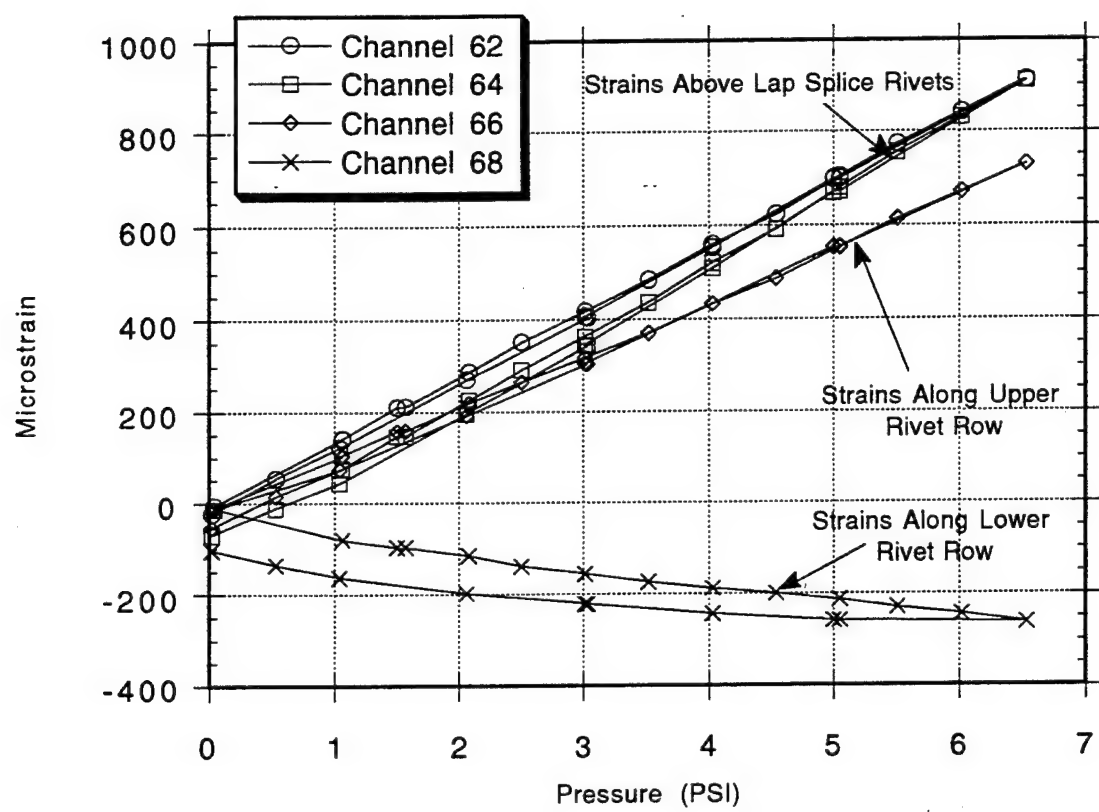


*Figure 3.3. External Skin Hoop Strains Along Midline at S-14L, BS475.
(Refer to Figure A.6.)*

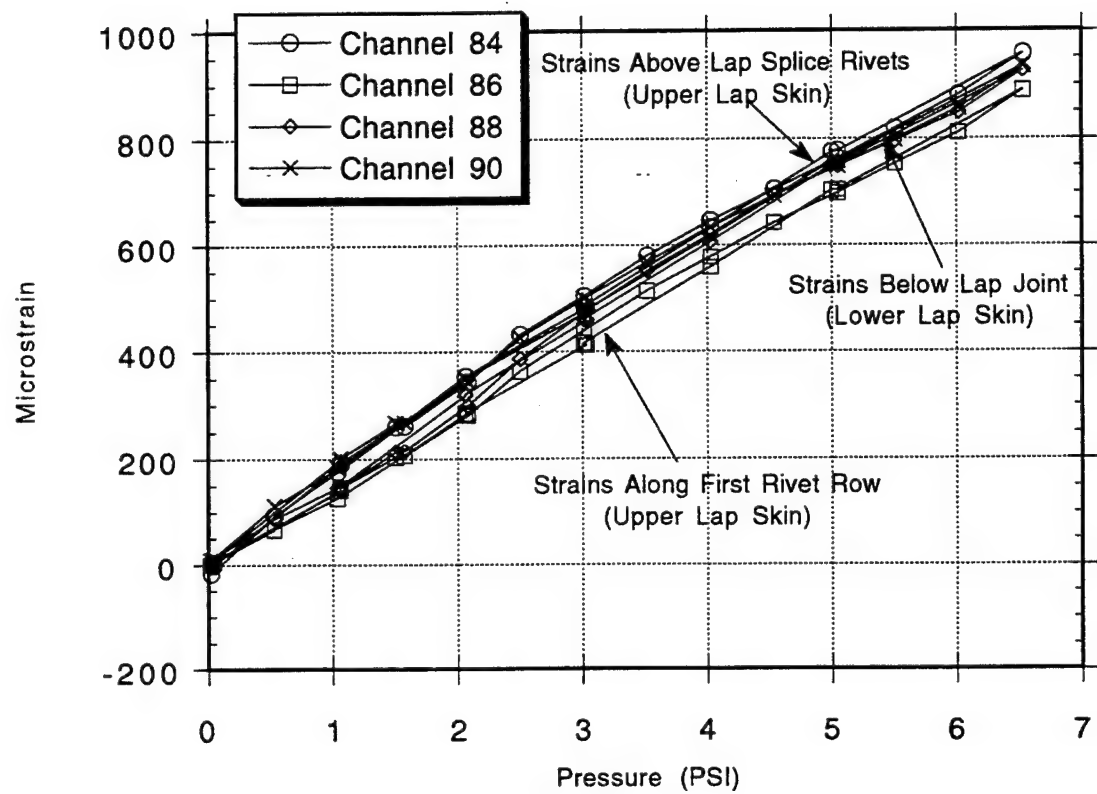


Figure 3.4. External Skin Hoop Strains Along Midline at S-4L, BS785.
(Refer to Figure A.10.)

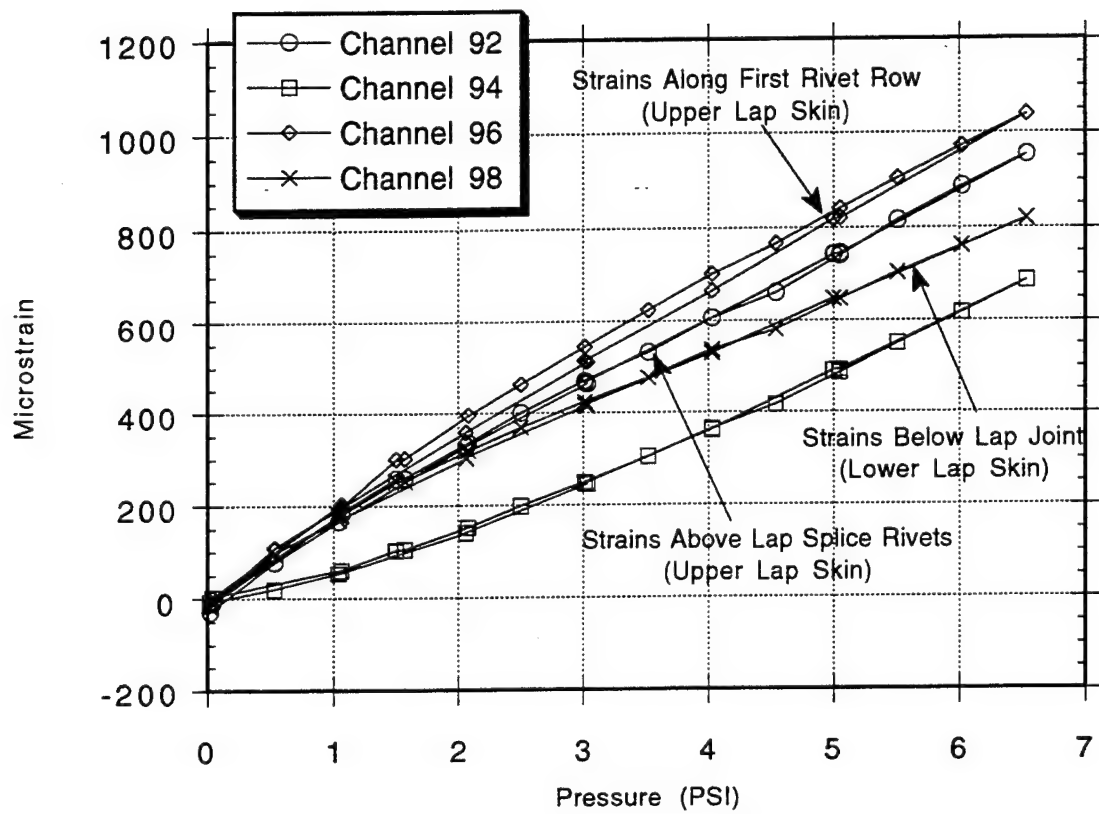


Figure 3.5. External Skin Hoop Strains Along Midline at S-10L, BS785.
(Refer to Figure A.11.)

- (2) Strain levels in the upper skin of the lap decrease drastically in the circumferential direction across the lap joint, from above the upper rivet row to the lower rivet row. Referring to Figure 3.1, the skin around the middle rivet row exhibits 17% of the strain in the upper rivet row. Table 3.1 summarizes the load transfer in each of the instrumented lap joints by listing the strain values measured at the peak pressure of 6.5 psi.
- (3) In general, the strain plots are reasonably linear with respect to pressure. Hysteresis is confined to strains in the lower rivet row.
- (4) Even though internal pressurization of the fuselage generally produces positive hoop strains, strains in the skin around the lower rivet rows in all bays (Channels 28, 58, and 68) are negative. Reverse or compression type bending in the lower rivet row develops as the lap joint deforms. This type of bending is depicted in Figure 3.6 which shows a schematic of a deformed lap splice joint. Deformation of the lap joint shifts the neutral axis of the structure which, in turn, induces a bending load into the lap skins. This reverse bending creates compressive or negative bending strains around the lower half of the lap joint. However, the total strain in the this area also comprises a membrane component that is positive but smaller in magnitude than the bending component. The magnitude of this membrane component is relatively small because nearly all the load at this point is transferred into the inner or lower skin of the lap. Since the negative bending strains are greater in magnitude than the positive membrane component, the gages show a net compressive strain.
- (5) Table 3.1 shows that the middle rivet row of the S-4L lap joint experiences only 17% of the total strain, while the same area of the S-10L lap joint experiences 56% of the total strain. A possible cause for this difference in load transfer between the S-4L and S-10L lap splice bays is a difference in the bond quality between these two joints. In other words, the adhesive bond in the S-10L lap splice may be more effective than the bond in the S-4L joint. This point is discussed further in Section 4.3.2.
- (6) Strain levels below the lap joint on the lower skin are approximately equal to the strain levels above the joint. Referring to Figure 3.2, the strain measured in Channel 60 (lower skin below lap joint) is 906×10^{-6} inch/inch ($\mu\epsilon$) compared to the strain measured in Channel 48 (upper skin above lap joint) which is $907 \mu\epsilon$. Similar results are evident in Figure 3.1 (Channel 18 versus 30: $813 \mu\epsilon$ compared to $1071 \mu\epsilon$), Figure 3.4 (Channel 86 versus 90: $889 \mu\epsilon$ compared to $933 \mu\epsilon$), and Figure 3.5 (Channel 94 versus 98: $687 \mu\epsilon$ compared to $819 \mu\epsilon$).

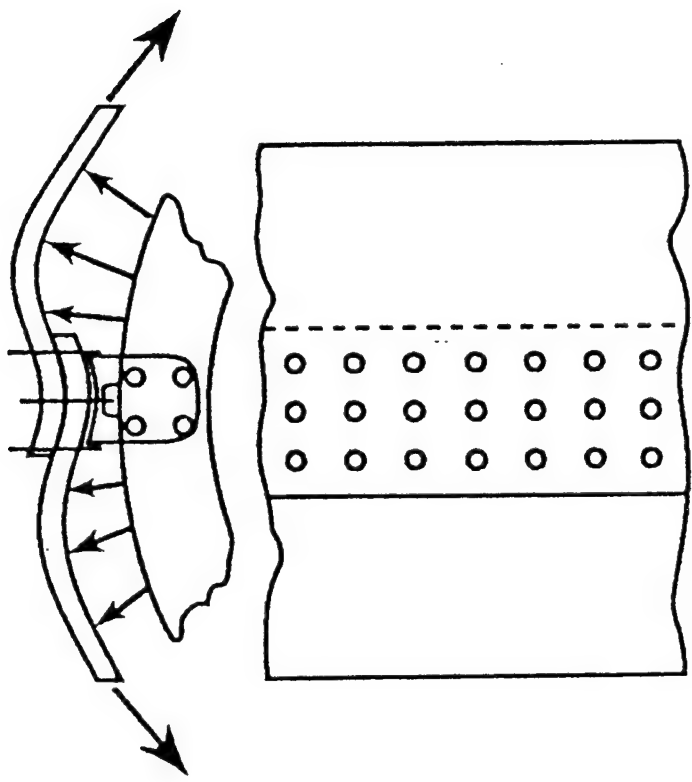


Figure 3.6. Deformation of Lap Splice Joint Due to Internal Pressurization.

Table 3.1. Load Transfer Through Different Lap Splice Joints at 6.5 psi.

(a) Stringer S-4L, Body Station 475

Channel	Location	Microstrain	Percent of Strain from Skin Above Lap Joint
18	Above Lap Splice	813	100%
24	Upper Rivet Row	771	95%
6	Middle Rivet Row	141	17%
28	Lower Rivet Row	-153	NA
30	Below Lap Splice	1071	131%

(b) Stringer S-10L, Body Station 475

Channel	Location	Microstrain	Percent of Strain from Skin Above Lap Joint
48	Above Lap Splice	907	100%
54	Upper Rivet Row	754	83%
36	Middle Rivet Row	506	56%
58	Lower Rivet Row	-104	NA
60	Below Lap Splice	906	100%

(c) Stringer S-14L, Body Station 475

Channel	Location	Microstrain	Percent of Strain from Skin Above Lap Joint
62	Above Lap Splice	911	100%
66	Upper Rivet Row	729	80%
68	Below Lap Splice	-263	NA

(d) Stringer S-14L, Body Station 790

Channel	Location	Microstrain	Percent of Strain from Skin Above Lap Joint
84	Above Lap Splice	956	100%
88	Upper Rivet Row	925	97%
90	Below Lap Splice	933	98%

(e) Stringer S-10L, Body Station 790

Channel	Location	Microstrain	Percent of Strain from Skin Above Lap Joint
92	Above Lap Splice	953	100%
96	Upper Rivet Row	1039	109%
98	Below Lap Splice	819	86%

3.1.2 Hoop Strains at Reinforced Areas of the Lap Skin

Figures 3.7 through 3.10 are plots of hoop strains in the external skin across the lap splice joint in the circumferential direction. These plots characterize strains in the areas where the skin is reinforced with substructure elements. The data from three circumferential positions are plotted in each figure: (1) 1 inch above the upper rivet row, (2) at the middle rivet row, and (3) 1 inch below the lower rivet row. Figures 3.7 and 3.9 show the strains over the tear straps (S-4L, BS470 and S-10L, BS470, respectively), and Figures 3.8 and 3.10 show the strains over the frames (S-4L, BS480 and S-10L, BS480; respectively). The strain levels and trends are the same as those for the unreinforced skin along the midline, as described in Section 3.1.1. In the S-4L bay, the maximum strains measured above and below the lap joint are between 900 $\mu\epsilon$ and 1000 $\mu\epsilon$, and the maximum strains in the middle rivet row are approximately 200 $\mu\epsilon$. In the S-10L bay, the maximum strains measured above and below the lap joint are also between 900 $\mu\epsilon$ and 1000 $\mu\epsilon$, and the maximum strains in the middle rivet row are approximately 500 $\mu\epsilon$. Again, a possible explanation for this difference in middle row strains is the difference in the adhesive bond quality between these two joints.

3.1.3 Hoop Strains Along the Lap Splice Joint

Figures 3.11 through 3.14 are plots of hoop strains in the external skin along the lap splice joint in the longitudinal direction at stringer S-4L between Body Stations 470 and 480. Three longitudinal locations on the fuselage were monitored above and below stringer S-4L: (1) over the tear strap, (2) at the midline location or center of the bay where there is no circumferential reinforcement, and (3) over the frame. Similarly, Figures 3.15 through 3.18 are plots of strains along the lap splice joint at stringer S-10L between BS470 and BS480. The following observations can be made from these plots:

- (1) The strains are generally linear with respect to pressure. The hysteresis observed between loading and unloading was insignificant.
- (2) In general, the strain levels are both uniform and consistent as the longitudinal position changes from the tear strap, through midbay, and over to the fuselage frame (see Figures 3.11, 3.12, and 3.14 to 3.18). Therefore, the reinforcing substructure elements do not affect the strain levels around the skin and rivets to which they are attached.

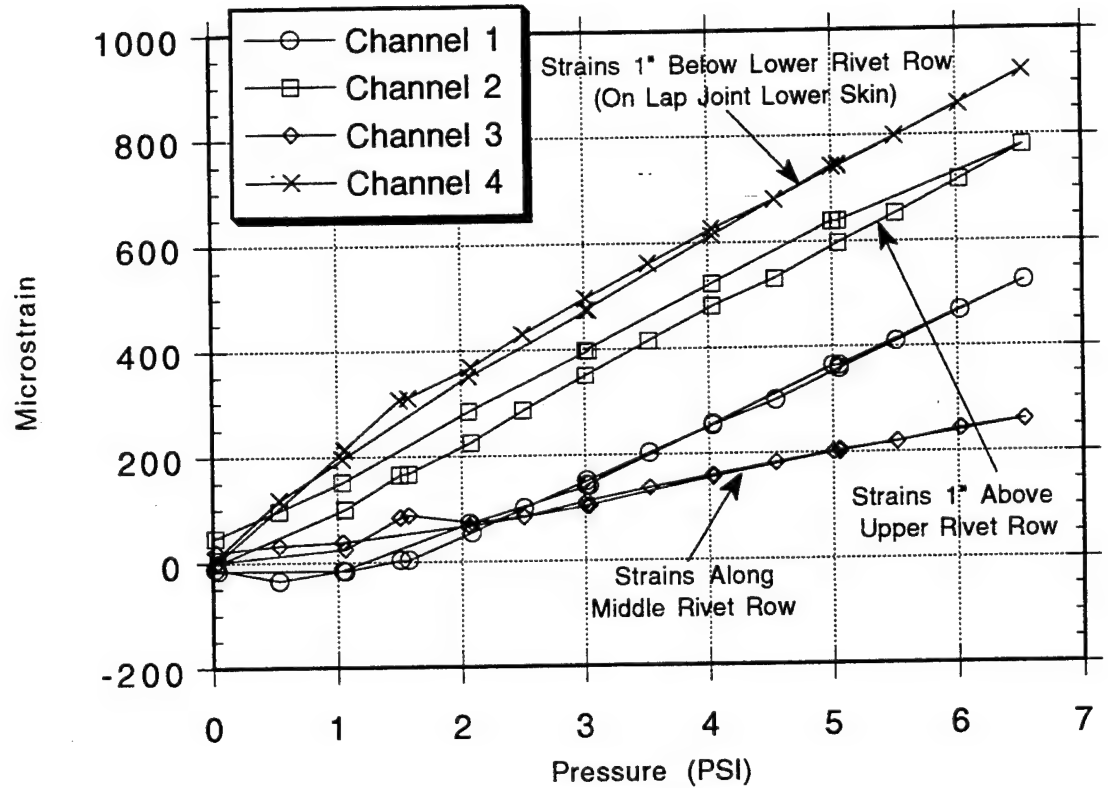


Figure 3.7. External Skin Hoop Strains Along Tear Strap at S-4L, BS470.
 (Refer to Figure A.4.)

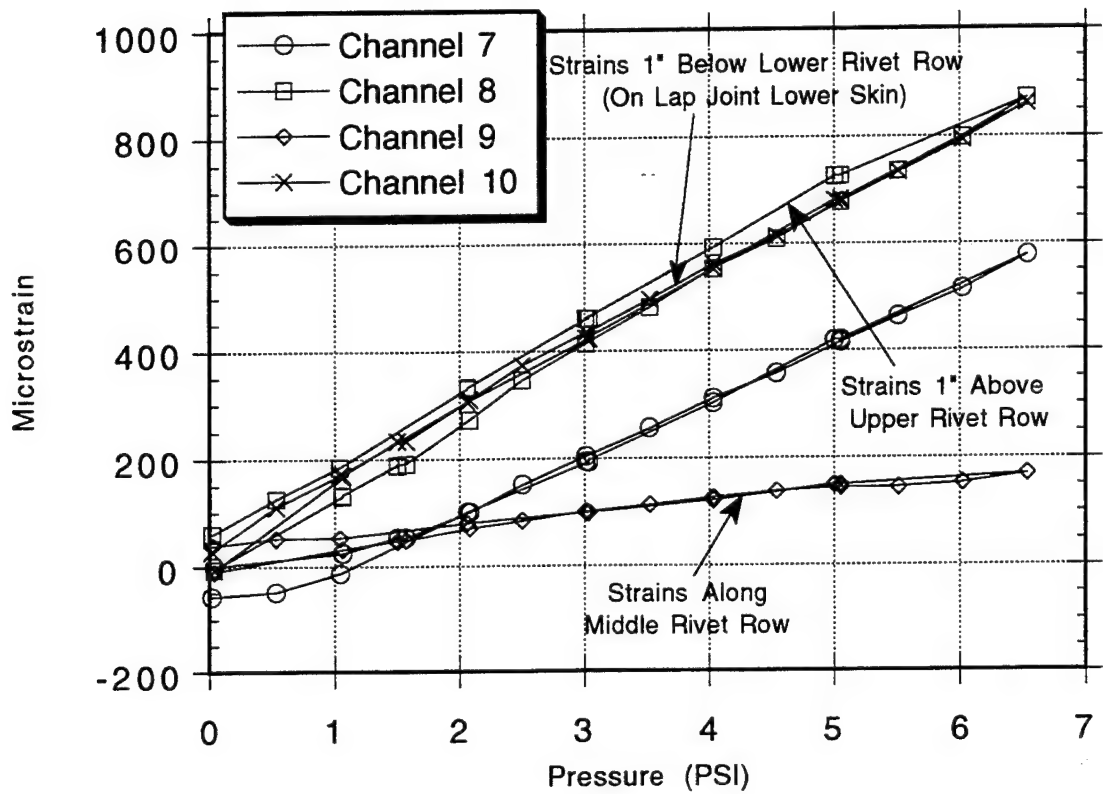


Figure 3.8. External Skin Hoop Strains Along Frame at S-4L, BS480.
(Refer to Figure A.4.)

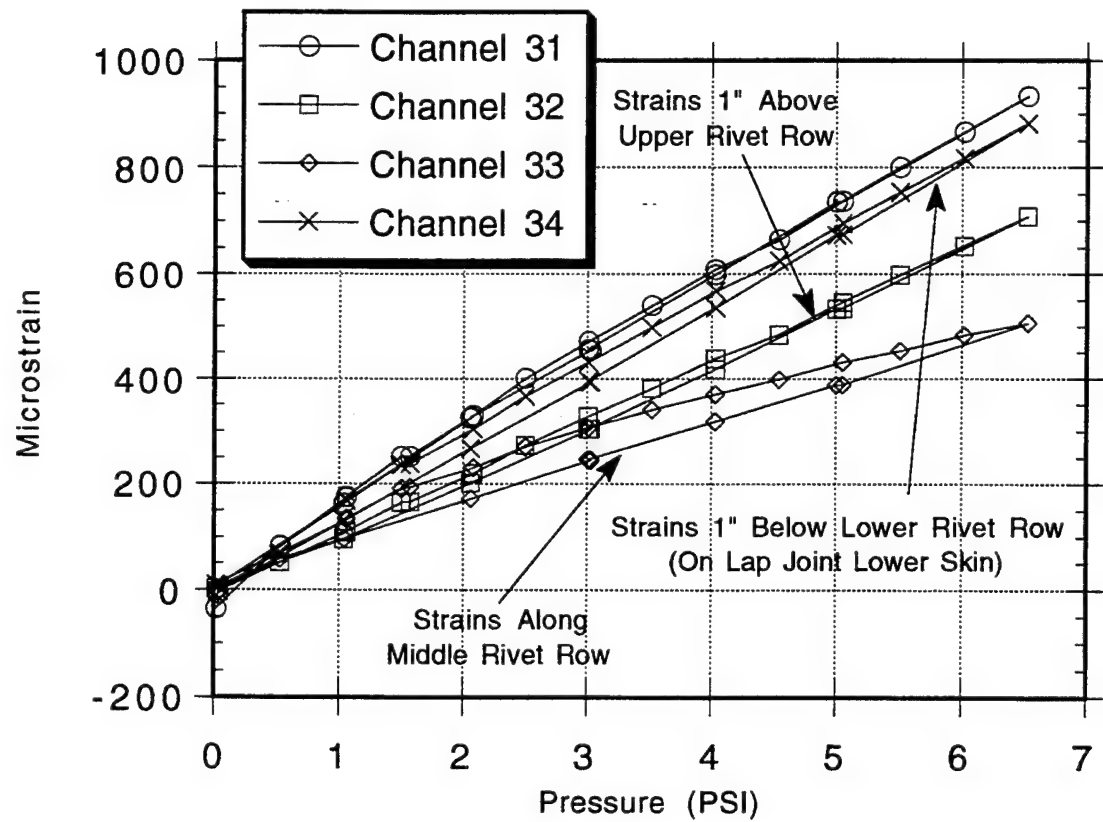


Figure 3.9. External Skin Hoop Strains Along Tear Strap at S-10L, BS470.
(Refer to Figure A.5.)

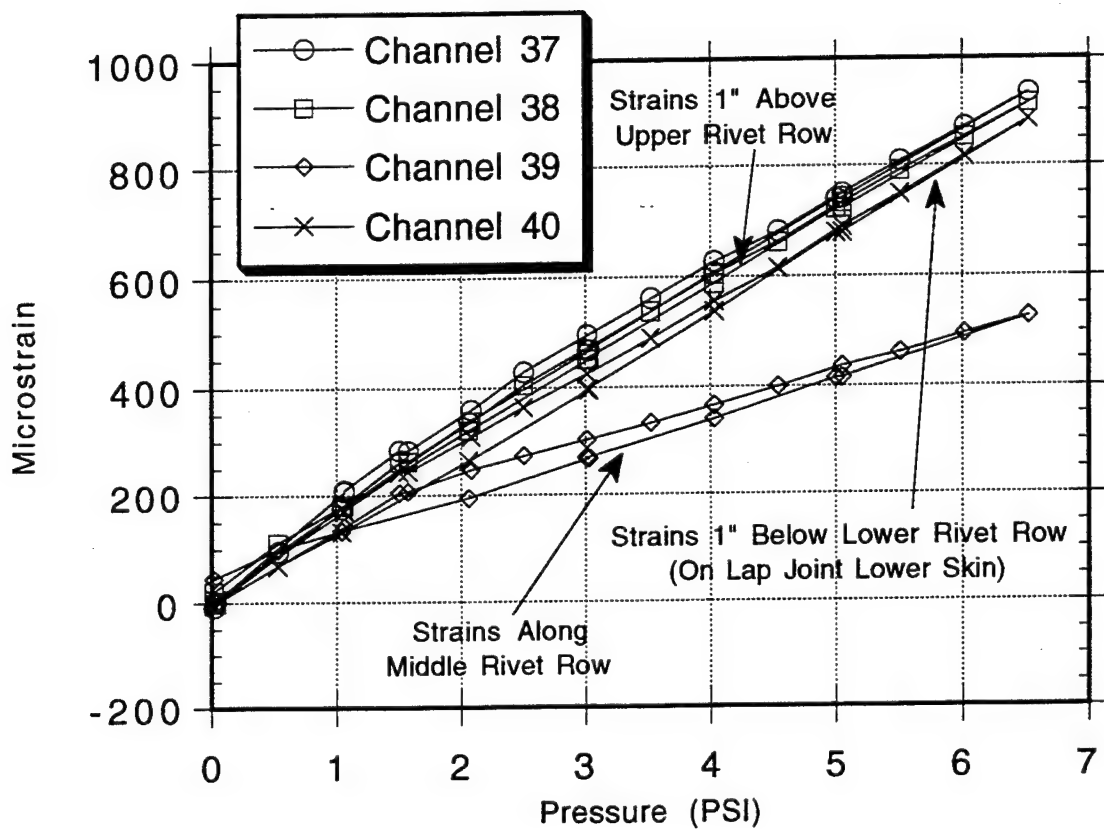


Figure 3.10. External Skin Hoop Strains Along Frame at S-10L, BS480.
(Refer to Figure A.5.)

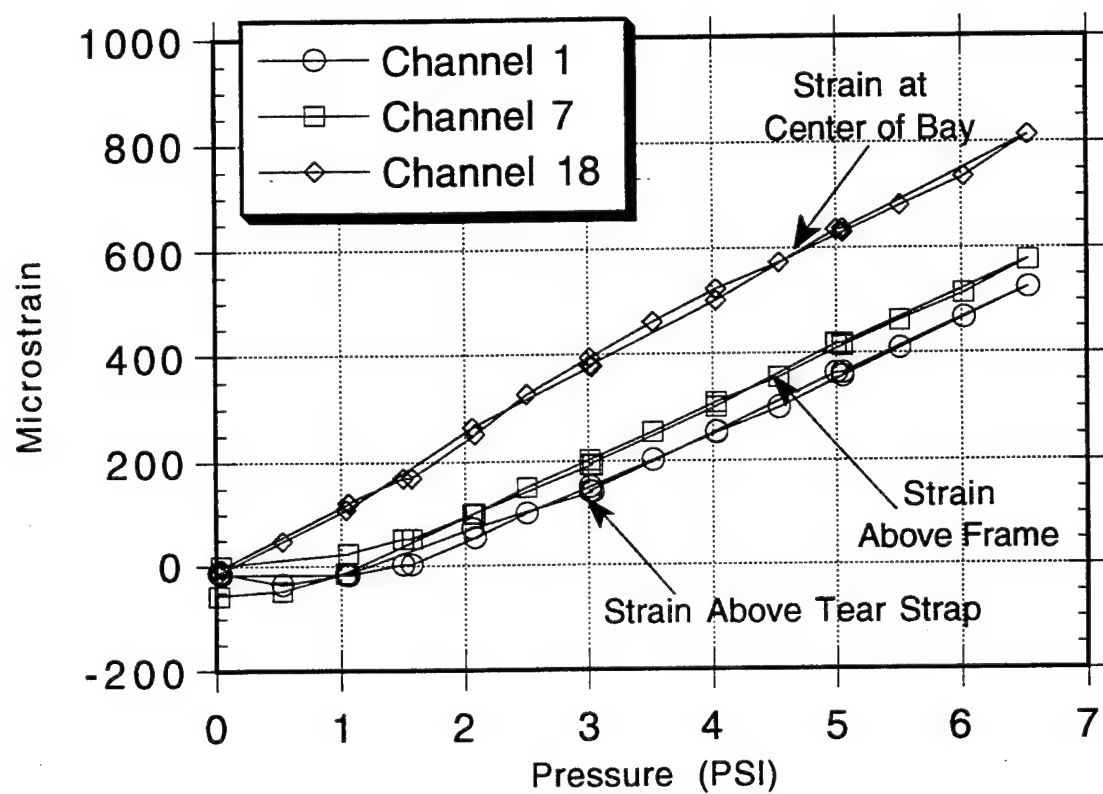
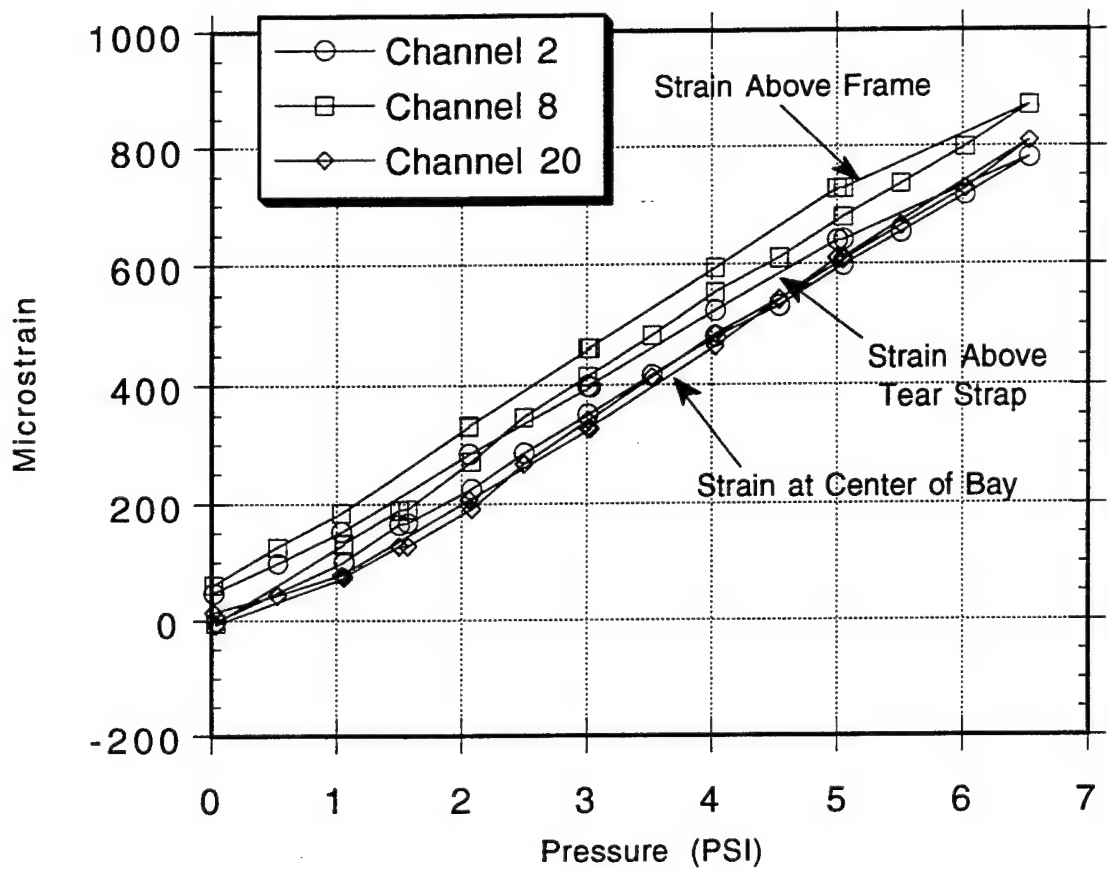
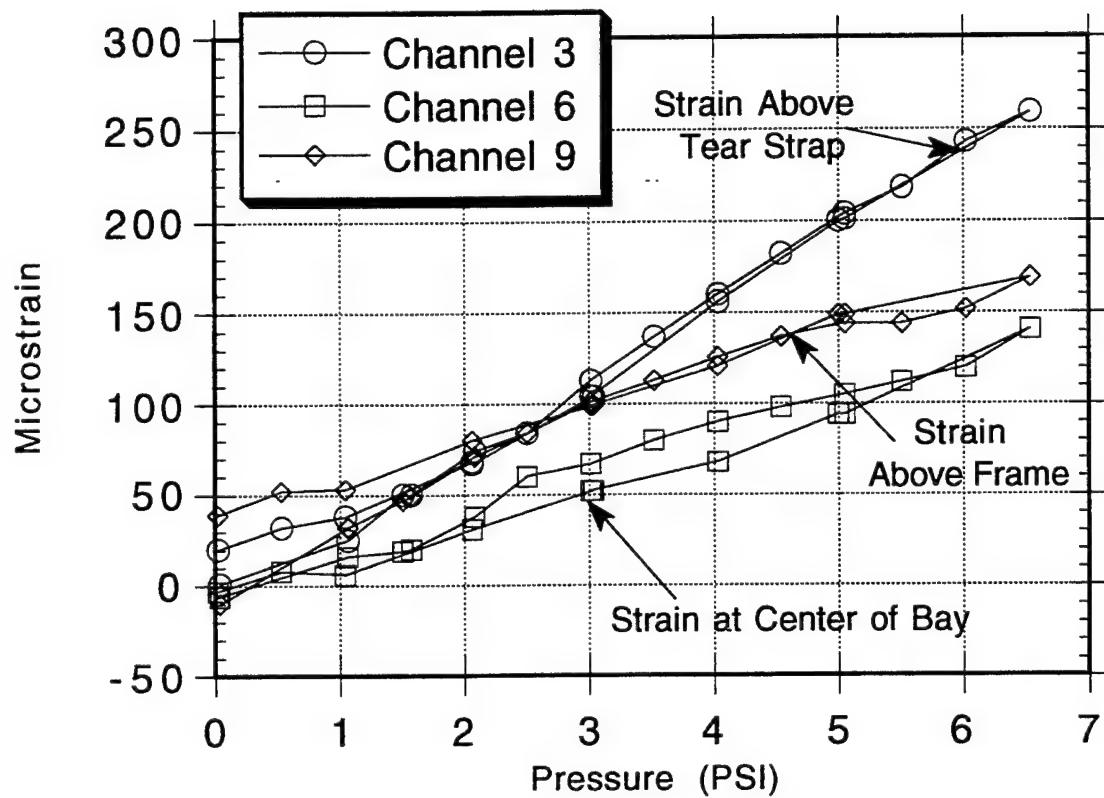


Figure 3.11. External Skin Hoop Strains Across Midbay at S-4L Lap Splice Bay Between BS470 and BS480.
 (Refer to Figure A.4.)



*Figure 3.12. External Skin Hoop Strains 1 Inch Above Upper Rivet Row at S-4L Lap Splice Bay Between BS470 and BS480.
(Refer to Figure A.4.)*



*Figure 3.13. External Skin Hoop Strains Across Middle Rivet Row at S-4L Lap Splice Bay Between BS470 and BS480.
(Refer to Figure A.4.)*

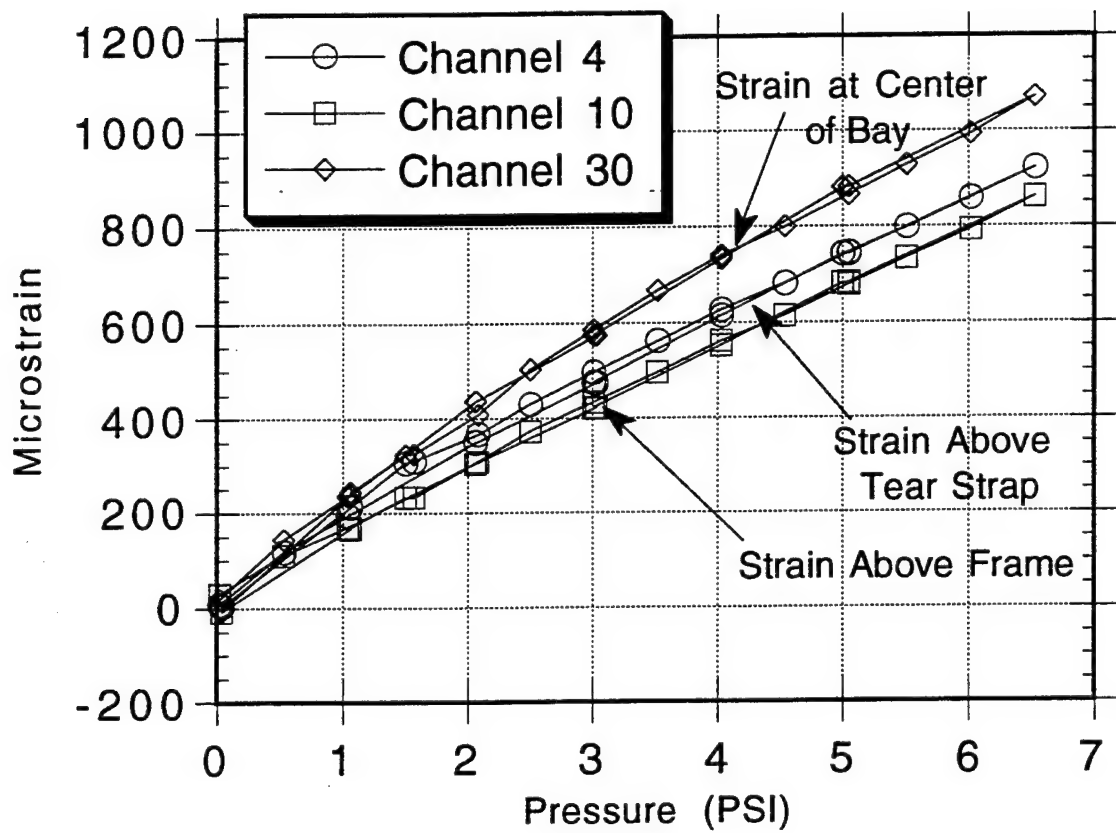


Figure 3.14. External Skin Hoop Strains 1 Inch Below Lower Rivet Row at S-4L Lap Splice Bay Between BS470 and BS480.
 (Refer to Figure A.4.)

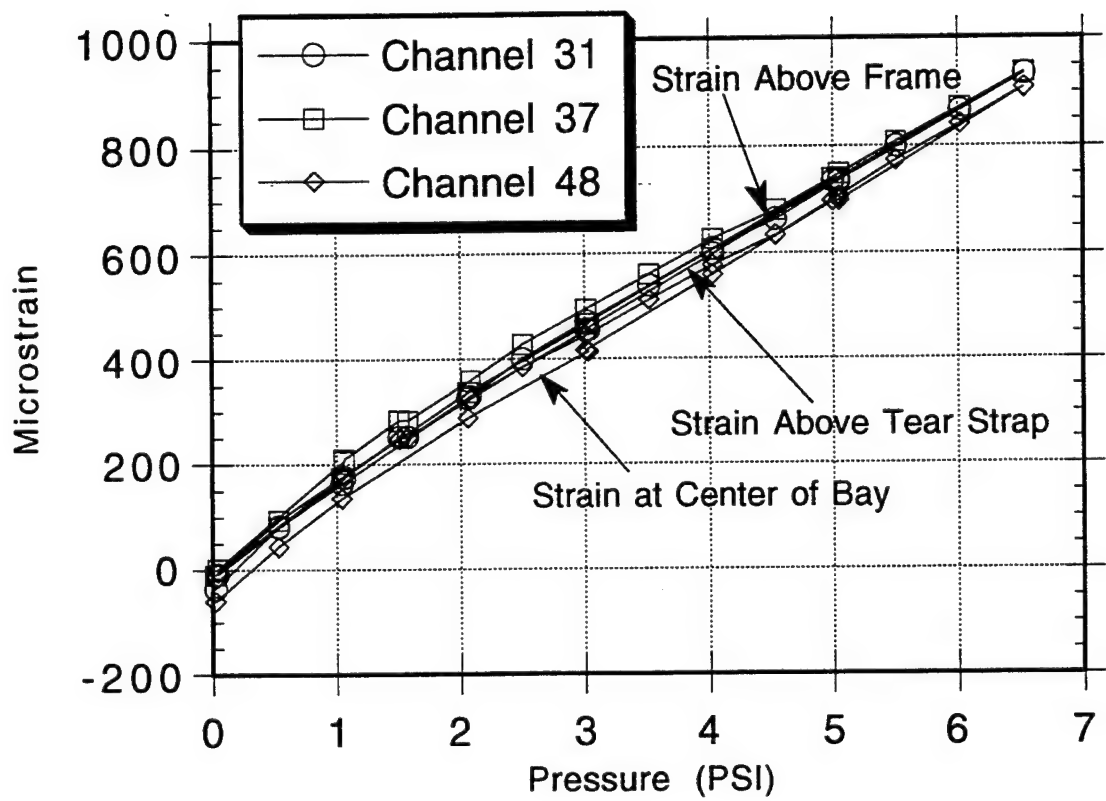
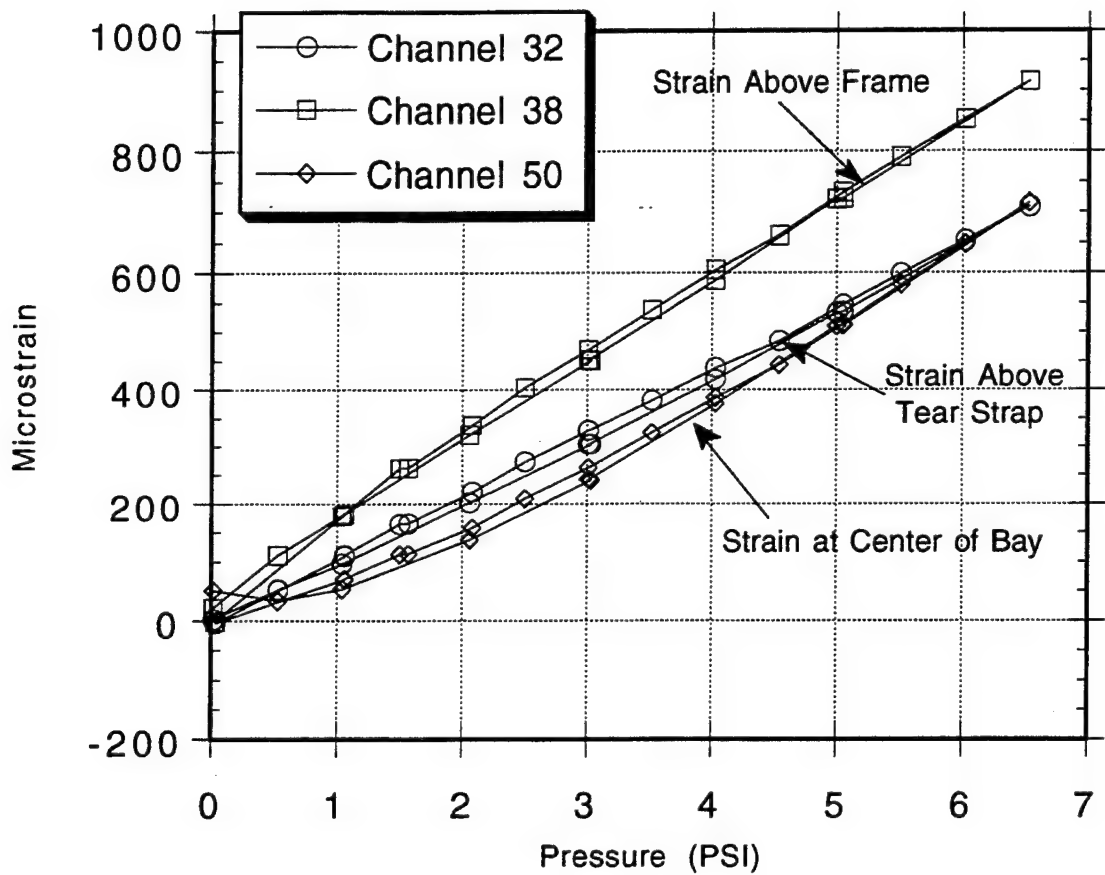


Figure 3.15. External Skin Hoop Strains Across Midbay at S-10L Lap Splice Bay Between BS470 and BS480.
(Refer to Figure A.5.)



*Figure 3.16. External Skin Hoop Strains 1 Inch Above Upper Rivet Row at S-10L Lap Splice Bay Between BS470 and BS480.
(Refer to Figure A.5.)*

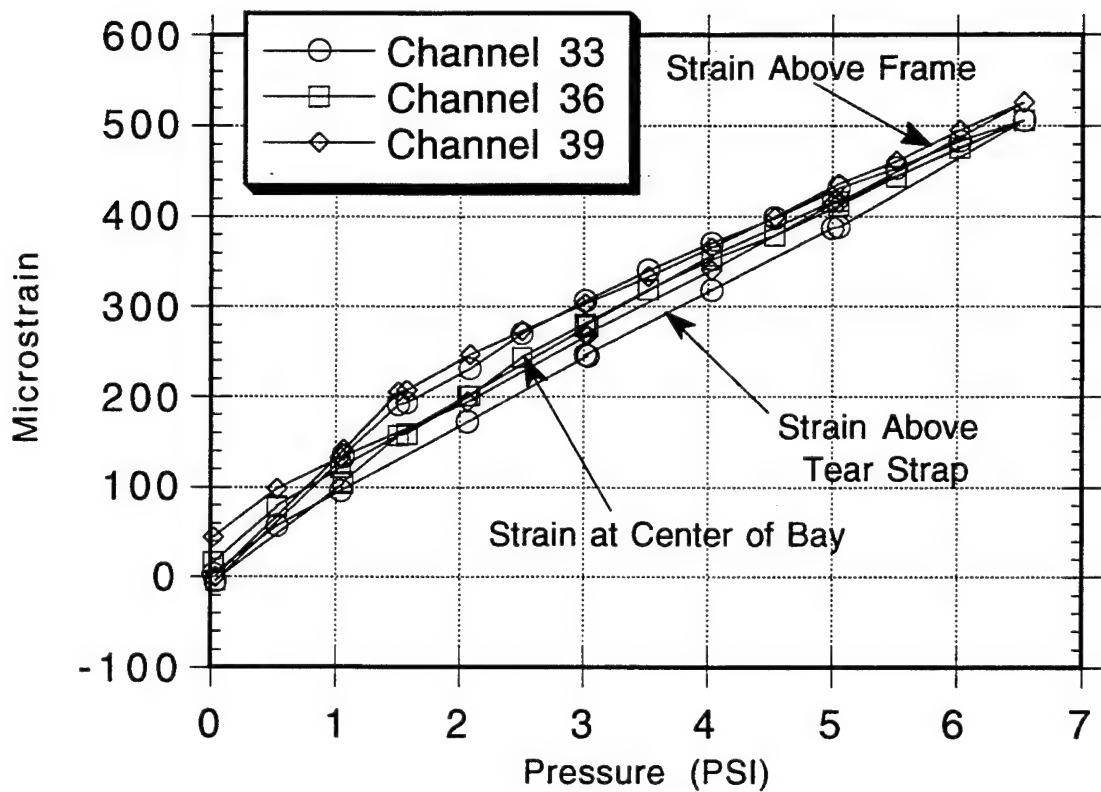


Figure 3.17. External Skin Hoop Strains Across Middle Rivet Row
at S-10L Lap Splice Bay Between BS470 and BS480.
(Refer to Figure A.5.)

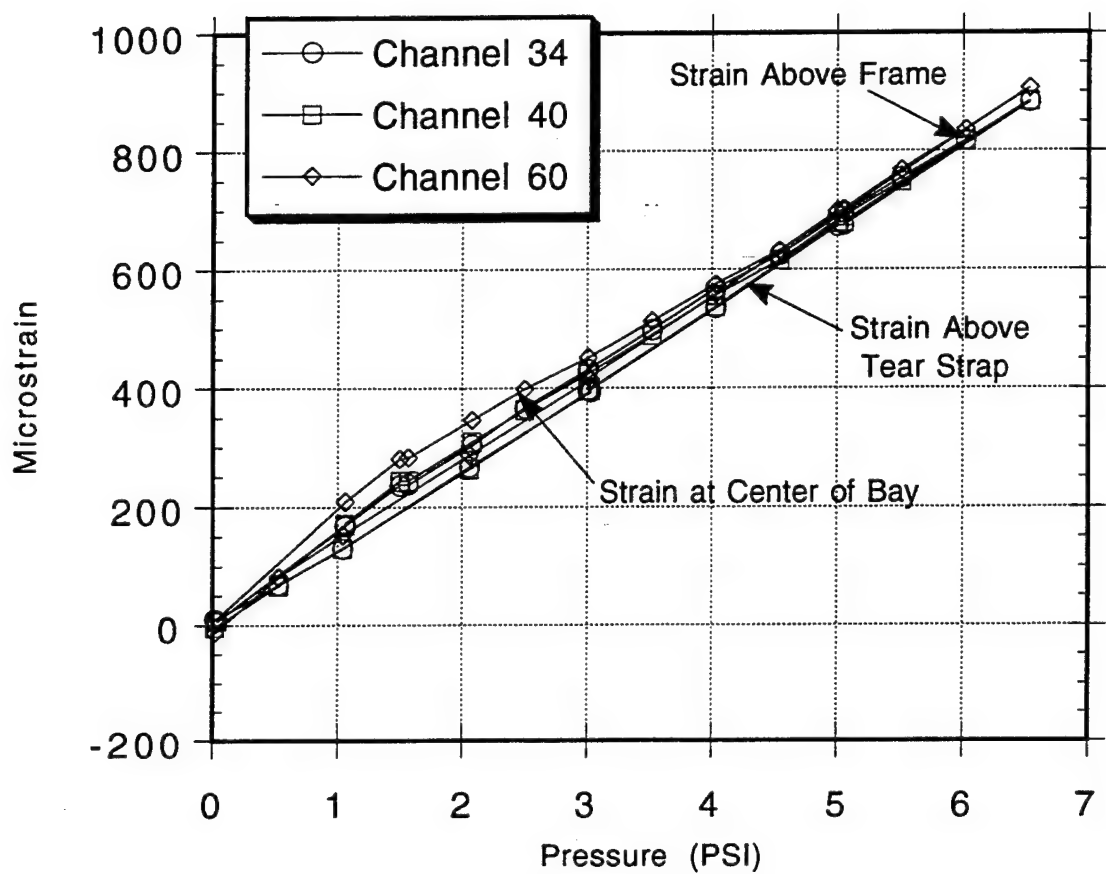


Figure 3.18. External Skin Hoop Strains 1 Inch Below Lower Rivet Row
at S-10L Lap Splice Bay Between BS470 and BS480.
(Refer to Figure A.5.)

- (3) The strain levels along the middle rivet row at stringer S-4L vary with longitudinal position (see Figure 3.13). The hoop strain at the midline is about 50% of the strain at the tear strap location. At stringer S-10L, however, the strain levels along the middle rivet row are nearly identical at each longitudinal position (see Figure 3.17). The difference in strain variations for these two stringers indicates a difference in load transfer into the inner/lower lap skin (see Section 3.1.1) which implies a difference in the bond quality between these two joints.
- (4) Tables 3.2 and 3.3 summarize the variations of strains across the S-4L and S-10L lap splice bays between Body Stations 470 and 480. Maximum strain values measured at the peak pressure of 6.5 psi are listed for different locations in the bay.

3.1.4 Longitudinal Strain Levels

Figures 3.19 through 3.23 are plots of longitudinal strains in the external skin measured at different locations throughout each of the instrumented lap splice joints. The following observations can be made from these plots:

- (1) Although the longitudinal strains are smaller in magnitude than the corresponding hoop strains, they are not insignificant. Most of the strains are less than 300 $\mu\epsilon$; the higher strain channels are plotted in Figures 3.19 to 3.23. The peak longitudinal strains are 380 $\mu\epsilon$ (Channel 55) and 400 $\mu\epsilon$ (Channel 67) which are shown in Figures 3.20 and 3.21, respectively.
- (2) The plots show no significant trends in the longitudinal strain field within the lap splice bay. The maximum strains occur in different areas from one bay to the next. The longitudinal strains are not as linear as those in the hoop direction with respect to pressure. Both of these results may be due to the sensitivity of longitudinal strains in the lap splice bays to real time load shifts and structural settling in this direction.
- (3) Figures 3.21 to 3.23 compare the longitudinal strains measured along the midline in three different lap splice bays. The general strain profiles and magnitudes were the same forward and aft of the wing, and above and below the window. Otherwise, no significant trends were observed.

Table 3.2. Peak External Skin Hoop Strains Across S-4L Lap Splice Bay at 6.5 psi.

(a) Circumferential Position 4.75 inches Above Upper Rivet Row

<i>Channel</i>	<i>Body Station</i>	<i>Microstrain</i>
1	470 (over tear strap)	524
18	475 (midline)	813
7	480 (above frame)	577

(b) Circumferential Position 1.00 inch Above Upper Rivet Row

<i>Channel</i>	<i>Body Station</i>	<i>Microstrain</i>
2	470 (over tear strap)	780
13	471	636
20	475 (midline)	809
16	479	861
8	480 (above frame)	871

(c) Circumferential Position Along Middle Rivet Row over S-4L

<i>Channel</i>	<i>Body Station</i>	<i>Microstrain</i>
3	470 (over tear strap)	259
6	475 (midline)	141
9	480 (above frame)	169

(d) Circumferential Position 1.00 inch Below Lower Rivet Row

<i>Channel</i>	<i>Body Station</i>	<i>Microstrain</i>
4	470 (over tear strap)	921
30	475 (midline)	1071
10	480 (above frame)	861

Table 3.3. Peak External Skin Hoop Strains Across S-10L Lap Splice Bay at 6.5 psi.

(a) Circumferential Position 4.75 inches Above Upper Rivet Row

Channel	Body Station	Microstrain
31	470 (over tear strap)	933
37	475 (midline)	935
48	480 (above frame)	907

(b) Circumferential Position 1.00 inch Above Upper Rivet Row

Channel	Body Station	Microstrain
32	470 (over tear strap)	709
43	471	641
38	475 (midline)	915
45	479	707
50	480 (above frame)	715

(c) Circumferential Position Along Middle Rivet Row Over S-4L

Channel	Body Station	Microstrain
33	470 (over tear strap)	506
36	475 (midline)	506
39	480 (above frame)	526

(d) Circumferential Position 1.00 inch Below Lower Rivet Row

Channel	Body Station	Microstrain
34	470 (over tear strap)	882
40	475 (midline)	884
60	480 (above frame)	906

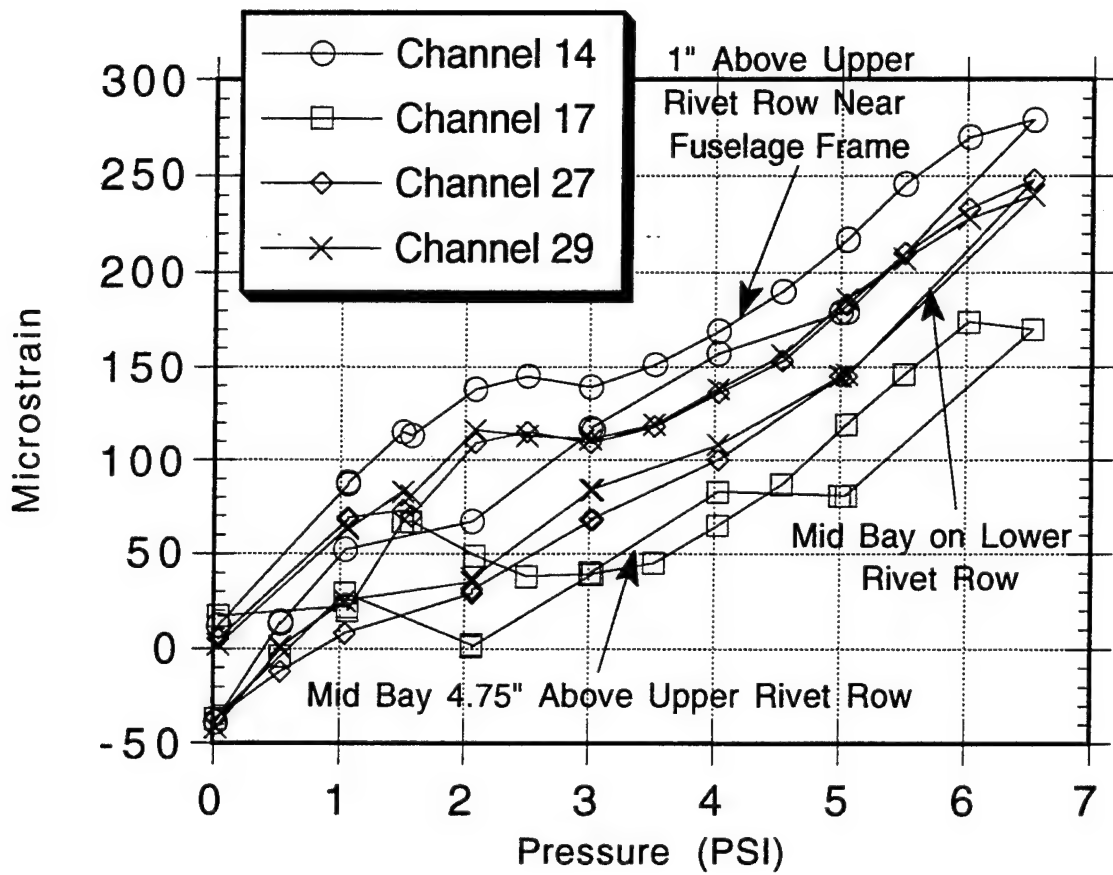


Figure 3.19. External Skin Longitudinal Strains at S-4L, BS475.
(Refer to Figure A.4.)

NOTE: In this figure, "midbay" refers to the longitudinal location halfway between the tear strap and the frame. In the text, this location is referred to as the "midline."

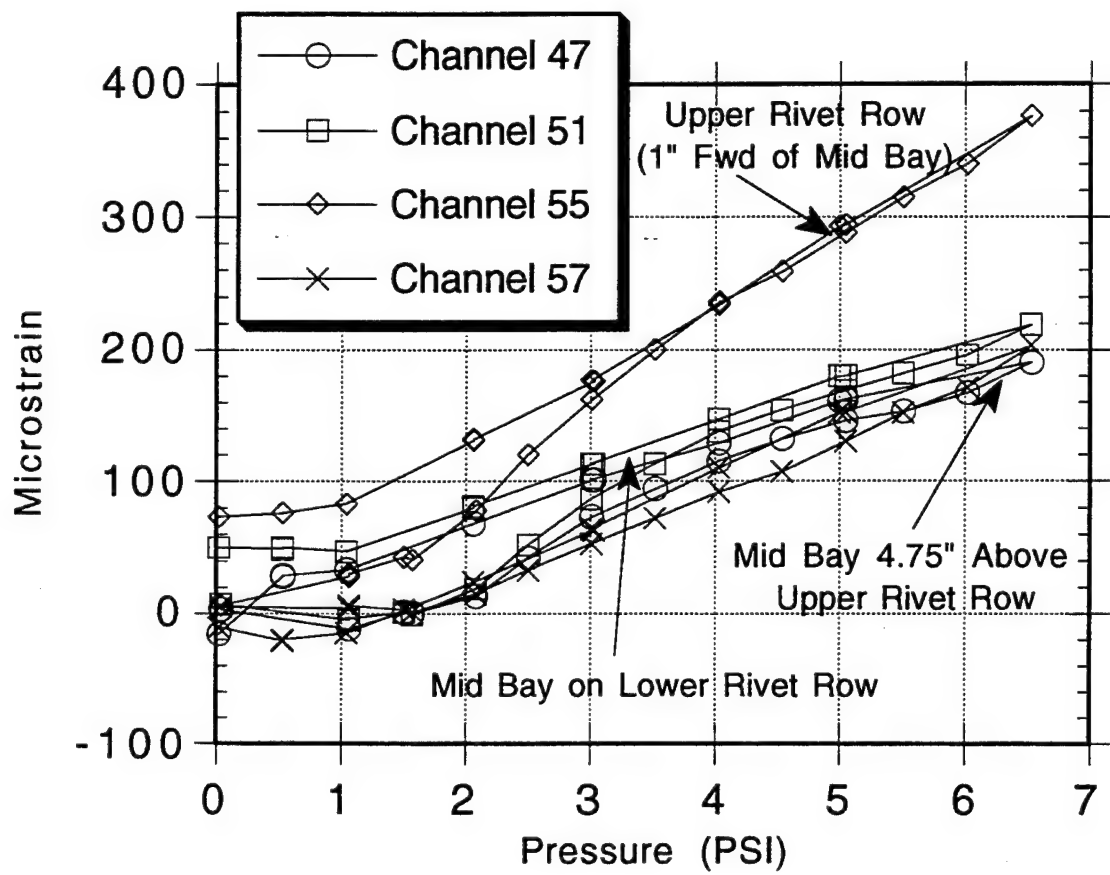


Figure 3.20. External Skin Longitudinal Strains at S-10L, BS475.
(Refer to Figure A.5.)

NOTE: In this figure, "midbay" refers to the longitudinal location halfway between the tear strap and the frame. In the text, this location is referred to as the "midline."

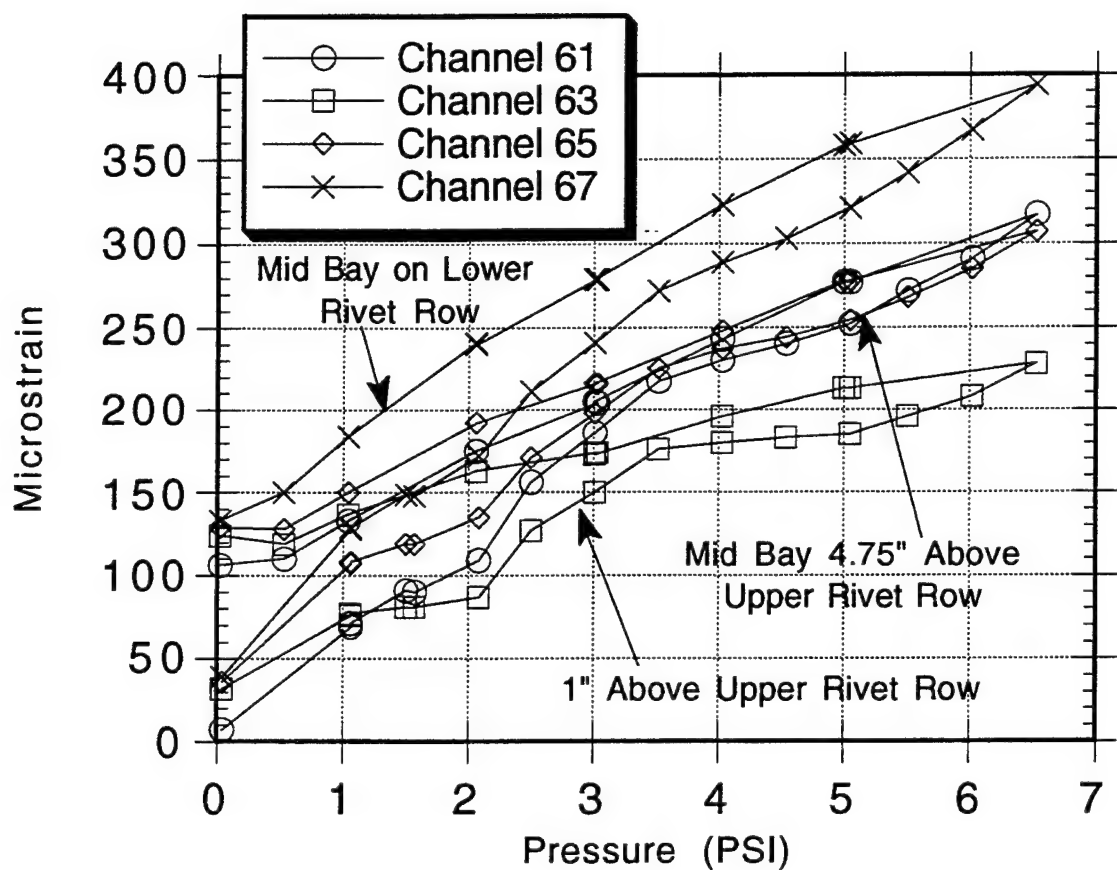


Figure 3.21. External Skin Longitudinal Strains at S-14L, BS475.
(Refer to Figure A.6.)

NOTE: In this figure, "midbay" refers to the longitudinal location halfway between the tear strap and the frame. In the text, this location is referred to as the "midline."

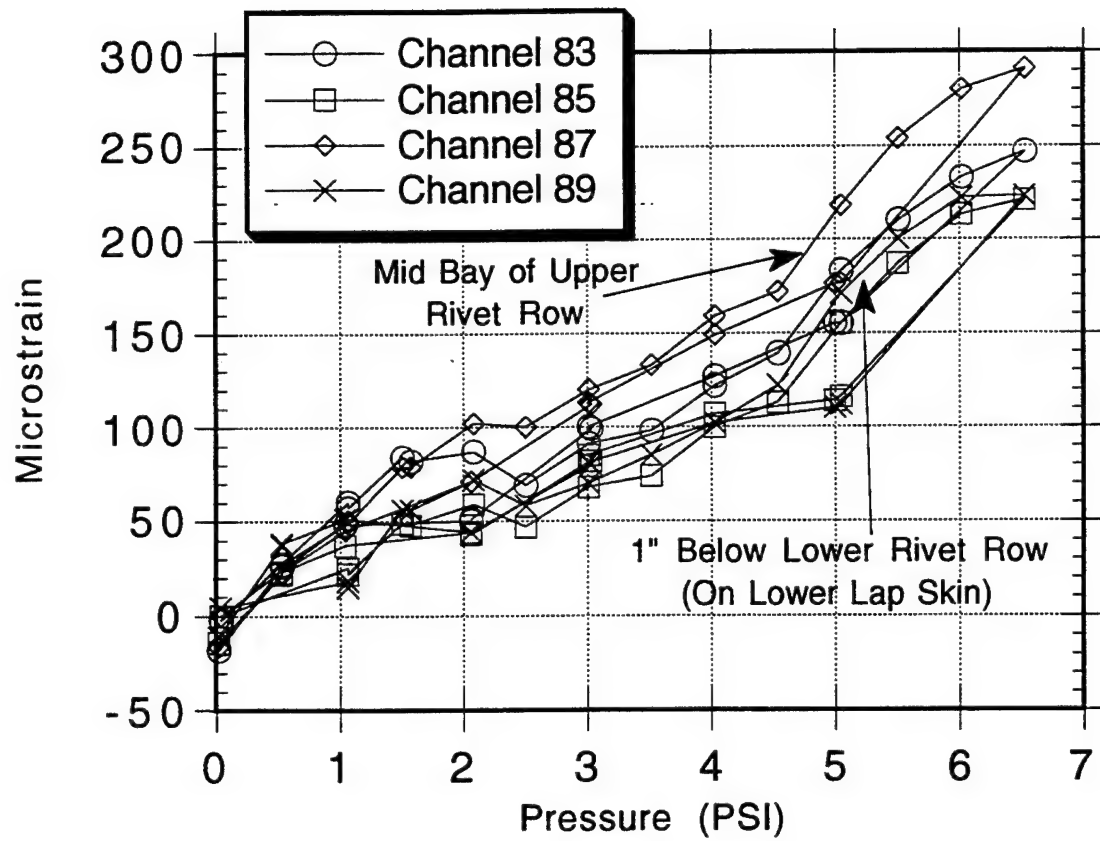


Figure 3.22. External Skin Longitudinal Strains at S-4L, BS785.
(Refer to Figure A.10.)

NOTE: In this figure, "midbay" refers to the longitudinal location halfway between the tear strap and the frame. In the text, this location is referred to as the "midline."

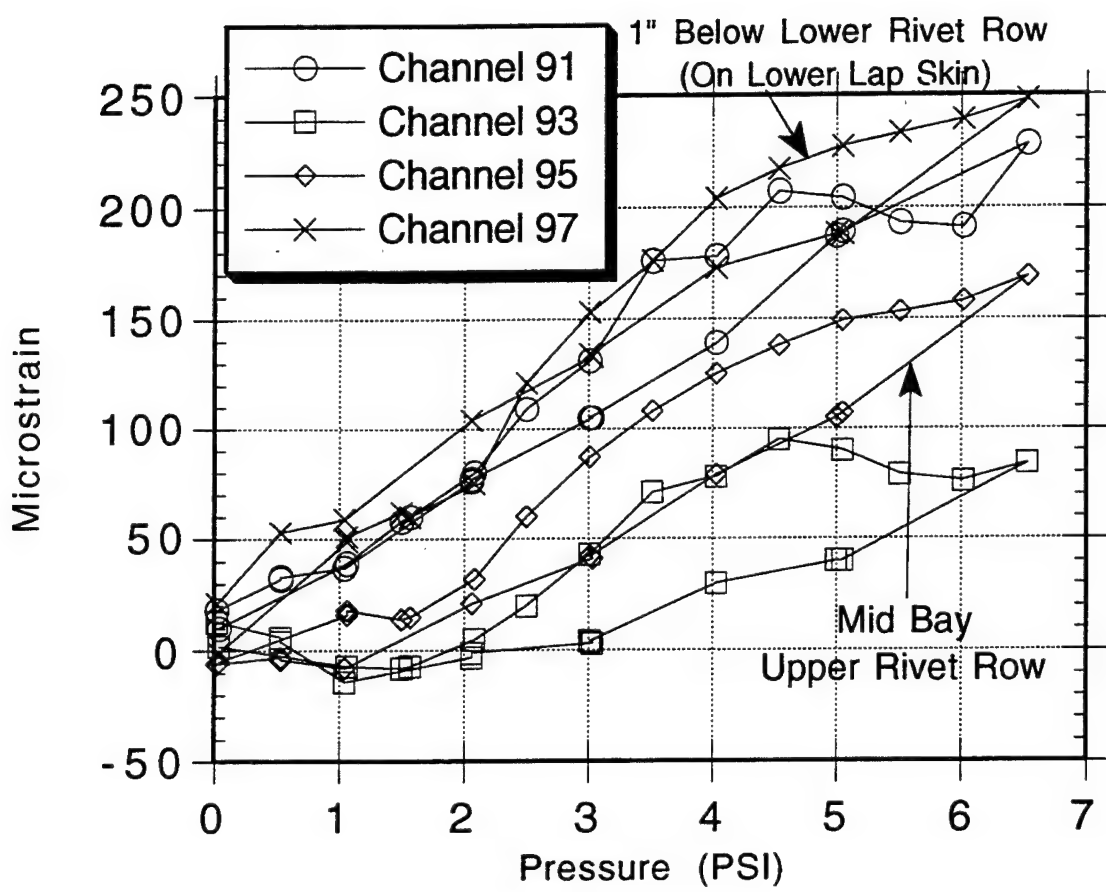


Figure 3.23. External Skin Longitudinal Strains at S-10L, BS785.
(Refer to Figure A.11.)

NOTE: In this figure, "midbay" refers to the longitudinal location halfway between the tear strap and the frame. In the text, this location is referred to as the "midline."

3.2 BENDING STRAINS IN THE SKIN

As discussed in Section 3.1.1, deformation of the lap splice joint from internal pressurization shifts the neutral axis of the structure down through the joint which induces bending in the circumferential direction (Figure 3.6). In order to evaluate bending strains, gages were installed on both the exterior and interior sides of the same skin at matching locations in each of the instrumented lap joint bays. Bending strains were then calculated using the following equation:

$$\varepsilon_b = \frac{1}{2}(\varepsilon_e - \varepsilon_i) \quad (3.1)$$

where ε_b is the bending strain, ε_e is the external strain, and ε_i is the internal strain.

Figures 3.24 to 3.26 show comparisons of the internal and external strains measured at two locations along the midline (BS475) in the lap splice joints at stringers S-4L and S-10L. Figures 3.24 and 3.25 compare the internal and external hoop strains for the same skin location. Figure 3.26 compares the longitudinal strains (BS475, S-10L). Numerical values for internal and external strains were taken from these figures, and substituted into equation (3.1) to produce plots of bending strain which are shown in Figures 3.27 to 3.29. Figure 3.27 indicates that bending strains in the longitudinal direction are less than 50 $\mu\epsilon$. In Figures 3.28 and 3.29, the maximum bending strain in the hoop direction is 130 $\mu\epsilon$. These three plots of bending show that: (1) the bending effects increase in the circumferential direction down the lap splice joint, and (2) the bending strains are compressive. Thus, in areas of low strain, such as in the external skin at the lower rivet row, the bending strains dominate and the total hoop strain is compressive, as discussed in Section 3.1.1. (Bending strains in the riveted area could not be measured because the back of the skin in the overlapping area was not accessible.) Overall, the magnitude of the bending strains are relatively small compared to the strains in the hoop direction.

3.3 LOAD TRANSFER INTO LOWER/INNER SKIN OF LAP SPLICE JOINT

Another way to analyze the load transfer from the upper/outer lap skin into the lower/inner skin is to examine the strain values on both skins of the riveted assembly. Figures 3.30 to 3.34 compare strains measured on the inner and outer skins at the same location; namely, the lower rivet row (refer to Figures A.4 to A.9 in Appendix A for exact gage locations). The hoop strains on the outer skin are less than 200 $\mu\epsilon$ and compressive. This result was discussed in Section 3.1.1. Most of the load at the lower rivet row is transferred into the inner skin where the strain values are equal in magnitude to those observed in the external, upper rivet row.

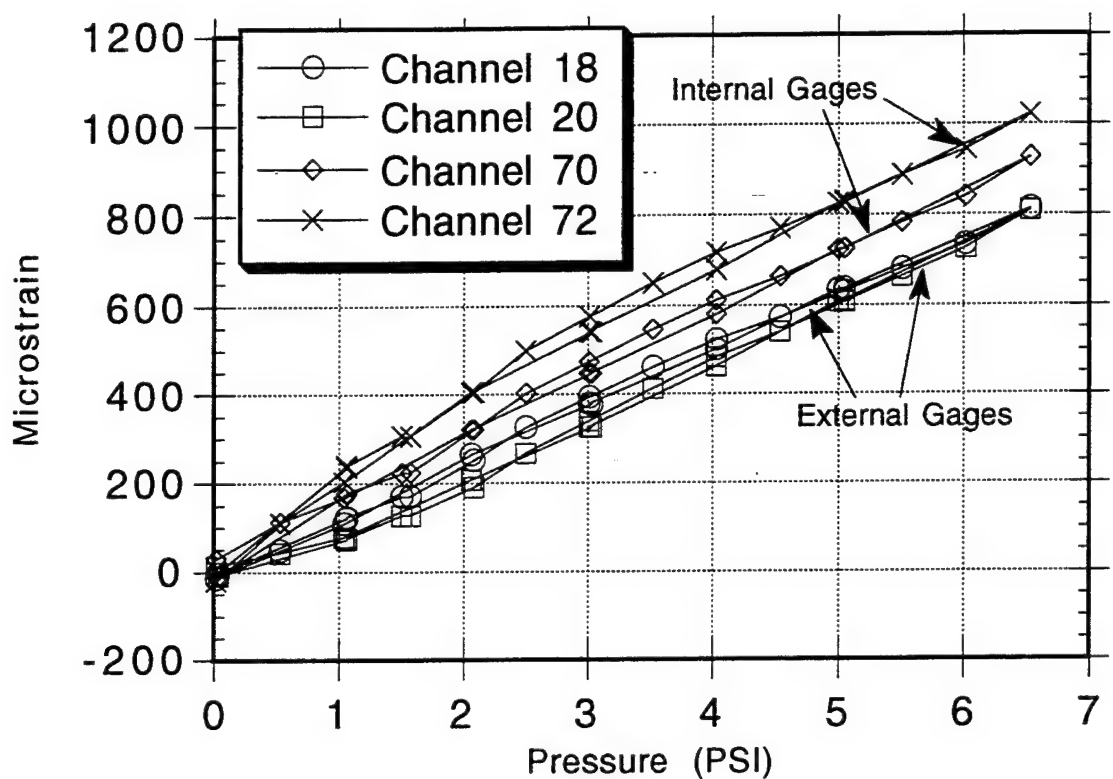


*Figure 3.24. Comparison of Internal and External Hoop Strains
Measured at S-4L Lap Splice Joint, BS475.
(Refer to Figure A.4 and A.7.)*

NOTE: All gages are above the upper rivet row.

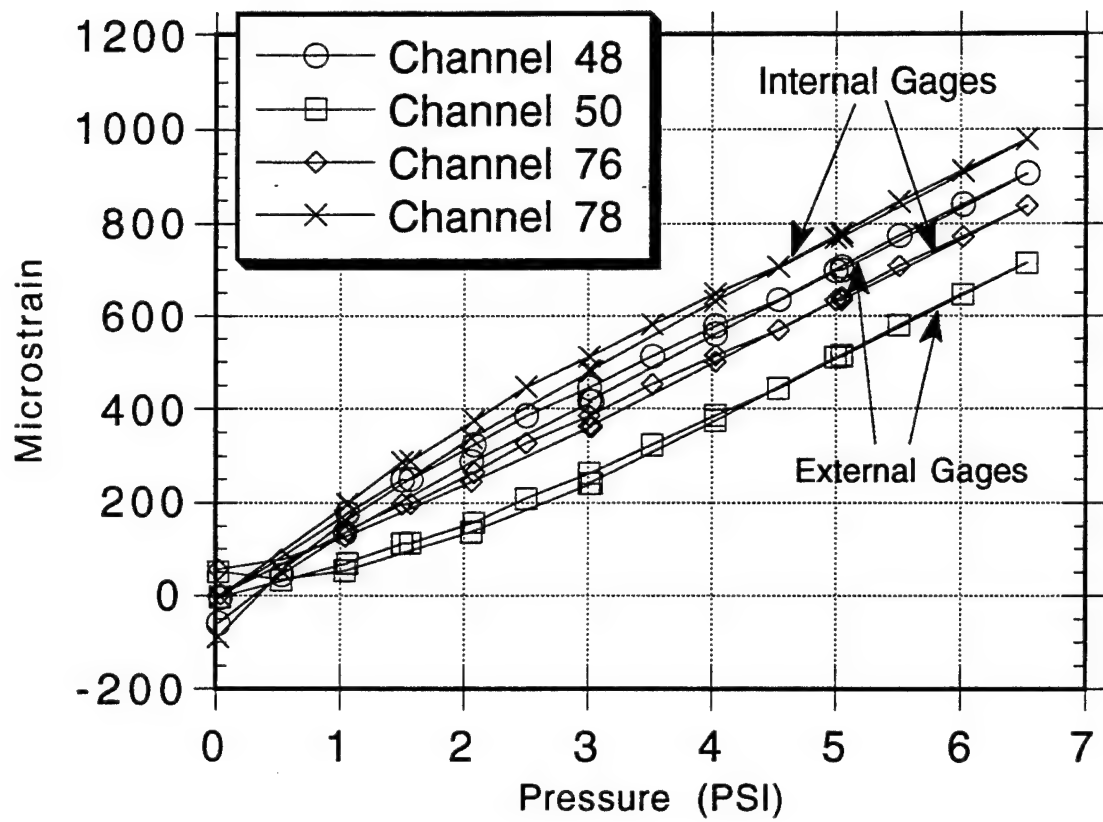


*Figure 3.25. Comparison of Internal and External Hoop Strains
Measured at S-10L Lap Splice Joint, BS475.
(Refer to Figure A.5 and A.8.)*

NOTE: All gages are above the upper rivet row.

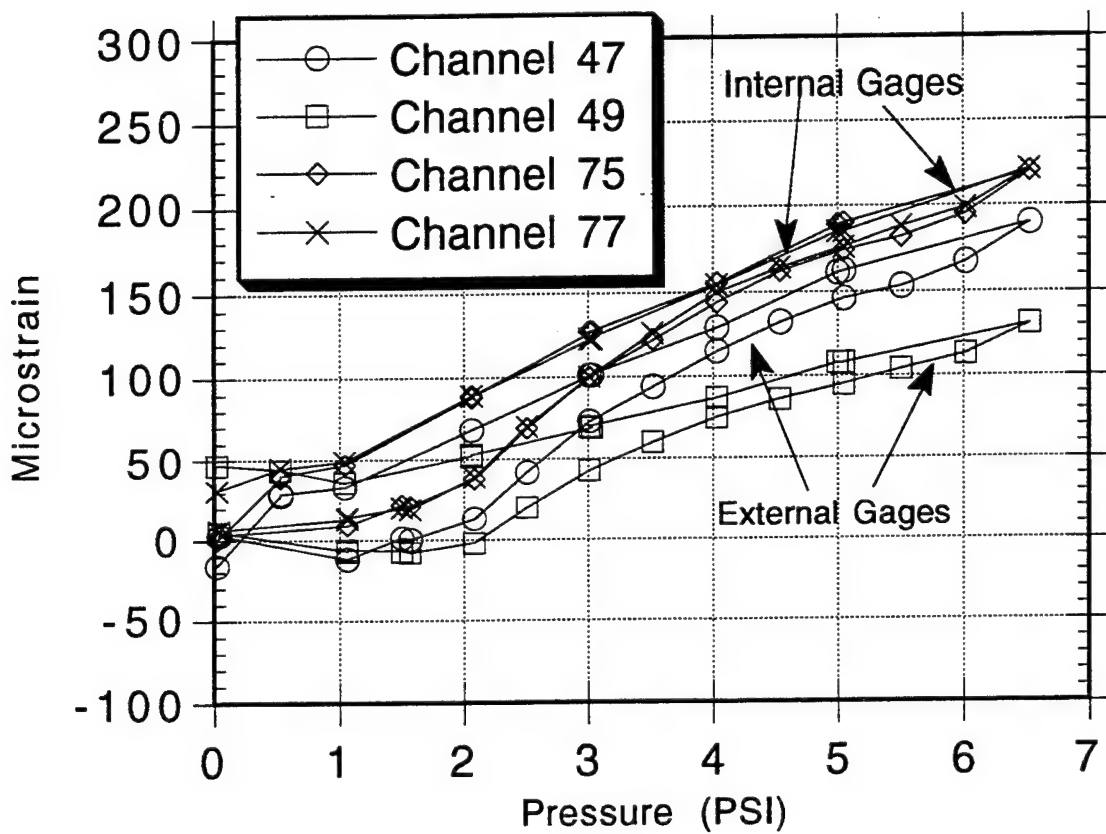


Figure 3.26. Comparison of Internal and External Longitudinal Strains
Measured at S-10L Lap Splice Joint, BS475.
(Refer to Figure A.5 and A.8.)

NOTE: All gages are above the upper rivet row.

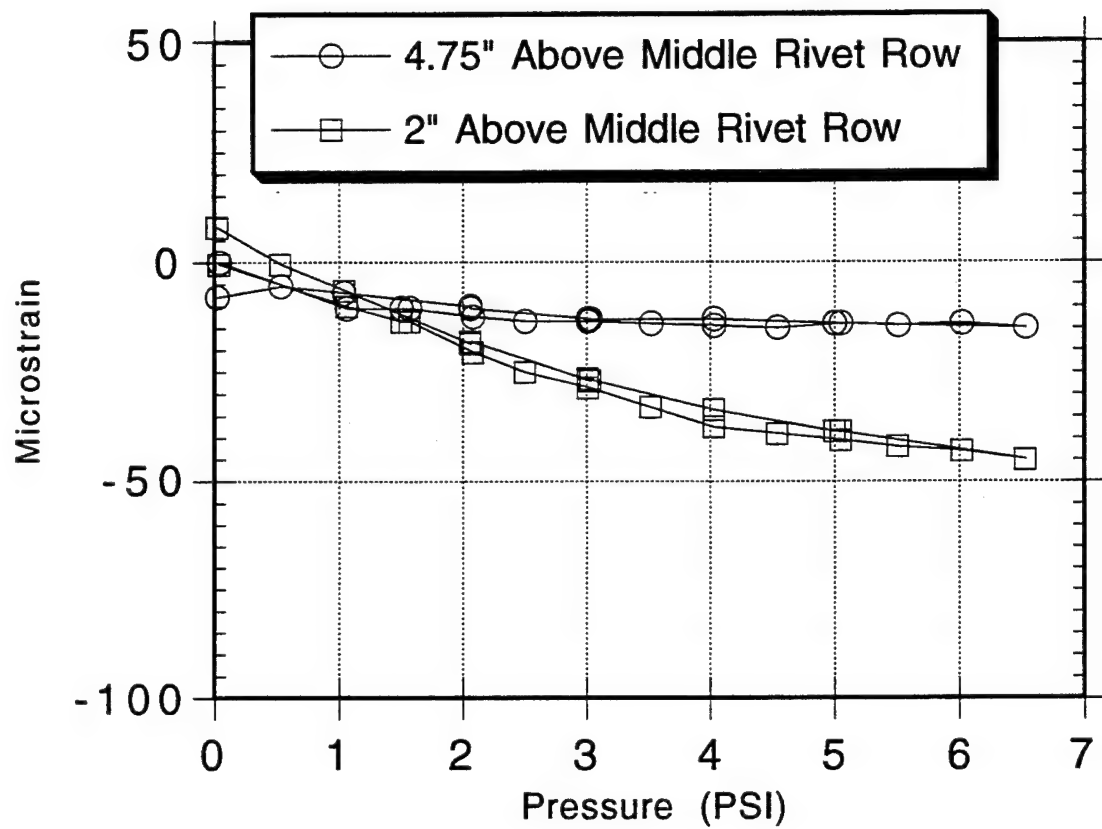


Figure 3.27. Bending Strains in Longitudinal Direction at S-10L Lap Splice Joint, BS475. (Refer to Figure A.5.)

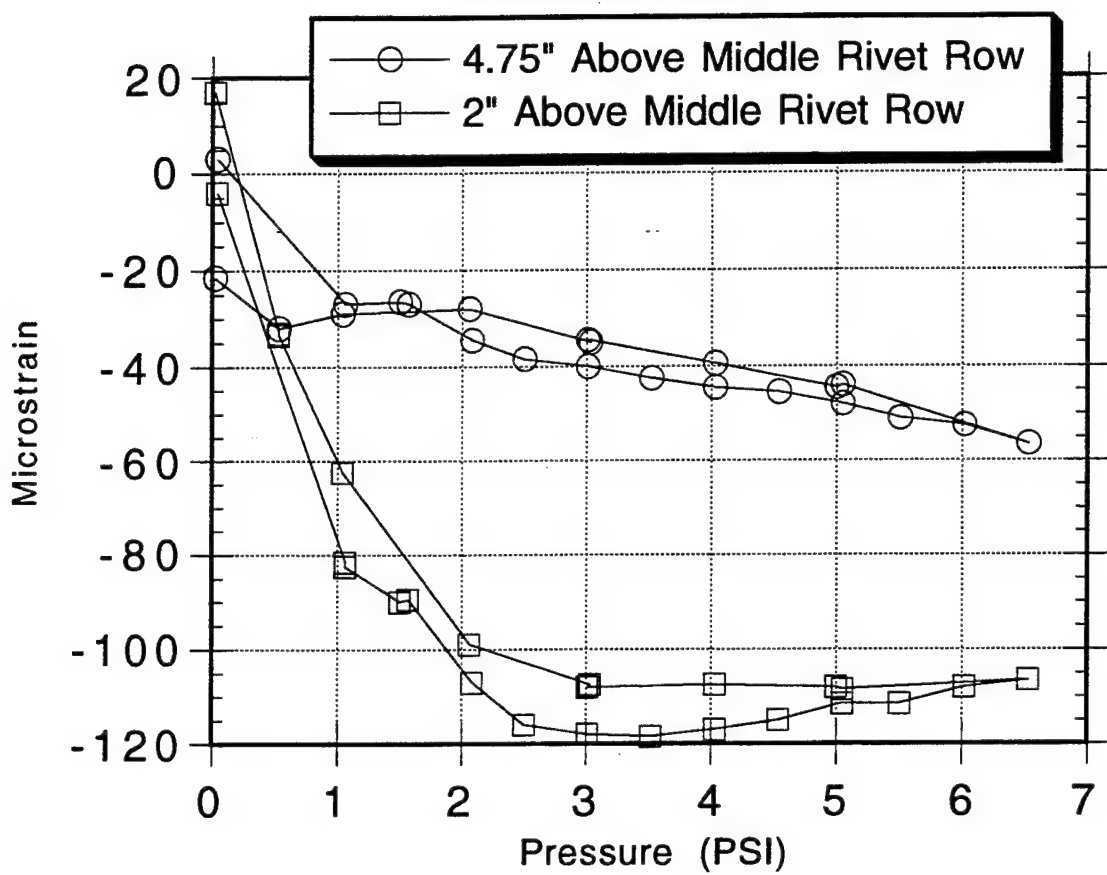


Figure 3.28. Bending Strains in Hoop Direction at S-4L, BS475.
(Refer to Figure A.4.)

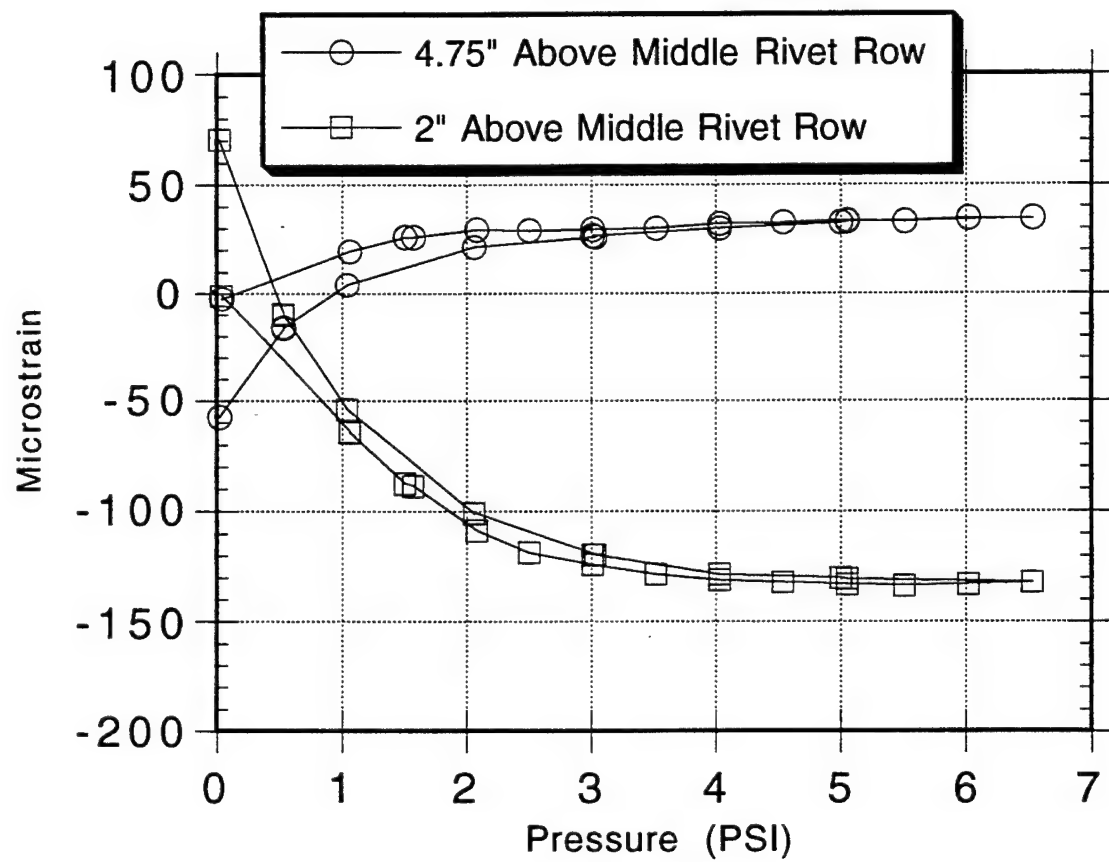


Figure 3.29. Bending Strains in Hoop Direction at S-10L, BS475.
(Refer to Figure A.5.)

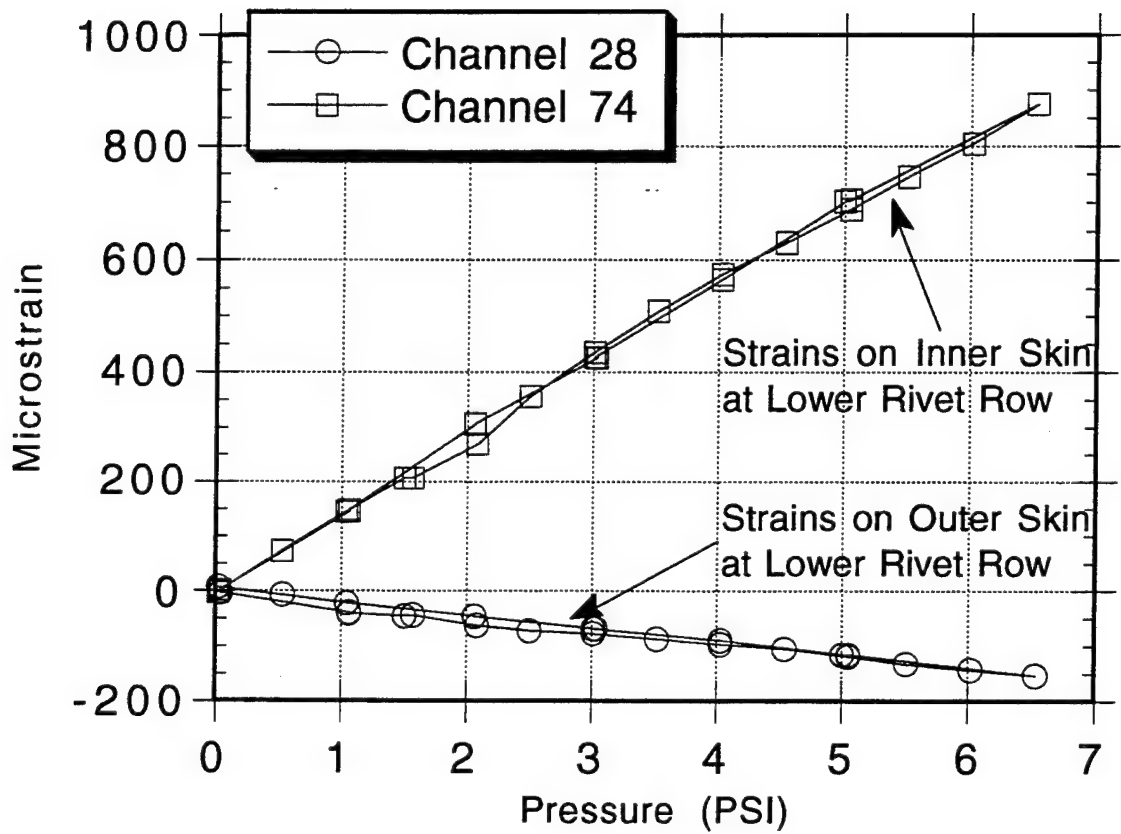


Figure 3.30. Hoop Strains in Lower Rivet Row on Inner and Outer Lap Skins at S-4L, BS475. (Refer to Figure A.4 and A.7.)

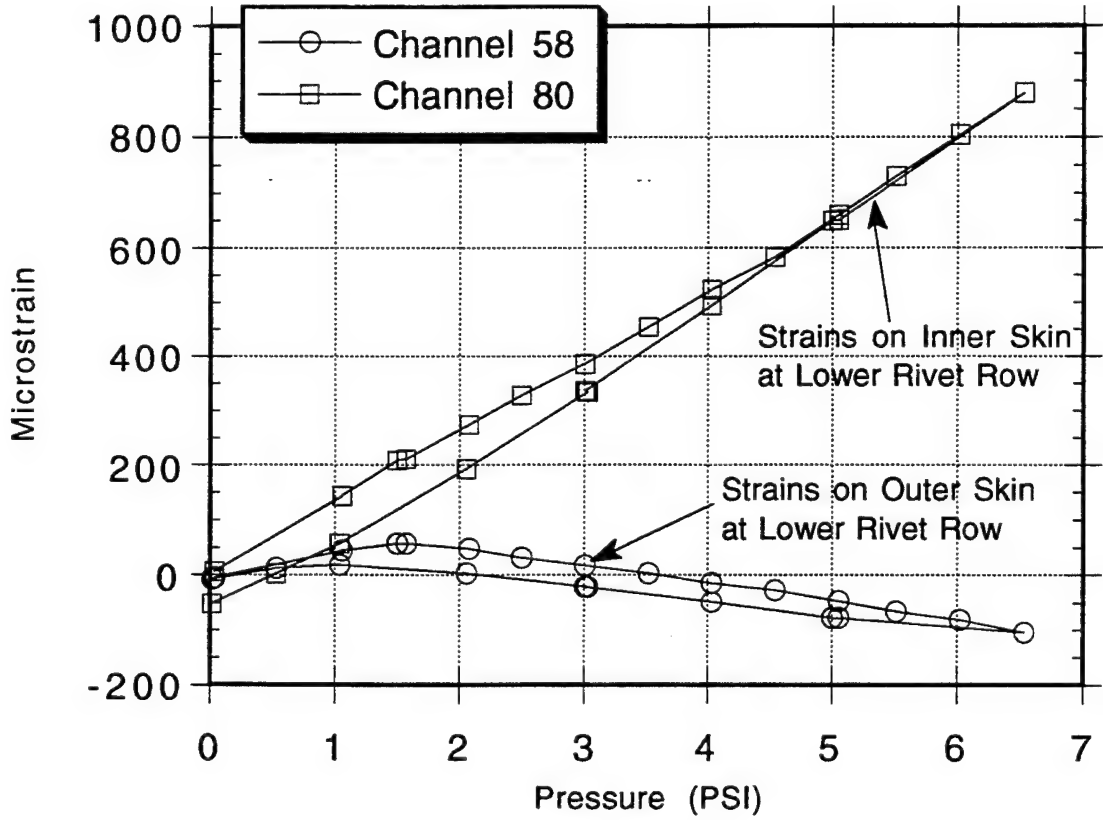


Figure 3.31. Hoop Strains in Lower Rivet Row on Inner and Outer Lap Skins at S-10L, BS475. (Refer to Figure A.5 and A.8.)

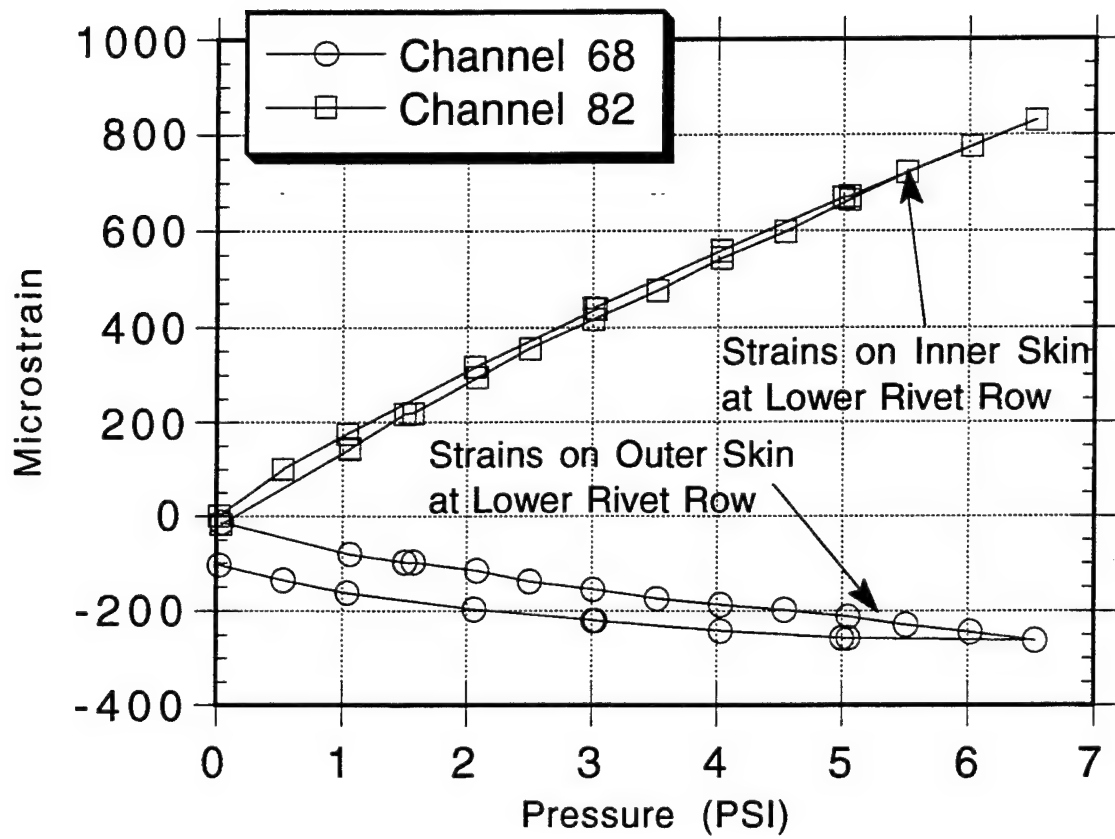


Figure 3.32. Hoop Strains in Lower Rivet Row on Inner and Outer Lap Skins at S-14L, BS475. (Refer to Figure A.6 and A.9.)

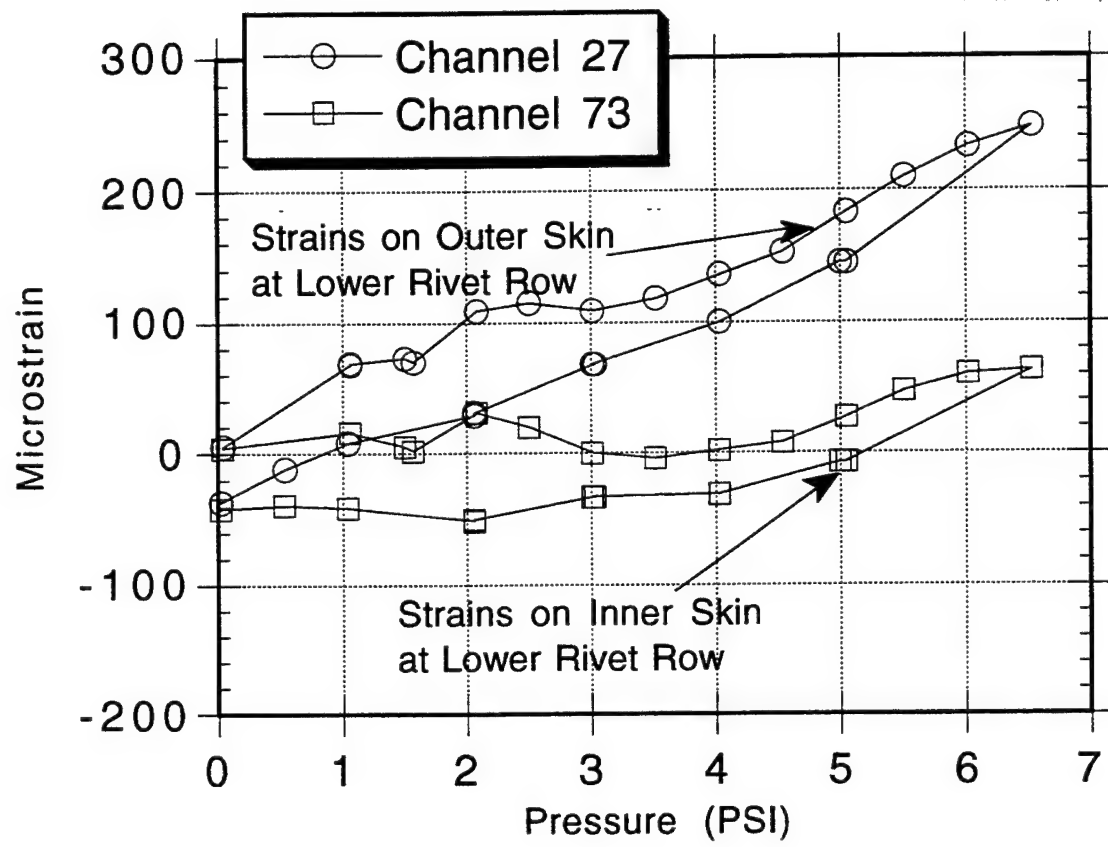


Figure 3.33. Longitudinal Strains in Lower Rivet Row on Inner and Outer Lap Skins at S-4L, BS475. (Refer to Figure A.4 and A.7.)

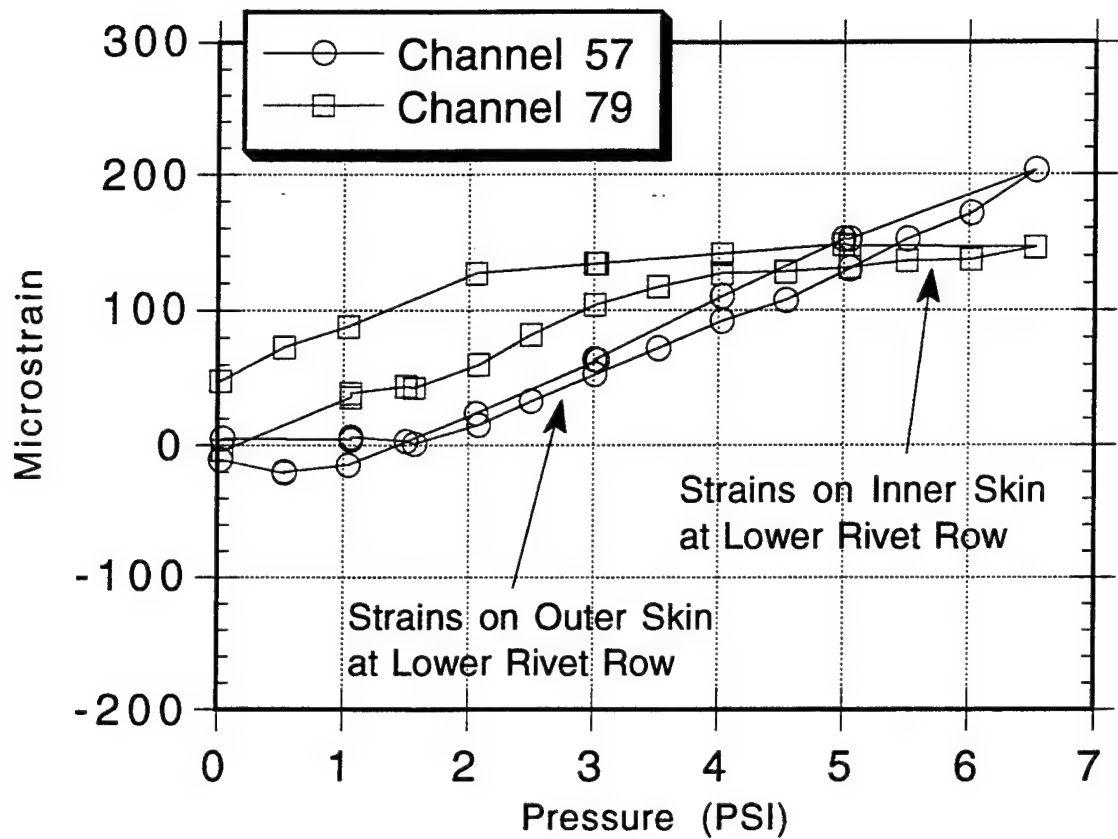


Figure 3.34. Longitudinal Strains in Lower Rivet Row on Inner and Outer Lap Skins at S-10L, BS475. (Refer to Figure A.5 and A.8.)

The maximum strains are approximately 900 $\mu\epsilon$ in the hoop direction and 250 $\mu\epsilon$ in the longitudinal direction. These results show that the lower rivet row of the inner skin experiences the same peak strains as the upper rivet row of the outer skin. Thus, these two areas should be treated similarly in fatigue and damage tolerance analyses.

3.4 STRAINS IN SUBSTRUCTURE ELEMENTS

Gages were installed on the frames and stringers directly beneath the S-4L and S-10L lap joints between Body Stations 470 and 480 to study the strains in fuselage substructure elements. Figures 3.35 and 3.36 show the hoop and radial strains, respectively, in the frame at Body Station 480. The maximum hoop strains measured in the frame are between 600 $\mu\epsilon$ and 700 $\mu\epsilon$ which are approximately 30 to 40% lower than the maximum strains in the skin directly above the frame (see Figures 3.8 and 3.10). The strains measured in stringers S-4L and S-10L (BS475) are plotted in Figures 3.37 and 3.38 (refer to Figures A.14, A.15, and 2.10 for exact locations). As expected, the longitudinal strains are positive and, again, are slightly lower than those measured on the attached skin (maximum strains in the stringer vary between 200 $\mu\epsilon$ and 350 $\mu\epsilon$; in the skin between 250 $\mu\epsilon$ and 400 $\mu\epsilon$). The stringer cap strains in the transverse or hoop direction are negative with maximum values between -350 $\mu\epsilon$ and -400 $\mu\epsilon$ at a differential pressure of 6.5 psi.

3.5 COMPENSATION FOR THERMAL AND AMBIENT NOISE INDUCED STRAINS

Thermocouples mounted inside (air temperature) and outside (skin temperature) the aircraft showed that the maximum temperature difference between the inside air and external skin was only 24 °F (86 °F inside air; 66 °F outside skin); the skin temperature changed by only 12 °F during one pressure cycle. Since the strain gages have self-temperature compensation, their thermally induced output is insignificant over the temperature ranges measured. In order to assess the amount of strain induced by thermal excursions and ambient noise in the data acquisition system, several strain gages were mounted to unstrained 2024-T3 aluminum plates. The plates were the same thickness as the fuselage skin. They were placed both inside and outside the aircraft near the instrumented lap splice bays. Strain measurements were taken at each pressure interval. Figure 3.39 shows the strains measured by these gages. For the most part, no more than 5 $\mu\epsilon$ of error was introduced as a result of the combined effect of temperature and signal noise. The maximum error during the course of a pressure cycle was 10 $\mu\epsilon$. Since these strains represent only a few percent of the full-range strains measured, the data were not corrected for errors introduced by temperature and signal noise effects.

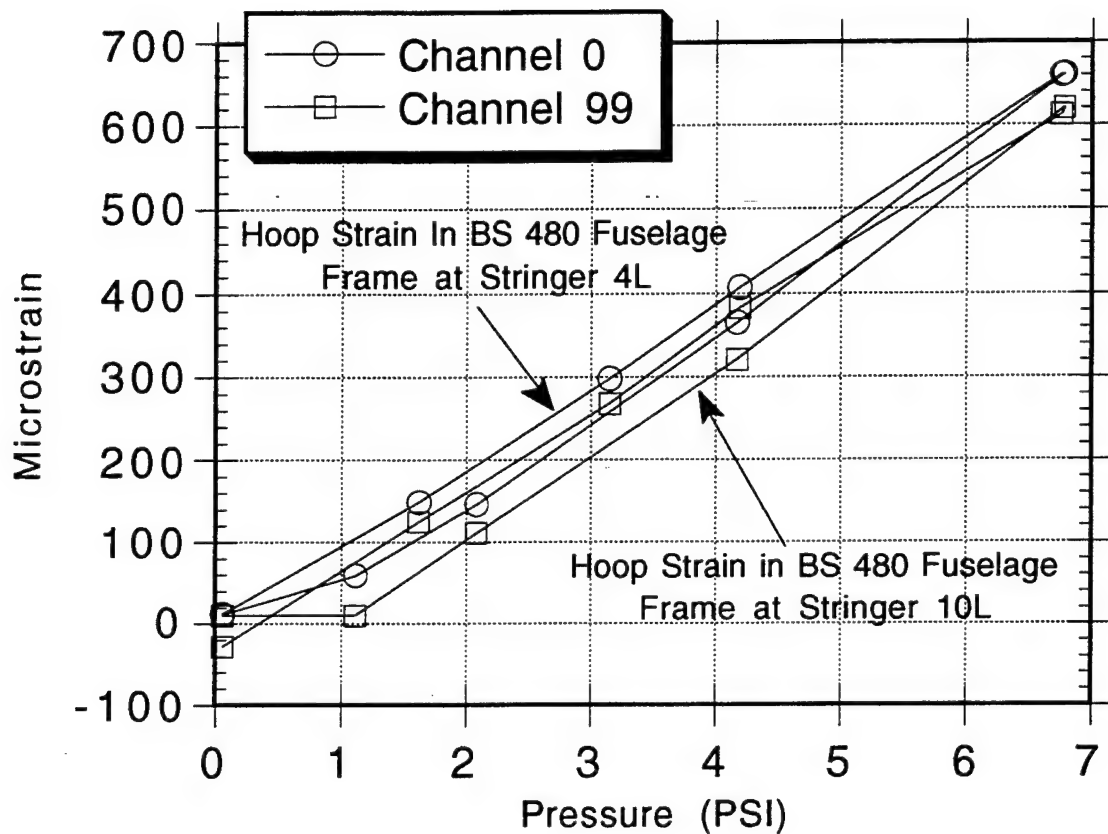


Figure 3.35. Hoop Strains in BS480 Fuselage Frame at Stringers S-4L and S-10L. (Refer to Figure A.14 and A.15.)

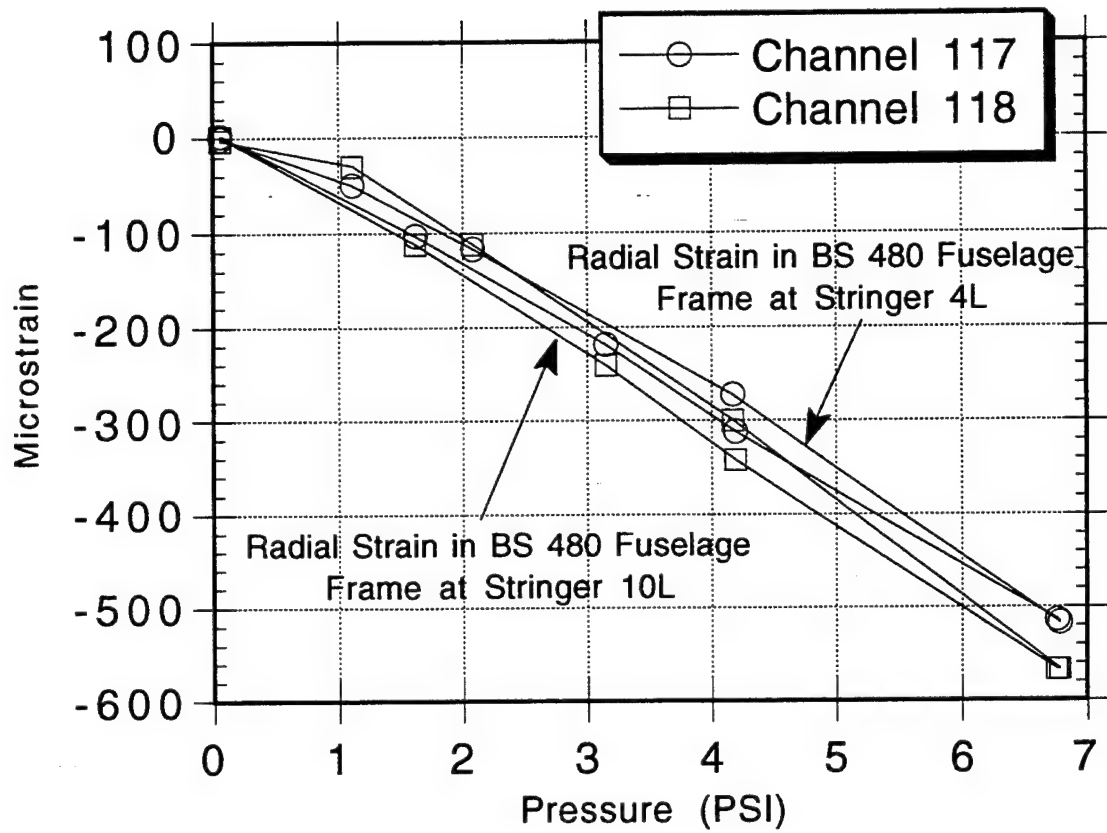


Figure 3.36. Radial Strains in BS480 Fuselage Frame at Stringers S-4L and S-10L. (Refer to Figure A.14 and A.15.)

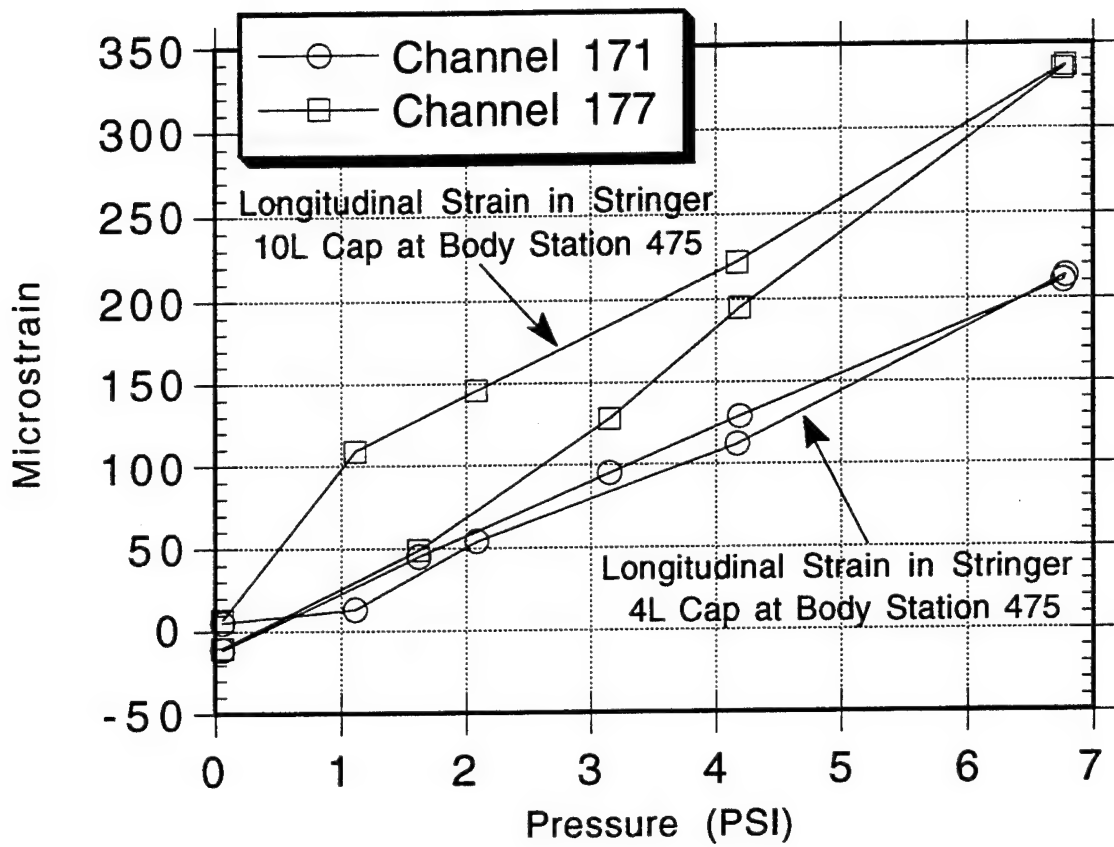


Figure 3.37. Longitudinal Strains in S-10L and S-4L Stringer Caps at BS475.
(Refer to Figure A.14 and A.15.)

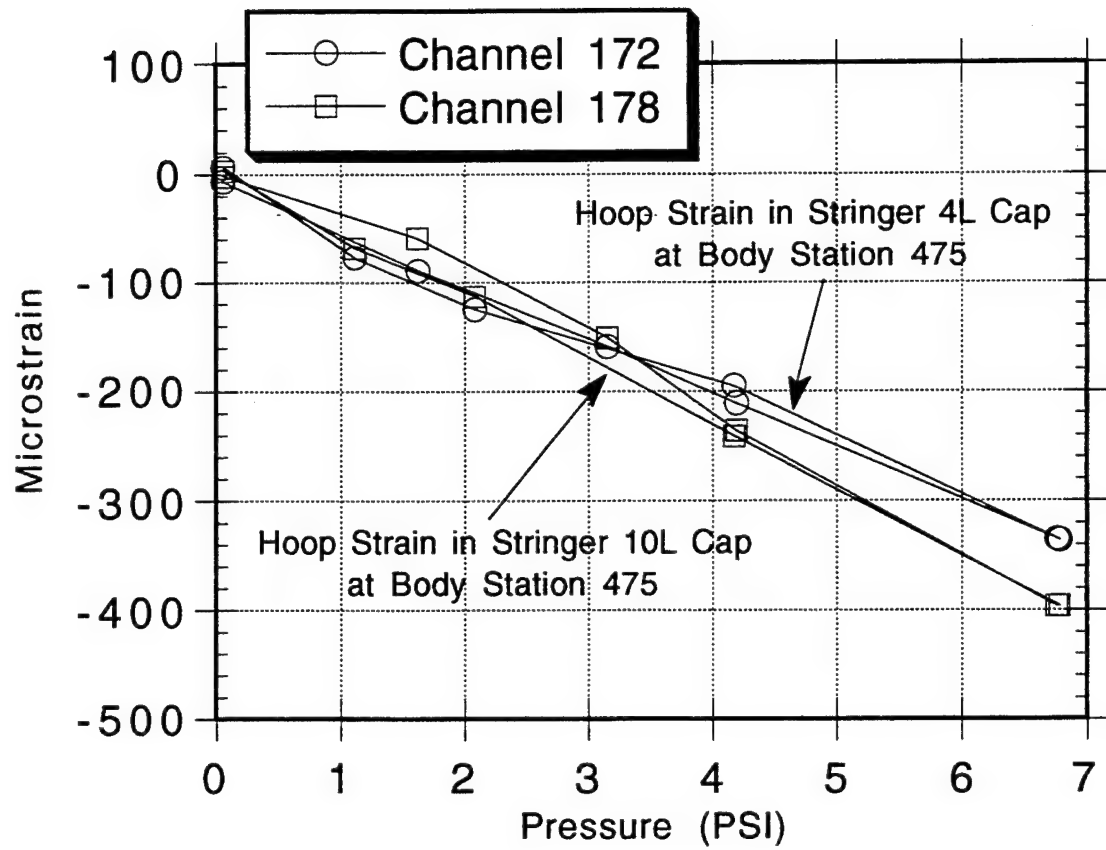
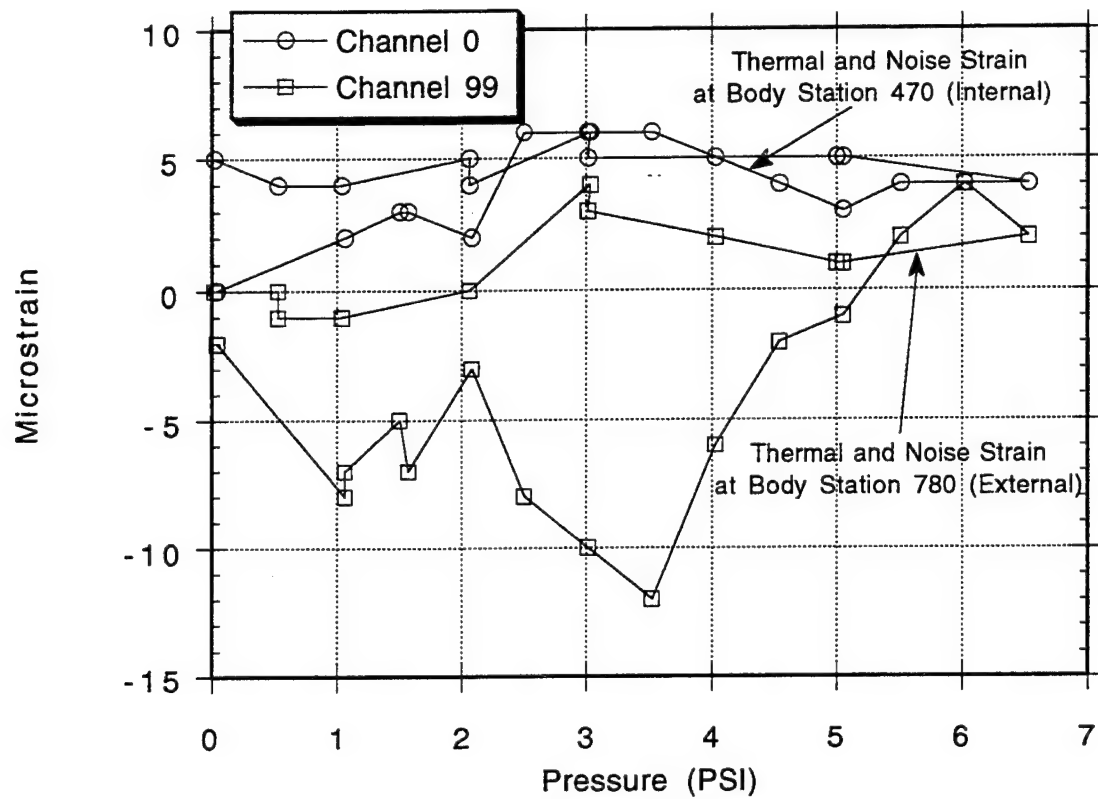


Figure 3.38. Hoop Strains in S-10L and S-4L Stringer Caps at BS475.
(Refer to Figure A.14 and A.15.)



*Figure 3.39. Strains Induced by Temperature and Signal Noise Effects.
(Refer to Figure A.14 and A.15.)*

3.6 STRAIN CONSISTENCY OVER SEVERAL PRESSURE CYCLES

Figures 3.40 to 3.42 show four sets of strain data collected from different pressure cycles. Specifically, strains were measured at four different locations: (1) upper rivet row at the midline (S-4L, BS475), (2) 1 inch above the upper rivet row over the frame (S-10L, BS480), (3) upper rivet row at the midline (S-10L, BS785), and (4) 1 inch below the lower rivet row at the midline (S-10L, BS475). Therefore, these plots show strain profiles from gages mounted both forward and aft of the wings, as well as near substructure elements. Moreover, these plots show that: (1) the test set-up provided consistent aircraft loads, and (2) strain fields could be repeated for consistent loads. The maximum variation in strain from one pressure cycle to another was less than 10% at any pressure level. The data presented in Figures 3.40 to 3.42 demonstrate repeatability of hoop strains. Although the data are not displayed here, the same repeatability can be shown for the longitudinal strains as well.

3.7 STRESS FIELDS IN LAP SPLICING BAYS

In this section, strain data collected from the biaxial and rosette gages are used to calculate stresses in the skin, frames, and stringers. The orientation of the principal stresses is also calculated to quantify local shearing stresses.

3.7.1 Membrane Stresses

Strains measured from the biaxial (hoop and longitudinal) gages can be used to calculate the corresponding membrane stresses from the following equations:

$$\sigma_{\theta} = \frac{E}{1-\nu^2} [\varepsilon_{\theta} + \nu \varepsilon_z] \quad (3.2)$$

$$\sigma_z = \frac{E}{1-\nu^2} [\varepsilon_z + \nu \varepsilon_{\theta}] \quad (3.3)$$

where E is the modulus of elasticity, ν is Poisson's ratio, σ_{θ} is the hoop stress in the skin or the frame, σ_z is the longitudinal stress in the skin or the stringer, ε_{θ} is the hoop strain, and ε_z is the longitudinal strain.

Table 3.4 lists hoop and longitudinal strains measured at the midbay and midline location in each of the five lap splice test sections in the AANC airplane. The corresponding hoop and longitudinal stresses, calculated from equations (3.2) and (3.3), are also listed in the table. For comparison, the hoop and longitudinal stresses in a closed-end, thin-walled cylinder subjected to internal pressure can be calculated from:

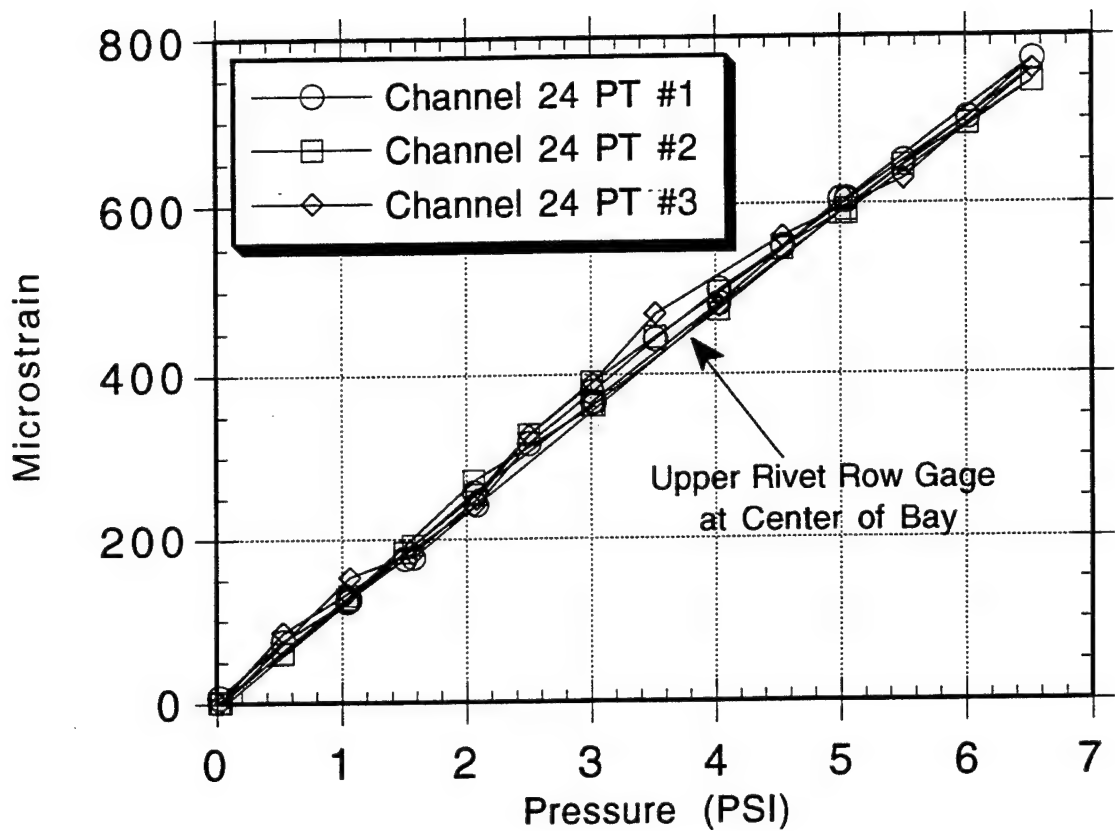


Figure 3.40. Hoop Strains Measured in Upper Rivet Row at S-4L, BS475 from Tests 1, 2, and 3. (Refer to Figure A.4.)

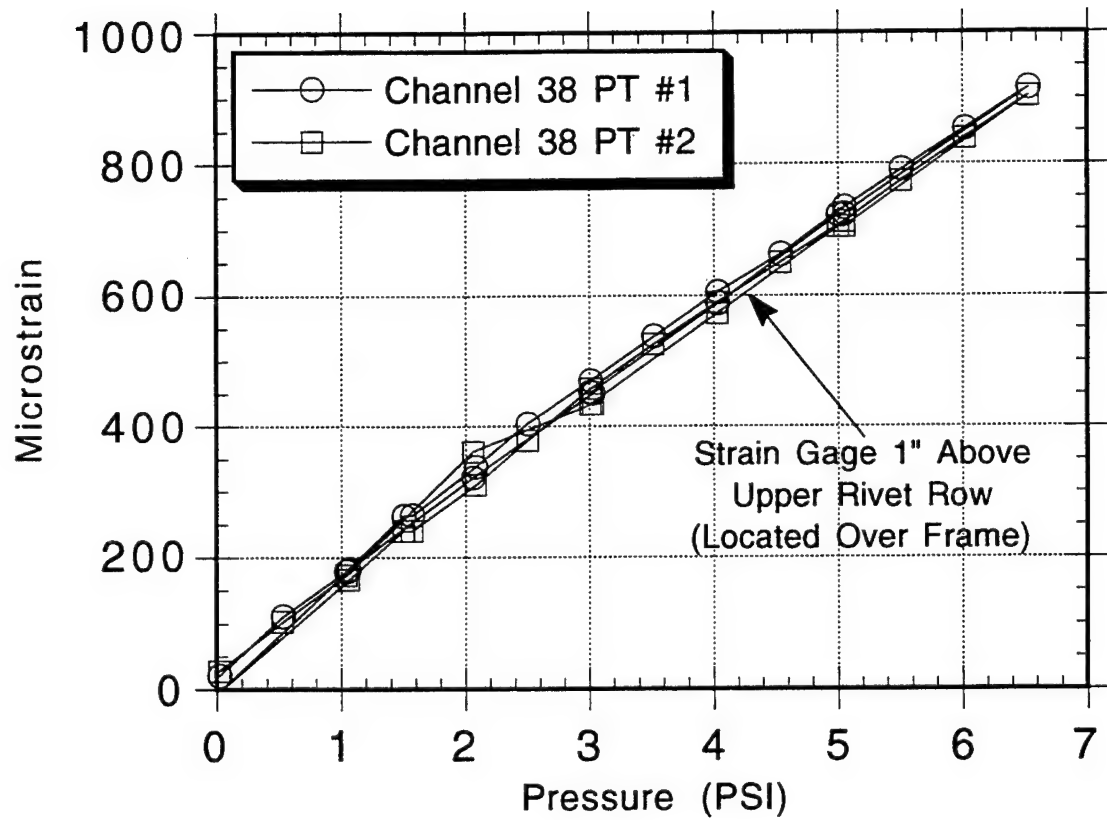


Figure 3.41. Hoop Strains Measured 1 Inch Above Upper Rivet Row at S-10L, BS480 from Tests 1 and 2. (Refer to Figure A.5.)

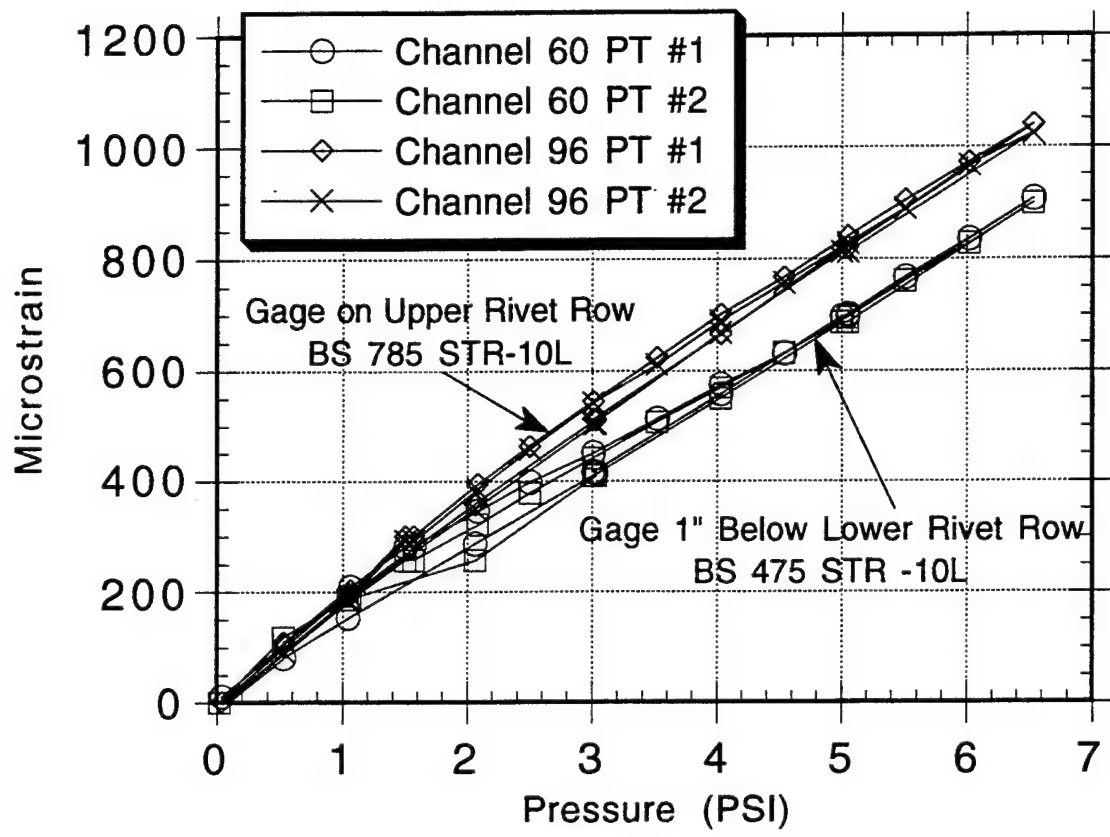


Figure 3.42. Hoop Strains Measured by Channels 60 and 96 from Tests 1 and 2. (Refer to Figures A.5 and A.11.)

Table 3.4. Comparison of Strains and Stresses at Midline/Midbay Location in Various Test Sections at 6.5 psi.

Test Section Location	Measured Strain ($\mu\text{inch/inch}$)			Calculated Stress (ksi)		
	ε_θ	ε_z	$\varepsilon_z / \varepsilon_\theta$	σ_θ	σ_z	σ_z / σ_θ
S-4L, BS475 (Channels 17 and 18)	825 (0.776)	189 (0.875)	0.229	9.7 (0.724)	4.8 (0.716)	0.495
S-10L, BS475 (Channels 47 and 48)	931 (0.876)	222 (1.028)	0.238	11.0 (0.821)	5.5 (0.821)	0.503
S-14L, BS475 (Channels 61 and 62)	929 (0.874)	190 (0.880)	0.205	10.8 (0.806)	5.2 (0.776)	0.475
S-4L, BS785 (Channels 83 and 84)	948 (0.892)	266 (1.231)	0.281	11.3 (0.843)	6.0 (0.896)	0.536
S-10L, BS785 (Channels 91 and 92)	961 (0.904)	225 (1.042)	0.234	11.3 (0.843)	5.6 (0.836)	0.499

NOTES:

- (1) Numbers in parentheses are ratios of measured quantities to theoretical values based on thin-walled cylinder approximation.
- (2) These comparisons are valid only at the midline and midbay location. The thin-walled cylinder estimate may not be applicable for strains near the lap splice. Section 4.3 discusses finite element models that were developed to analyze strains near the lap joint.

$$\sigma_\theta = \frac{pR}{t} \quad (3.4)$$

$$\sigma_z = \frac{pR}{2t} \quad (3.5)$$

where p is the differential pressure, R is the radius of the cylinder, and t is the skin thickness. From equations (3.2) and (3.3), the theoretical strains are

$$\varepsilon_\theta = \frac{pR}{2Et} (2 - \nu) \quad (3.6)$$

$$\varepsilon_z = \frac{pR}{2Et} (1 - 2\nu) \quad (3.7)$$

From Mil-Handbook 5 [8], the modulus of elasticity and Poisson's ratio for 2024-T3 aluminum are: $E = 10.5$ ksi and $\nu = 0.33$, respectively. Also, for the AANC Boeing 737 airplane, $R = 74$ inches, $t = 0.036$ inch. Therefore, for an internal pressure of 6.5 psi, the thin-walled cylinder approximation yields the following values for strains and stresses: $\varepsilon_\theta = 1135 \mu\varepsilon$, $\varepsilon_z = 267 \mu\varepsilon$, $\sigma_\theta = 13.4$ ksi, and $\sigma_z = 6.7$ ksi. These theoretical values are compared to the actual strains and stresses at the midline and midbay location in Table 3.4. The actual stresses

vary between 70% to 90% of the thin-walled cylinder estimates. Similarly, the measured hoop strains differ from the theoretical value by similar percentages. When the actual strains in the longitudinal direction are compared to the thin-walled cylinder estimate, some are less than the theoretical value, and some are greater. This result is reasonable since an actual airplane fuselage contains stiffening elements that carry load and generally reduce strain.

From the thin-walled cylinder approximation, the ratio of the longitudinal strain to hoop strain is

$$\frac{\varepsilon_z}{\varepsilon_\theta} = \frac{1-2\nu}{2-\nu} \quad (3.8)$$

For $\nu = 0.33$, this ratio is 0.204. Again, because of stiffening elements, the actual ratio of longitudinal strain to hoop strain should be different from the value given by equation (3.8). In fact, the actual ratio of strains is a maximum of 40% higher than the estimated value (see Table 3.4). Similarly, the ratio of longitudinal stress to hoop stress is exactly one-half for a thin-walled cylinder. The actual ratios vary between 5% lower to 7% higher than this theoretical value.

Hoop and longitudinal skin stresses for various areas of different lap splice bays are plotted in Figures 3.43 to 3.48. Hoop stresses for the S-10L lap joint at Body Station 475 external skin, Body Station 475 internal skin, and Body Station 785 external skin are plotted in Figures 3.43, 3.45, and 3.47, respectively. Longitudinal stresses for the same three areas are plotted in Figures 3.44, 3.46, and 3.48, respectively. The maximum hoop stresses are between 9 and 13 ksi at a differential pressure of 6.5 psi, compared to a calculated value of 13.4 ksi from equation (3.4). Again, the combined effect of the load transfer and reverse bending produces a large difference in hoop stresses between the internal and external skins near the lower rivet row. Figure 3.43 shows that the hoop stresses in the upper skin on the outside at the lower rivet row are negligible, but Figure 3.45 shows that the same stresses in lower skin on the inside reach a peak value of 11 ksi. The longitudinal stresses are approximately one-half of the hoop stresses. The maximum longitudinal stresses vary between 5 and 6.5 ksi at a differential pressure of 6.5 psi, compared to a calculated value of 6.7 ksi from equation (3.5).

Hoop and longitudinal stresses in the substructure elements were also calculated using equations (3.2) and (3.3). The longitudinal stresses in the S-10L stringer at BS475 and the S-4L stringer at BS475 are plotted in Figure 3.49. The peak longitudinal stresses in the stringers vary between 1300 and 2400 psi at a differential pressure of 6.5 psi. These values are approximately one-third of those in the mating lap splice skin.

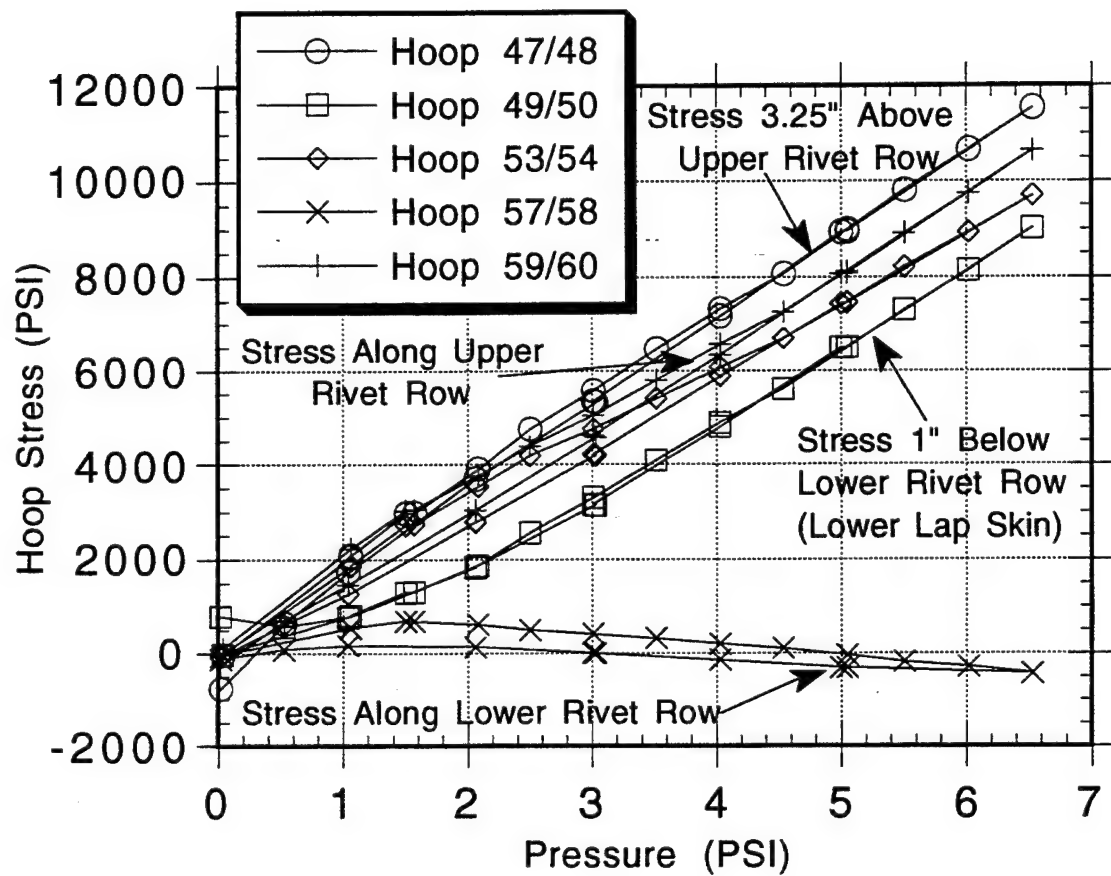


Figure 3.43. External Hoop Stresses at S-10L, BS475.
 (Refer to Figure A.5.)

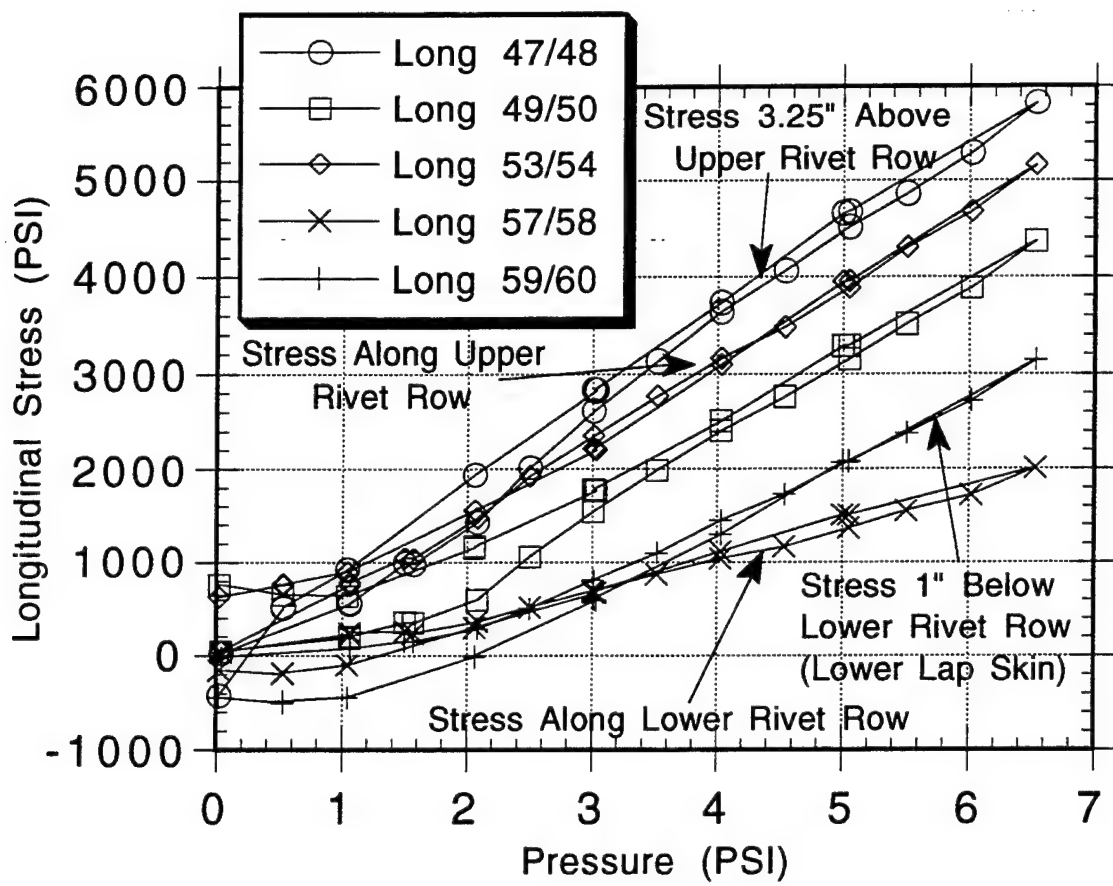


Figure 3.44. External Longitudinal Stresses at S-10L, BS475.
(Refer to Figure A.5.)

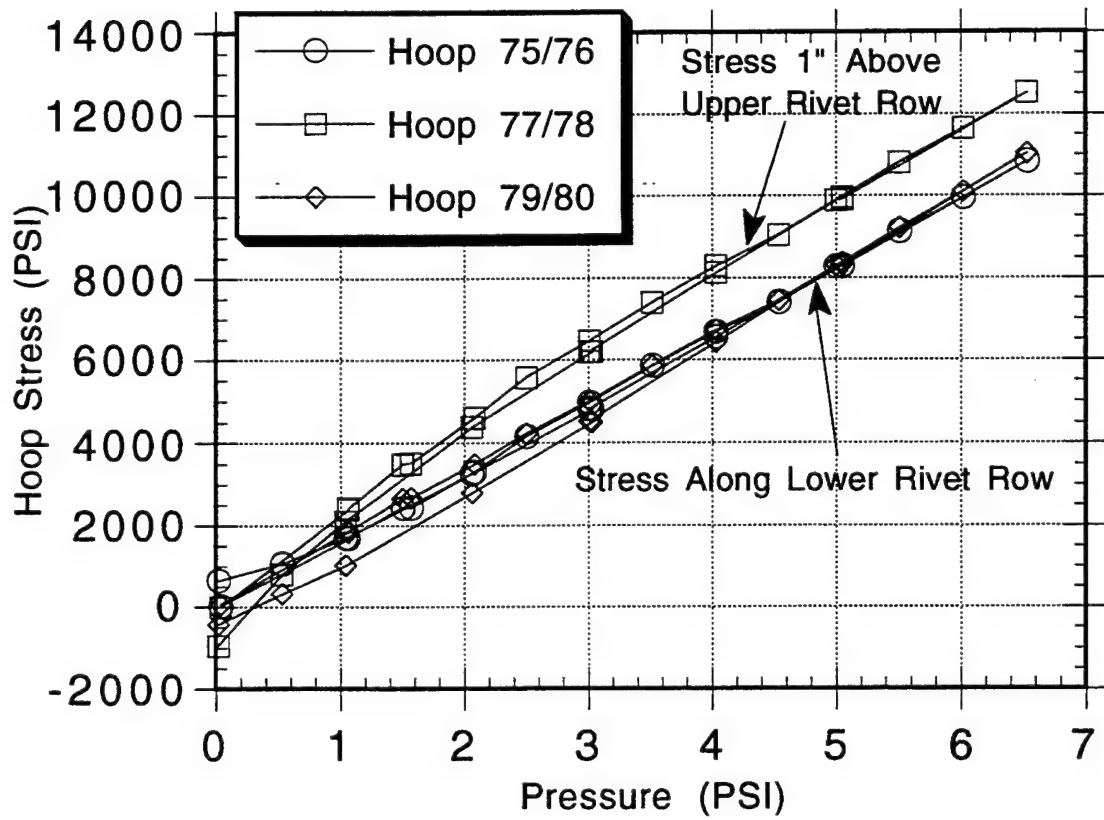


Figure 3.45. Internal Hoop Stresses at S-10L, BS475.
 (Refer to Figure A.8.)

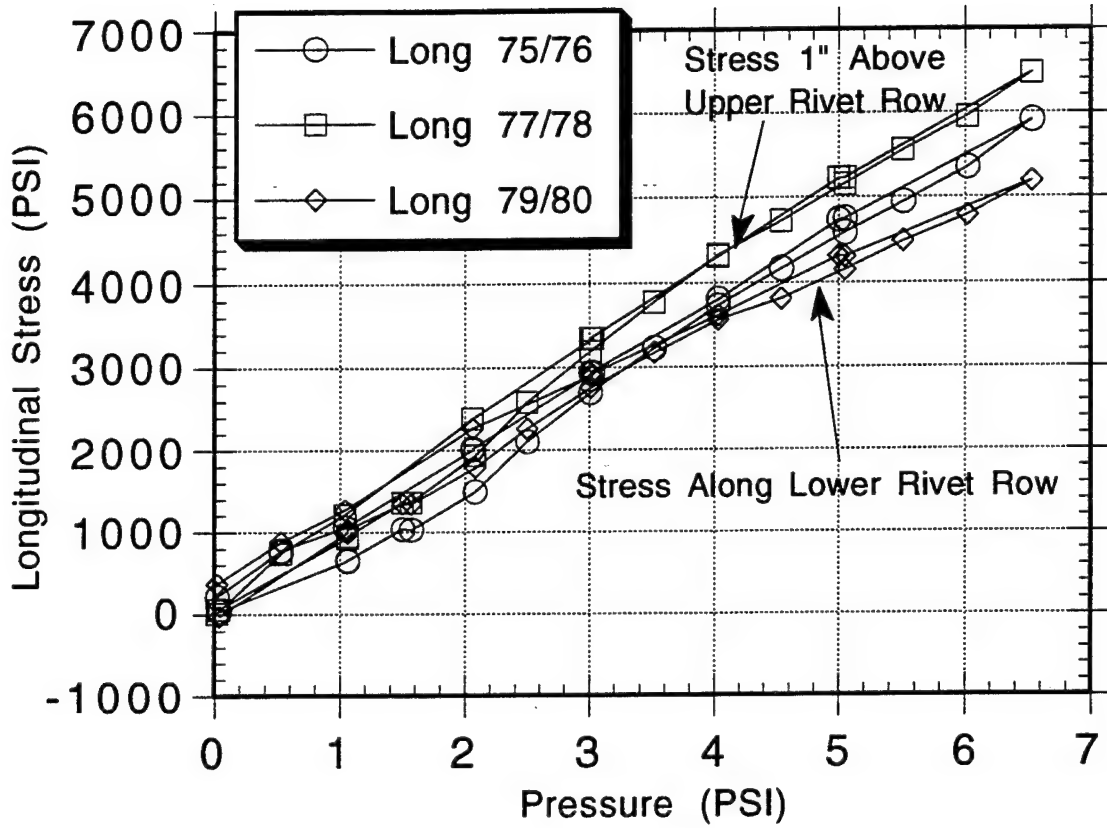


Figure 3.46. Internal Longitudinal Stresses at S-10L, BS475.
(Refer to Figure A.8.)

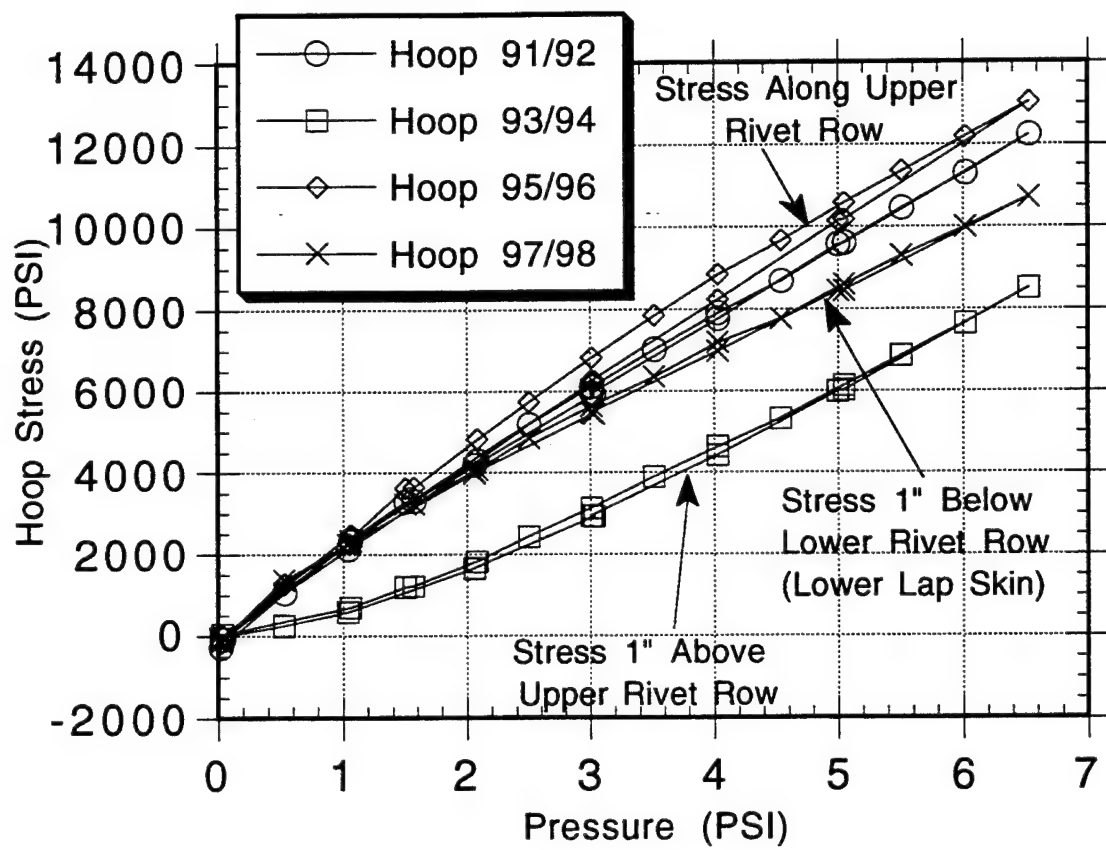


Figure 3.47. External Hoop Stresses at S-10L, BS785.
(Refer to Figure A.11.)

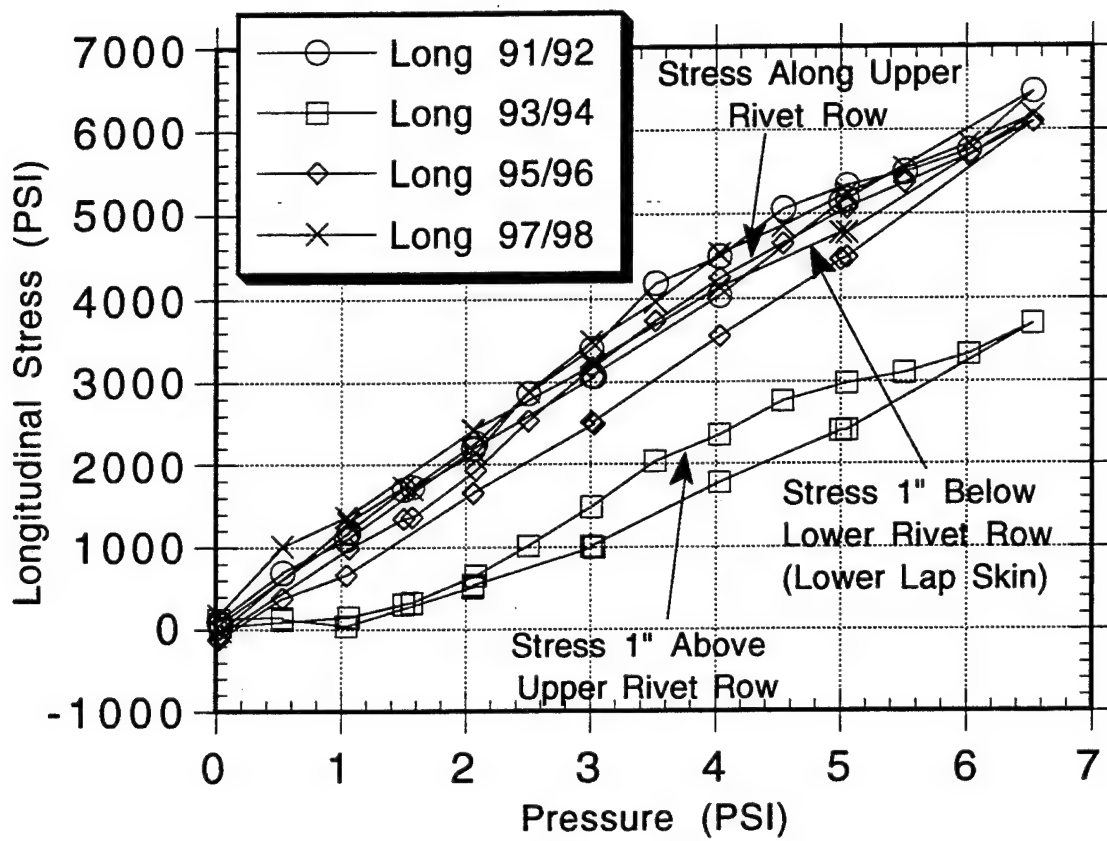
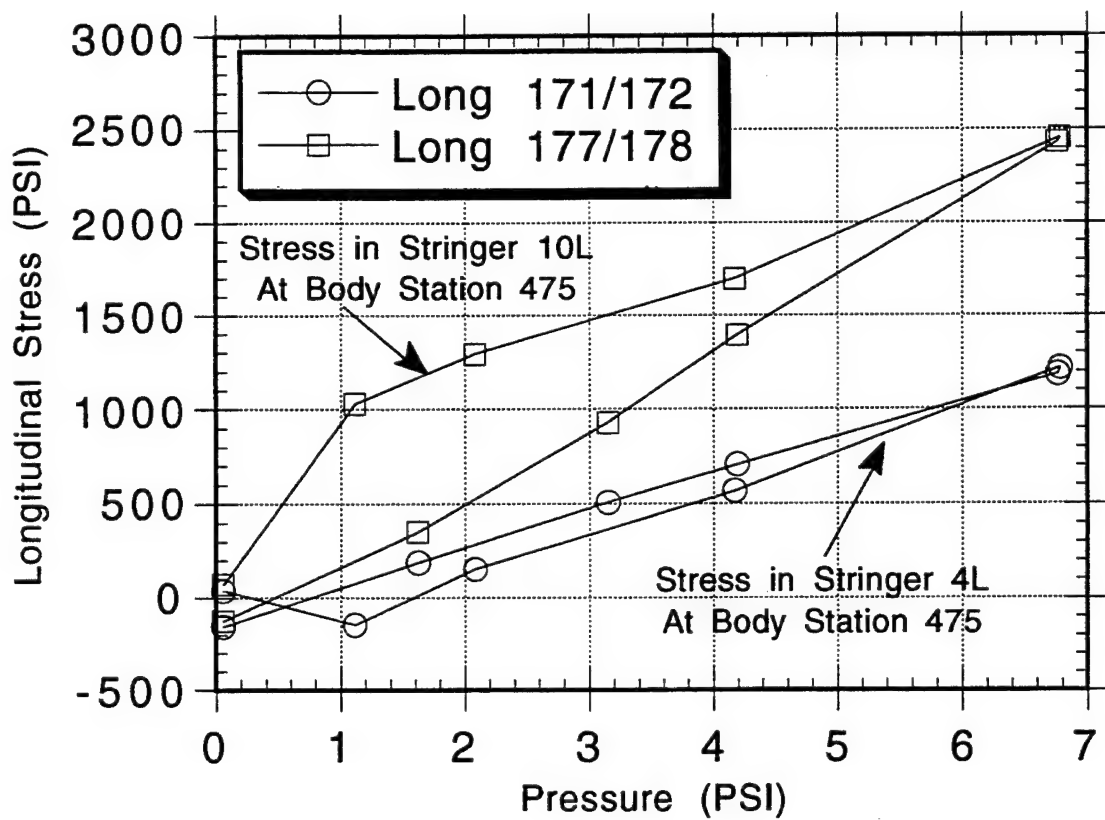


Figure 3.48. External Longitudinal Stresses at S-10L, BS785.
(Refer to Figure A.11.)



*Figure 3.49. Longitudinal Stresses in Stringers S-4L and S-10L at BS475.
(Refer to Figures A.14 and A.15.)*

For comparison, the longitudinal stress in the stringer can be estimated using a modified thin-walled cylinder analysis. In this analysis, the fuselage is assumed to be a thin-walled cylinder with circular cross section and stringers attached to the skin at uniform spacing. Equilibrium of forces in the longitudinal direction dictates that

$$p\pi R^2 = (2\pi R t)\sigma_z + N A \sigma_L \quad (3.9)$$

where N is the number of stringers, A is the cross-sectional area of the stringers, and σ_L is the longitudinal stress in the stringers. Compatibility of strains between the stringer and the skin requires that

$$\varepsilon_z = \frac{\sigma_L}{E} = \frac{1}{E}(\sigma_z - \nu \sigma_\theta) \quad (3.10)$$

where σ_θ is the hoop stress as defined in equation (3.4). After combining equations (3.5), (3.9), and (3.10); the longitudinal stresses in the skin and the stringer are

$$\sigma_z = \frac{pR}{2t} \left[\frac{1+2\nu\alpha}{1+\alpha} \right] \quad (3.11)$$

$$\sigma_L = \frac{pR}{2t} \left[\frac{1-2\nu}{1+\alpha} \right] \quad (3.12)$$

In these equations, α is a dimensionless quantity defined as

$$\alpha = \frac{NA}{2\pi R t} = \frac{A}{Lt} \quad (3.13)$$

where L is the stringer spacing. For the AANC 737 airplane, $L = 9.6$ inches. The cross-sectional area of stringers S-4L and S-10L are identical and equal to 0.116 in². (The dimensions of these stringers are listed in Table 4.1.) Thus, the longitudinal stress in the stringer calculated from equation (3.12) is 2.0 ksi at an internal pressure of 6.5 psi. This theoretical value compares reasonably well with the experimental values of 1.3 and 2.4 ksi.

Hoop stresses in the fuselage frame at BS480 at both the S-4L and S-10L stringer locations are shown in Figure 3.50. The hoop stresses in the frame (peak values of 5 to 6 ksi) are much lower than in the adjacent areas measured in the lap splice skin, as shown in Figures 3.43, 3.45, and 3.47.

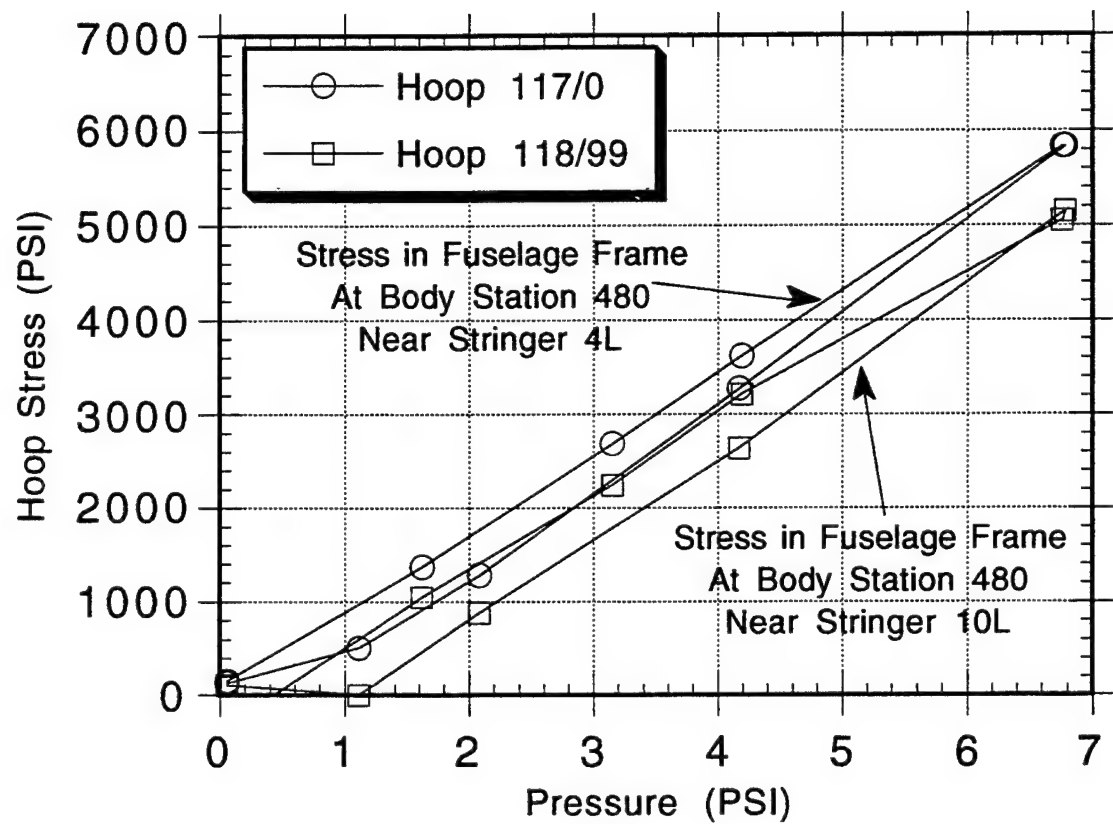


Figure 3.50. Hoop Stresses in Fuselage Frames at BS480, Stringers S-4L and S-10L. (Refer to Figures A.14 and A.15.)

3.7.2 Principal Stresses

The principal stresses were determined from strain data obtained from the rosette gages. Figures A.4 and A.5 show the locations of the four rosette strain gages employed in the AANC pressurization tests. In these three-element rectangular rosettes, gages were placed at 0°, 45°, and 90° orientations corresponding to strains ε_1 , ε_2 , and ε_3 , as shown in Figure 3.51. From these individual strains, the maximum and minimum principal stresses can be calculated using the following equations

$$\sigma_{\max} = \frac{E(\varepsilon_1 + \varepsilon_3)}{2(1-\nu)} + \frac{E}{2(1-\nu)} [(\varepsilon_1 - \varepsilon_2)^2 + (\varepsilon_2 - \varepsilon_3)^2]^{1/2} \quad (3.14)$$

$$\sigma_{\min} = \frac{E(\varepsilon_1 + \varepsilon_3)}{2(1-\nu)} - \frac{E}{2(1-\nu)} [(\varepsilon_1 - \varepsilon_2)^2 + (\varepsilon_2 - \varepsilon_3)^2]^{1/2} \quad (3.15)$$

The orientation of the maximum principal stress σ_{\max} is defined by the angle θ (see Figure 3.51) which is determined from

$$\tan 2\theta = \frac{2\varepsilon_2 - \varepsilon_1 - \varepsilon_3}{\varepsilon_1 - \varepsilon_3} \quad (3.16)$$

In the AANC tests, all rosette gages were located 1 inch above the upper rivet row. Also, the rosettes were identified as R1 through R4 which correspond to the following strain channels:

- R1 = Channels 11, 12, 13 (S-4L, BS 471 near tear strap)
- R2 = Channels 14, 15, 16 (S-4L, BS 479 near fuselage frame)
- R3 = Channels 41, 42, 43 (S-10L, BS 471 near tear strap)
- R4 = Channels 44, 45, 46 (S-10L, BS 479 near fuselage frame)

The maximum principal stresses for rosettes R1 through R4 are plotted in Figure 3.52. The stresses in the fuselage crown (Stringer S-4L: R1 and R2) were the same as those near the window (Stringer S-10L: R3 and R4). Stresses measured near the fuselage frame (R2 and R4) were greater than the stresses near the tear straps (R1 and R3). Near the frame, the principal stresses reached 11 ksi at a differential pressure of 6.5 psi; near the tear strap, the stresses were approximately 8 ksi. These stress levels correspond to 82% and 60% of the thin-walled cylinder approximation of hoop stress as given by equation (3.4).

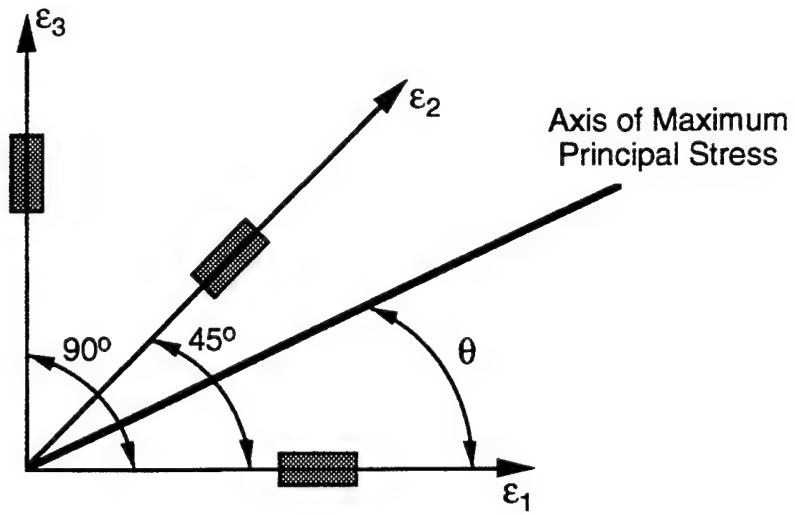


Figure 3.51. Strain Components Measured by Rectangular Gage Rosette.

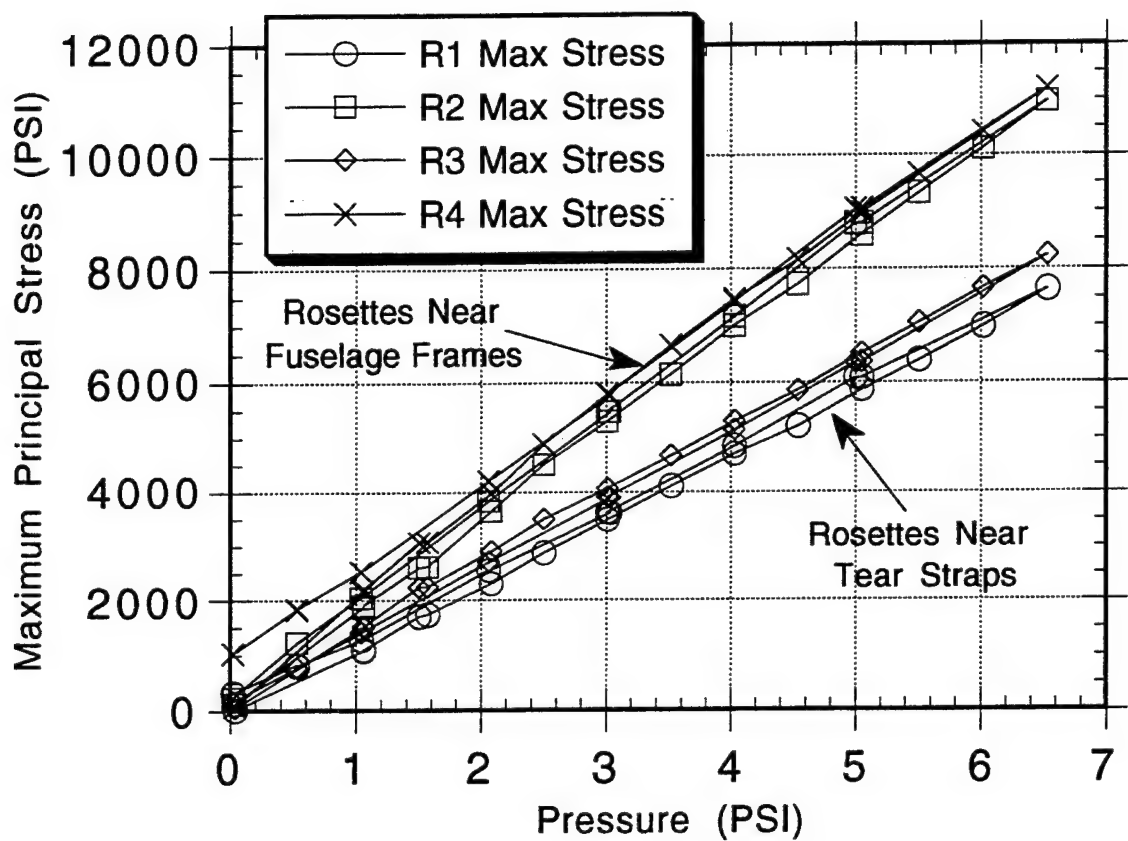


Figure 3.52. Maximum Principal Stresses One Inch Above Upper Rivet Row.
 (Refer to Figures A.4 and A.5.)

Figure 3.53 shows the direction of principal stress for each of the four rosettes. As a point of reference, the direction of principal stress for an internally pressurized thin-walled cylinder with uniform cross section is 90°, which corresponds to the hoop direction. In an actual fuselage structure, internal pressurization creates local shear and axial loads that shift the direction of principal stress from this theoretical value. The effect of local shearing is accentuated near substructure reinforcements such as stringers and frames. From the rosette data, the orientation of the principal stress varies between 76° to 86° at the peak pressure of 6.5 psi. At lower pressures, the principal stress direction was as low as 65°.

The magnitude of the local shearing stresses can be quantified from the angles defining the direction of principal stress. Assuming the ratio of longitudinal stress to hoop stress is exactly one-half, application of Mohr's circle for a two-dimensional state of stress shows that the ratio of shearing stress to hoop stress can vary between 0.04 (corresponding to $\theta = 86^\circ$) and 0.30 ($\theta = 65^\circ$).

3.8 FUSELAGE RADIAL GROWTH

The change in radius of the fuselage due to pressurization can also be estimated using a thin-walled cylinder approximation. From equation (3.6), the theoretical hoop strain is

$$\varepsilon_\theta = \frac{1}{E}(\sigma_\theta - \nu\sigma_z) = \frac{pR}{2Et}(2-\nu) = \frac{\Delta R}{R} \quad (3.17)$$

Therefore, the change in radius of a thin-walled cylinder due to internal pressurization can be estimated using the following equation:

$$\Delta R = \frac{pR^2}{2Et}(2-\nu). \quad (3.18)$$

Assuming $R = 74$ inches, $t = 0.036$ inch, $\nu = 0.33$, and $E = 10.5$ ksi for the AANC airplane, the change in radius, ΔR is 0.079 inch at a differential pressure, p , of 6.5 psi. In other words, the diameter increases by 0.158 inch. Since the actual airplane contains stiffening elements and its cross section is not exactly circular, the actual deformation should be smaller than this estimated value.

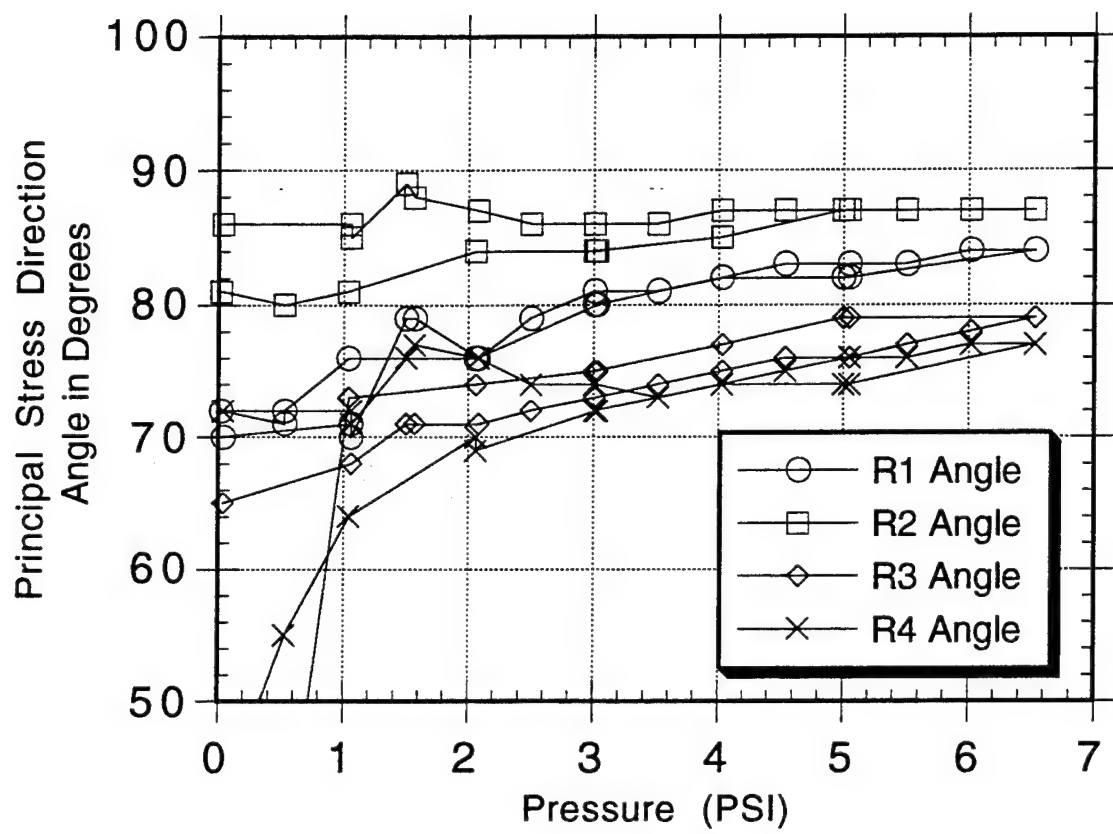


Figure 3.53. Principal Stress Directions Measured by Rosettes One Inch Above Upper Rivet Row. (Refer to Figures A.4 and A.5.)

In the AANC test set-up, the displacement gages measured the increased distance between stringers S-14L and S-10R at Body Stations 485 and 785 as the fuselage was pressurized. As such, these measurements approximated the increase in diameter because stringers S-14L and S-10R were not diametrically opposed.

Figure 3.54 shows the displacements measured at the forward (BS475) and aft (BS785) lap splice bays as the internal pressure was varied. A considerable amount of hysteresis is evident in these displacement curves. At an internal pressure of 6.5 psi, the radial displacements are 0.122 inch at BS475 and 0.156 inch at BS785. These measured values compare reasonably well with the estimated value of 0.158 inch. As expected, the measured displacements are slightly less than the theoretical value for an unstiffened, thin-walled cylinder.

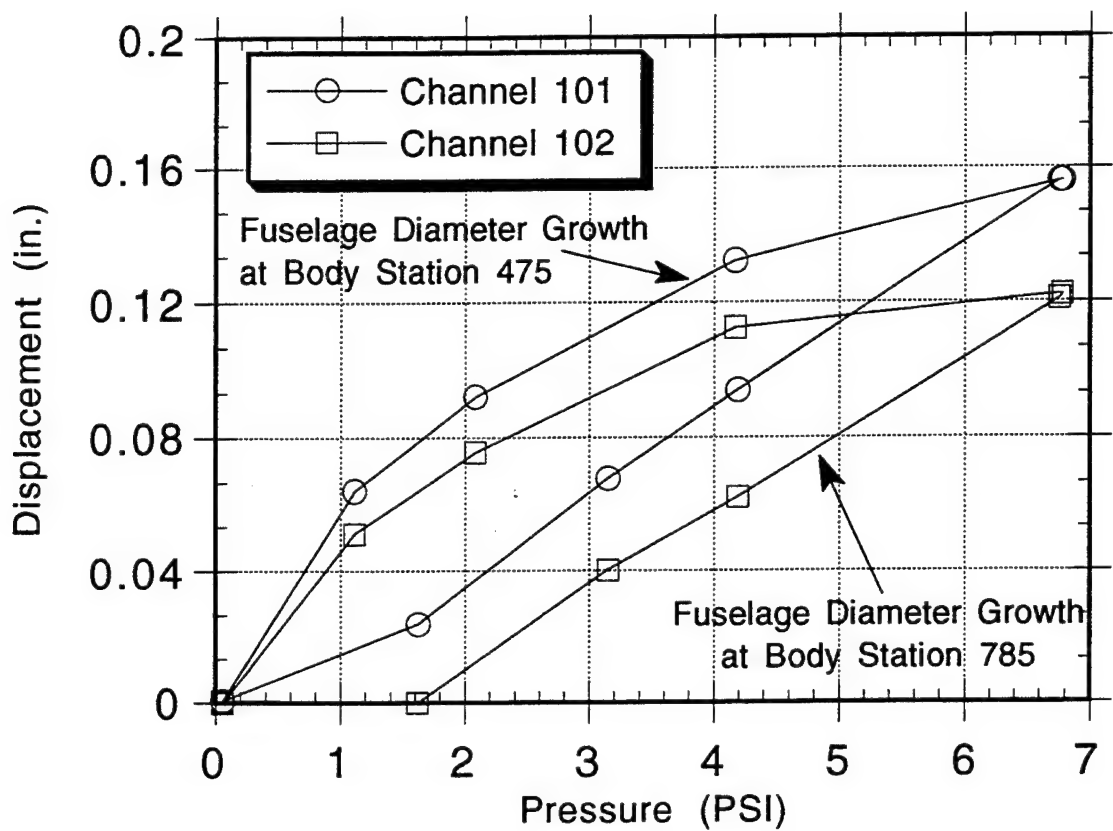


Figure 3.54. Fuselage Diameter Growth Measured Forward and Aft of the Wing.
(Refer to Figures A.12 and A.13.)

4. STRAIN GAGE DATA CORRELATIONS

One of the objectives in conducting the AANC strain gage tests was to validate results from other research areas supported by the FAATC. Four comparisons are included in this report. Specifically, the AANC strain gage data are compared to: (1) strain gage data from the Foster-Miller full-scale panel tests, (2) strain gage data from the NASA Boeing 737 test, (3) results from finite element models developed at the Volpe Center, and (4) data among different sections of the AANC airplane.

4.1 CORRELATIONS WITH FOSTER-MILLER DATA

Full-scale panel testing has been conducted at Foster-Miller, Inc. (FMI) using a fixture that employs water as a pressurization medium. Several residual strength and fatigue tests have been conducted at the FMI facility using curved stiffened panels with structural details similar to a lap splice section in the crown of a Boeing 737 fuselage. A description of the procedures and results of these tests can be found in References [2], [3], and [4].

Strain gage measurements were collected from one of the full-scale panels tested by Foster-Miller to ensure that loading conditions were similar to those in a pressurized fuselage. Most of these strain gages were deployed at midbay locations away from the lap splice. Although relatively few gages were deployed at areas experiencing large strain gradients (i.e., near the lap splice), the data agreed favorably with other, limited data [4].

In this section of the report, the AANC strain measurements from the lap splice test section between Body Stations 470 and 480 at stringer S-4L are compared to those obtained from the Foster-Miller full-scale panels.

4.1.1 FMI Strain Gage Designations

Designations for the various gages used in the FMI panel are indicated on the strain gage layouts shown in Figures 4.1 and 4.2. Figure 4.1 corresponds to the exterior of the panel; Figure 4.2 corresponds to the interior. The last letter in the FMI strain gage designation refers to the component of strain being measured: "H" refers to the hoop direction and "L" refers to the longitudinal direction. Gages installed on the underside or interior of the panel can be identified by "U" in the first letter of the strain gage designation. For example, UB3H refers to a gage measuring hoop strain on the interior of the panel at a circumferential location midbay between stringers and a longitudinal location at the midline between the frame and tear strap (see Figure 4.2).

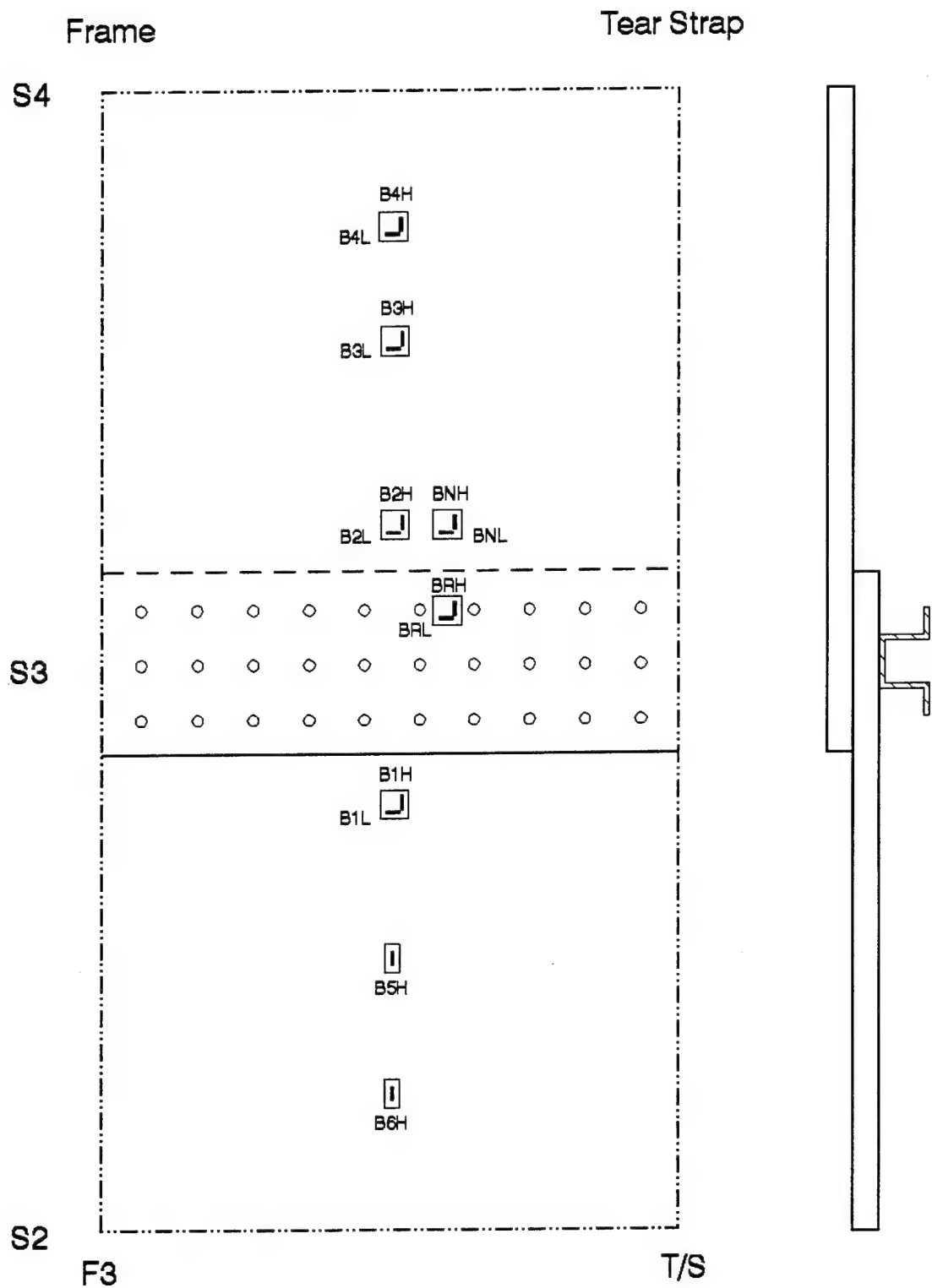


Figure 4.1. Strain Gage Deployment for FMI Panel (Exterior Gages).

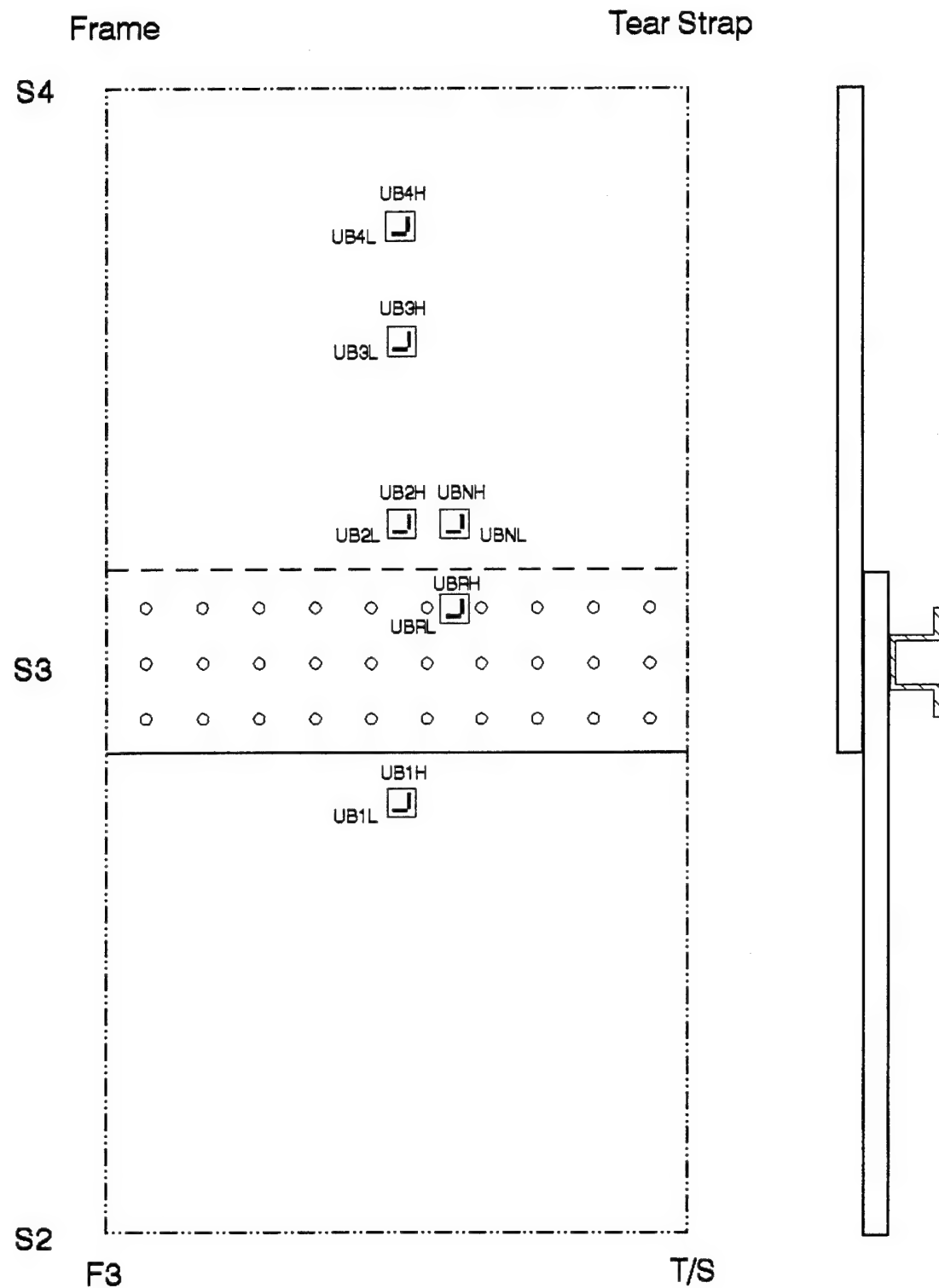


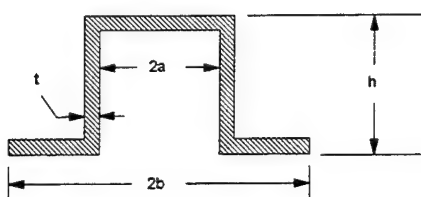
Figure 4.2. Strain Gage Deployment for FMI Panel (Interior Gages).

4.1.2 Structural and Procedural Considerations

Some physical differences between the FMI full-scale curved panel and the AANC B737 airplane should be noted before comparing the strain gage data.

- (1) The FMI full-scale panel was constructed with a completely debonded lap splice. The lap splices in the AANC aircraft were assembled with a cold bond adhesive.
- (2) The FMI panel has 0.040-inch skin thickness. The nominal skin thickness in the AANC B737 airplane is 0.036 inch.
- (3) The radius of curvature for the FMI panel is 75 inches. Figure 4.3 shows that the cross section of the Boeing 737 fuselage is not exactly circular. The radius for the upper lobe of the fuselage (i.e., above the floor beam) is 74 inches, and for the lower lobe it is 68 inches. All test sections on the AANC airplane were located in the upper lobe. According to equations (3.6) and (3.7), these differences in radius and skin thickness would account for a 10% difference in measured strain. If only dimensional differences are considered, the strains measured in the AANC airplane would be 10% higher than those measured in the FMI panel.
- (4) Stringer dimensions throughout the airplane are not uniform. That is, the dimensions of stringers S-4L, S-10L, and S-14L have some slight variations. Furthermore, the dimensions of the stringers on the airplane are different from those on the FMI stiffened panel. The stringer dimensions for each of these test sections are listed in Table 4.1 for comparison.

Table 4.1. Stringer Dimensions for Various Test Sections.



	FMI Panel	AANC B737		
		S-4L	S-10L	S-14L
2a (inches)	0.96	0.90	0.90	0.90
2b (inches)	2.80	1.80	1.80	2.25
h (inches)	1.25	1.125	1.125	1.25
t (inches)	0.050	0.029	0.029	0.033

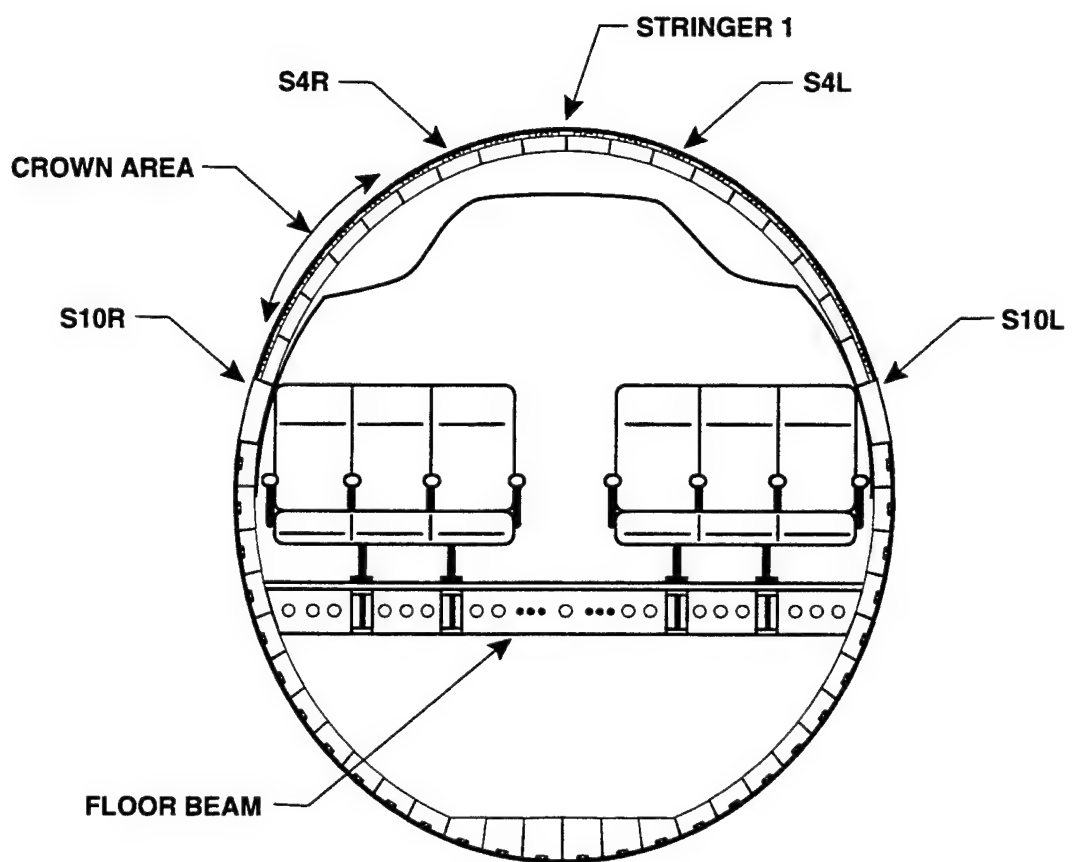


Figure 4.3. Cross Section of Boeing 737 Airplane.

- (5) The FMI panel is constructed with a tear strap and filler strip arrangement rather than the waffle doubler design found in actual aircraft. Typical aircraft construction consists of bonding two pieces of skin together, and then chemically removing all the material that is not a tear strap or does not lie over a stringer. Thus, a continuous waffle-pattern doubler is produced beneath the skin, see Figure 4.4. In the FMI panels, continuous tear straps are bonded to the skin and longitudinal filler strips were attached between the skin and stringers. This deviation in panel construction was employed to simplify manufacturing and to reduce the cost of the test panels. It is believed that this modification in construction does not impact structural performance of the fuselage panels. The strain gage correlations between the FMI and AANC data can be used to assess this assertion.
- (6) An obvious physical difference between the FMI panel and the Boeing 737 airplane is the age of the material. Apparently, aluminum alloys used in older airplanes (20 years or older) are not exactly identical in microstructure to modern aluminum alloys. Such differences are attributed to hot water quenching procedures used in the past versus cold water quenching used in modern practice. Fractographic analysis has revealed that aluminum manufactured over 20 years ago is more susceptible to corrosion and fatigue damage than present day aluminum [9]. These differences in microstructure affect the formation and growth of cracks that may occur in the material, but should not affect the measurement of strains.

In terms of test procedure, the maximum differential pressure during the FMI strain gage measurements was 8.5 psi. Under normal operating service, the differential pressure for a Boeing 737 is 7.5 psi. An additional 1.0 psi was included in the FMI tests to account for any aerodynamic effects or transverse shear due to fuselage bending [4]. In the AANC tests, the maximum differential pressure was 6.5 psi. The difference in maximum pressure between the FMI and AANC tests should not affect the comparison of strain data since the strains measured in both tests appear to be reasonably linear with respect to pressure.

4.1.3 Results of Correlations Between FMI and AANC Data

Individual measurements from the FMI and AANC strain gage tests are compared in Figures 4.5 to 4.16. These comparisons are presented in the form of plots showing measured microstrain as a function of applied pressure. Each figure includes a schematic of a lap splice bay indicating the location of the measured strains. Table 4.2 lists the figure numbers that correspond to the plots comparing the various strain gage measurements from each test.

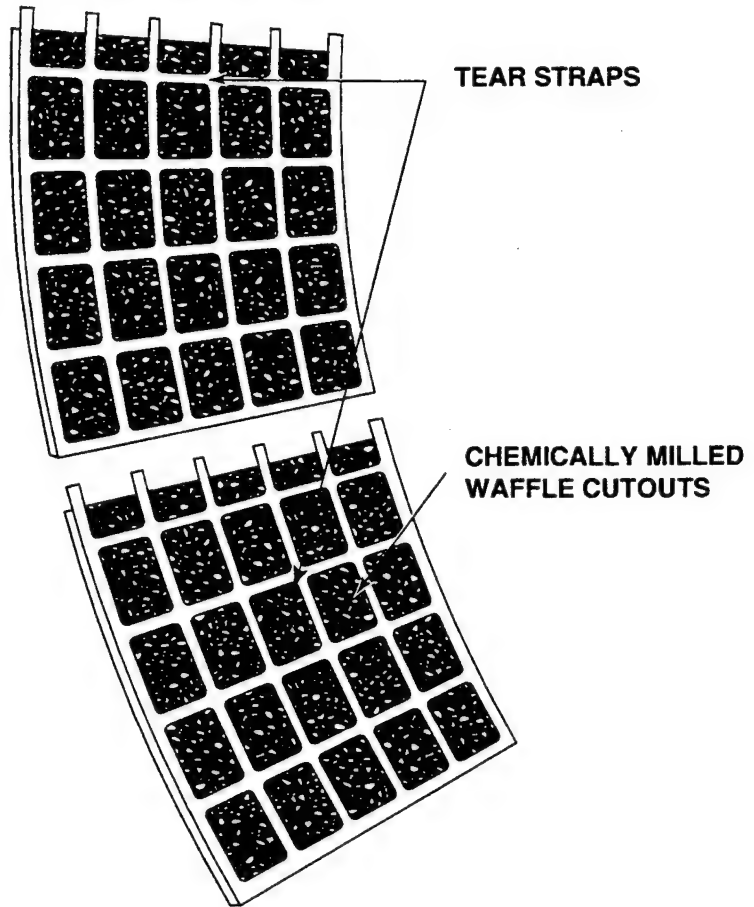


Figure 4.4. Waffle Doubler Tear Strap Design in Boeing 737 Airplane.

Table 4.2. Figure Numbers Corresponding to One-to-One Strain Gage Comparisons Between AANC and FMI Measurements.

Figure Number	AANC Channel Numbers ^(a)	FMI Gage Designation ^(b)
4.5	18	B3H
4.6	20	B2H
4.7	21	BNL
4.8	22	BNH
4.9	25	BRL
4.10	26	BRH
4.11	29	B1L
4.12	30	B1H
4.13	69	UB3L
4.14	70	UB3H
4.15	71	UB2L
4.16	72	UB2H

NOTES:

- (a) The AANC Channels correspond to the test section located between Body Stations 470 and 480 at Stringer S-4L.
- (b) The last letter in the FMI strain gage designation refers to the strain in either the hoop direction (H) or the longitudinal direction (L).

The best agreement between the FMI and AANC data was achieved at the midline and midbay location where the hoop strains differ by less than 10%. Figure 4.5 shows this comparison for hoop strains on the exterior side of the panel, and Figure 4.14 shows the corresponding strains on the interior. Near the lap joint, however, the differences become greater. The hoop strains near the lap joint in the FMI panel are 20 to 40% greater than those in the AANC B737 (see Figures 4.8 and 4.10). A possible explanation for these differences could be that the adhesive bond in the lap joint of the AANC airplane may be transferring some load. This explanation is consistent with the results shown in Figure 4.8 and 4.10 where the FMI panel (which is completely debonded) experiences higher strains than the AANC airplane.

The largest discrepancy in hoop strains between the FMI and AANC data is shown in Figure 4.12 which compares strains below the lap joint. The hoop strains in the FMI panel at this particular location are approximately 45% lower than those in the actual airplane. On one hand, the AANC gage is located 2.0 inches from the middle rivet row, while the FMI gage is located 2.1 inches from the same location. On the other hand, results from the finite element models (described in Section 4.3) indicate that less than 1% of the strain is due to the non-coincident location of the gages. A better correlation can be achieved by comparing the strain at FMI Gage B1H to the strain measured by AANC Channel 98 which is located near the tail of the airplane (BS785, S-10L). In this comparison, the FMI strains below the lap joint are approximately 27% lower than the AANC strains. Disregarding this location below the lap joint, the hoop strains from both tests agree within 30% of each other.

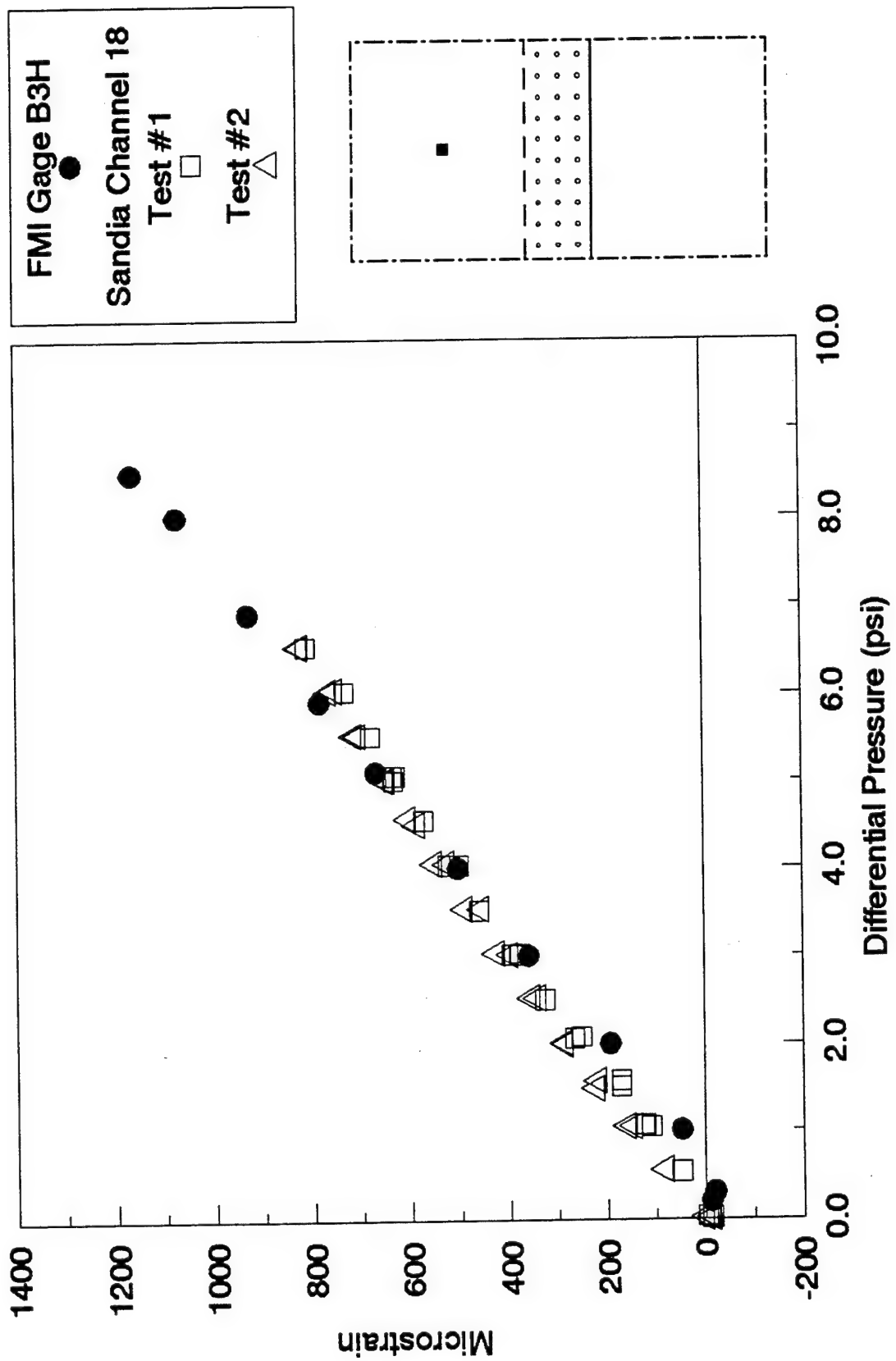


Figure 4.5. Comparison Between AANC Channel 18 and FMI Gage B3H.

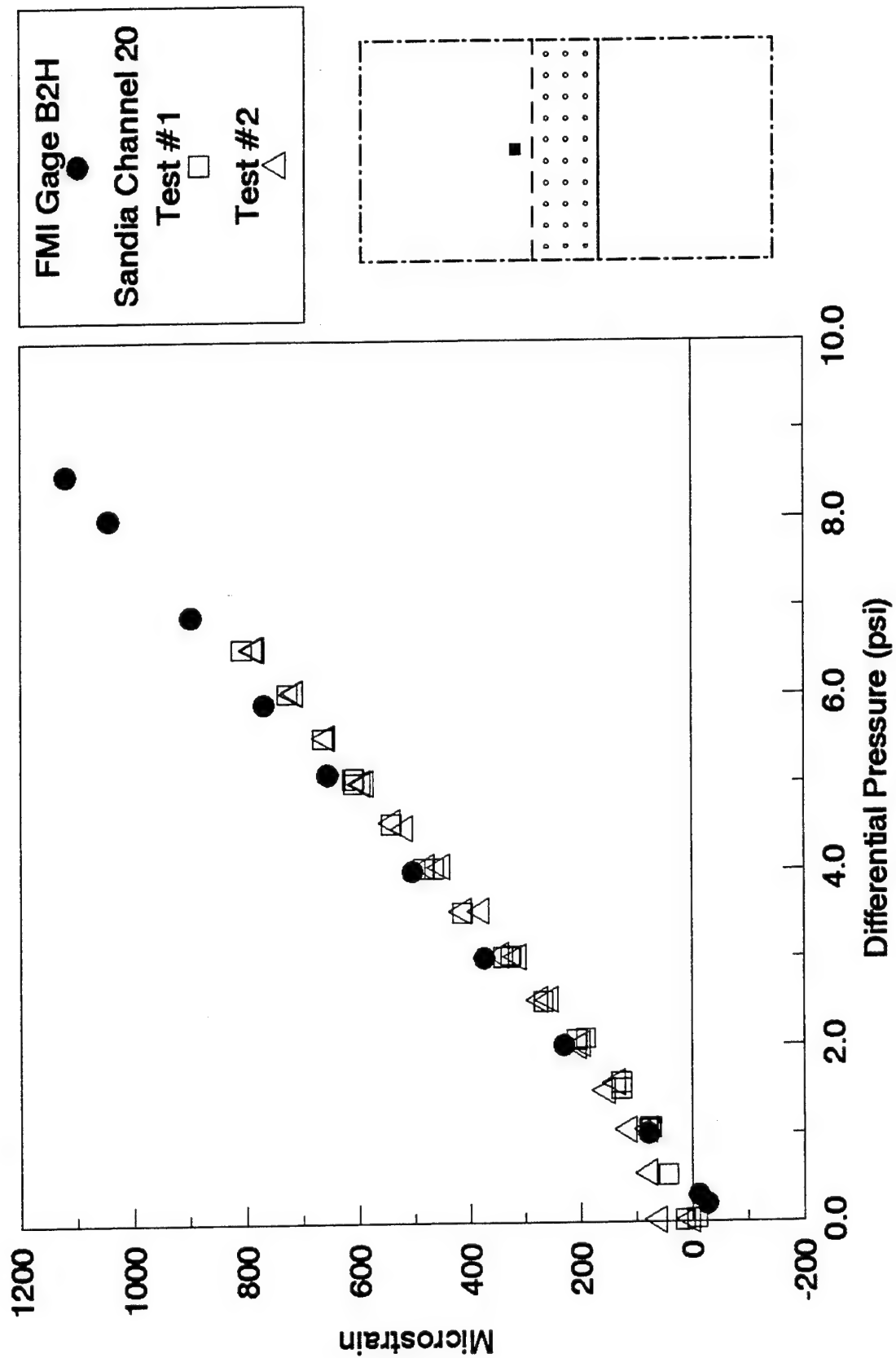


Figure 4.6. Comparison Between AANC Channel 20 and FMI Gage B2H.

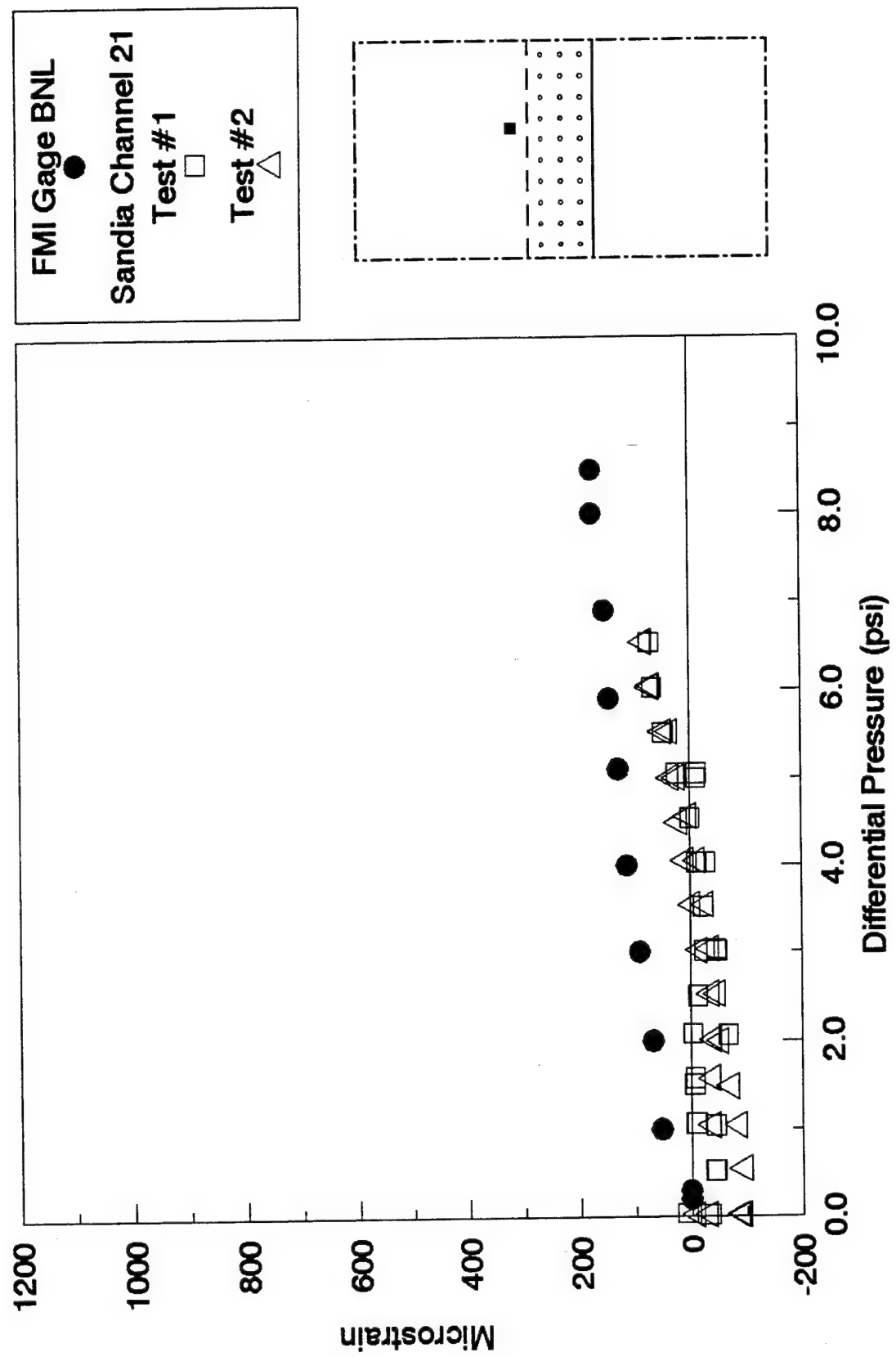


Figure 4.7. Comparison Between AANC Channel 21 and FMI Gage BNL.

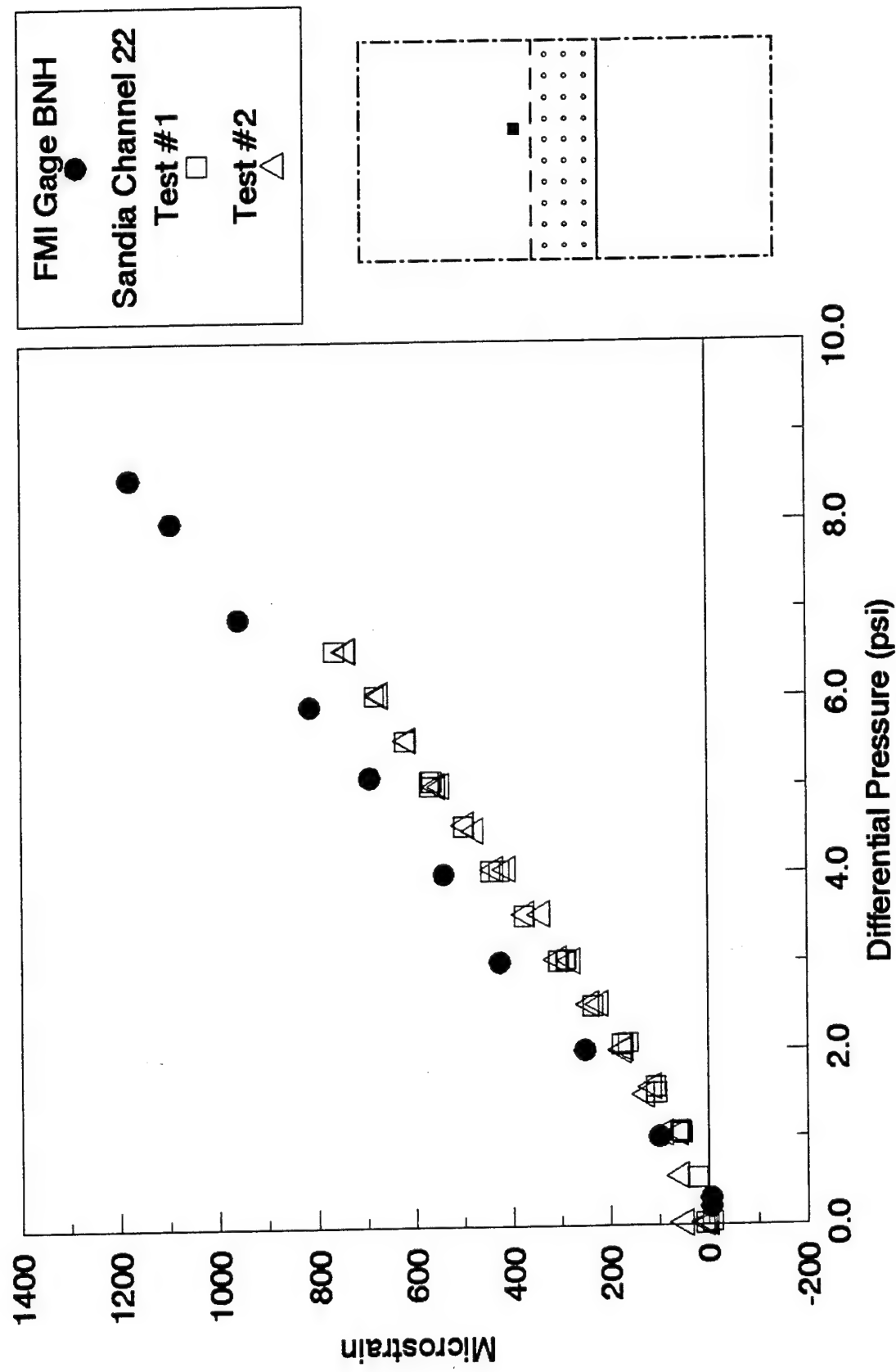


Figure 4.8. Comparison Between AANC Channel 22 and FMI Gage BNH.

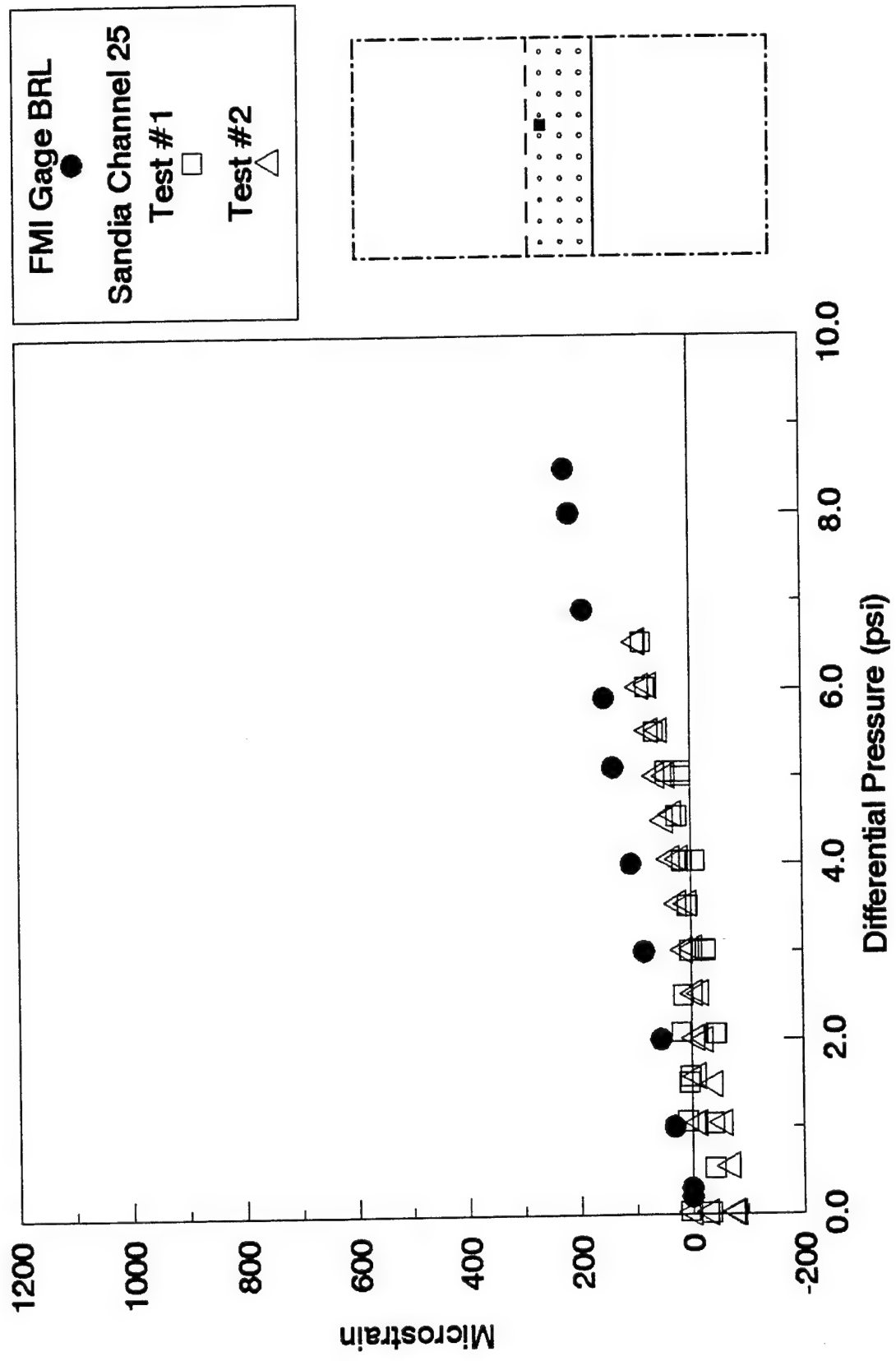


Figure 4.9. Comparison Between ANC Channel 25 and FMI Gage BRL.

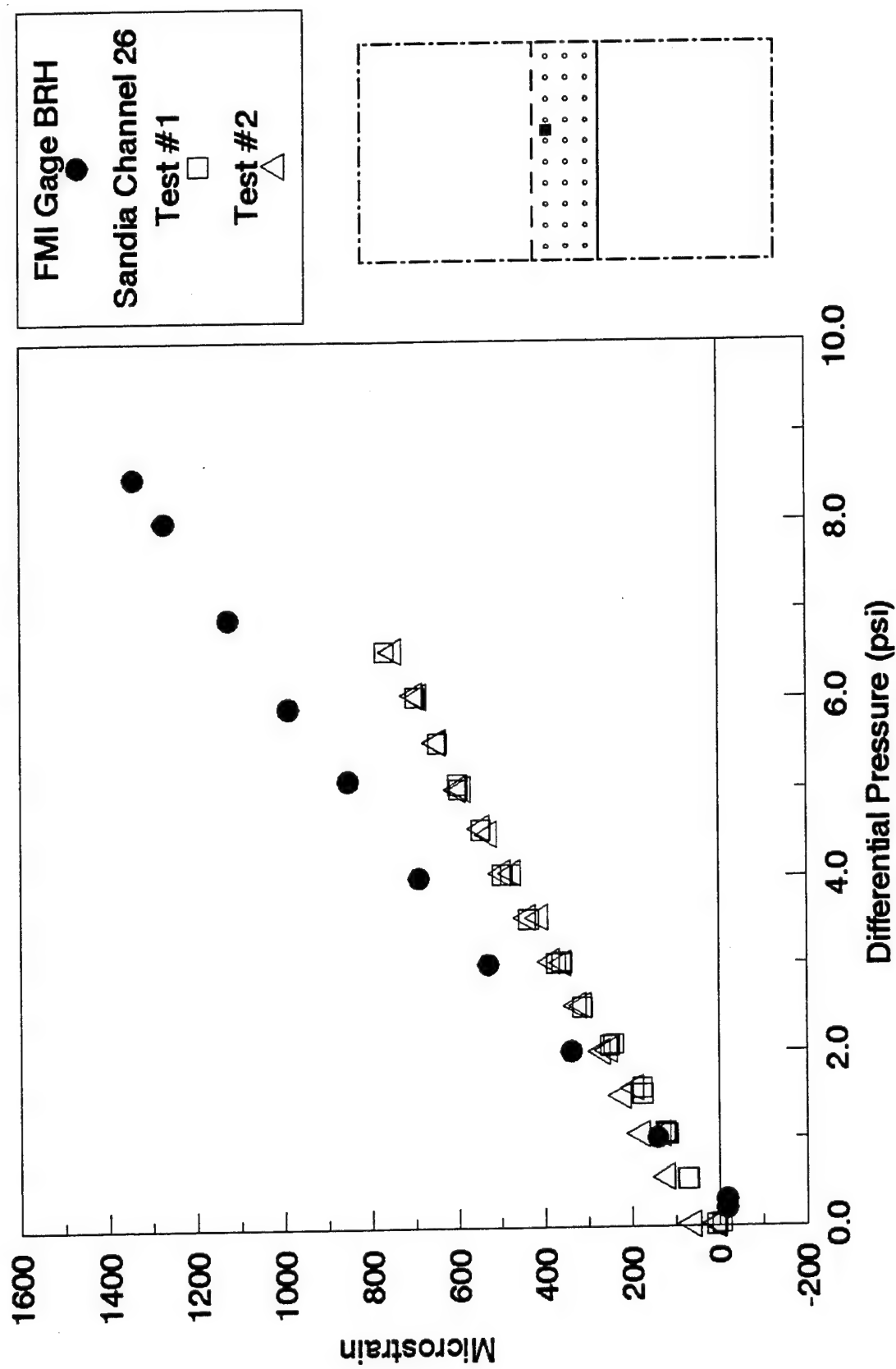


Figure 4.10. Comparison Between AANC Channel 26 and FMI Gage BRH.

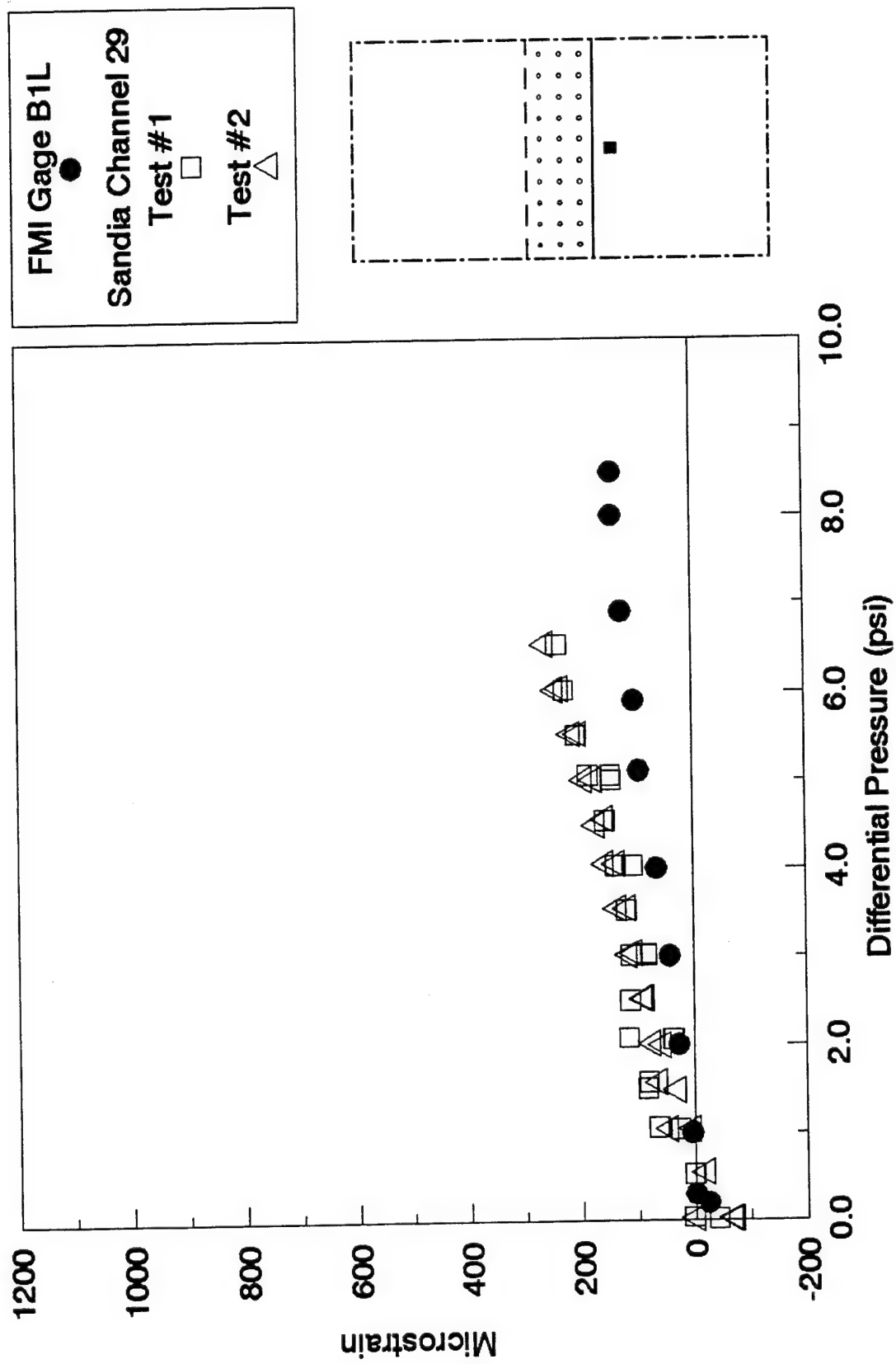


Figure 4.11. Comparison Between AANC Channel 29 and FMI Gage B1L.

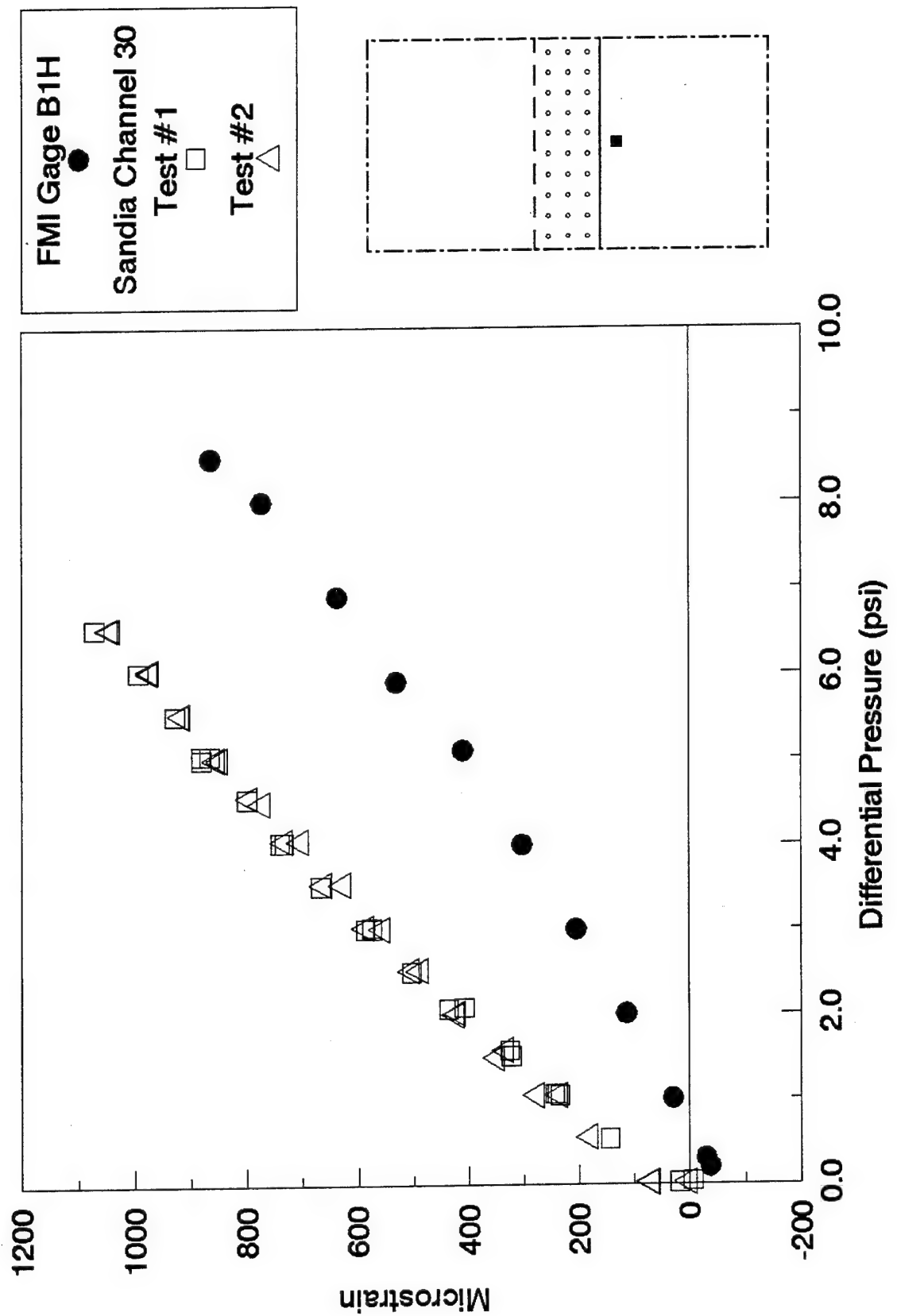


Figure 4.12. Comparison Between ANC Channel 30 and FMI Gage B1H.

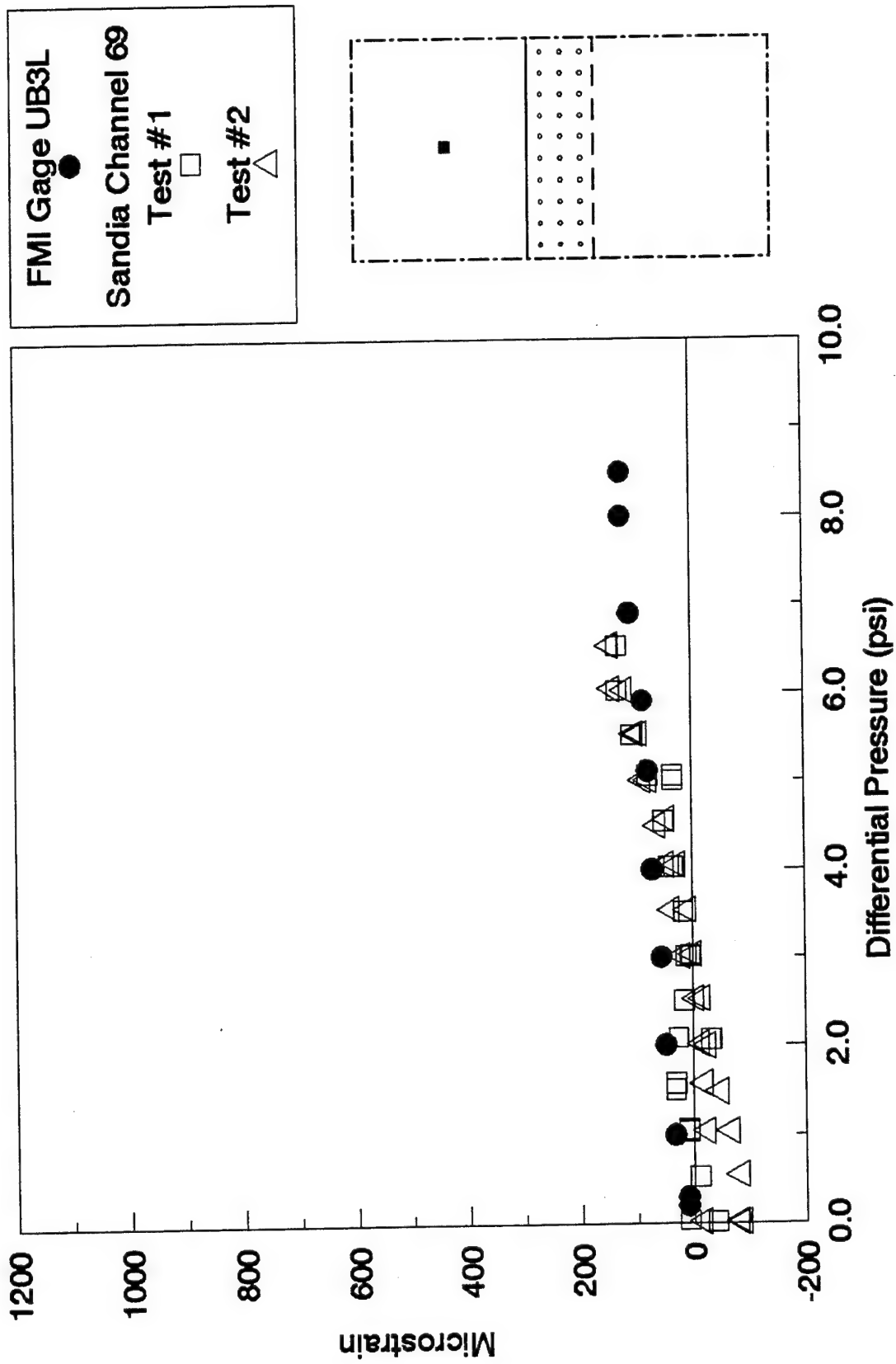


Figure 4.13. Comparison Between ANC Channel 69 and FMI Gage UB3L.

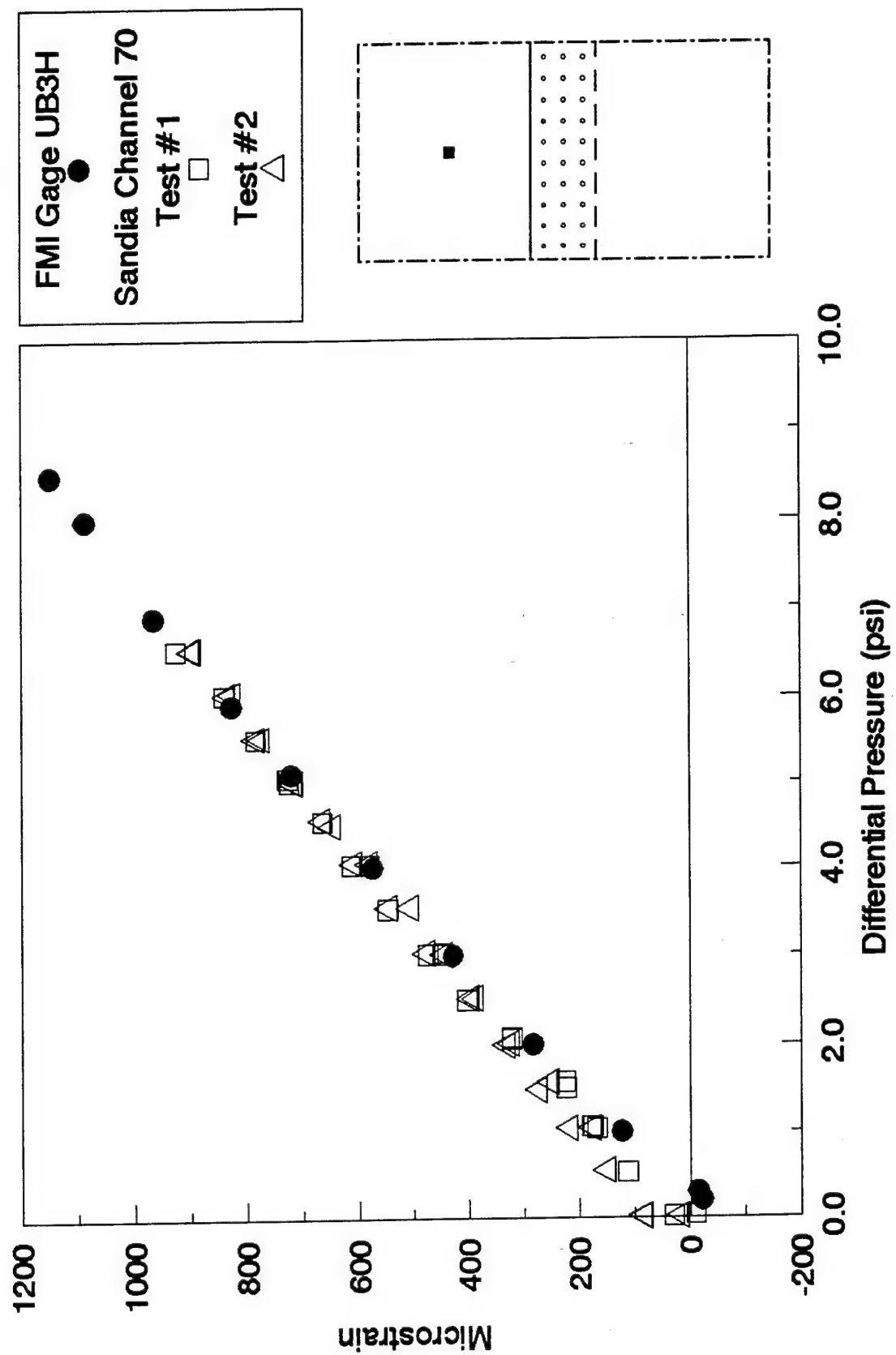


Figure 4.14. Comparison Between AANC Channel 70 and FMI Gage UB3H.

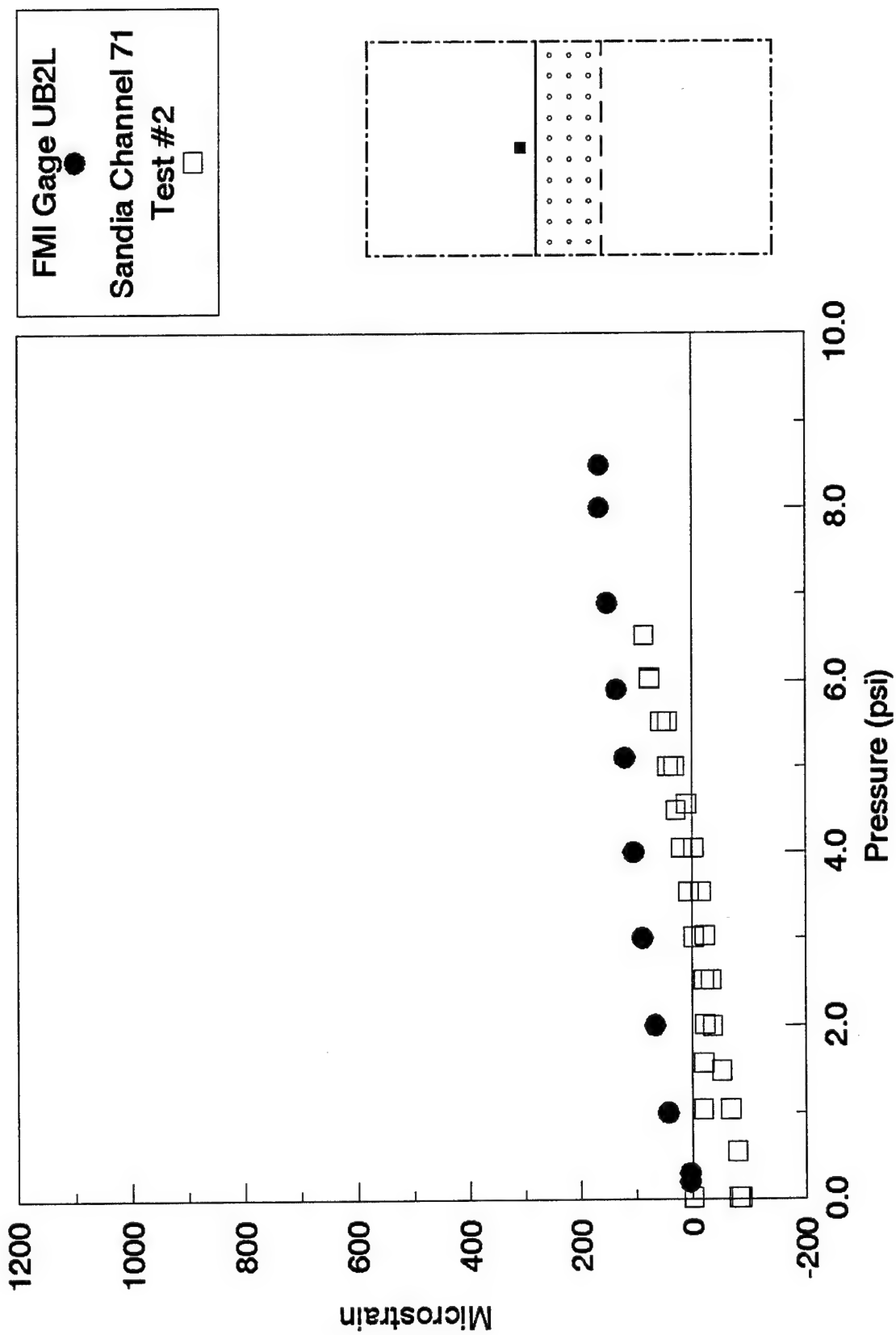


Figure 4.15. Comparison Between AANC Channel 71 and FMI Gage UB2L.

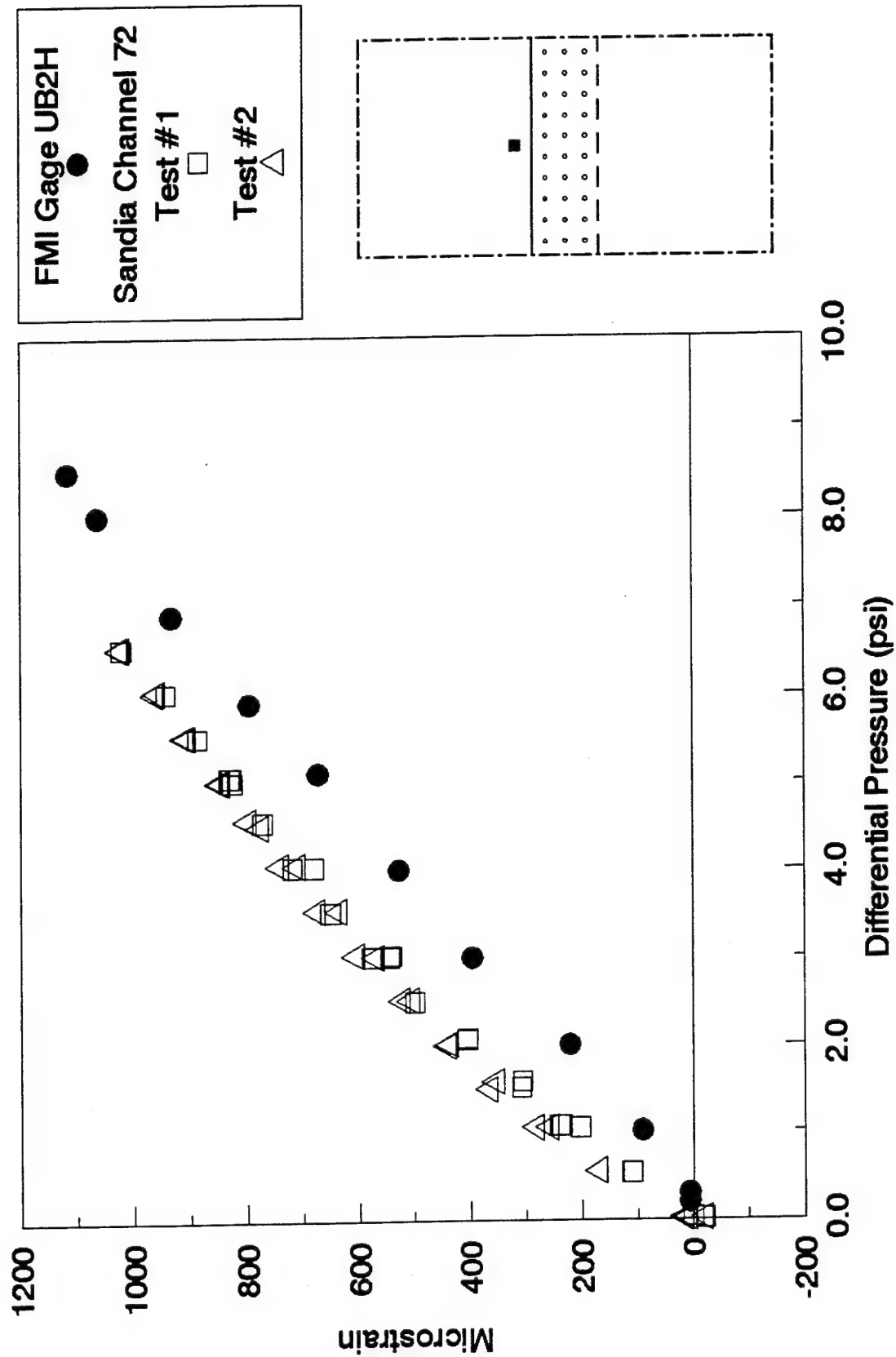


Figure 4.16. Comparison Between AANC Channel 72 and FMI Gage UB2H.

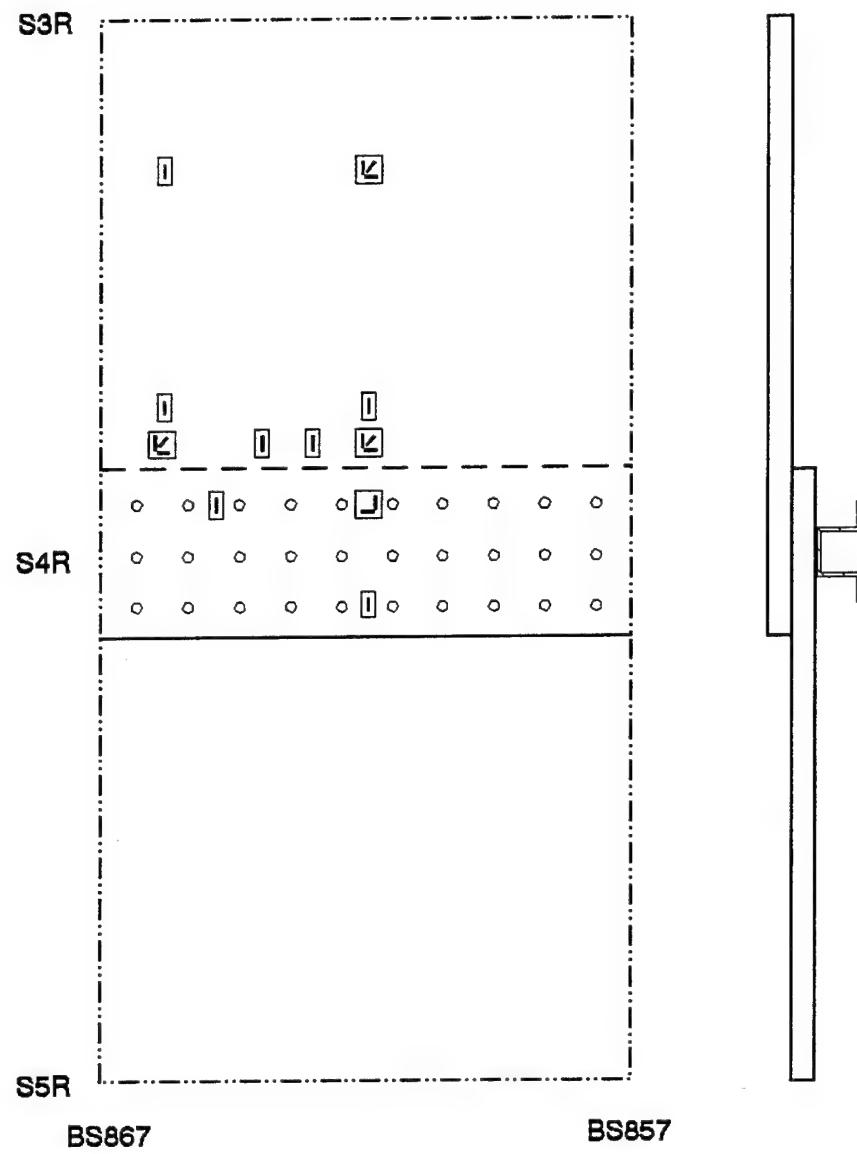
Discrepancies between the FMI and AANC data are also evident when longitudinal strains are considered. Near the lap joint, the longitudinal strains in the FMI panel are more than twice as much as those in the AANC airplane. But similar differences in longitudinal strains can be shown by comparing strains at common locations within the AANC airplane itself. Such comparisons are discussed in Section 4.4. Such variability occurs from the sensitivity of the longitudinal strains in the lap splice to real time load shifts and structural settling, as discussed in Section 3.1.4. In addition, the relative magnitude of the longitudinal strains is much lower than the magnitude of the hoop strains which magnifies the discrepancy.

Despite these discrepancies, the overall comparison between the FMI and AANC test data is reasonable. Aside from the location below the lap joint, the hoop strains from both tests agree within 30%. Based on these comparisons, the pressurized FMI panel appears to produce strains that are representative of those in an actual aircraft structure. Thus, the use of the tear strap and filler arrangement appears to be an acceptable structural alternative to the waffle doubler construction design, in terms of producing representative strains in a test article.

4.2 CORRELATIONS WITH NASA BOEING 737 DATA

Strain gage data from a Boeing 737 airplane have also been collected by NASA Langley Research Center during a ground pressurization test [5]. In the NASA test, the peak pressure was 6.2 psi. One test section, located at the longitudinal lap splice between Body Stations 857 and 867 at stringer S-4R, was monitored with 36 channels. Figure 4.17 shows the strain gage layout for the NASA test. The most comparable test section in the AANC B737 airplane was the one between Body Stations 780 and 790 at stringer S-4L. Five common strain gage locations were identified relative to stringer S-4 in both test sections. The strains measured at these locations are shown in Figures 4.18 to 4.22.

Figure 4.18 compares the hoop strain measured in the upper rivet row from both tests. The hoop strain measured in the AANC test is approximately 2.5 times higher than the strain measured in the NASA test at 6.0 psi. Figure 4.19 shows a comparison of the longitudinal strains at the same location. The longitudinal strain measured in the AANC test is about 40% higher than the strain obtained in the NASA test at a differential pressure of 6.0 psi. Figures 4.20 and 4.21 compare the hoop and longitudinal strains at the midbay-midline position from both tests. The strains from both tests at this location are within 20% of each other at a differential pressure of 6.0 psi.



Legend for Various Gages

- Single element hoop strain gage
- Two element strain gage rosette
- Three element strain gage rosette

Figure 4.17. Strain Gage Deployment for NASA Boeing 737 Test.

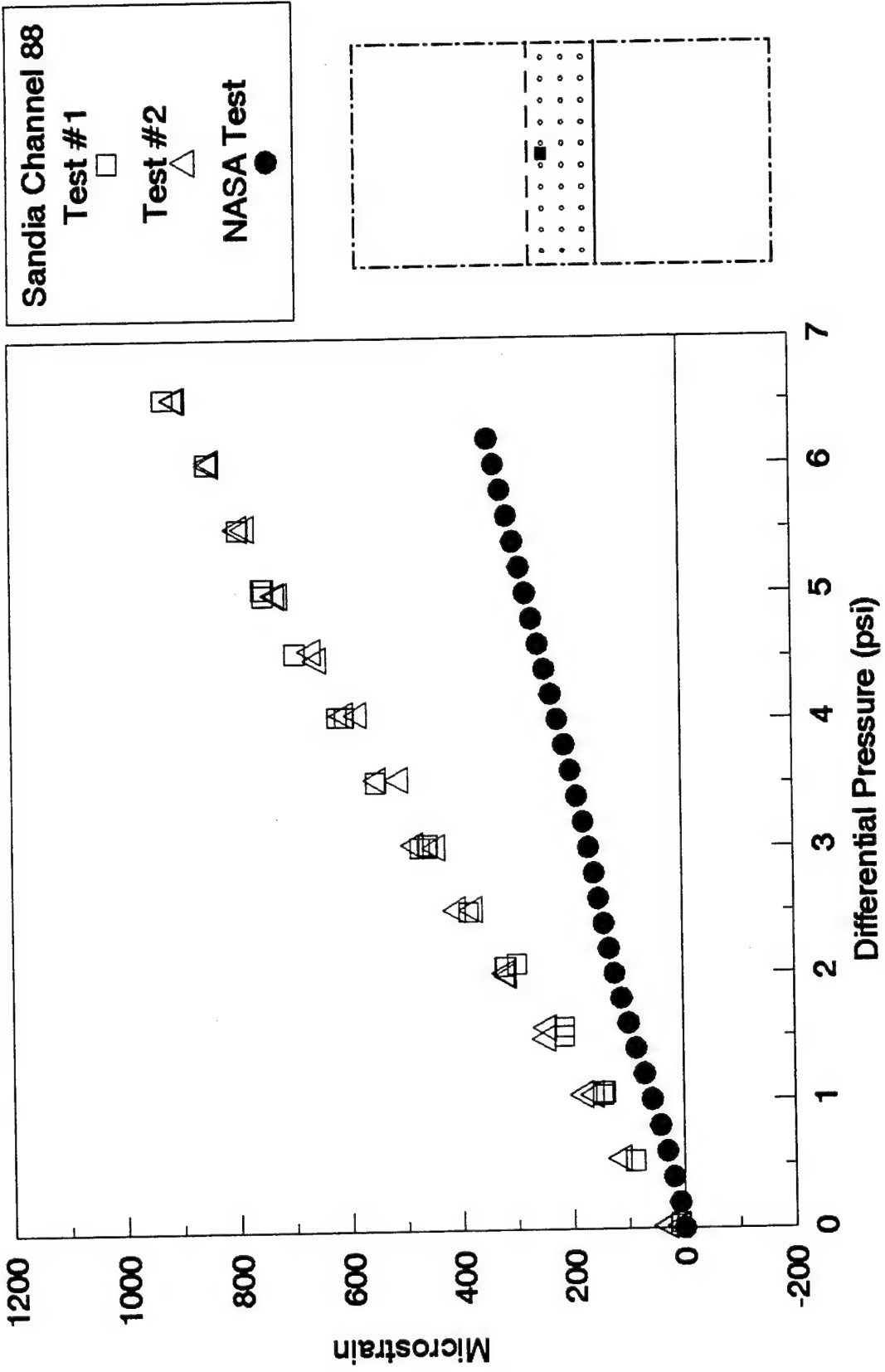


Figure 4.18. Comparison of Hoop Strains in Upper Rivet Row.

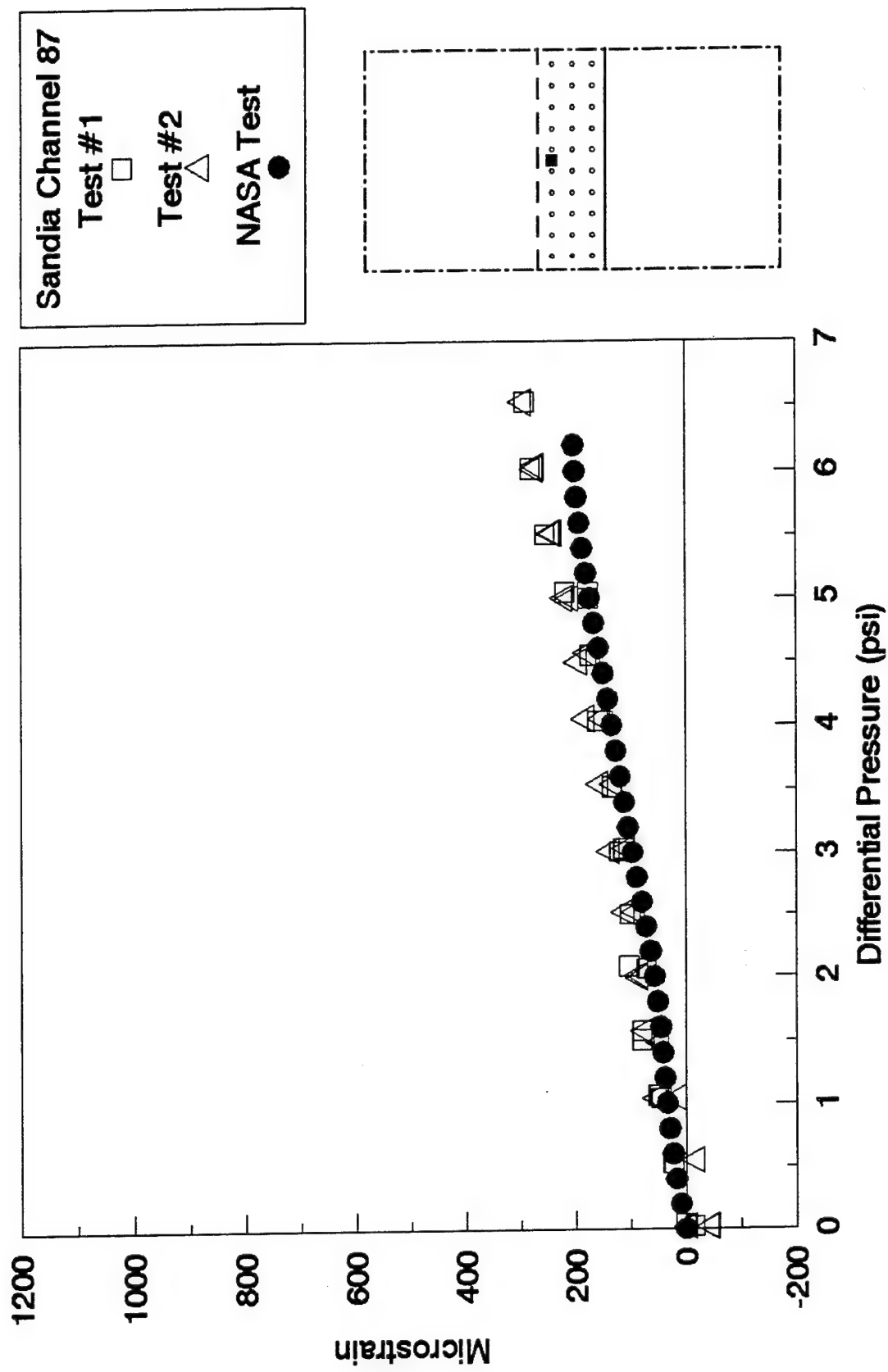


Figure 4.19. Comparison of Longitudinal Strains in Upper Rivet Row.

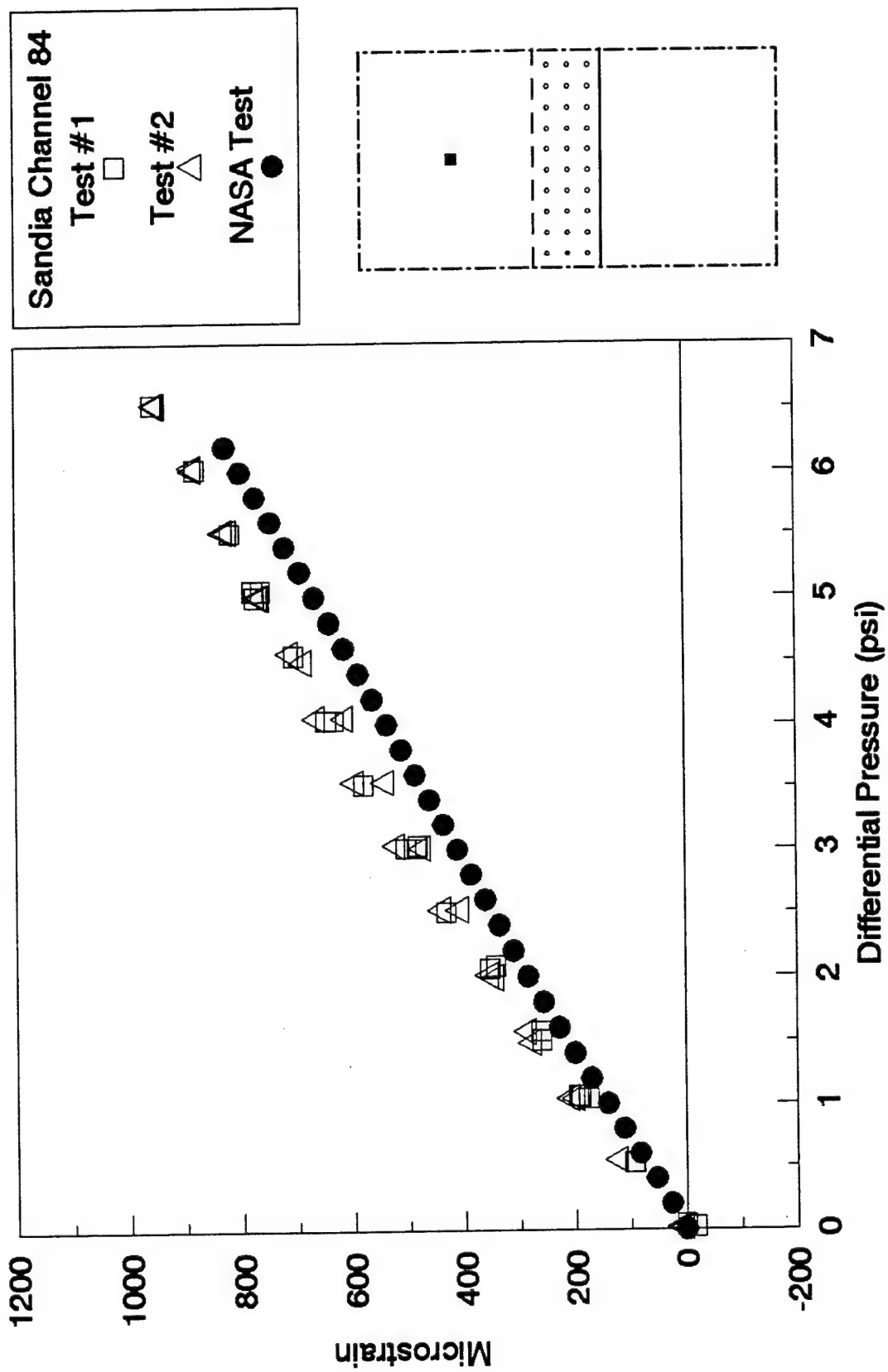


Figure 4.20. Comparison of Hoop Strains at Midbay/Midline Location.

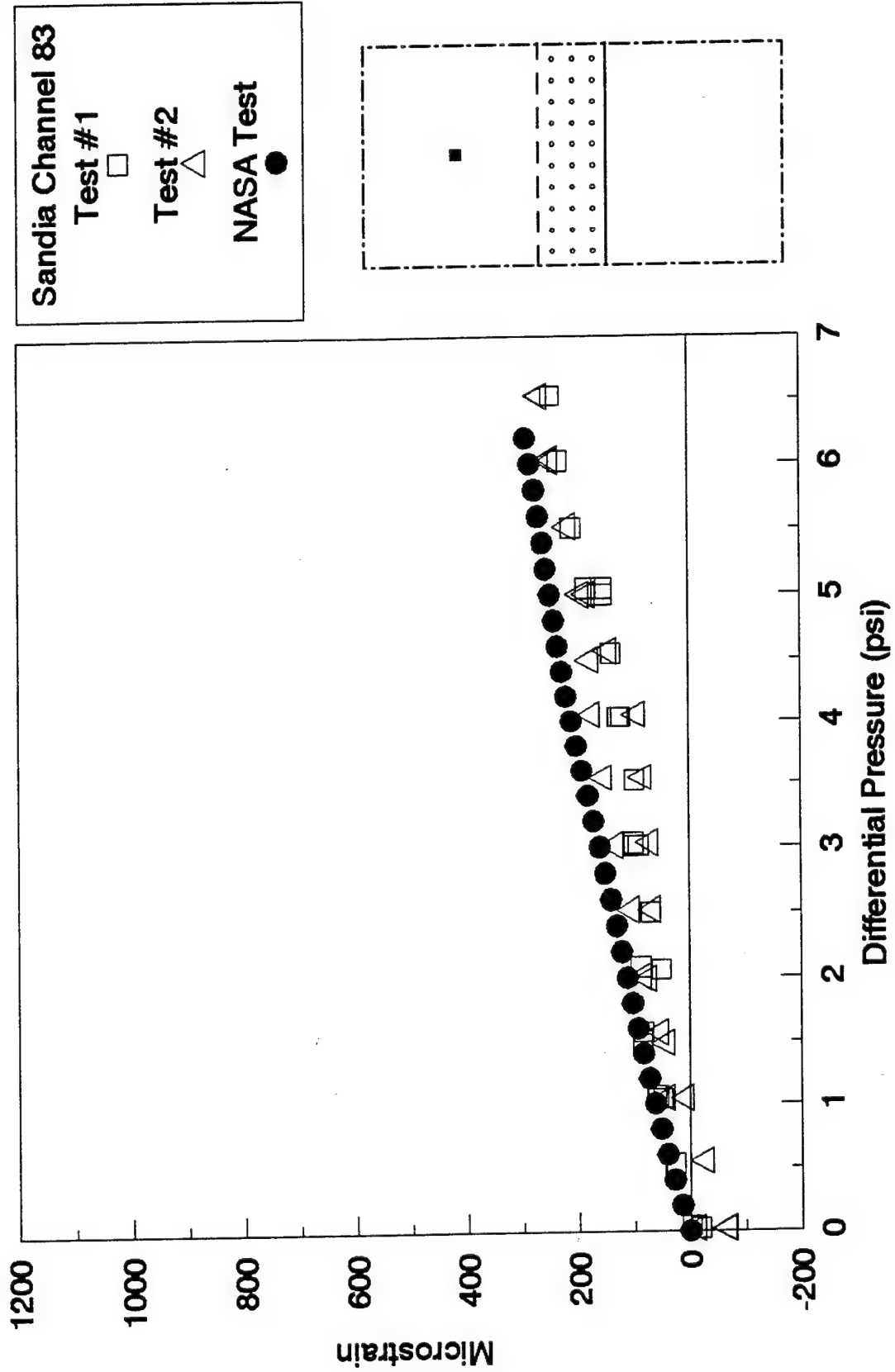


Figure 4.21. Comparison of Longitudinal Strains at Midbay/Midline Location.

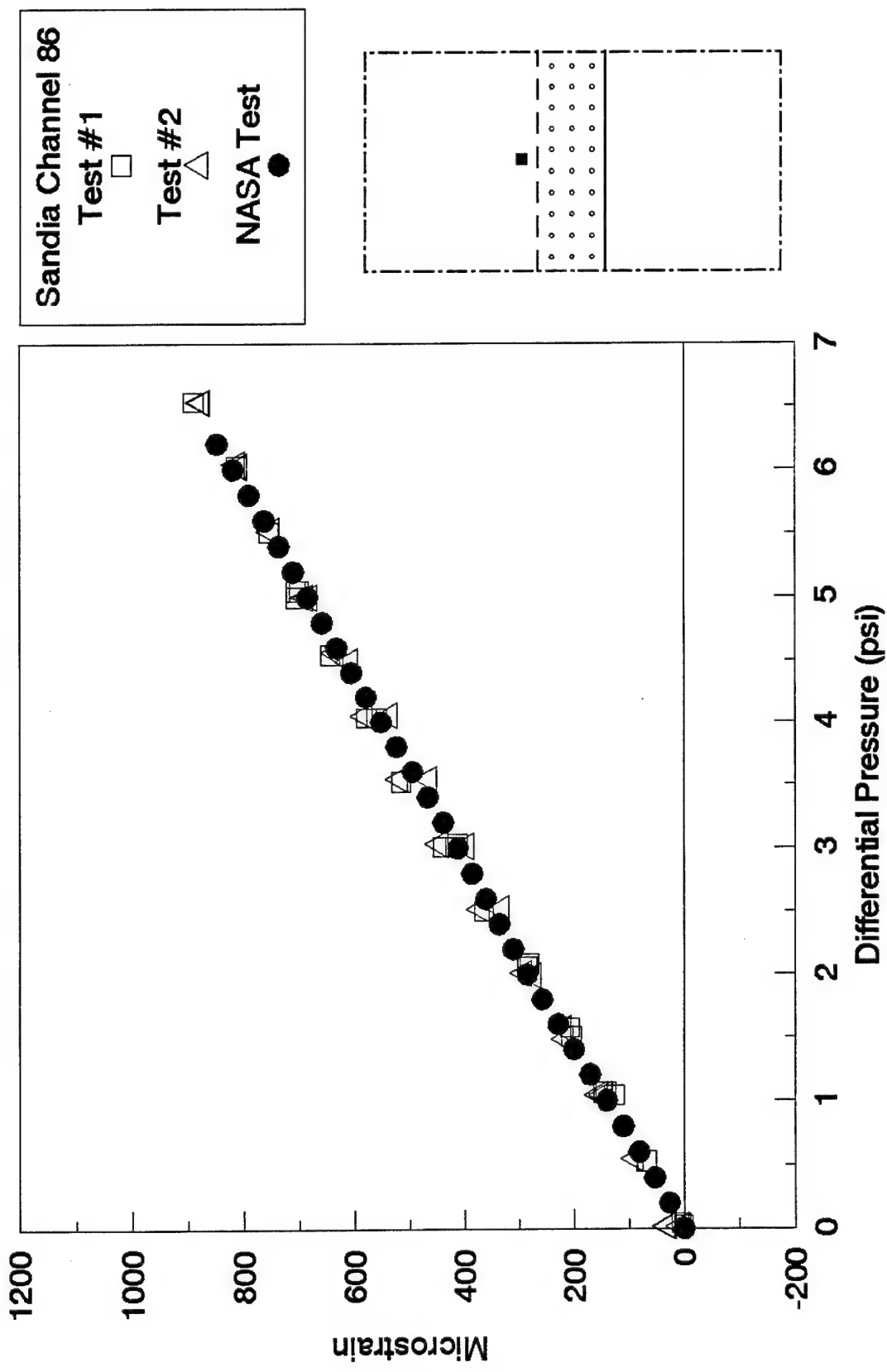


Figure 4.22. Comparison of Hoop Strains Near Top Edge of Lap Joint at Midbay.

The large discrepancy in hoop strains in the upper rivet row can be explained by the difference in bond quality in the two lap joint test sections. Based on the strain comparisons with the FMI panels, the lap joints in the AANC airplane appear to be debonded. On the other hand, the bond in the lap joint test section of the NASA B737 is transferring load, which produces less strain in the upper rivet row. This explanation is plausible since the other strain data away from the lap joint compare reasonably well. The difference in bond quality between the AANC and NASA lap splice test sections is discussed further in Section 4.3.2.

Differences in strain levels between the AANC and NASA data may also be caused by the difference in test location (i.e. BS780 in the AANC test versus BS857 in the NASA test) which implies an effect from fuselage bending. Aside from the strains measured in the upper rivet row which are affected by the quality of the adhesive bond, the strain data from both the AANC and NASA tests agree within 30% of each other, which is reasonable.

4.3 CORRELATIONS WITH RESULTS FROM FINITE ELEMENT MODELS

Results from computational models of an aircraft fuselage are compared to strains measured in the test section between Body Stations 470 and 480 at stringer S-4L. This particular test section of the AANC aircraft is considered the most appropriate for such comparisons because it is relatively isolated from structural effects such as windows, floor beams, and fuselage bending.

4.3.1 Description of Finite Element Models

Finite element models of fuselage lap joint structures are being developed at the Volpe Center using the commercial finite element code ANSYS [10,11]. These finite element models include structural details such as tear straps, stringers, structural fillers, frames, stringer ties, and rivets. Two models were developed for direct comparisons with the AANC data. The first model assumed that the skins, tear straps, and structural fillers are attached by an adhesive bond, and all other components are attached by rivets. In this report, this model is referred to as the adhesive lap splice model. The second model, referred to as the riveted lap splice model, assumed no adhesive, and all structural components are attached by rivets only. Thus, the two models effectively bound the possible conditions of bonding in the lap joint between entirely bonded and completely debonded.

Both finite element models employ four-noded shell elements to represent the skins, tear straps, structural fillers, frames, and stringer ties of the aircraft fuselage. In the adhesive lap splice model, the adhesive bond between the skins, tear straps, and structural fillers was modeled using three-dimensional, eight-noded, anisotropic material elements. In the riveted lap splice model, three-dimensional beam elements represent the rivets at the individual rivet locations throughout the model. Rivets were assumed to behave as linear elastic springs. The flexibility of these rivets was estimated using the empirical formula derived by Swift [12]. All rivets in the model were assumed to have the same rivet flexibility. The riveted lap splice model consists of 13,382 nodes and 12,740 elements which result in a total of 76,737 active degrees of freedom. The adhesive lap splice model uses 6,684 nodes and 7,042 elements which combine for 37,739 active degrees of freedom. Furthermore, the adhesive model includes 144 beam elements and 1,112 adhesive elements. Figure 4.23 shows the finite element mesh pattern used to model a section of the aircraft fuselage containing a riveted lap joint.

In Section 3.8, the expansion of the fuselage radius was estimated from elasticity considerations to be 0.079 inch at an internal pressure of 6.5 psi. Since this out-of-plane deformation is on the order of the skin thickness, geometric nonlinearity (i.e., large deformation theory) was assumed in the development of these finite element models. In a nonlinear analysis, however, an iterative solution procedure is required. In the present analysis, 13 load steps were used to calculate strains at pressures varying between 0 and 6.5 psi.

4.3.2 Results of Correlations Between Finite Element Models and AANC Data

Figure 4.24 compares measured hoop strains at various locations across the lap splice at Body Station 475, stringer S-4L, with results from the riveted lap splice model. The solid, dotted, and dashed lines in the figure represent results from the finite element models; the symbols indicate the measured strain gage data. Similarly, Figure 4.25 shows the same comparison for the adhesive lap splice model. Clearly, the strain data are characterized more accurately by the riveted lap splice model, especially in the upper rivet row, suggesting that the cold-bond adhesive has substantially degraded at that location in the AANC airplane. This result was confirmed when nondestructive inspection detected extensive corrosion and debonds in the lap joints.

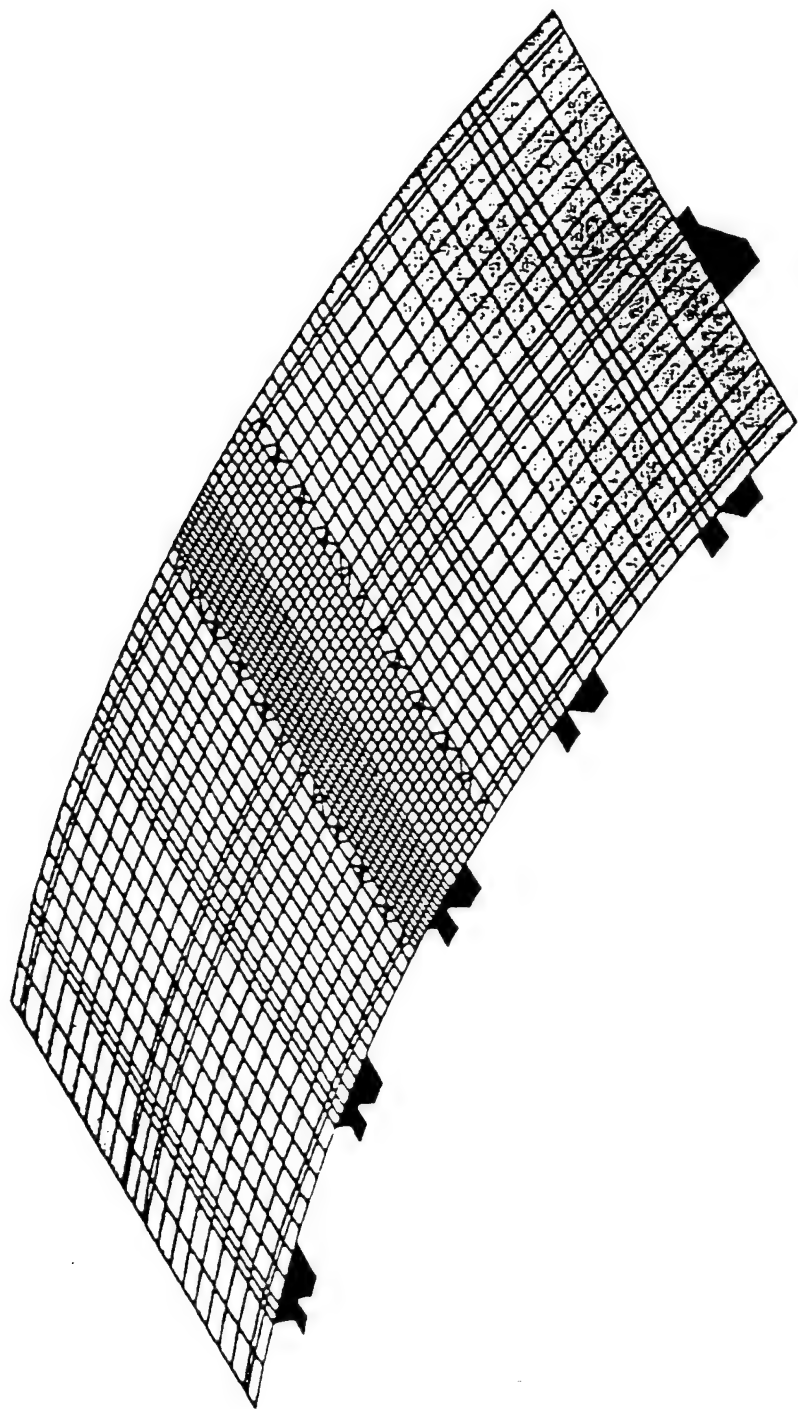


Figure 4.23. Finite Element Mesh Pattern for Pressurized Aircraft Section.

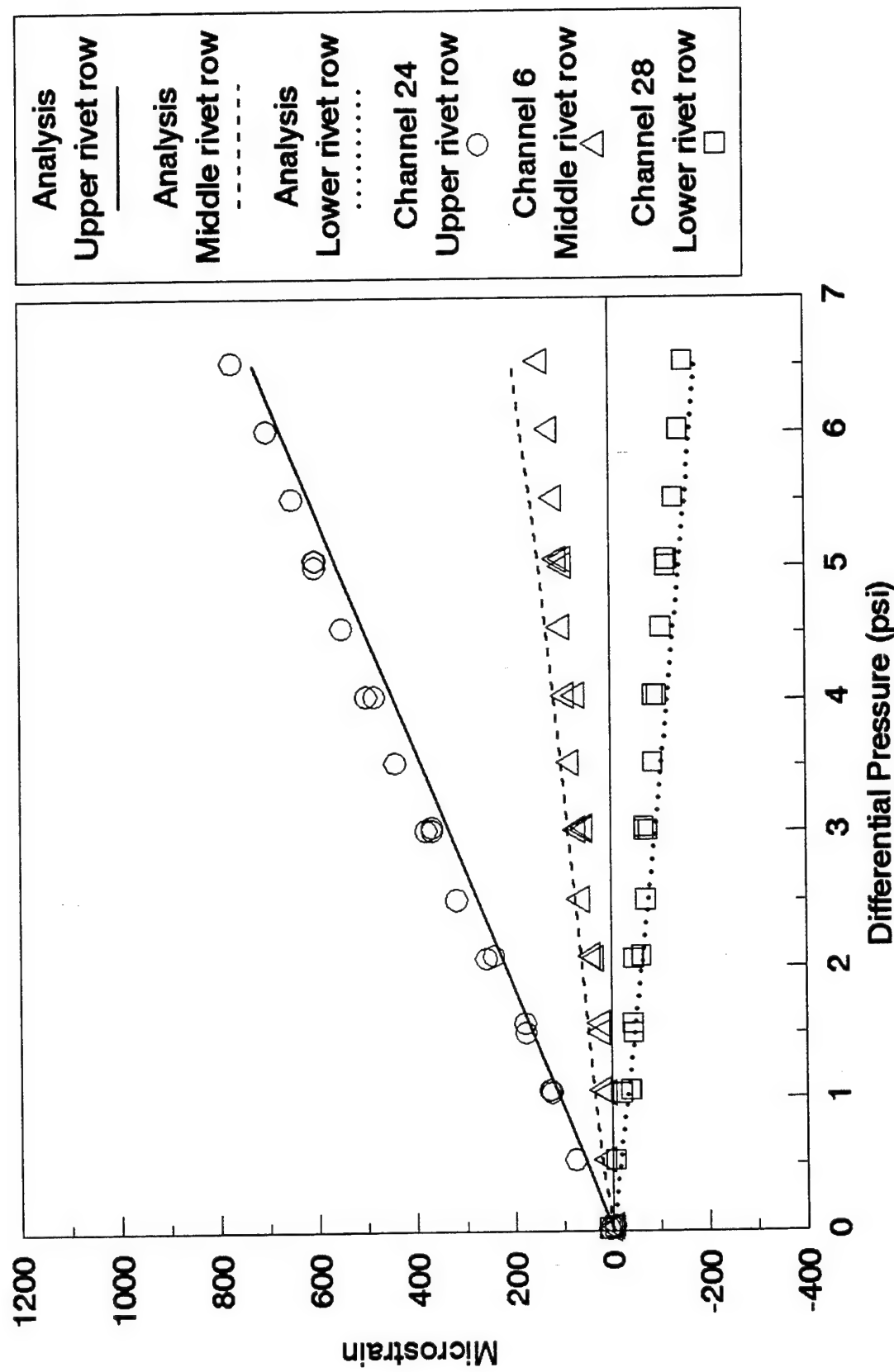


Figure 4.24. Comparison of Strains Across Lap Splice at S-4L, BS475 (Riveted Lap Splice Model).

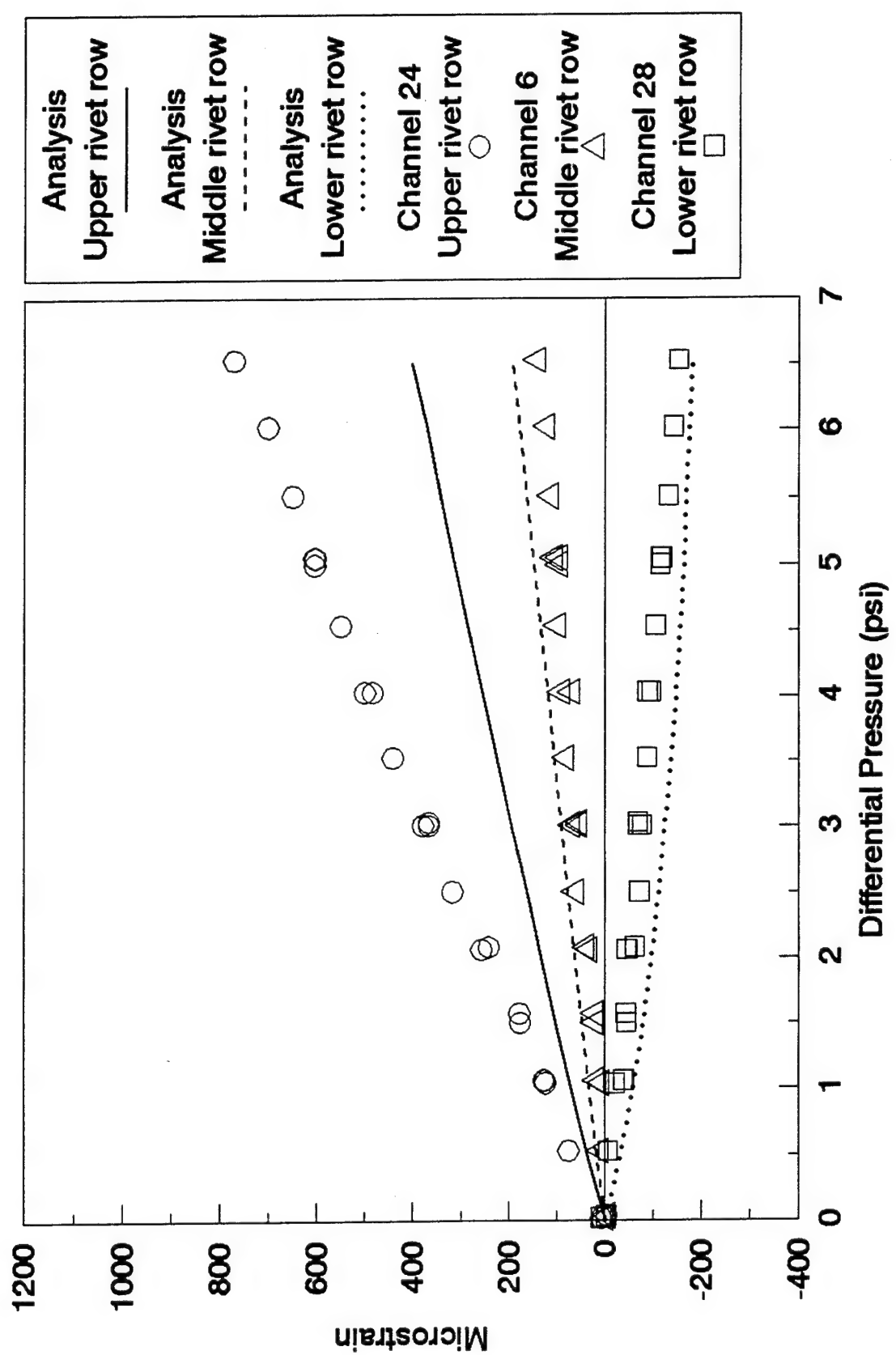


Figure 4.25. Comparison of Strains Across Lap Splice at S-4L, BS475
(Adhesively Bonded Lap Splice Model).

The comparison between the predicted hoop strains in the upper rivet row (riveted versus adhesive models) resembles the comparison between strains measured at the same location in the AANC and NASA tests. The strain predicted by the riveted model is almost twice as much as that predicted by the adhesive model at 6.0 psi, and the AANC test measured a strain of 2.5 times that in the NASA test. This resemblance is illustrated in Figure 4.26. Hoop strains measured in the upper rivet row of different lap splices on the AANC and NASA airplanes are compared with results predicted by the two finite element models. As shown previously, the results from the riveted lap joint model correlate reasonably well with the AANC data in this area. The NASA data, however, correlate better with results from the adhesive lap joint model. Therefore, the difference in strains measured in the upper rivet row between the AANC and NASA airplanes can be attributed to the difference in bond quality between the lap splice test sections. Apparently, the bond in the lap splice of the NASA airplane is effective, and the adhesive in the lap splices of the AANC airplane has degraded.

The hoop strains in the inner and outer skins along the lower rivet row are shown in Figures 4.27 and 4.28 as functions of pressure for each finite element model. The strain gage data for these plots correspond to BS475, stringer S-4L on the AANC B737 airplane. For this particular area of interest, the two different models predict similar strains.

Figure 4.29 compares test data and predictions from the riveted lap splice model for internal and external strains on the same skin at two different locations. The specific gage locations for these strains is along the midline at BS475 (between the tear strap and frame), 2.0 and 4.8 inches above the lap splice stringer S-4L. Figure 4.30 shows the same comparison for the adhesively bonded lap splice model. The adhesive lap splice model predicts a wider difference in strain than the riveted model, but the riveted model approximates the strain data more accurately.

The agreement between results from the finite element models and the experimental data is reasonable, especially considering the complexity and nonlinear character of the lap joint structure. The results from the finite element models can be improved by using a finer mesh pattern particularly in the lap joint area. The present model uses, at most, two shell elements in the area between rivet locations. Additional load steps may also improve accuracy. Such modifications, however, would increase computational time. To generate the results presented in this report, the riveted lap joint model required more than 44 hours in execution time for 13 load steps on a Hewlett-Packard 9000/730 workstation.

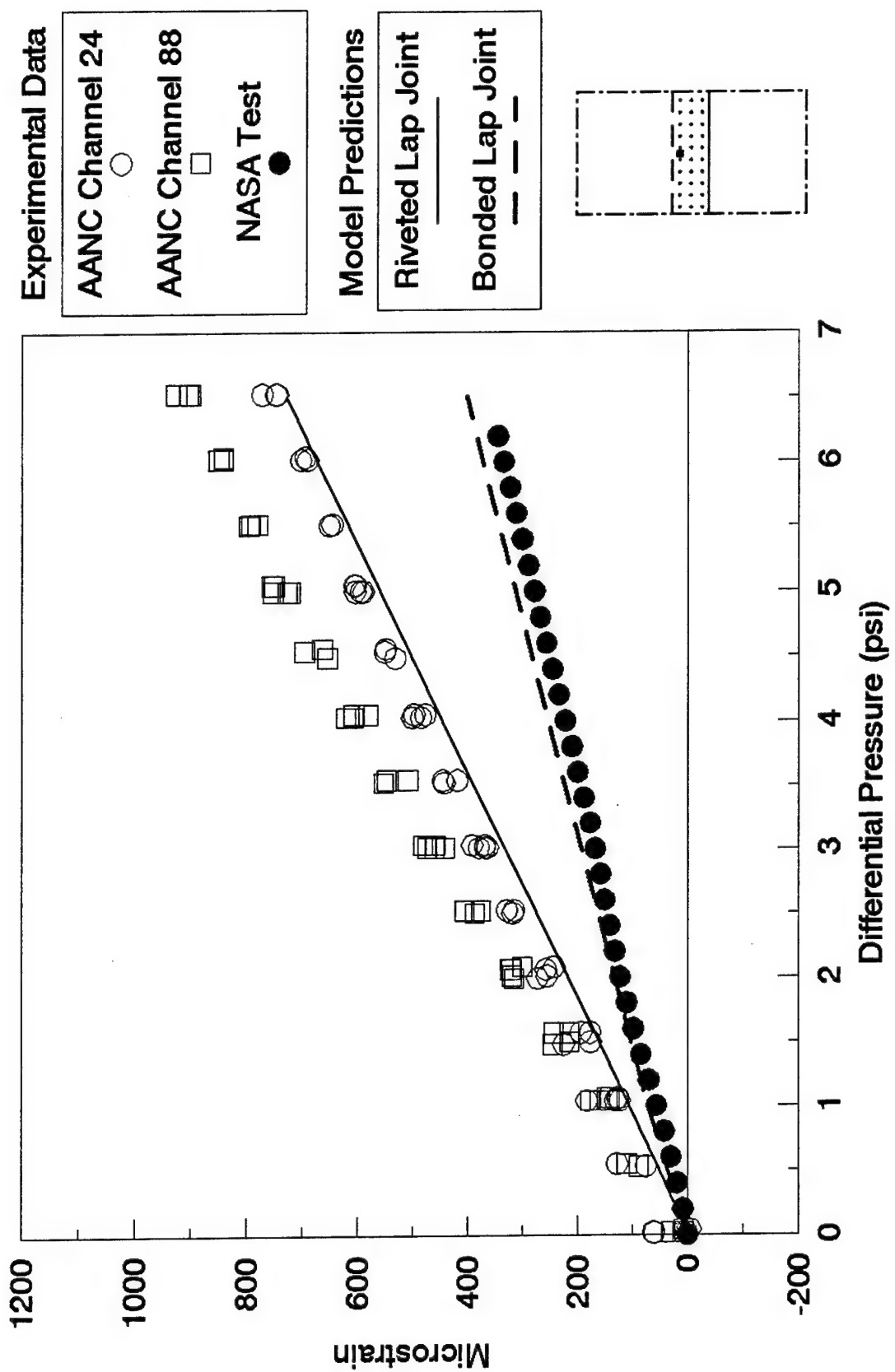


Figure 4.26. Comparison of Strains in Upper Rivet Row of AANC and NASA B737 Lap Splices with Results from Finite Element Models.

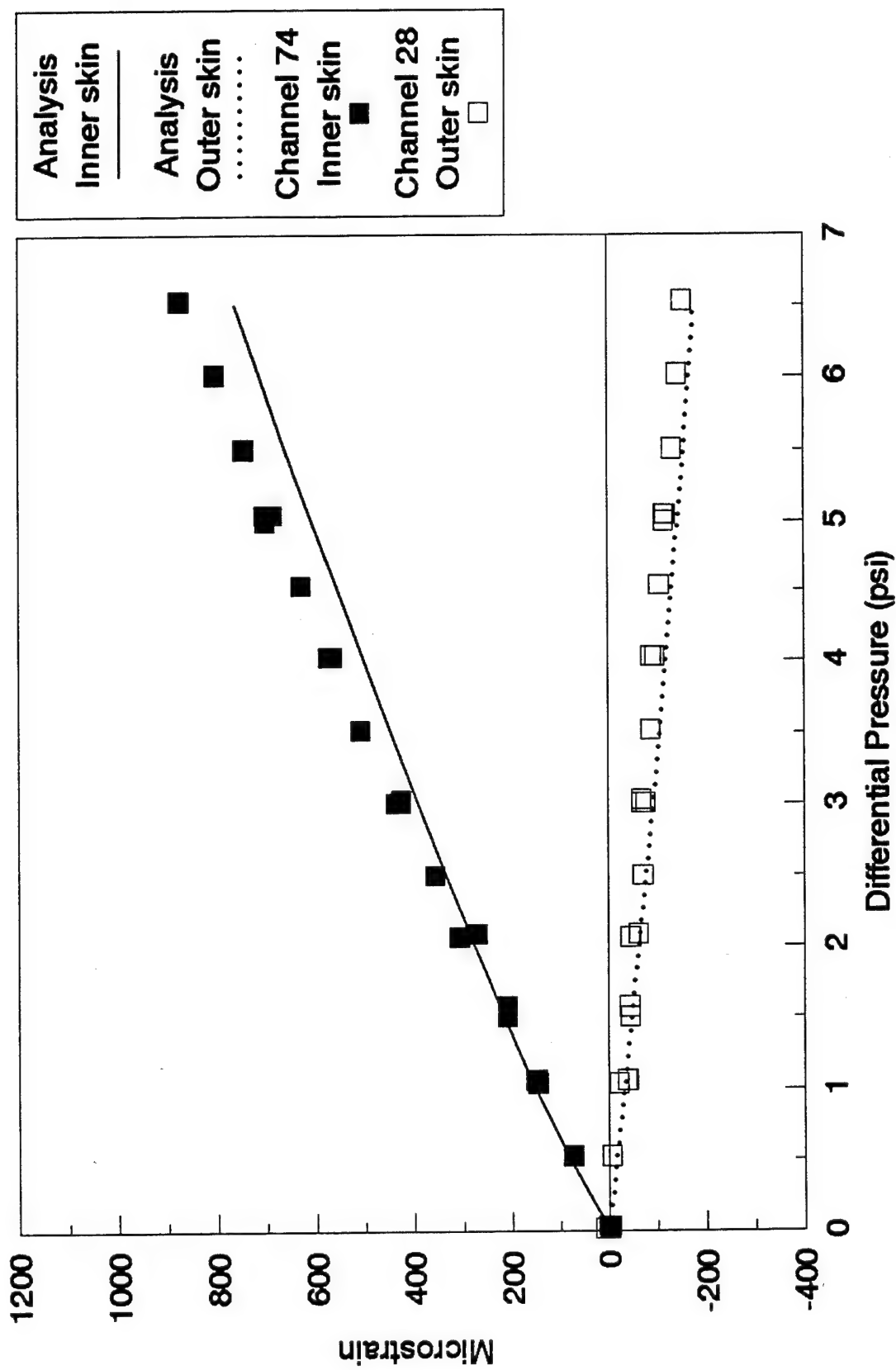


Figure 4.27. Comparison of Strains in Inner and Outer Skin at S-4L, BS475 (Riveted Lap Splice Model).

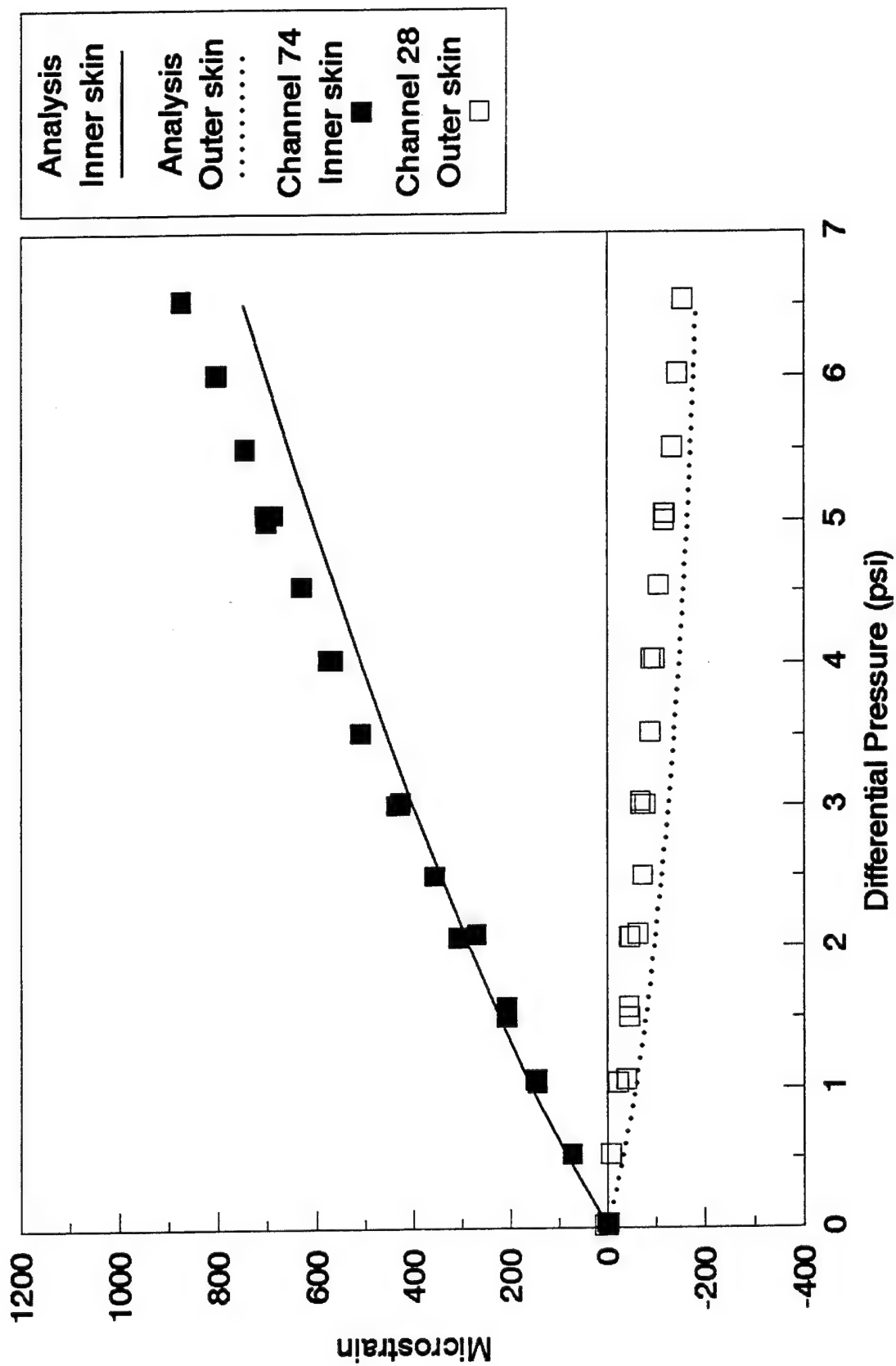


Figure 4.28. Comparison of Strains in Inner and Outer Skin at S-4L, BS475 (Adhesively Bonded Lap Splice Model).

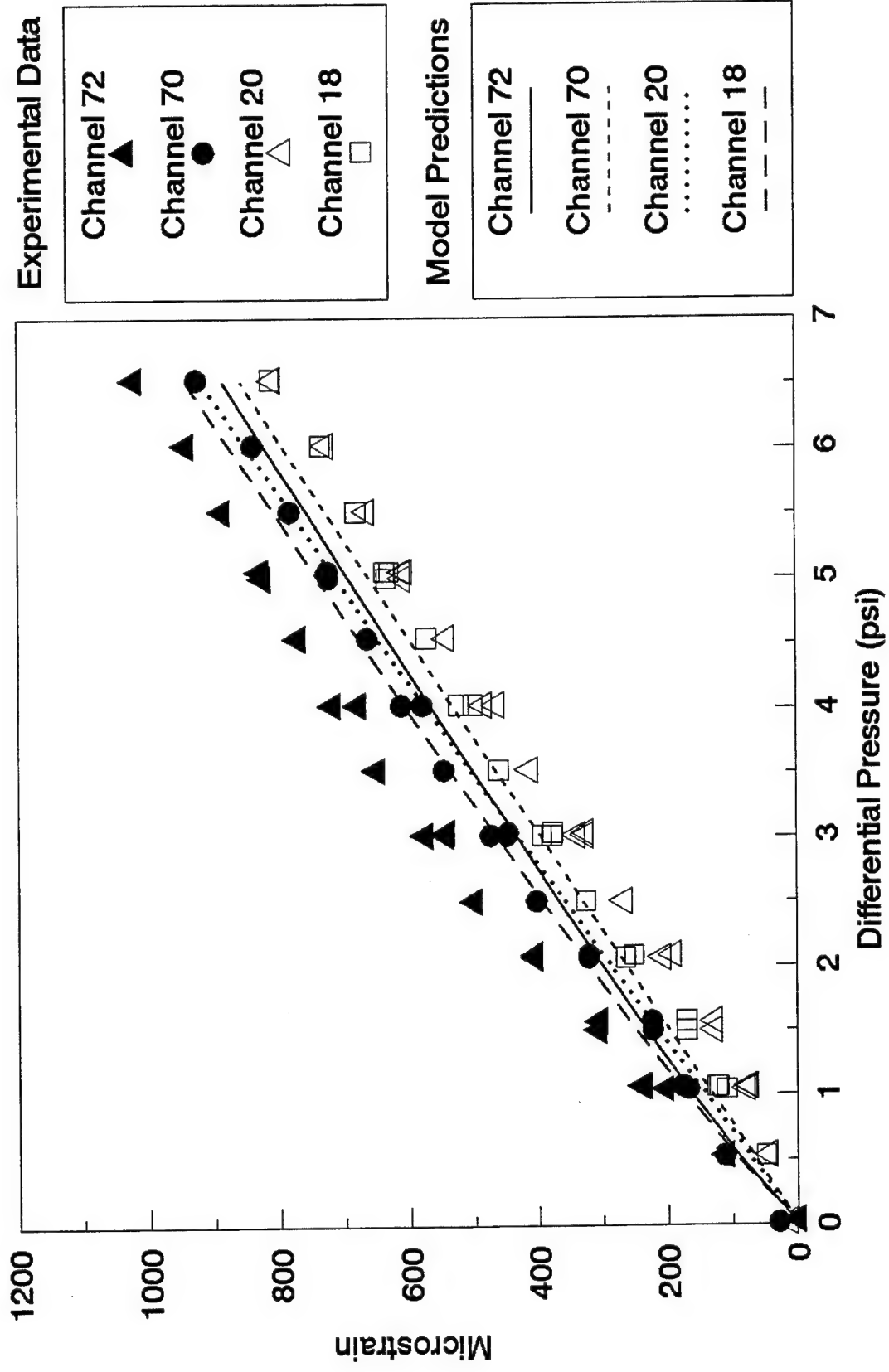


Figure 4.29. Comparison of Internal and External Strains on the Same Skin at S-4L, BS475 (Riveted Lap Splice Model).

Experimental Data

Channel 72
Channel 70
Channel 20
Channel 18

Model Predictions

Channel 72
Channel 70
Channel 20
Channel 18

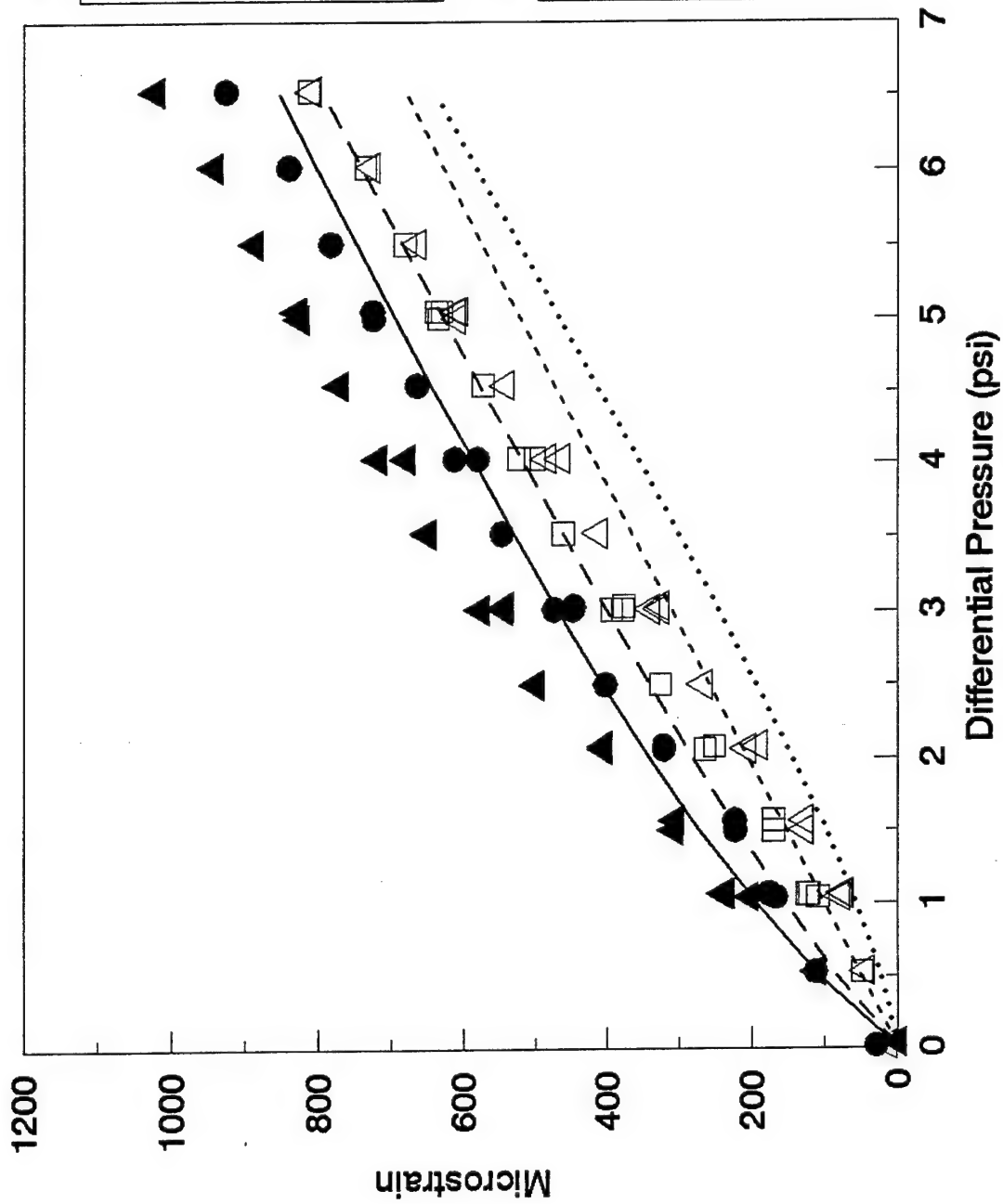


Figure 4.30. Comparison of Internal and External Strains on the Same Skin at S-4L, BS475 (Adhesively Bonded Lap Splice Model).

4.4 COMPARISONS AMONG DIFFERENT TEST SECTIONS IN THE AANC BOEING 737

Strain gage measurements from the various test sections in the AANC B737 airplane are compared to assess the influence of various structural features (such as windows, floor beams, and fuselage bending) on the strain fields in the fuselage. Eight (8) gages in each test section of the AANC airplane have coincident locations relative to a common point of reference. These gages are located along the midline; i.e., halfway between the tear strap and the frame; and are designated by the letters A through H in Figure 4.31. These specific gage designations can be summarized as follows:

- A - Longitudinal strain at midbay
- B - Hoop strain at midbay
- C - Longitudinal strain near top edge of lap joint
- D - Hoop strain near top edge of lap joint
- E - Longitudinal strain in upper rivet row
- F - Hoop strain in upper rivet row
- G - Longitudinal strain near bottom edge of lap joint
- H - Hoop strain near bottom edge of lap joint

Thus, two of these common gages (E and F) are located on the lap joint.

Comparisons among individual measurements at common locations in the AANC airplane are shown in Figures 4.32 to 4.39. These comparisons are presented in the form of plots showing microstrain as a function of applied pressure. Table 4.3 provides an index of strain gage channels with their common locations in each bay of the AANC airplane. The table also lists the figure numbers corresponding to the various comparisons of strain data.

Table 4.3. List of AANC Channels with Common Strain Gage Locations.

Gage Location	Test Section Location in AANC B737					Figure Number
	S-4L BS475	S-10L BS475	S-14L BS475	S-4L BS785	S-10L BS785	
A	17	47	61	83	91	4.32
B	18	48	62	84	92	4.33
C	19	49	63	85	93	4.34
D	20	50	64	86	94	4.35
E	23	53	65	87	95	4.36
F	24	54	66	88	96	4.37
G	29	59*	-	89	97	4.38
H	30	60	-	90	98	4.39

* Data obtained from this strain gage were inconsistent with other data, and were not included in these comparisons.

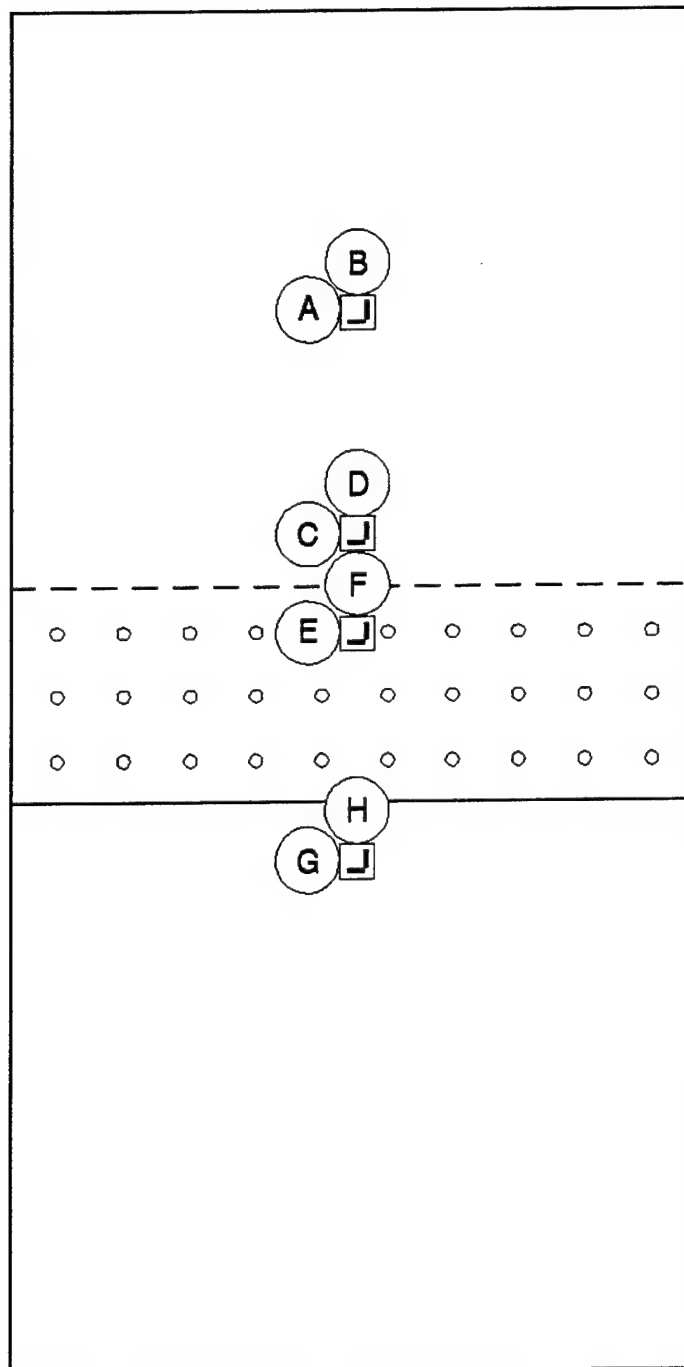


Figure 4.31. Common Strain Gage Locations in Each Bay of AANC Tests.

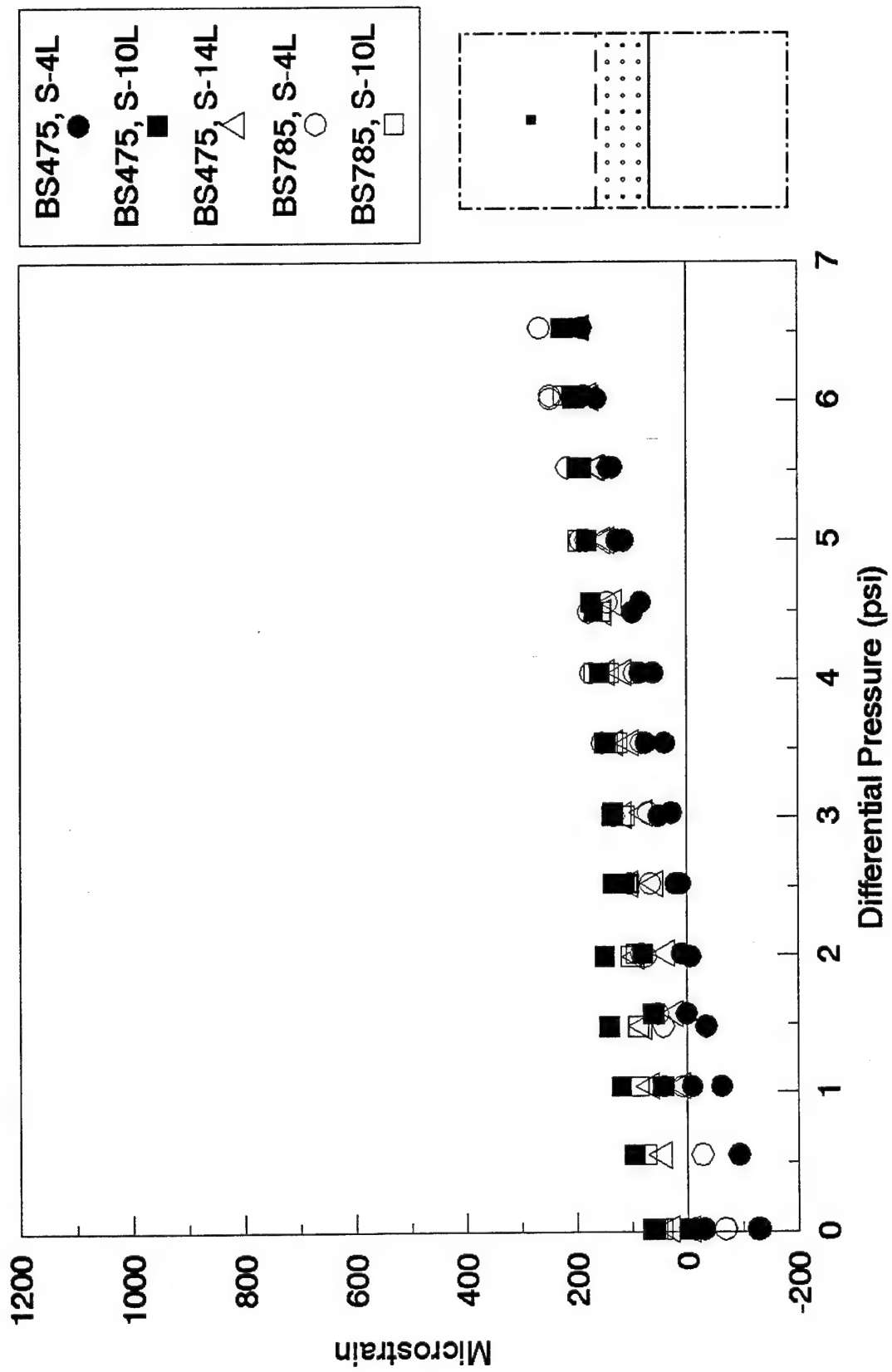


Figure 4.32. Comparison of Longitudinal Strains at Midbay Locations in ANNC Airplane.

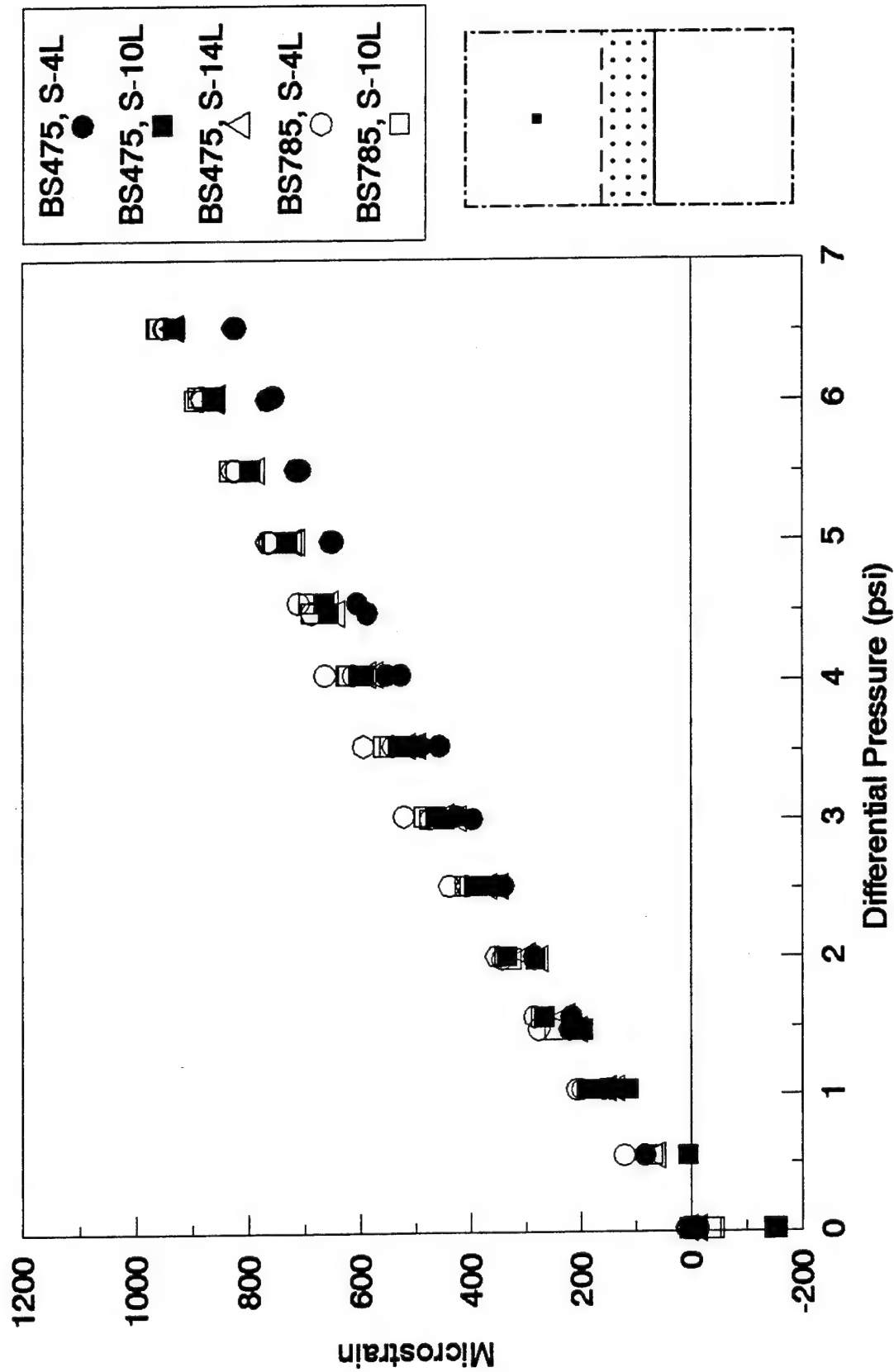


Figure 4.33. Comparison of Hoop Strains at Midbay Locations in AANC Airplane.

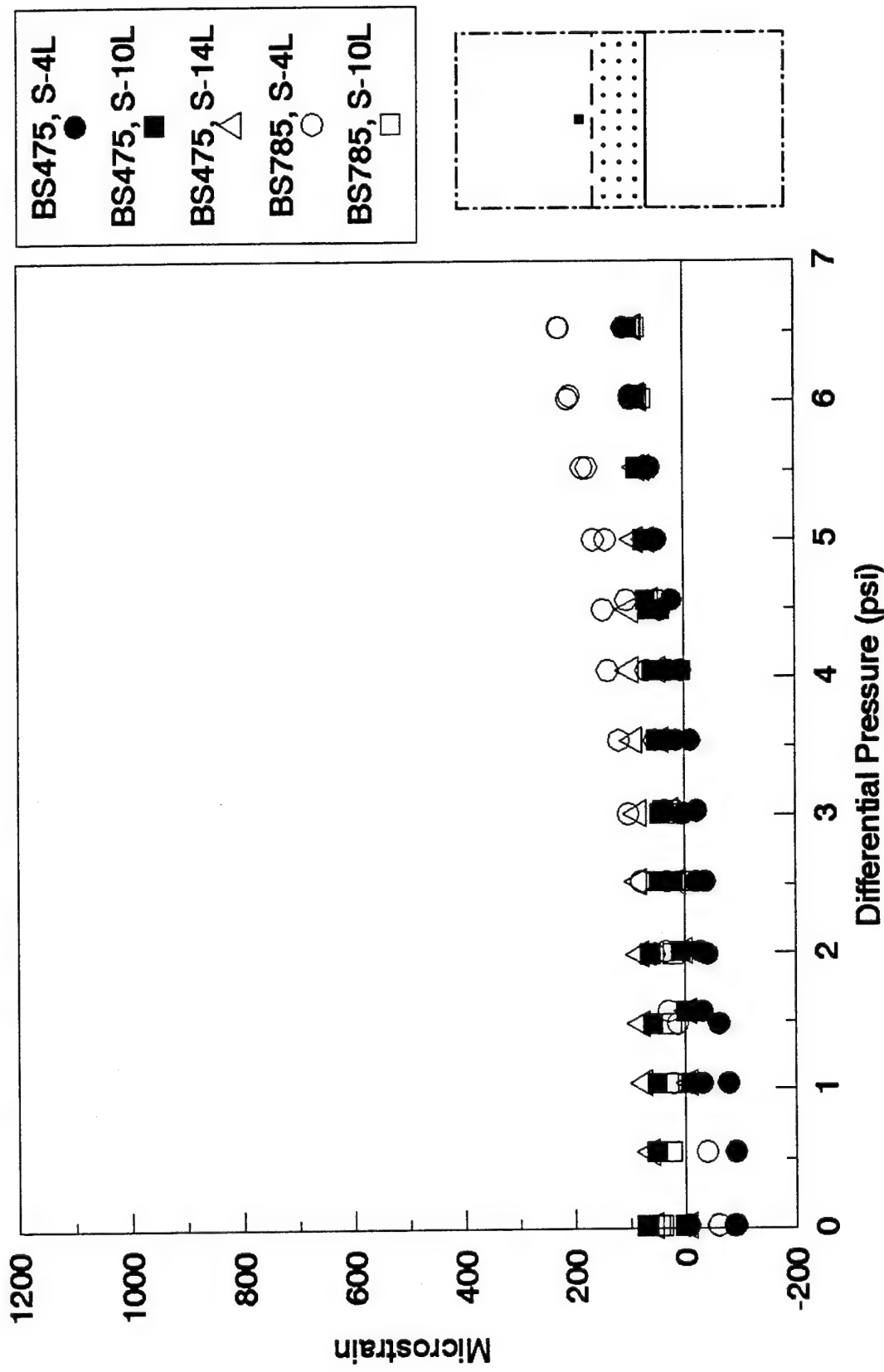


Figure 4.34. Comparison of Longitudinal Strains Near Top Edge of Lap Joint in ANC Airplane.

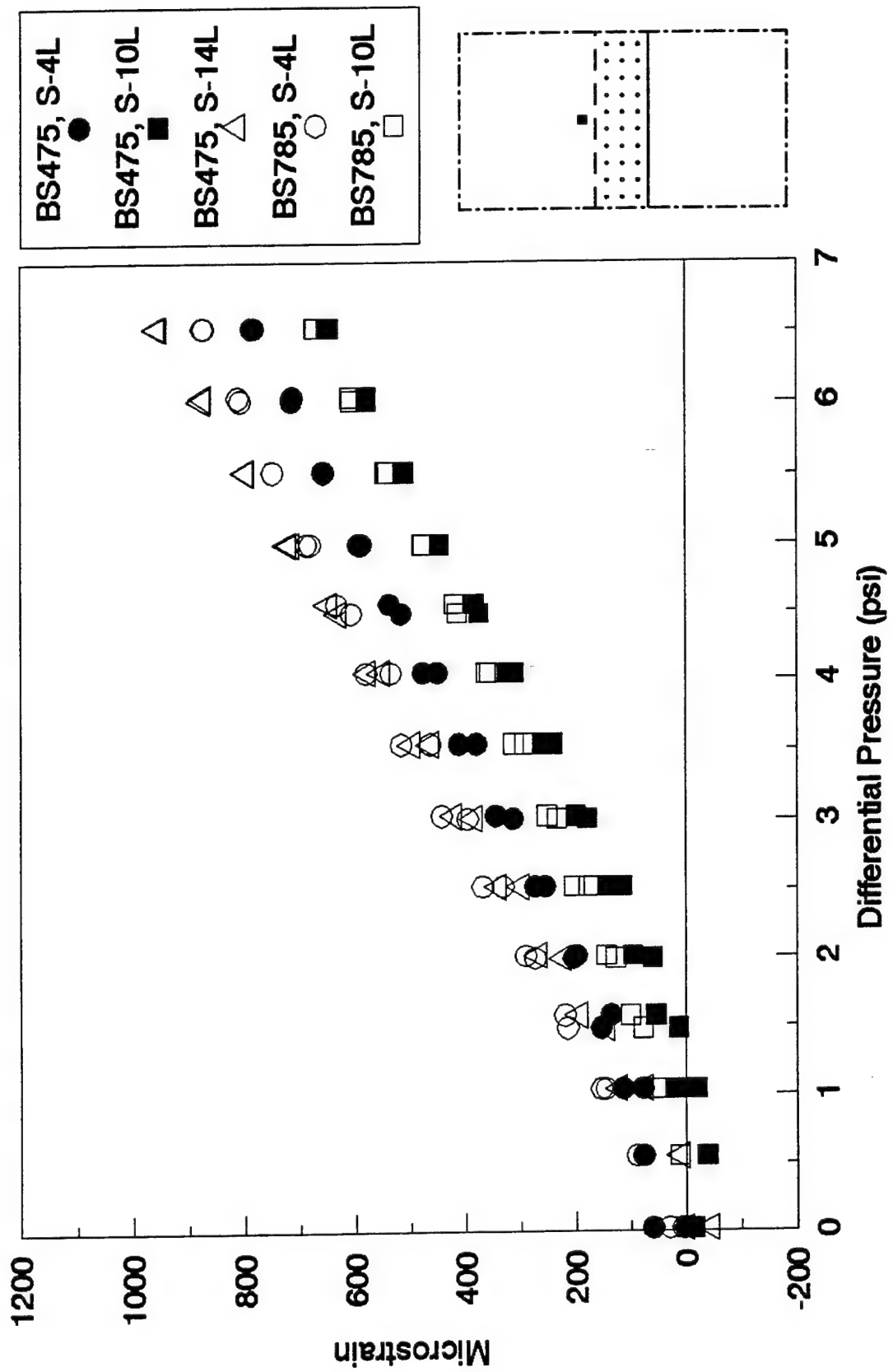


Figure 4.35. Comparison of Hoop Strains Near Top Edge of Lap Joint in AANC Airplane.

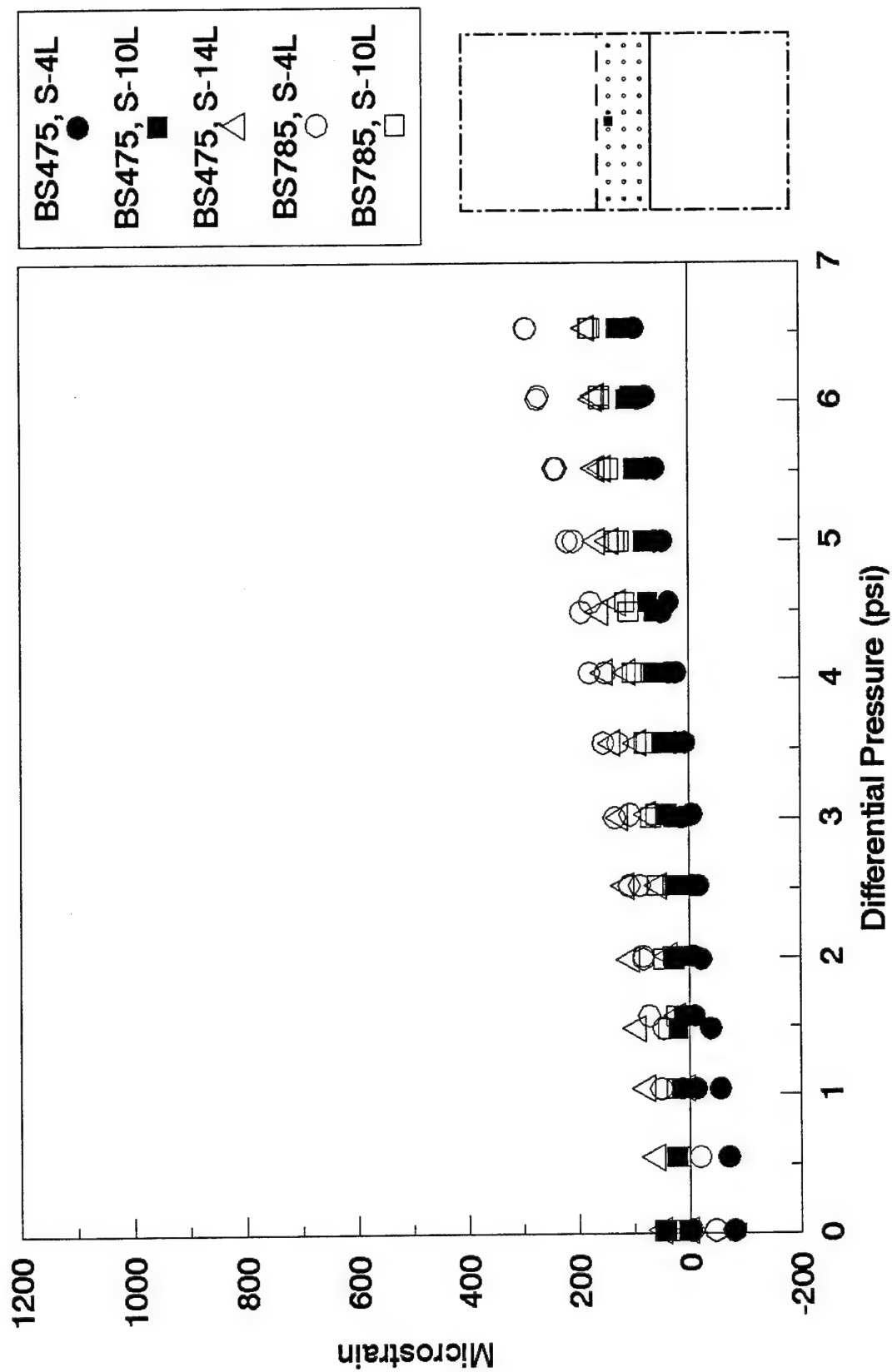


Figure 4.36. Comparison of Longitudinal Strains in Upper Rivet Row in AANC Airplane.

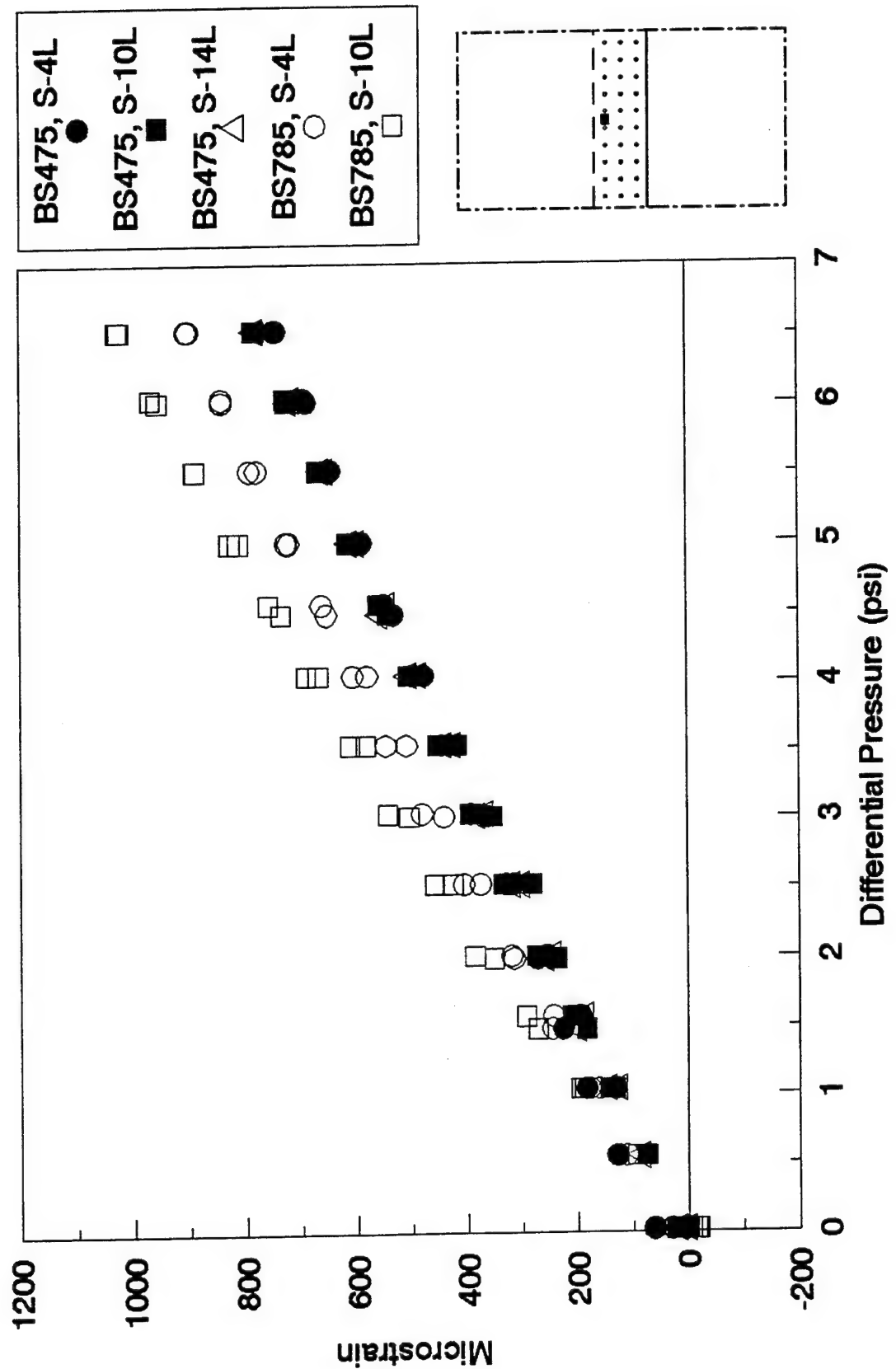


Figure 4.37. Comparison of Hoop Strains in Upper Rivet Row in AANC Airplane.

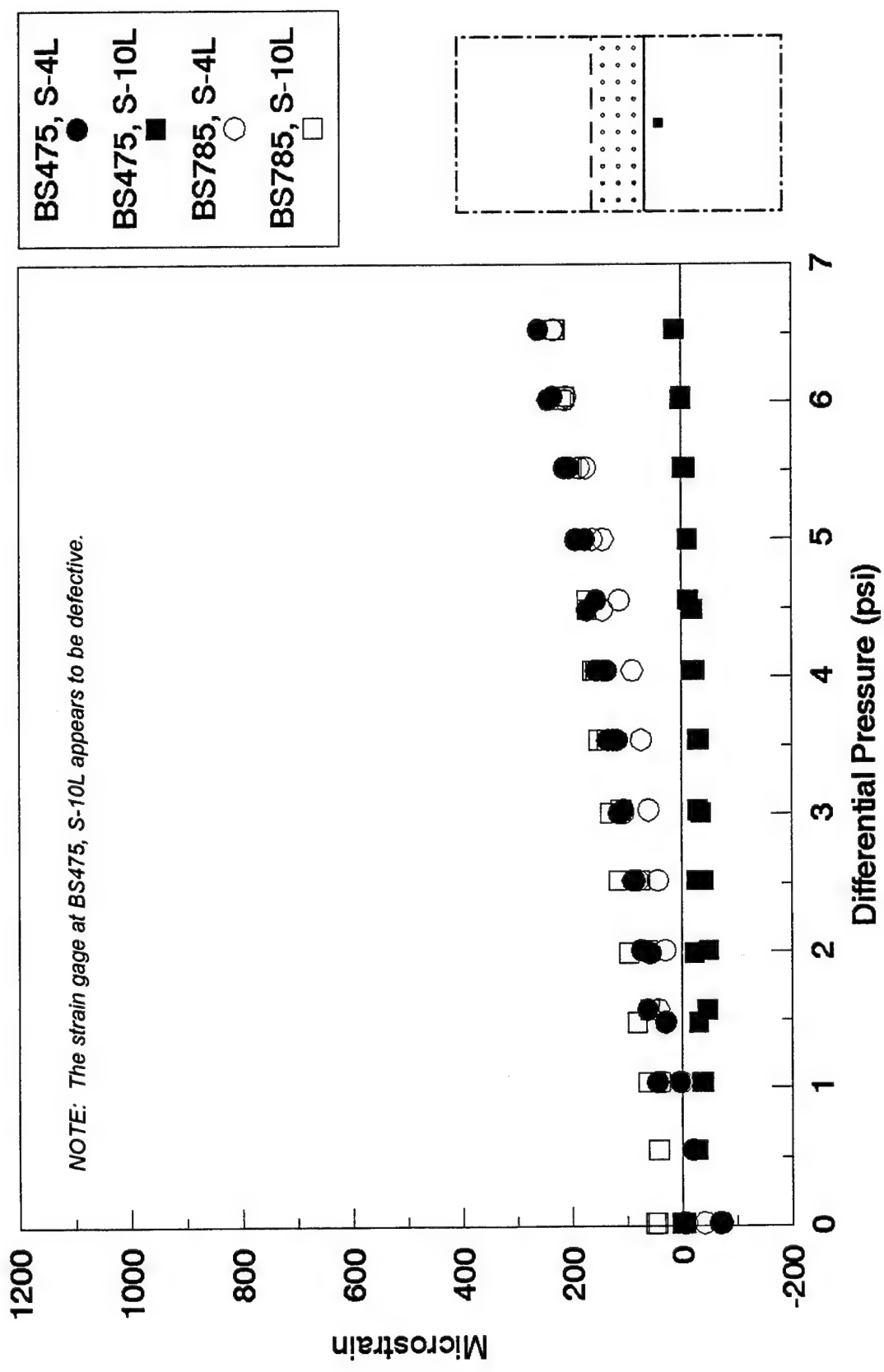


Figure 4.38. Comparison of Longitudinal Strains Near Bottom Edge of Lap Joint in AANC Airplane.

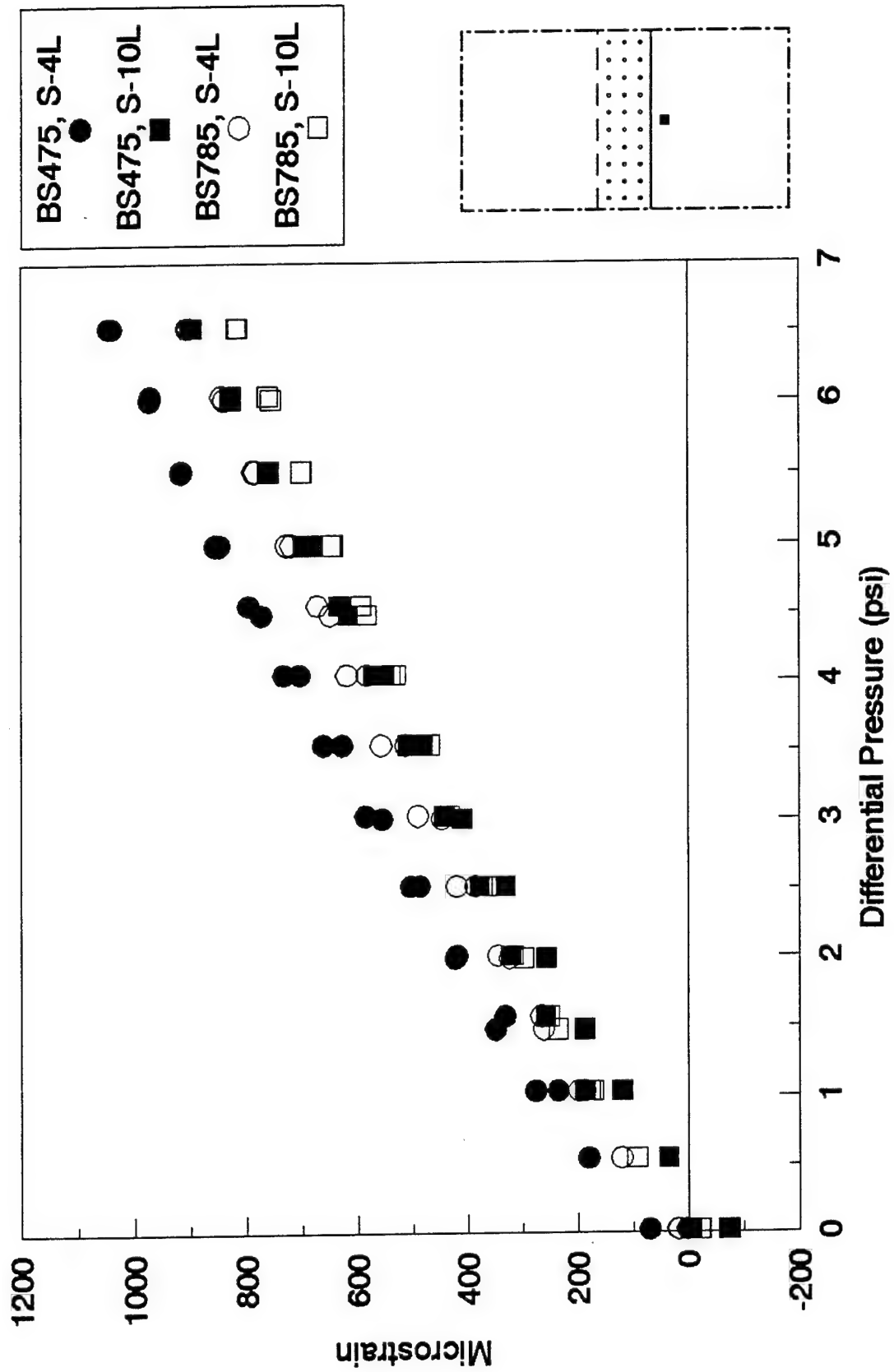


Figure 4.39. Comparison of Hoop Strains Near Bottom Edge of Lap Joint in AANC Airplane.

Comparisons of strains measured in two different test sections are expressed in terms of average percent difference in Table 4.4. These differences were calculated at the peak pressure of 6.5 psi. Strains for the first test section listed in the first column of the table were considered as the baseline value. That is, strains at S-10L, BS475 are the baseline values for the first comparison, and those at S-4L, BS475 are the baseline values for the remaining cases. Average values listed in the table are divided into two parts: (a) "off" lap refers to locations A-D, G, and H which were located away from the lap joint; and (b) "on" lap refers to two locations (E and F) which were located in the upper rivet row of the lap splice. Apparently, the location of the test section has a greater influence on the strains near the lap joint than those away from it. In other words, the variation of strains near the lap joint for the different test sections is greater than the variation of strains away from the lap joint.

*Table 4.4. Comparisons Among Test Sections in AANC Airplane.
Average Percent Difference at 6.5 psi differential pressure.*

<i>Test sections</i>	<i>"Off" Lap</i>	<i>"On" Lap</i>	<i>Comments</i>
S-10L BS475 versus BS785	-2.4%	+36.0%	Front versus tail
S-4L BS475 versus BS785	+25.4%	+111.3%	Front versus tail
S-4L versus S-14L BS475	+4.4%	+45.6%	Effect of window/floor beam
S-4L versus S-10L BS475	-1.5%	+17.5%	FMI baseline location versus Aloha accident location

The largest difference in strains occurs between BS475 and BS785 at stringer S-4L, which compares the front of the airplane to the tail end. The difference can be attributed to fuselage bending which is greater near the tail. Another comparison between the front and tail was made at stringer S-10L. This comparison also shows that strains near the tail of the airplane are higher than those in the front. Based on these two comparisons, fuselage bending increases strain levels by approximately 30%. Both comparisons also reiterate that location of the test section has a greater effect on strains in the lap joint than those away from it.

Strain data can also be compared between different stringer locations at the same body station. The data from the three test sections at Body Station 475, indicate that the strains at stringer S-14L are higher than those at S-10L, which are higher than those at S-4L. The difference in strains between S-4L and S-14L at BS475 implies a combined effect of windows and floor beams on the strain field. Apparently, strains are increased by 4% (away from the lap joint) to 46% (in the lap splice) due to the structural effects of the windows and floor beams. It should be noted that these results are influenced by the quality of the adhesive bond.

The comparison of strain data between S-4L and S-10L at Body Station 475 correlates the Foster-Miller baseline location with the probable site of the failure initiation in the Aloha accident. The overall difference between strains at these two test sections is less than 5%, on average. On the lap joint, strains at S-10L are 18% higher than those at S-4L, but away from the lap joint the difference in strains is negligible.

5. CONCLUSIONS

One of the concerns facing the civil aviation community is ensuring the continued integrity and safety of airframes and engines, as these flight systems age. The extended usage of aircraft means that the occurrence of fatigue cracks and other flaws can be expected to increase. Fatigue cracks occur in aircraft structures from cyclic loading caused by repeated pressurization. Research is being conducted to ensure that the continued structural airworthiness of airplanes operated beyond their projected fatigue lives is not compromised due to structural degradation caused by aging.

The results presented in this report provide detailed information regarding strain fields in the lap splices of an early Boeing 737-200 series aircraft (line number 49). In particular, the strains in both the skin and the substructure elements were measured experimentally on a retired Boeing 737 aircraft, and predicted analytically by finite element analysis. The AANC B737 strain data were then correlated with data obtained from the Foster-Miller full-scale panel tests and the NASA B737 pressurization tests.

Correlations between the AANC B737 strain data and results from other research areas are summarized as follows:

- (1) Strains measured in the curved, water-pressurized panels used by Foster-Miller, Inc. (FMI) were in reasonable agreement with strains collected from the ground pressurization tests on the AANC Boeing 737 aircraft.
- (2) The tear strap and filler strip construction of the FMI panels appears to be an acceptable alternative to the waffle doubler design used in actual aircraft, in terms of producing representative strains.
- (3) Strain data from the NASA Boeing 737 test were in reasonable agreement with data obtained from a similar section on the AANC B737 aircraft.
- (4) Agreement between results from finite element models developed by the Volpe Center and strain gage data was reasonable. The AANC B737 data agreed better with results from the riveted lap splice model than those from the adhesive lap splice model. The detection of corrosion and debonds in the lap joints of the AANC aircraft through nondestructive inspections confirmed this finding. Conversely, the NASA B737 data agreed better with results from the adhesive model than those from the riveted model. This finding suggested that the adhesive bond in the lap splice test section of the NASA B737 is still effective. Although some discrepancies between the finite element results and test data were

evident, the accuracy of the results may be improved by modifying the finite element mesh pattern to include additional elements between rivets.

The strain data collected from the AANC airplane were analyzed to characterize the state of strain in the fuselage structure. Particular attention was given to the strains near the lap splices and to the load transfer through the joints. The results of the strain characterization are summarized as follows:

- (1) In each test section of the AANC airplane, most of the load in the skin above the lap joint was transferred into the skin around the upper rivet row. Strain levels in the upper skin of the lap decrease drastically in the circumferential direction across the joint. The skin around the middle rivet row exhibited only a fraction of the strain around the upper rivet row; the lower rivet row experienced even less strain. Differences in load transfer among the different test sections appear to be related to differences in bond quality.
- (2) Even though the internal pressurization of the fuselage generally produced positive hoop strains, strains in the skin around the lower rivet rows in all bays were negative. These negative or compressive strains were a consequence of reverse bending that develops when the lap joint deforms from internal pressure loading.
- (3) The maximum strains at a differential pressure of 6.5 psi measured above (in the upper skin on the outside) and below (in the lower skin on the inside) the lap joint were 900 to 1100×10^{-6} inch/inch ($\mu\epsilon$). The maximum strains at the middle rivet row ranged from $200 \mu\epsilon$ to $550 \mu\epsilon$. Again, the difference in middle row strains can be attributed to differences in the adhesive bond quality between various joints. Strains in the lower rivet row of the outer skin were smaller in magnitude and compressive (between $-100 \mu\epsilon$ and $-200 \mu\epsilon$).
- (4) Hoop strains on the external skin across the lap splice joint were both uniform and consistent as the location of interest varied from over the tear strap, through midbay, and over the frame. That is, the reinforcing substructure elements did not affect the strain levels around the skin and rivets to which they were attached. Thus, the peak strains were the same as those listed in item (3) above.
- (5) Deformation of the lap splice from internal pressurization displaces the neutral axis of the structure which creates bending strains in the circumferential direction. Data collected from gages mounted on the inside skin with matching gages on the outside or exterior skin determined that: 1) the bending effects increase as the location of interest varies circumferentially down across the lap splice joint, and 2) the bending

strains are compressive. Thus, in areas of low strain, such as in the external skin at the lower rivet row, bending strains dominated. The maximum bending strains in the hoop direction varied between 100 $\mu\epsilon$ and 150 $\mu\epsilon$ at the peak pressure of 6.5 psi.

- (6) The lower rivet row of the inner skin experiences the same peak strains as the upper rivet row of the outer skin (900 $\mu\epsilon$ to 1000 $\mu\epsilon$ in the hoop direction and 200 $\mu\epsilon$ to 300 $\mu\epsilon$ in the longitudinal direction). Therefore, these two areas should be treated similarly in fatigue and damage tolerance analyses.
- (7) The maximum hoop strains in the fuselage frames were measured between 600 $\mu\epsilon$ and 700 $\mu\epsilon$. These values are approximately 30% to 40% lower than the maximum strains measured on the skin directly above the frame. The longitudinal strains measured in the stringers were slightly lower than those on the attached skin (maximum strains in the stringer were between 200 $\mu\epsilon$ and 350 $\mu\epsilon$; in the skin between 250 $\mu\epsilon$ and 400 $\mu\epsilon$).
- (8) The maximum hoop stresses measured in the skins of the lap joint were in the range of 9 to 13 ksi. The combined effect of the load transfer and reverse bending produced a large difference in hoop stresses between the internal and external skins near the lower rivet row. The stresses in the upper skin on the outside at the lower rivet row were negligible, but the same stresses on the lower skin on the inside reached a peak value of 11 ksi. The longitudinal stresses were approximately one-half of the hoop stresses. The maximum longitudinal stresses at 6.5 psi varied between 5 and 6.5 ksi.
- (9) Hoop stresses at the midbay-midline location in each test section were between 70% and 84% of the thin-walled cylinder estimate; the corresponding longitudinal stresses varied between 70% and 90% of the theoretical value. These percentages are reasonable since the actual airplane contains stiffening elements which carry load and generally reduce strain.
- (10) The peak longitudinal stresses in the stringers varied between 1.3 and 2.4 ksi which were approximately one-third of those in the mating skin of the lap splice. Hoop stresses in the frames (peak values of 5 to 6 ksi) were as much as 50% lower than those in the adjacent lap splice skin. A thin-walled cylinder analysis, modified to account for the stringers, predicted a longitudinal stringer stress of 2.0 ksi.
- (11) The maximum principal stresses measured near the frame were greater than the stresses near the tear straps. Near the frame, the principal stresses were as high as 11 ksi; near the tear strap, the stresses were

approximately 8 ksi. The principal stresses at the fuselage crown were the same as those near the window.

- (12) The maximum growth of the fuselage diameter was 0.156 inch at the peak test pressure of 6.5 psi. As expected, this experimental value was slightly less than the theoretical diameter growth of an unstiffened, thin-walled cylinder (0.158 inch).
- (13) The combined structural influence of windows and floor beams increased strains by 4% to 46%. This result, however, is influenced by the quality of the adhesive bond.
- (14) Fuselage body bending increased strains by approximately 30%. In flight, the magnitude of the bending at the tail would probably not be as severe.

REFERENCES

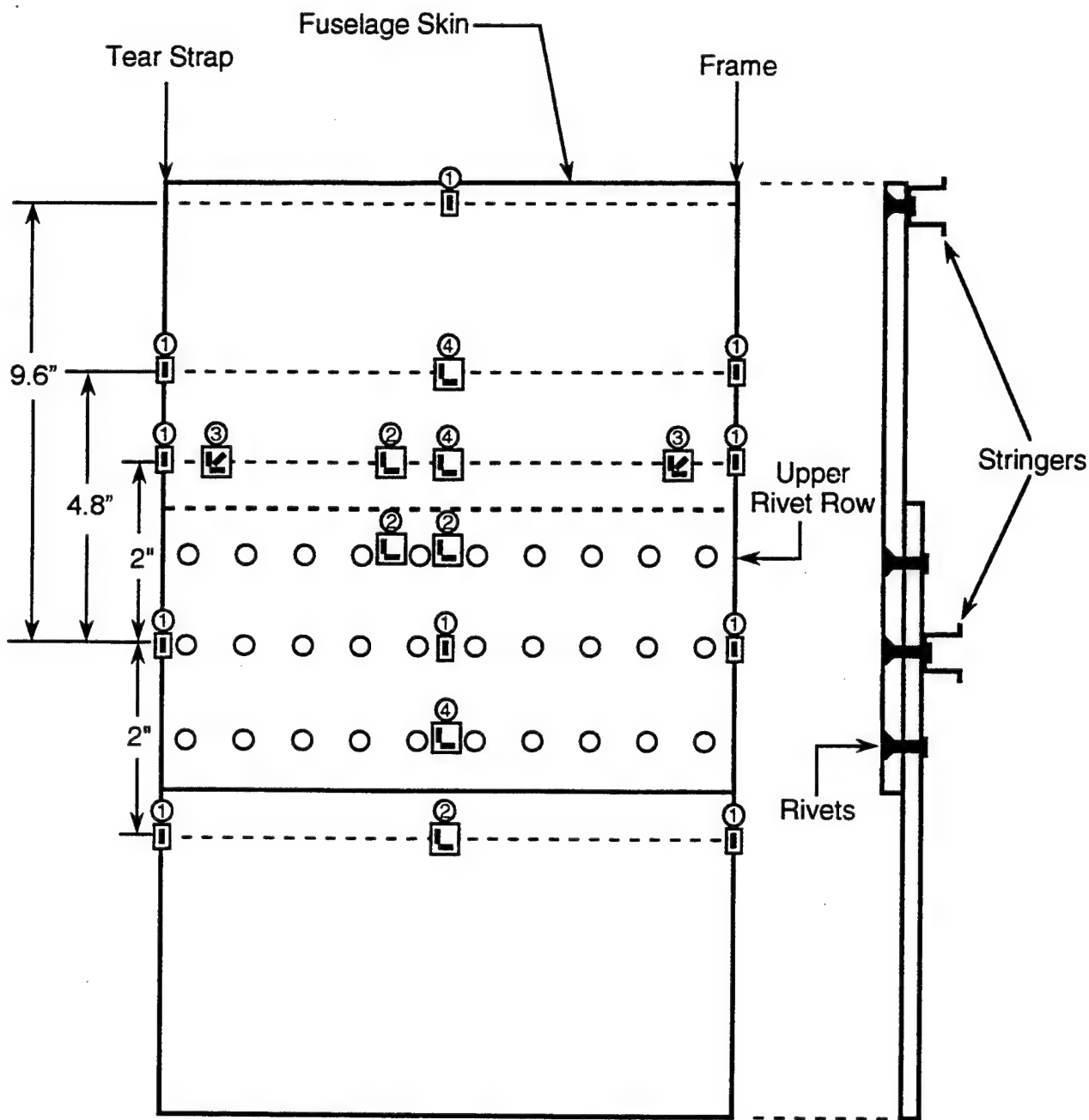
- [1] National Transportation Safety Board, "Aircraft Accident Report - Aloha Airlines Flight 243, Boeing 737-200, N73711, Near Maui, Hawaii, April 28, 1988," NTSB/AAR-89/03, PB89-910404, June 1989.
- [2] Thomson, D., G. Samavedam, D. Hoadley, and D.Y. Jeong, "Aircraft Fuselage Lap Joint Fatigue and Terminating Action Repair," draft final report , August 1993.
- [3] Samavedam, G., and D. Hoadley, " Fracture and Fatigue Strength Evaluation of Multiple Site Damaged Aircraft Fuselages - Curved Panel Testing and Analysis," final report, DOT/FAA/CT-94/10, DOT-VNTSC-FAA-93-8, January 1994.
- [4] Samavedam, G., D. Hoadley, and D. Thomson, "Full-Scale Testing and Analysis of Curved Aircraft Fuselage Panels," final report, DOT/FAA/CT-93/78, DOT-VNTSC-FAA-93-10, December 1993.
- [5] Phillips, E.P., and V.O. Britt, "Measurements of Fuselage Skin Strains and Displacements Near a Longitudinal Lap Joint in a Pressurized Aircraft, NASA Technical Memorandum 104163, October 1991.
- [6] Aircraft Utilization Database, Aviation Research and Support Limited, United Kingdom.
- [7] Boeing Service Bulletin No. 737-53A1039, "Body Skin Lap Joint Inspection and Repair," Revision 3, August 20,1987.
- [8] *Mil-Handbook 5*, U.S. Department of Defense, Washington, D.C., 1987.
- [9] Kobayashi, T., J.H. Giovanola, and D.A. Shockley, "Comparison of Fracture Behavior of 40-Year Old and More Recently Made Aluminum Sheets," Stanford Research International, Inc. Report to Volpe National Transportation Systems Center, June 1992.
- [10] Canha, J.V., "Finite Element Analysis of Foster-Miller Full-Scale Curved Fuselage Test Panel," Volpe Center Technical Interchange Document, October 1992.

REFERENCES (continued)

- [11] Canha, J.V., "Aircraft Section Model for Strain Field Characterization," Volpe Center Technical Interchange Document, April 1993.
- [12] Swift, T., "Development of the Fail-Safe Design Features of the DC-10," *Damage Tolerance in Aircraft Structures*, ASTM STP 486, American Society for Testing and Materials, Philadelphia, PA, 1971, pp. 164-214.

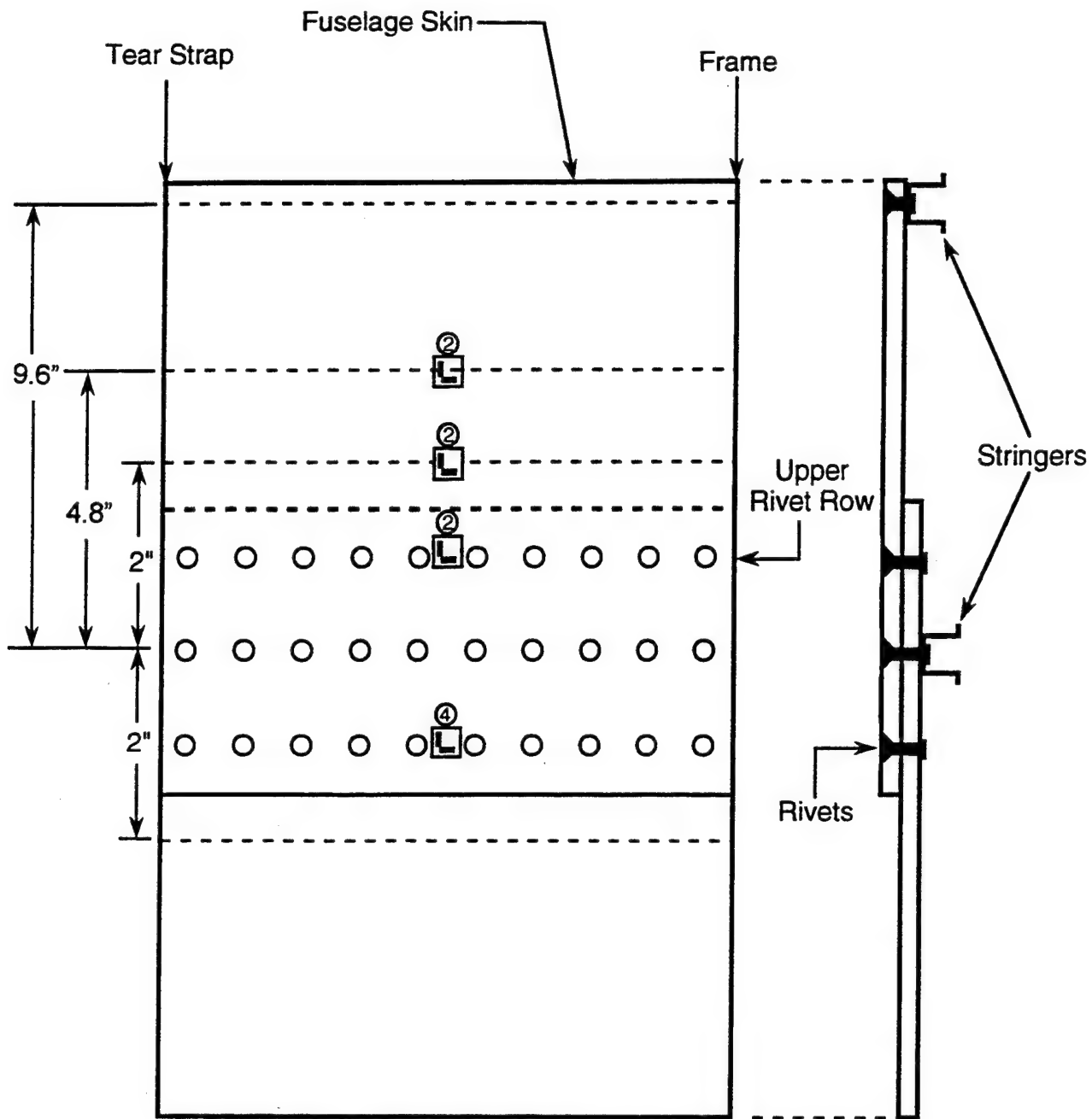
APPENDIX A

DEPLOYMENT OF STRAIN GAGES AT SPECIFIC LAP SPLIC BAYS



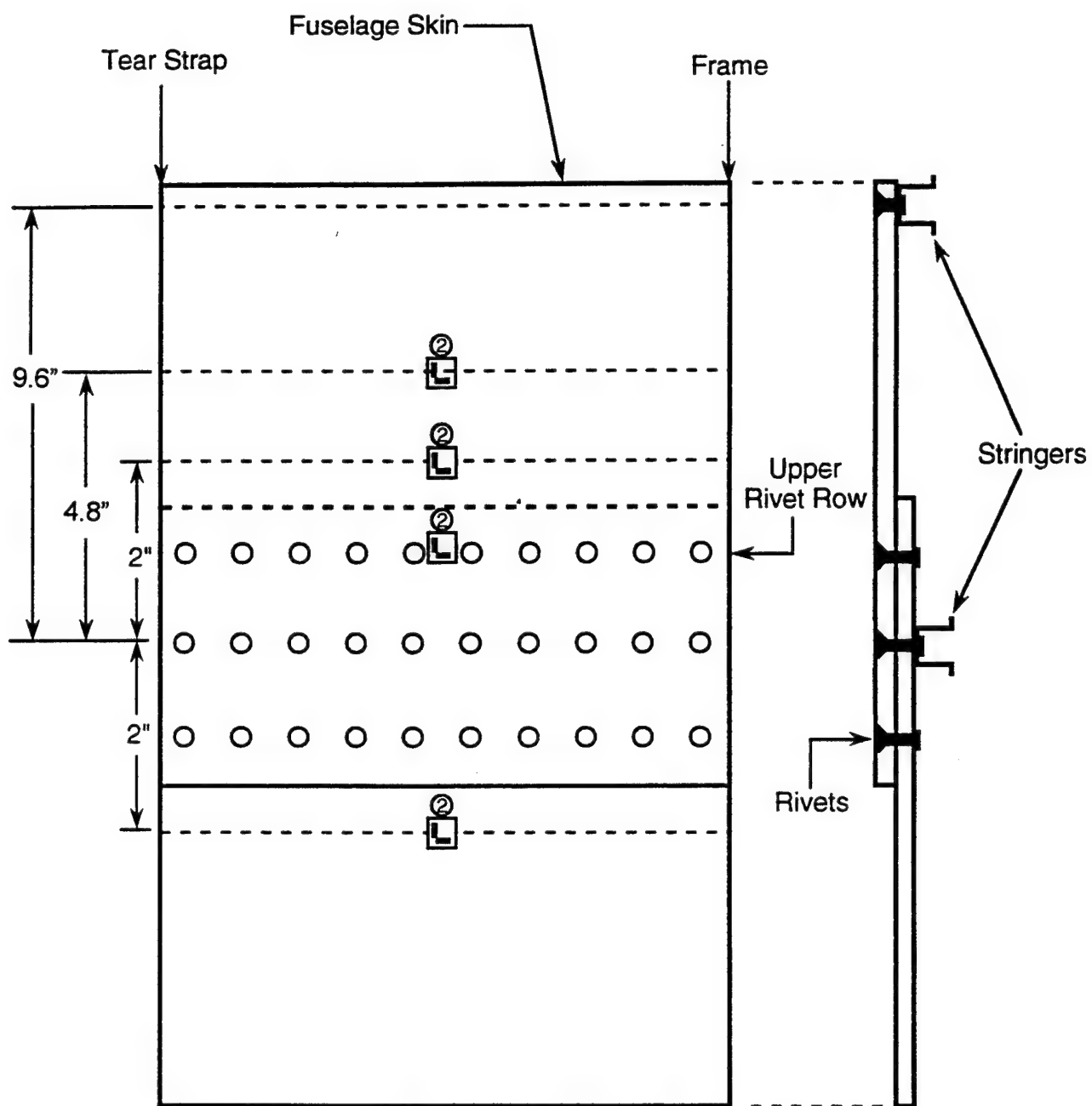
- ① Uniaxial Strain Gage - Hoop Direction, Exterior
- ② 0° / 90° Biaxial Strain Gage - Exterior
- ③ Rosette Strain Gage - Exterior
- ④ 0° / 90° Biaxial Strain Gage - Interior and Exterior

Figure A.1. Strain Gage Layout for Lap Joints Around Stringers S-4L and S-10L; Body Stations 470-480 (36 Gage Configuration).



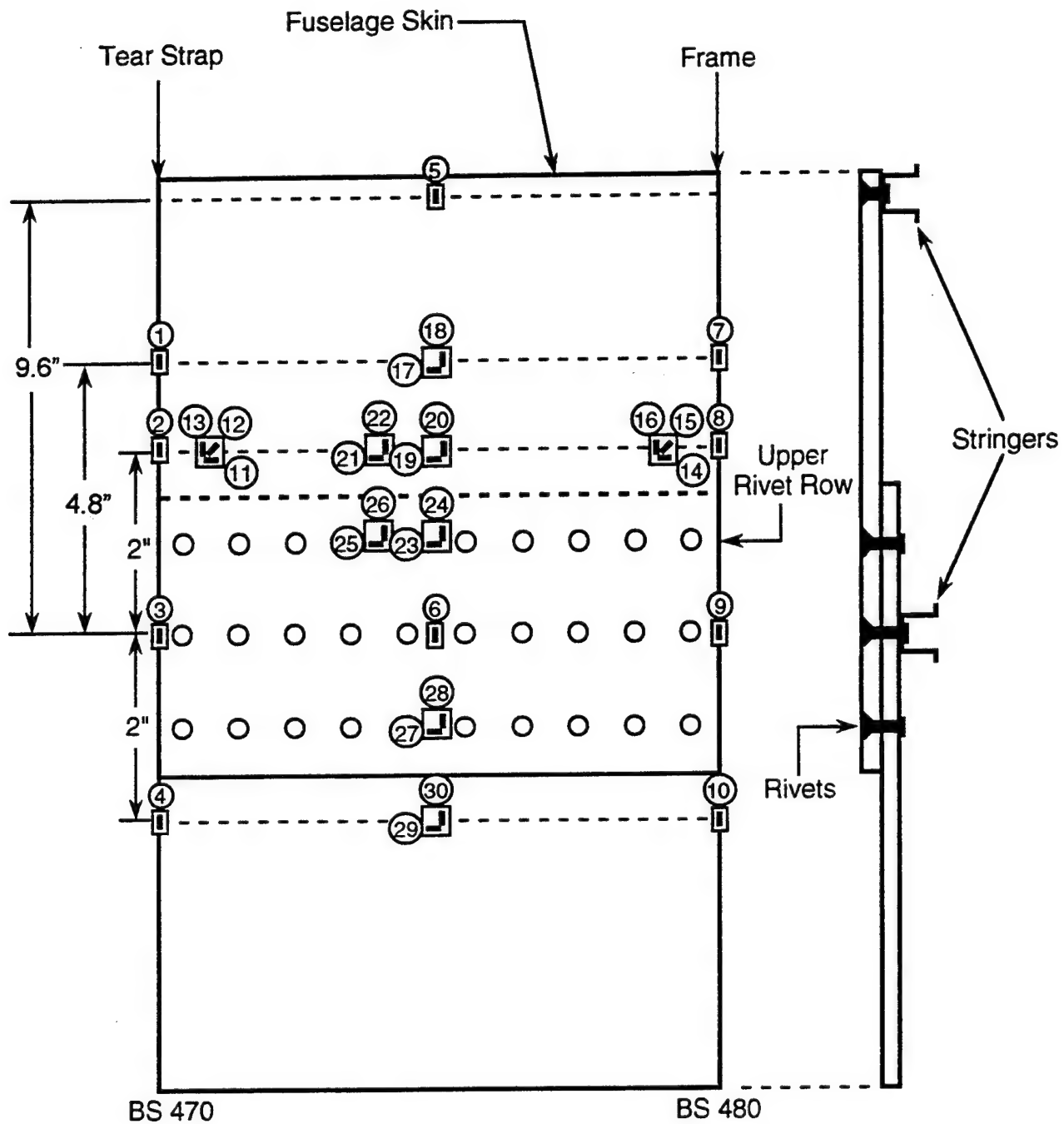
- ② 0° / 90° Biaxial Strain Gage - Exterior
- ④ 0° / 90° Biaxial Strain Gage - Interior and Exterior

Figure A.2. Strain Gage Layout for Lap Joint Around Stringer S-14L;
Body Stations 470-480 (10 Gage Configuration).



② 0° / 90° Biaxial Strain Gage - Exterior

Figure A.3. Strain Gage Layout for Lap Joints Around Stringers S-4L and S-10L; Body Stations 780-790 (8 Gage Configuration).



*Figure A.4. Strain Gage Numbers for Lap Joint at Stringer S-4L;
Body Stations 470-480; External (30 Gages).*

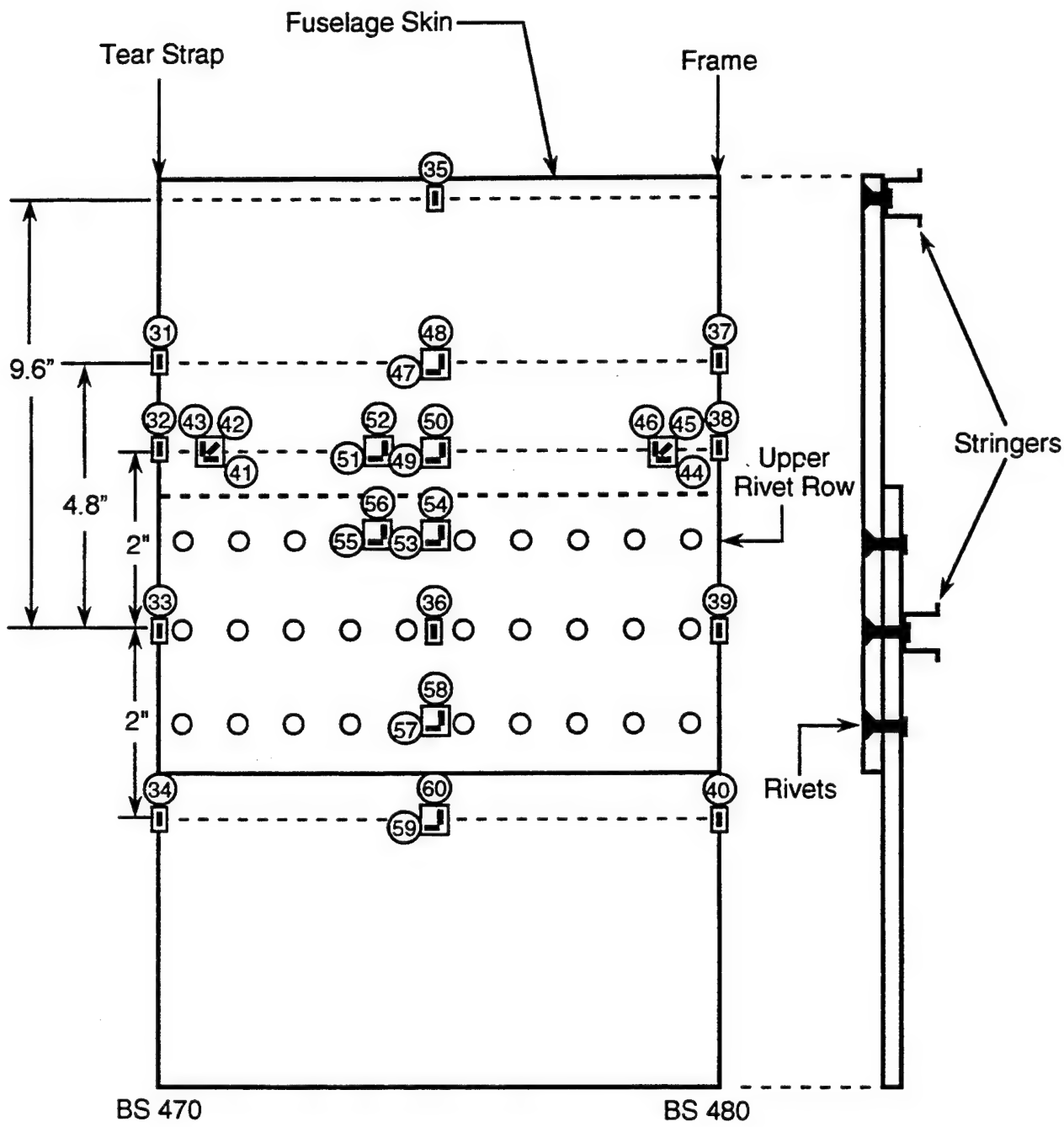


*Figure A.5. Strain Gage Numbers for Lap Joint at Stringer S-10L;
Body Stations 470-480; External (30 Gages).*

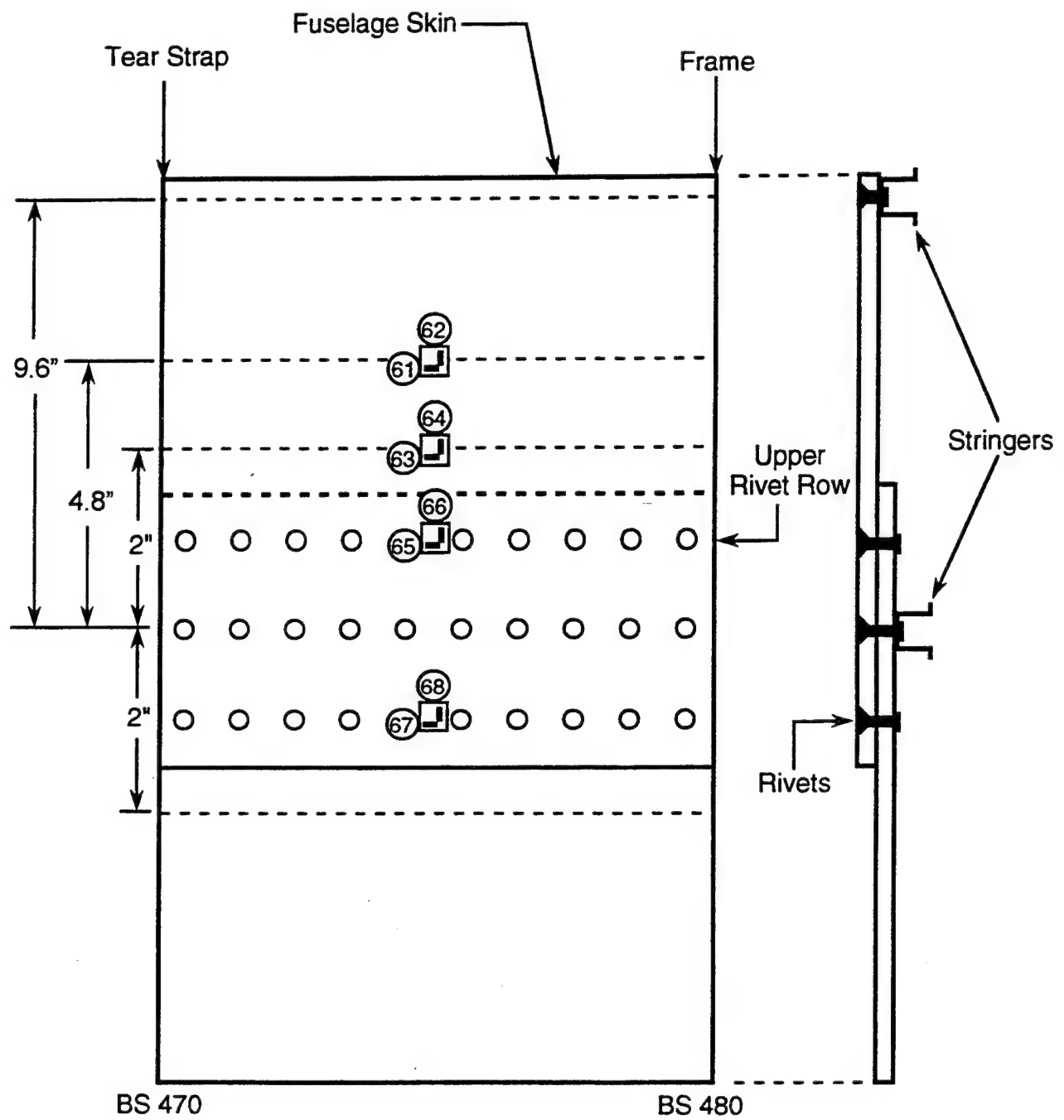


Figure A.6. Strain Gage Numbers for Lap Joint at Stringer S-14L;
Body Stations 470-480; External (8 Gages).

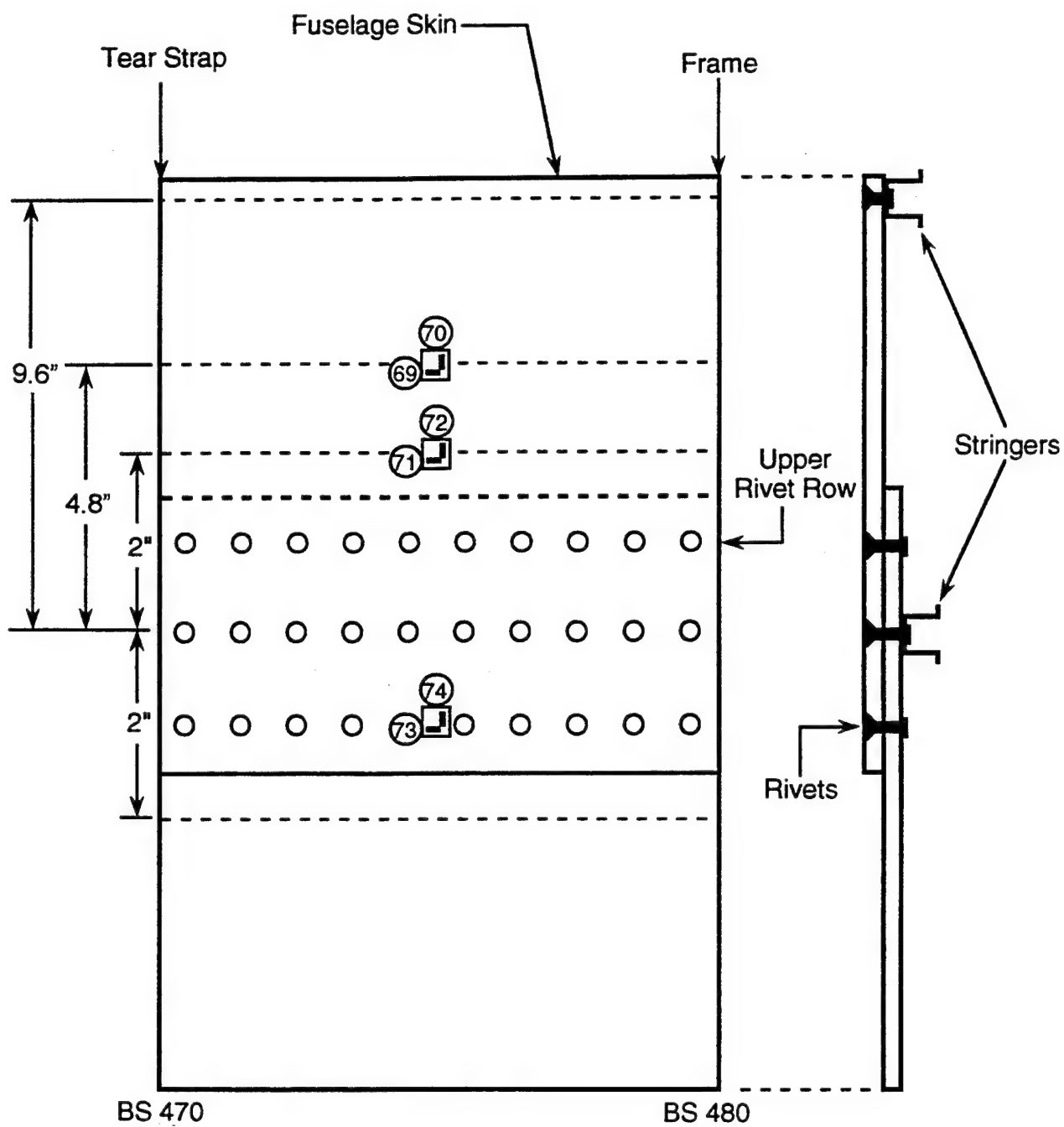


Figure A.7. Strain Gage Numbers for Lap Joint at Stringer S-4L;
Body Stations 470-480; Internal (6 Gages).

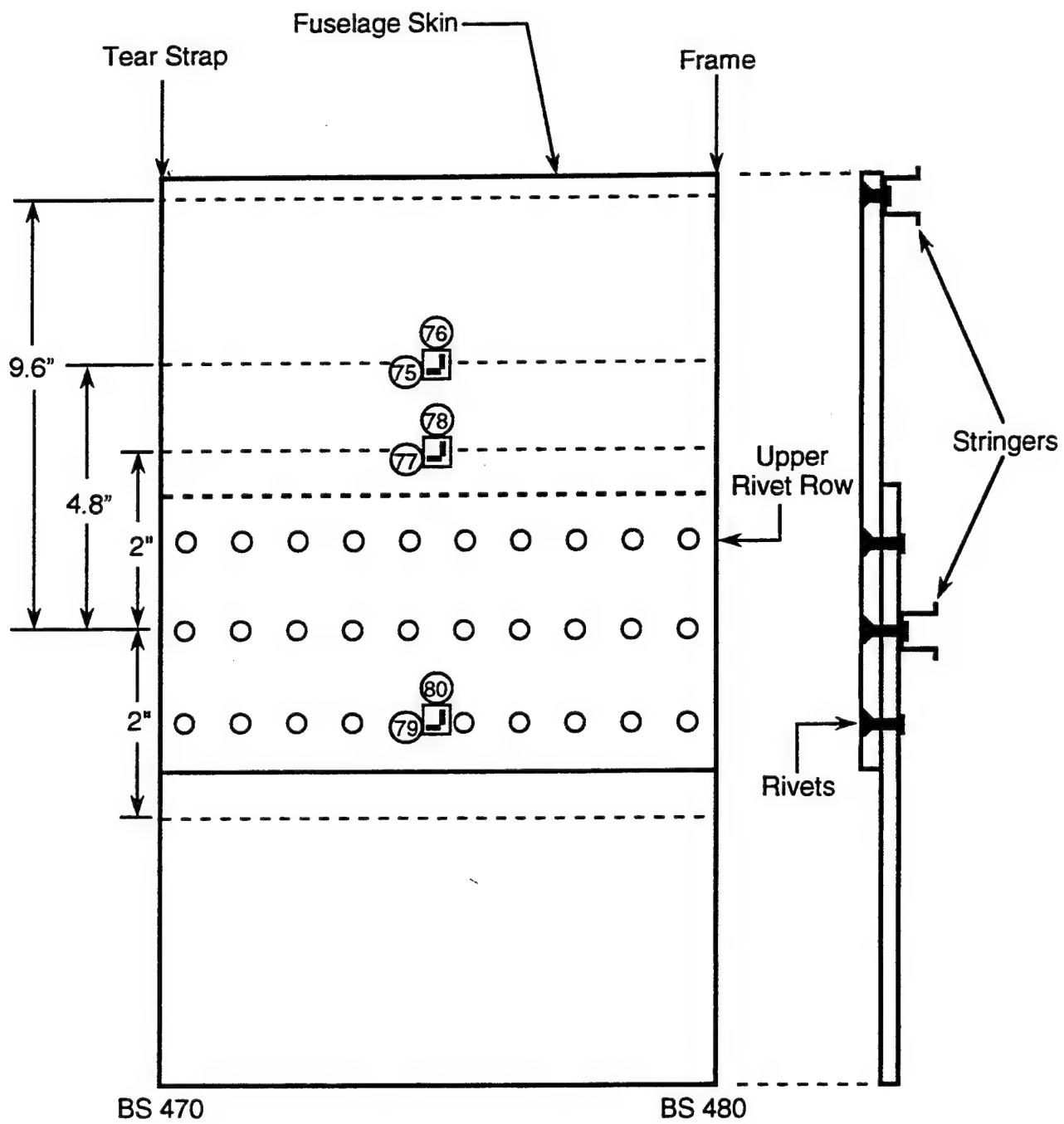


Figure A.8. Strain Gage Numbers for Lap Joint at Stringer S-10L;
Body Stations 470-480; Internal (6 Gages).

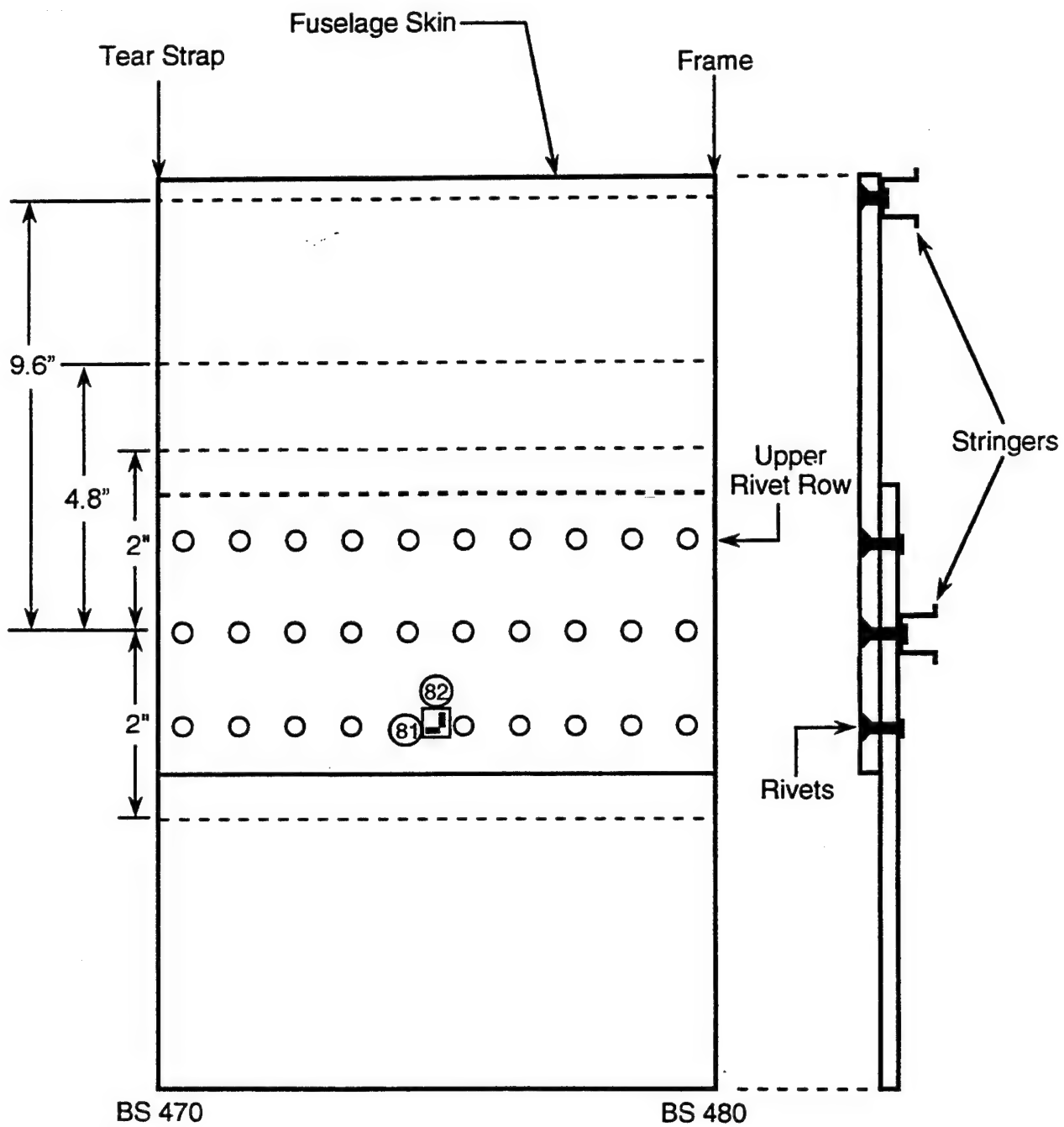
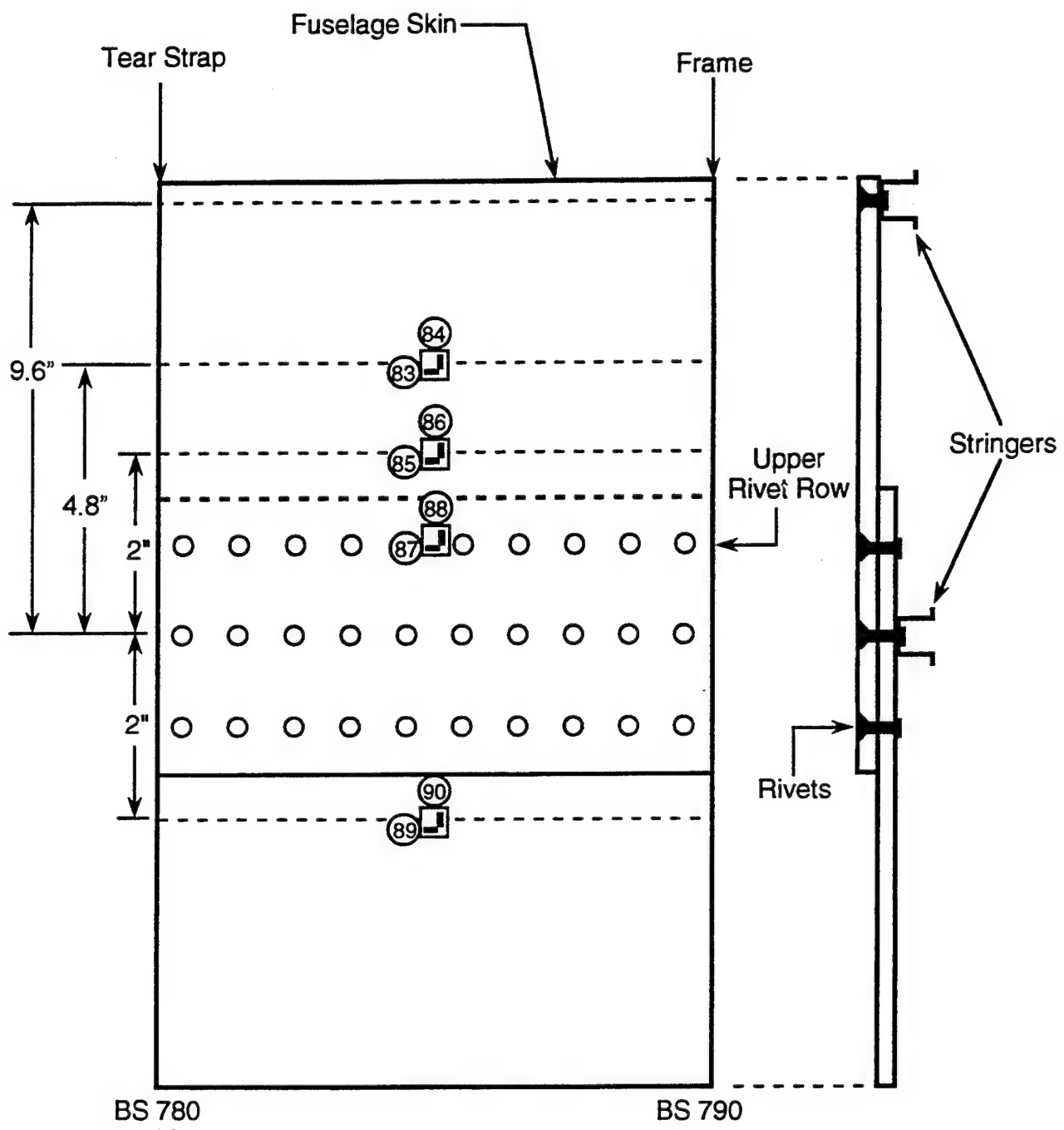


Figure A.9. Strain Gage Numbers for Lap Joint at Stringer S-14L;
Body Stations 470-480; Internal (2 Gages).



*Figure A.10. Strain Gage Numbers for Lap Joint at Stringer S-4L;
Body Stations 780-790; External (8 Gages).*

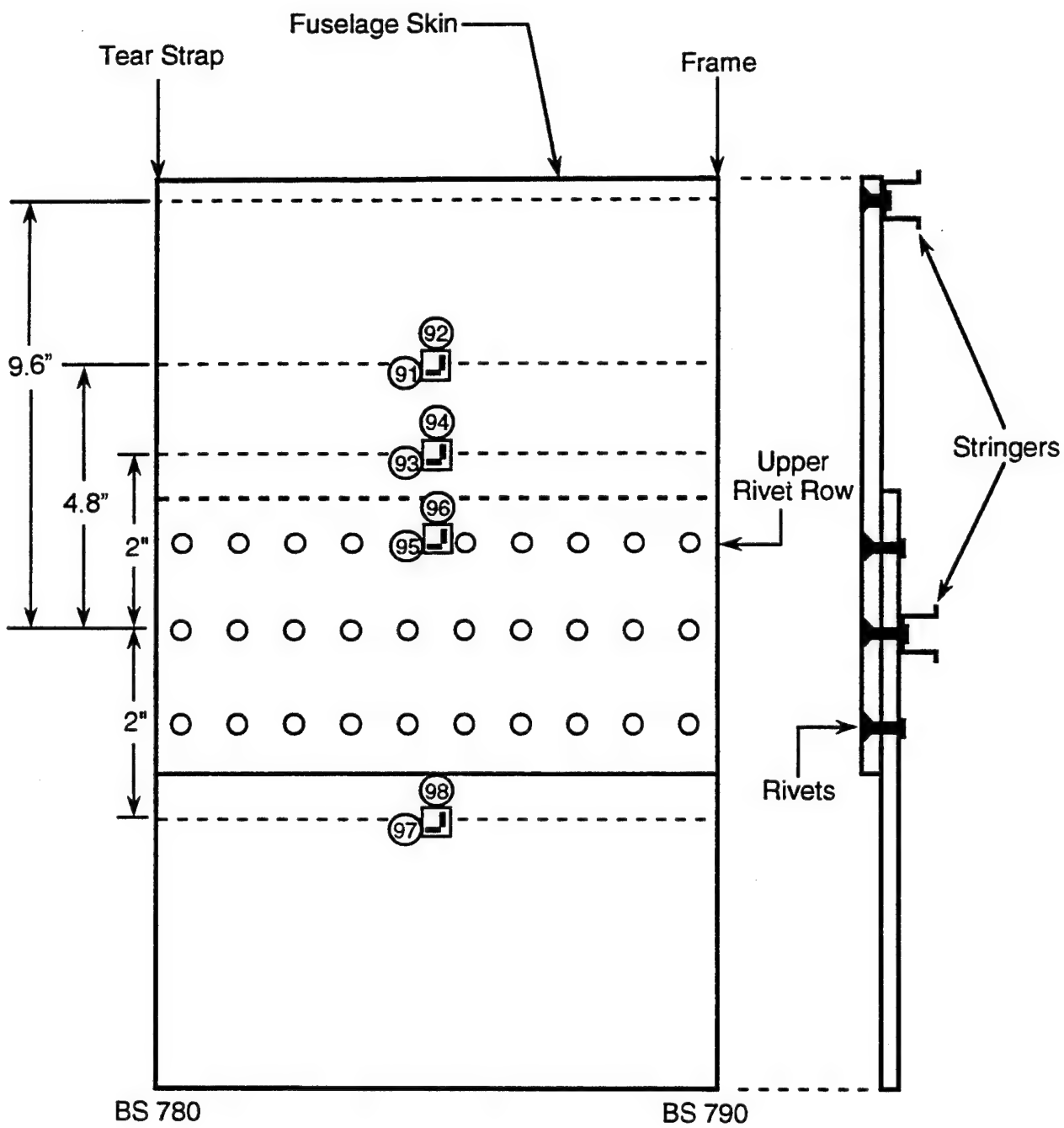


Figure A.11. Strain Gage Numbers for Lap Joint at Stringer S-10L;
Body Stations 470-480; Internal (8 Gages).

Channel	Description	Location
(00)	Thermal Load and Noise Monitoring Gage	Body Station 470 - Interior
(99)	Thermal Load and Noise Monitoring Gage	Body Station 780 - Exterior
(100)	Fuselage Internal Pressure Transducer	Aft Fuselage Aux Port
(101)	Fuselage Radial Growth Displacement	Body Station 470
(102)	Fuselage Radial Growth Displacement	Body Station 780
(103)	Thermocouple - Internal Air Temperature	Body Station 470
(104)	Thermocouple - External Fuselage Temp	Body Station 780

Figure A.12. Other Data Channels for Pressure Tests 1 and 2.

Channel	Description	Location
(00)	Hoop Strain in Fuselage Frame @ S-4L	Body Station 480 - Interior
(99)	Hoop Strain in Fuselage Frame @ S-10L	Body Station 480 - Interior
(100)	Fuselage Internal Pressure Transducer	Aft Fuselage Aux Port
(101)	Fuselage Radial Growth Displacement	Body Station 470
(102)	Fuselage Radial Growth Displacement	Body Station 780
(103)	Thermocouple - Internal Air Temperature	Body Station 470
(104)	Thermocouple - External Fuselage Temp	Body Station 780
(117)	Lateral Strain in Fuselage Frame @ S-4L	Body Station 480 - Interior
(118)	Lateral Strain in Fuselage Frame @ S-10L	Body Station 480 - Interior

Figure A.13. Other Data Channels for Pressure Tests 3 and 4.

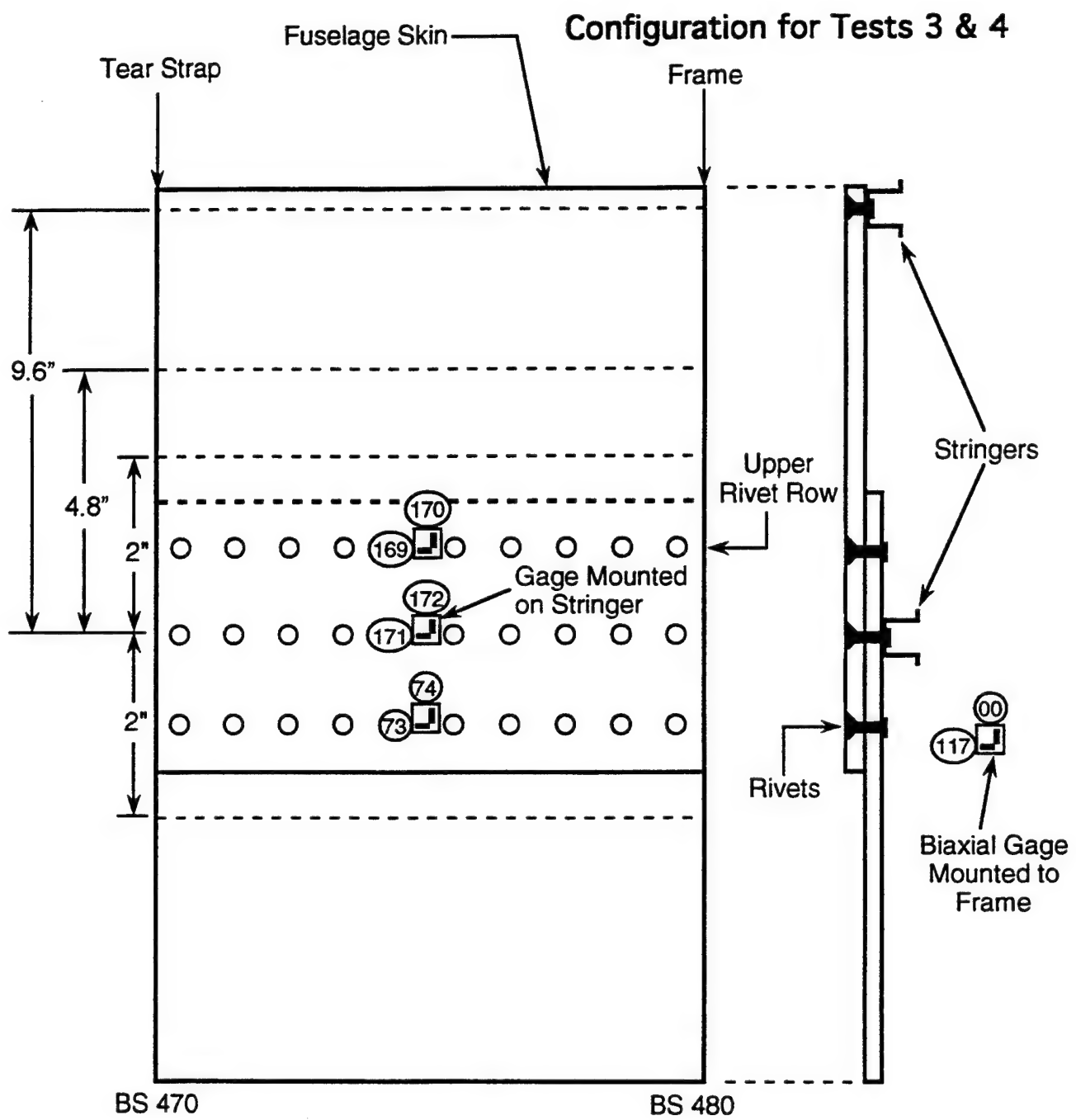


*Figure A.14. Strain Gage Numbers for Lap Joint Around Stringer S-4L;
Body Stations 470-480; Internal (6 Gages).*

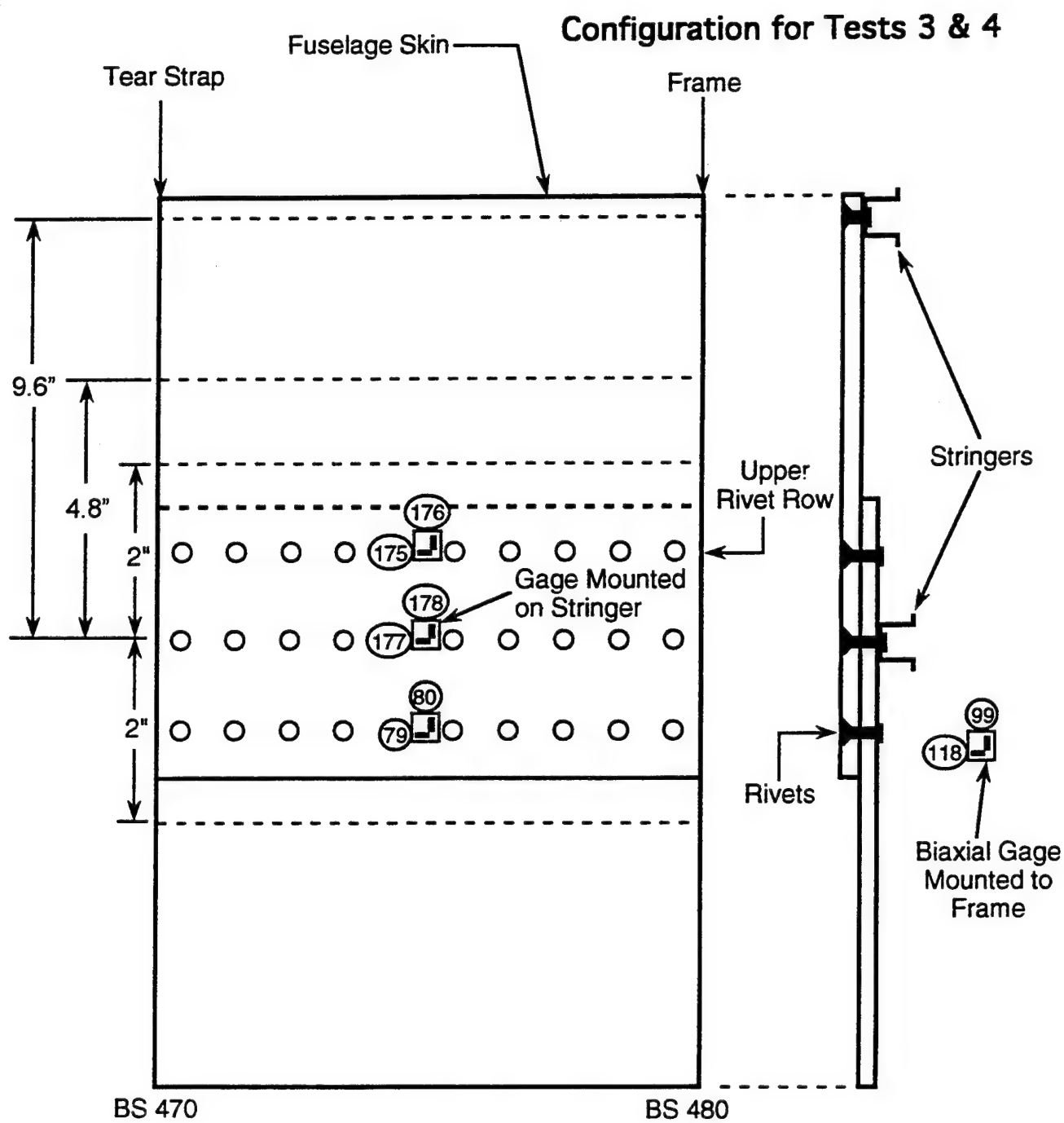


*Figure A.15. Strain Gage Numbers for Lap Joint Around Stringer S-10L;
Body Stations 470-480; Internal (6 Gages).*

APPENDIX B

TABLES OF MEASURED STRAIN DATA

	Pressure	Chan 0	Chan 1	Chan 2	Chan 3	Chan 4	Chan 5	Chan 6	Chan 7
1	0.04	0	-16	-2	1	3	-5	-6	0
2	1.06	2	-17	100	25	212	66	16	24
3	1.06	2	-17	101	25	214	67	16	25
4	1.50	3	3	165	84	306	89	19	53
5	1.57	3	3	167	88	310	89	20	53
6	2.08	2	54	225	74	367	137	38	101
7	2.50	6	101	285	84	430	170	60	151
8	3.01	6	151	350	113	497	189	67	203
9	3.52	6	202	415	137	562	218	80	255
10	4.03	5	253	480	160	626	242	90	310
11	4.54	4	299	531	182	681	263	98	356
12	5.05	3	357	598	204	745	279	105	414
13	5.51	4	409	653	218	798	295	112	462
14	6.02	4	467	716	243	858	320	120	514
15	6.53	4	524	780	259	921	361	141	577
16	5.05	5	363	640	201	743	278	94	419
17	5.00	5	363	639	200	742	278	94	418
18	4.03	5	255	523	156	614	236	68	301
19	3.01	5	143	398	104	475	184	52	194
20	3.03	6	142	396	104	474	183	52	193
21	2.06	4	72	284	67	349	137	31	100
22	2.06	5	73	284	68	350	138	31	100
23	1.04	4	-16	152	38	195	108	6	-13
24	0.53	4	-35	98	32	118	93	8	-48
25	0.53	4	-35	98	32	118	93	8	-48
26	0.02	5	-12	47	20	7	66	-3	-57

Strain Gage Measurements

	Pressure	Chan 8	Chan 9	Chan 10	Chan 11	Chan 12	Chan 13	Chan 14	Chan 15
1	0.04	-5	-10	-7	-3	-7	-2	12	3
2	1.06	131	32	167	50	52	76	87	115
3	1.06	133	32	170	50	51	77	88	118
4	1.50	189	47	233	39	67	133	115	154
5	1.57	191	49	233	36	67	136	113	155
6	2.08	272	71	309	62	88	175	138	213
7	2.50	346	84	373	64	111	224	145	258
8	3.01	414	101	434	54	130	280	139	297
9	3.52	482	113	496	52	149	334	151	340
10	4.03	554	126	562	52	172	385	169	385
11	4.54	610	137	614	53	191	428	190	422
12	5.05	679	144	679	54	213	484	217	471
13	5.51	736	144	734	58	234	528	246	517
14	6.02	799	152	793	58	259	579	270	557
15	6.53	871	169	861	55	284	636	279	602
16	5.05	728	149	683	26	199	509	179	473
17	5.00	727	149	682	26	198	509	179	473
18	4.03	594	121	553	30	165	404	157	398
19	3.01	461	99	423	33	119	297	117	308
20	3.03	461	99	422	33	118	296	116	307
21	2.06	332	80	305	28	71	204	67	213
22	2.06	330	80	305	28	70	204	67	213
23	1.04	185	53	170	27	43	98	52	123
24	0.53	126	52	111	12	19	62	13	72
25	0.53	126	52	111	12	18	63	14	72
26	0.02	61	39	29	-15	-9	28	-39	7

Strain Gage Measurements

	Pressure	Chan 16	Chan 17	Chan 18	Chan 19	Chan 20	Chan 21	Chan 22	Chan 23
1	0.04	-5	17	-4	#####	-8	8	-7	5
2	1.06	136	22	121	#####	73	-9	56	11
3	1.06	138	20	123	#####	75	-11	58	11
4	1.50	191	67	170	#####	127	-7	106	12
5	1.57	193	67	170	#####	127	-8	107	10
6	2.08	274	49	252	#####	191	-5	163	25
7	2.50	346	38	326	#####	267	-14	235	24
8	3.01	415	39	394	#####	340	-26	305	17
9	3.52	484	45	461	#####	413	-24	376	22
10	4.03	553	65	523	#####	484	-13	444	34
11	4.54	609	87	573	#####	541	-1	500	46
12	5.05	675	119	630	#####	607	22	564	66
13	5.51	729	146	681	#####	664	47	620	87
14	6.02	790	174	735	#####	727	66	682	103
15	6.53	861	170	813	#####	809	71	764	111
16	5.05	704	81	637	#####	610	-13	570	40
17	5.00	703	81	635	#####	609	-12	569	39
18	4.03	569	83	501	#####	464	-29	427	12
19	3.01	436	40	379	#####	327	-48	292	-9
20	3.03	436	39	377	#####	326	-47	290	-9
21	2.06	310	1	265	#####	207	-68	176	-30
22	2.06	309	2	265	#####	207	-68	177	-30
23	1.04	159	29	109	#####	78	-45	54	-31
24	0.53	100	-4	48	#####	43	-45	23	-36
25	0.53	100	-4	48	#####	43	-44	22	-35
26	0.02	30	-37	-14	#####	13	-33	6	-28

Strain Gage Measurements

	Pressure	Chan 24	Chan 25	Chan 26	Chan 27	Chan 28	Chan 29	Chan 30	Chan 31
1	0.04	-5	5	-5	5	-3	2	-6	-8
2	1.06	125	7	122	68	-39	64	239	174
3	1.06	127	7	124	69	-40	63	244	176
4	1.50	176	4	175	73	-45	83	323	252
5	1.57	177	2	176	70	-44	81	325	252
6	2.08	242	18	242	109	-62	116	408	329
7	2.50	317	14	314	115	-72	113	503	400
8	3.01	379	3	375	109	-77	111	586	471
9	3.52	442	6	438	118	-87	119	667	539
10	4.03	500	15	497	136	-96	138	740	608
11	4.54	550	24	546	153	-105	156	799	664
12	5.05	603	44	600	183	-118	186	866	737
13	5.51	650	64	647	210	-132	207	928	800
14	6.02	701	79	699	233	-143	228	993	866
15	6.53	771	86	769	248	-153	240	1071	933
16	5.05	605	16	601	145	-115	146	882	736
17	5.00	604	16	599	145	-115	145	881	735
18	4.03	484	-8	478	100	-89	108	733	599
19	3.01	367	-26	362	68	-68	84	575	456
20	3.03	367	-26	361	68	-68	84	574	455
21	2.06	257	-44	250	31	-46	37	436	326
22	2.06	257	-45	250	29	-45	35	436	325
23	1.04	123	-40	118	8	-22	25	235	163
24	0.53	75	-41	72	-12	-7	1	144	81
25	0.53	75	-41	70	-12	-7	0	144	82
26	0.02	7	-33	6	-37	7	-42	18	-36

Strain Gage Measurements

	Pressure	Chan 32	Chan 33	Chan 34	Chan 35	Chan 36	Chan 37	Chan 38	Chan 39
1	0.04	-4	-5	7	5	-4	2	-1	0
2	1.06	109	133	168	149	104	207	181	141
3	1.06	111	135	170	150	106	210	182	141
4	1.50	165	191	236	206	157	284	262	205
5	1.57	166	193	238	205	159	283	263	207
6	2.08	220	231	304	252	201	359	338	247
7	2.50	273	270	366	299	244	428	404	273
8	3.01	328	306	431	343	281	495	470	303
9	3.52	381	340	498	398	319	561	538	333
10	4.03	438	370	567	452	352	627	605	365
11	4.54	484	398	624	504	379	681	662	399
12	5.05	546	431	695	566	412	749	733	436
13	5.51	598	453	754	623	444	808	791	461
14	6.02	653	483	817	682	476	871	853	495
15	6.53	709	506	882	741	506	935	915	526
16	5.05	534	388	674	558	417	741	723	415
17	5.00	533	387	673	557	416	739	722	414
18	4.03	418	318	535	441	356	607	588	340
19	3.01	304	246	395	326	279	467	452	269
20	3.03	304	245	393	326	278	467	451	268
21	2.06	202	172	267	225	201	337	321	194
22	2.06	202	172	267	225	201	337	321	194
23	1.04	96	96	130	158	122	175	179	133
24	0.53	52	57	69	133	79	94	111	98
25	0.53	51	57	68	132	78	94	111	98
26	0.02	2	3	9	119	16	-9	21	44

	Pressure	Chan 40	Chan 41	Chan 42	Chan 43	Chan 44	Chan 45	Chan 46	Chan 47
1	0.04	7	6	0	-6	7	3	-2	3
2	1.06	170	43	107	108	54	147	161	-12
3	1.06	172	44	108	109	56	150	163	-12
4	1.50	243	59	153	165	71	198	236	1
5	1.57	244	58	154	166	70	196	237	0
6	2.08	309	74	200	215	86	255	307	13
7	2.50	363	94	238	260	108	322	373	42
8	3.01	424	111	271	305	131	385	439	73
9	3.52	489	126	308	351	147	444	506	94
10	4.03	556	139	346	402	162	493	570	115
11	4.54	615	150	379	446	171	533	626	132
12	5.05	689	156	417	500	177	574	696	146
13	5.51	748	161	445	546	183	613	752	153
14	6.02	816	169	478	595	189	656	815	167
15	6.53	884	181	507	641	206	707	876	190
16	5.05	679	165	396	490	184	593	694	162
17	5.00	678	164	395	489	184	593	693	161
18	4.03	537	149	327	390	159	494	566	129
19	3.01	396	132	257	290	136	393	435	101
20	3.03	395	131	255	289	135	392	433	101
21	2.06	264	107	179	196	109	296	308	68
22	2.06	264	107	179	196	108	294	308	68
23	1.04	131	70	94	99	74	188	175	33
24	0.53	68	51	52	50	69	146	111	29
25	0.53	67	51	51	50	68	145	110	28
26	0.02	-4	7	-20	-8	45	93	33	-16

Strain Gage Measurements

	Pressure	Chan 48	Chan 49	Chan 50	Chan 51	Chan 52	Chan 53	Chan 54	Chan 55
1	0.04	-4	5	-4	7	-2	5	-3	6
2	1.06	177	-7	69	-5	66	13	152	28
3	1.06	179	-6	70	-4	67	15	153	30
4	1.50	249	-7	112	1	110	14	224	43
5	1.57	250	-8	113	-1	111	13	226	41
6	2.08	324	-2	158	19	161	29	287	78
7	2.50	385	20	209	52	214	51	335	120
8	3.01	444	43	263	87	269	74	375	162
9	3.52	512	60	324	113	329	93	423	200
10	4.03	578	75	386	138	391	109	474	236
11	4.54	634	86	443	154	447	120	523	259
12	5.05	707	95	514	169	515	134	584	288
13	5.51	774	104	580	182	580	150	641	315
14	6.02	841	113	647	196	647	163	697	340
15	6.53	907	131	715	219	715	185	754	376
16	5.05	699	108	511	180	513	141	580	294
17	5.00	698	108	510	180	512	141	578	293
18	4.03	560	87	375	147	378	109	458	234
19	3.01	416	70	242	113	246	78	328	177
20	3.03	414	69	241	113	244	77	327	176
21	2.06	288	53	138	81	138	60	214	132
22	2.06	288	52	137	80	138	60	215	131
23	1.04	135	36	53	47	45	45	92	83
24	0.53	44	44	33	50	21	53	34	76
25	0.53	44	44	33	49	21	52	34	76
26	0.02	-60	47	51	50	37	62	-28	73

Strain Gage Measurements

	Pressure	Chan 56	Chan 57	Chan 58	Chan 59	Chan 60	Chan 61	Chan 62	Chan 63
1	0.04	-1	5	-5	-5	11	7	-7	32
2	1.06	153	4	44	-63	209	69	140	76
3	1.06	154	6	44	-63	209	71	142	77
4	1.50	220	3	57	-80	281	91	211	81
5	1.57	222	1	57	-81	283	90	212	81
6	2.08	283	15	47	-90	346	109	288	87
7	2.50	337	33	31	-89	398	156	352	127
8	3.01	390	53	17	-81	451	186	418	150
9	3.52	450	72	3	-77	513	217	485	176
10	4.03	509	92	-14	-68	575	230	559	180
11	4.54	562	107	-27	-63	631	240	623	183
12	5.05	627	130	-47	-56	701	252	703	185
13	5.51	688	152	-66	-53	767	272	772	196
14	6.02	750	171	-81	-47	835	291	841	208
15	6.53	813	203	-104	-35	906	317	911	228
16	5.05	640	152	-77	-56	698	277	700	213
17	5.00	638	152	-77	-56	697	277	698	213
18	4.03	520	110	-49	-75	558	243	553	196
19	3.01	393	64	-21	-87	417	205	406	173
20	3.03	392	63	-21	-87	414	204	404	174
21	2.06	273	24	3	-95	287	175	271	163
22	2.06	273	24	3	-96	287	175	271	163
23	1.04	139	-15	19	-88	153	133	122	137
24	0.53	69	-20	13	-68	82	110	54	119
25	0.53	69	-21	13	-69	81	110	53	119
26	0.02	-6	-11	-7	-33	-13	106	-24	124

Strain Gage Measurements

	Pressure	Chan 64	Chan 65	Chan 66	Chan 67	Chan 68	Chan 69	Chan 70	Chan 71
1	0.04	-14	36	-13	39	-13	8	-10	7
2	1.06	74	107	102	128	-81	8	175	4
3	1.06	76	108	105	129	-81	7	177	4
4	1.50	147	119	158	149	-98	31	223	0
5	1.57	148	119	159	148	-98	30	224	-2
6	2.08	226	135	220	172	-116	25	321	7
7	2.50	292	171	265	211	-139	15	403	-2
8	3.01	364	198	318	241	-156	11	474	-19
9	3.52	437	225	371	272	-175	16	546	-19
10	4.03	521	237	433	289	-188	33	612	-11
11	4.54	592	244	487	303	-199	50	664	-1
12	5.05	680	254	553	321	-213	78	726	20
13	5.51	755	268	613	342	-230	107	783	46
14	6.02	831	285	671	367	-245	132	840	63
15	6.53	909	307	729	394	-263	132	926	69
16	5.05	672	278	554	359	-258	34	725	-23
17	5.00	670	278	553	358	-258	34	724	-23
18	4.03	509	248	433	323	-243	41	580	-37
19	3.01	346	216	306	279	-221	4	448	-50
20	3.03	344	216	305	279	-221	3	447	-50
21	2.06	197	192	192	240	-198	-33	321	-71
22	2.06	196	192	192	241	-198	-32	321	-71
23	1.04	44	150	73	184	-163	7	167	-46
24	0.53	-12	128	14	150	-136	-11	112	-47
25	0.53	-12	128	14	150	-136	-11	112	-47
26	0.02	-71	129	-55	133	-104	-42	29	-47

Strain Gage Measurements

	Pressure	Chan 72	Chan 73	Chan 74	Chan 75	Chan 76	Chan 77	Chan 78	Chan 79
1	0.04	0	4	2	3	1	6	-2	-4
2	1.06	236	16	146	9	138	13	197	36
3	1.06	240	16	149	9	140	14	199	39
4	1.50	307	5	207	22	197	20	287	44
5	1.57	306	2	207	21	198	19	290	43
6	2.08	405	31	270	38	265	39	375	60
7	2.50	499	20	356	69	327	70	446	82
8	3.01	576	0	436	100	385	100	511	104
9	3.52	650	-4	509	122	452	126	581	117
10	4.03	718	2	575	144	514	150	648	127
11	4.54	771	8	630	162	569	164	707	128
12	5.05	830	27	688	174	640	176	780	131
13	5.51	887	47	746	182	708	188	847	136
14	6.02	943	60	804	195	772	199	913	137
15	6.53	1022	63	875	220	838	221	979	146
16	5.05	827	-7	704	190	633	185	772	147
17	5.00	825	-7	702	189	633	185	770	148
18	4.03	679	-31	566	155	500	154	632	141
19	3.01	543	-33	427	127	363	123	481	134
20	3.03	541	-33	426	127	362	123	480	134
21	2.06	405	-50	307	89	245	89	339	127
22	2.06	405	-51	306	88	245	89	339	127
23	1.04	203	-41	145	47	127	49	161	88
24	0.53	110	-39	73	40	76	45	53	73
25	0.53	109	-39	73	39	77	45	52	73
26	0.02	-21	-42	-2	0	55	31	-90	48

Strain Gage Measurements

	Pressure	Chan 80	Chan 81	Chan 82	Chan 83	Chan 84	Chan 85	Chan 86	Chan 87
1	0.04	7	56	-17	-2	-1	0	5	0
2	1.06	143	172	143	60	190	25	142	50
3	1.06	144	174	145	57	194	22	147	49
4	1.50	209	191	217	84	260	49	204	79
5	1.57	211	191	219	82	261	48	207	79
6	2.08	274	215	295	87	343	59	281	102
7	2.50	328	261	356	69	431	47	364	100
8	3.01	386	298	417	91	504	68	439	120
9	3.52	454	335	476	98	580	74	514	133
10	4.03	523	351	543	122	647	100	578	159
11	4.54	583	360	598	139	705	113	643	172
12	5.05	660	372	664	183	763	155	699	218
13	5.51	730	392	722	210	818	187	754	254
14	6.02	804	414	776	233	880	213	811	280
15	6.53	879	444	830	247	956	221	889	291
16	5.05	651	403	671	155	777	116	705	176
17	5.00	649	404	669	155	775	114	704	176
18	4.03	494	361	559	127	633	107	559	149
19	3.01	336	313	440	100	484	85	416	113
20	3.03	334	313	438	99	482	82	412	112
21	2.06	193	278	317	51	354	43	285	71
22	2.06	193	279	317	50	353	44	283	71
23	1.04	57	217	176	48	176	37	127	45
24	0.53	3	180	101	27	94	23	68	23
25	0.53	3	180	100	26	93	22	67	22
26	0.02	-52	167	0	-18	-17	-14	1	-16

	Pressure	Chan 88	Chan 89	Chan 90	Chan 91	Chan 92	Chan 93	Chan 94	Chan 95
1	0.04	7	4	10	10	-10	2	3	-5
2	1.06	141	18	199	39	182	-7	61	16
3	1.06	146	15	202	39	186	-7	61	18
4	1.50	214	56	267	58	257	-8	103	14
5	1.57	215	56	268	60	258	-7	105	15
6	2.08	299	72	344	80	334	5	152	32
7	2.50	386	58	426	109	400	20	198	60
8	3.01	473	70	499	131	470	43	249	87
9	3.52	552	85	569	176	532	71	304	108
10	4.03	620	102	634	178	606	78	364	125
11	4.54	695	122	694	207	661	95	417	138
12	5.05	749	171	749	204	741	90	486	149
13	5.51	795	200	799	193	815	79	551	153
14	6.02	849	222	856	191	887	76	618	158
15	6.53	925	223	933	228	953	84	687	169
16	5.05	753	112	759	189	745	40	493	107
17	5.00	751	110	758	187	743	40	491	105
18	4.03	607	102	616	139	607	30	362	79
19	3.01	460	81	475	105	466	4	246	42
20	3.03	458	80	473	105	463	3	245	41
21	2.06	321	44	350	77	327	-1	141	21
22	2.06	319	44	349	76	327	-3	140	21
23	1.04	146	51	183	37	166	-14	54	-8
24	0.53	88	38	112	33	77	4	20	-4
25	0.53	88	37	111	32	78	6	20	-3
26	0.02	8	-11	9	18	-29	13	-7	-6

	Pressure	Chan 96	Chan 97	Chan 98	Chan 99	Chan 101	Chan 102
1	0.04	2	-1	-1	-2	-2.03E-04	2.03E-04
2	1.06	203	49	179	-8	-4.07E-04	1.42E-03
3	1.06	197	51	180	-7	-4.07E-04	1.42E-03
4	1.50	300	62	252	-5	-5.09E-03	0.00E+00
5	1.57	301	60	253	-7	-5.49E-03	0.00E+00
6	2.08	395	75	318	-3	-8.95E-03	-8.14E-04
7	2.50	463	121	368	-8	-1.18E-02	-5.09E-03
8	3.01	545	153	424	-10	-1.44E-02	-7.12E-03
9	3.52	624	176	476	-12	-1.75E-02	-7.53E-03
10	4.03	702	204	537	-6	-2.16E-02	-1.06E-02
11	4.54	767	217	581	-2	-2.50E-02	-1.28E-02
12	5.05	840	227	647	-1	-2.95E-02	-1.67E-02
13	5.51	904	233	704	2	-3.28E-02	-2.01E-02
14	6.02	972	239	761	4	-3.60E-02	-2.12E-02
15	6.53	1039	248	819	2	-3.87E-02	-2.32E-02
16	5.05	820	188	648	1	-3.54E-02	-2.30E-02
17	5.00	818	188	648	1	-3.54E-02	-2.30E-02
18	4.03	666	173	530	2	-2.97E-02	-2.10E-02
19	3.01	513	134	417	3	-2.32E-02	-1.73E-02
20	3.03	511	133	415	4	-2.30E-02	-1.71E-02
21	2.06	359	104	303	0	-1.55E-02	-1.42E-02
22	2.06	358	104	301	0	-1.53E-02	-1.42E-02
23	1.04	193	59	169	-1	-1.10E-02	-1.10E-02
24	0.53	109	53	97	-1	-8.14E-03	-8.95E-03
25	0.53	107	53	97	0	-8.14E-03	-8.95E-03
26	0.02	-13	21	-18	0	-2.44E-03	-4.88E-03

	Pressure	Chan 0	Chan 1	Chan 2	Chan 3	Chan 4	Chan 5	Chan 6	Chan 7
1	0.02	-1	5	0	-7	-1	-2	4	-5
2	1.04	1	18	92	21	200	46	22	42
3	1.57	0	52	149	37	280	74	31	84
4	2.01	0	92	206	54	349	107	44	128
5	2.52	0	138	265	75	411	154	72	171
6	3.03	0	184	324	98	484	185	84	228
7	3.54	1	237	391	124	551	203	89	283
8	4.05	1	289	455	144	615	221	94	337
9	4.56	1	335	508	165	670	240	100	386
10	5.00	1	380	561	195	731	263	111	431
11	5.52	1	437	625	217	788	283	119	485
12	6.04	2	484	674	243	842	310	130	538
13	6.53	2	547	743	256	902	334	133	597
14	6.53	1	550	747	258	905	335	133	599
15	6.02	2	493	689	220	837	300	120	541
16	5.52	1	442	644	196	781	279	113	491
17	5.00	2	385	589	171	719	249	102	435
18	4.49	2	325	530	146	652	220	91	377
19	4.05	1	274	475	126	591	187	81	323
20	3.54	1	218	416	105	524	157	68	268
21	3.01	0	171	361	84	463	134	62	217
22	2.52	0	126	305	72	401	122	62	169
23	1.99	1	85	256	65	343	113	64	123
24	1.48	0	48	201	57	277	107	65	77
25	1.04	0	15	148	53	212	108	68	31
26	0.55	-1	-3	82	39	120	103	63	-20
27	0.02	1	-15	26	56	35	96	53	-48
28	0.02	1	-14	26	58	36	95	53	-51

	Pressure	Chan 8	Chan 9	Chan 10	Chan 11	Chan 12	Chan 13	Chan 14	Chan 15
1	0.02	3	-2	2	0	-2	-1	-7	2
2	1.04	123	43	163	46	43	77	48	97
3	1.57	190	59	235	55	64	122	73	146
4	2.01	261	80	302	58	83	169	91	193
5	2.52	335	112	370	55	98	221	96	234
6	3.03	413	129	440	61	120	268	120	292
7	3.54	481	135	503	55	138	321	139	336
8	4.05	544	137	562	55	160	372	163	380
9	4.56	601	142	615	57	181	415	183	419
10	5.00	657	149	669	63	214	462	209	462
11	5.52	721	159	726	53	228	515	226	502
12	6.04	779	169	783	62	254	560	261	553
13	6.53	847	173	847	59	266	615	279	590
14	6.53	848	173	849	59	267	618	279	592
15	6.02	798	150	781	59	245	565	265	554
16	5.52	750	140	725	53	226	524	243	520
17	5.00	693	124	661	52	206	476	224	480
18	4.49	625	108	595	52	183	424	207	436
19	4.05	560	96	535	50	160	376	191	393
20	3.54	492	81	469	49	136	322	171	347
21	3.01	428	68	407	46	115	276	150	305
22	2.52	364	67	348	37	89	231	119	262
23	1.99	308	66	292	27	64	192	89	220
24	1.48	245	67	234	15	38	151	53	171
25	1.04	189	78	182	-1	10	116	14	126
26	0.55	126	86	122	-18	-18	72	-34	61
27	0.02	49	75	44	-55	-46	40	-93	-12
28	0.02	49	79	46	-58	-47	41	-96	-17

	Pressure	Chan 16	Chan 17	Chan 18	Chan 19	Chan 20	Chan 21	Chan 22	Chan 23
1	0.02	0	-30	0	-7	1	-9	-2	-2
2	1.04	133	-10	145	-33	77	-39	59	-14
3	1.57	201	0	217	-32	135	-40	112	-10
4	2.01	269	9	285	-29	198	-42	170	-8
5	2.52	345	11	353	-37	273	-49	239	-17
6	3.03	420	27	425	-23	344	-37	306	-5
7	3.54	486	39	490	-11	411	-29	371	7
8	4.05	548	60	552	6	477	-14	435	23
9	4.56	605	82	605	22	538	2	494	35
10	5.00	655	126	648	49	593	22	554	47
11	5.52	716	142	707	60	656	34	614	60
12	6.04	773	185	755	95	713	67	670	77
13	6.53	838	189	823	108	783	80	735	97
14	6.53	839	189	826	107	786	81	738	97
15	6.02	782	162	766	95	714	69	669	90
16	5.52	730	133	715	73	657	47	612	73
17	5.00	670	113	653	56	588	32	544	60
18	4.49	605	97	587	42	516	19	474	48
19	4.05	542	84	526	29	450	7	409	36
20	3.54	474	73	456	15	379	-5	339	24
21	3.01	409	50	397	1	313	-18	277	14
22	2.52	348	20	340	-21	255	-37	221	-5
23	1.99	291	-7	284	-42	204	-55	173	-22
24	1.48	230	-35	221	-62	153	-72	126	-39
25	1.04	174	-63	158	-79	113	-86	89	-56
26	0.55	109	-94	82	-92	76	-95	56	-71
27	0.02	32	-127	-13	-89	59	-90	49	-79
28	0.02	33	-130	-12	-92	59	-94	48	-82

	Pressure	Chan 24	Chan 25	Chan 26	Chan 27	Chan 28	Chan 29	Chan 30	Chan 31
1	0.02	1	-2	3	3	-4	-2	1	1
2	1.04	131	-14	128	42	-30	44	235	185
3	1.57	193	-11	192	58	-43	62	332	262
4	2.01	255	-10	252	69	-51	73	419	332
5	2.52	328	-18	323	74	-55	89	503	397
6	3.03	391	-6	384	94	-68	105	585	469
7	3.54	445	4	439	113	-80	117	661	535
8	4.05	497	19	496	135	-94	136	732	600
9	4.56	548	30	544	153	-104	155	795	660
10	5.00	593	41	599	168	-112	175	854	721
11	5.52	645	53	648	193	-123	203	915	786
12	6.04	694	72	699	220	-134	234	971	847
13	6.53	744	93	747	255	-151	260	1040	917
14	6.53	746	94	748	255	-151	260	1044	920
15	6.02	689	87	690	240	-145	242	972	850
16	5.52	645	70	645	211	-134	213	916	789
17	5.00	589	58	588	190	-124	192	847	722
18	4.49	531	45	527	168	-113	171	772	652
19	4.05	477	33	473	149	-101	155	703	590
20	3.54	418	21	411	126	-90	134	627	520
21	3.01	363	10	358	107	-79	114	555	455
22	2.52	315	-7	311	80	-63	85	487	385
23	1.99	272	-25	267	52	-48	56	422	316
24	1.48	225	-42	220	27	-32	30	349	242
25	1.04	183	-58	177	-1	-13	3	276	167
26	0.55	127	-71	119	-30	6	-20	180	79
27	0.02	60	-79	60	-73	32	-69	70	-27
28	0.02	61	-82	60	-77	33	-73	69	-26

Strain Gage Measurements

	Pressure	Chan 32	Chan 33	Chan 34	Chan 35	Chan 36	Chan 37	Chan 38	Chan 39
1	0.02	-1	-4	-3	-6	2	0	-1	-4
2	1.04	97	120	152	34	100	185	166	118
3	1.57	151	166	225	72	148	263	240	158
4	2.01	202	205	290	117	190	331	310	200
5	2.52	253	242	353	170	229	393	378	245
6	3.03	312	284	425	226	262	465	458	290
7	3.54	368	319	491	279	297	529	526	325
8	4.05	423	348	555	335	329	592	590	351
9	4.56	475	380	615	393	364	650	650	385
10	5.00	529	414	677	452	398	709	712	419
11	5.52	585	447	741	511	430	769	774	453
12	6.04	640	481	804	573	462	831	839	496
13	6.53	700	509	873	630	493	896	903	527
14	6.53	702	511	875	633	494	898	906	527
15	6.02	640	467	804	570	463	829	834	479
16	5.52	585	433	739	513	432	768	771	439
17	5.00	526	396	670	454	401	704	704	400
18	4.49	466	359	598	393	367	635	635	361
19	4.05	412	326	533	343	336	574	573	328
20	3.54	352	283	460	285	299	506	504	291
21	3.01	297	239	388	227	258	440	434	246
22	2.52	239	206	324	158	215	374	361	197
23	1.99	193	183	265	95	216	305	291	169
24	1.48	140	142	199	100	195	226	232	156
25	1.04	91	103	133	103	163	146	173	138
26	0.55	39	54	60	96	122	47	103	106
27	0.02	-13	2	-12	97	72	-67	28	64
28	0.02	-14	1	-13	95	72	-68	28	63

	Pressure	Chan 40	Chan 41	Chan 42	Chan 43	Chan 44	Chan 45	Chan 46	Chan 47
1	0.02	-8	-1	0	-7	-1	-5	-1	-5
2	1.04	156	53	111	97	37	103	147	44
3	1.57	226	76	161	146	60	157	215	61
4	2.01	289	92	204	193	77	207	281	80
5	2.52	356	111	250	239	101	264	349	111
6	3.03	425	129	293	290	113	315	423	133
7	3.54	492	136	328	341	121	363	491	148
8	4.05	556	146	361	388	133	413	553	158
9	4.56	616	154	395	434	143	460	612	173
10	5.00	681	158	424	482	146	498	673	179
11	5.52	747	162	456	533	150	536	735	190
12	6.04	816	168	493	582	158	579	799	207
13	6.53	885	176	525	632	167	625	862	221
14	6.53	888	177	527	634	169	626	864	223
15	6.02	810	168	489	582	158	582	797	205
16	5.52	744	163	455	536	153	547	738	198
17	5.00	672	154	417	485	141	502	675	180
18	4.49	598	149	383	434	132	456	607	167
19	4.05	535	146	353	387	124	413	549	157
20	3.54	464	143	321	334	115	363	480	145
21	3.01	391	135	285	283	107	317	415	134
22	2.52	317	137	240	227	104	273	342	133
23	1.99	254	133	186	174	122	280	283	149
24	1.48	189	122	150	122	122	266	233	140
25	1.04	123	106	113	77	110	224	179	118
26	0.55	49	89	79	23	99	169	113	95
27	0.02	-31	69	36	-36	91	117	42	59
28	0.02	-33	73	40	-37	95	116	41	63

	Pressure	Chan 48	Chan 49	Chan 50	Chan 51	Chan 52	Chan 53	Chan 54	Chan 55
1	0.02	-1	0	-3	-1	-3	3	-1	4
2	1.04	190	-11	17	-4	18	2	140	17
3	1.57	266	-3	53	13	59	10	208	40
4	2.01	334	7	96	31	104	16	273	61
5	2.52	393	20	143	54	153	26	333	87
6	3.03	463	38	199	83	211	40	393	118
7	3.54	531	47	260	99	272	48	451	142
8	4.05	602	59	323	117	333	63	505	175
9	4.56	664	69	383	134	392	73	560	198
10	5.00	730	73	447	142	453	81	614	219
11	5.52	796	79	512	153	517	92	669	243
12	6.04	860	86	579	162	583	102	727	263
13	6.53	929	100	647	183	649	125	781	299
14	6.53	932	101	649	184	652	127	783	301
15	6.02	863	90	579	168	583	110	725	273
16	5.52	797	84	513	158	519	98	667	250
17	5.00	730	73	446	142	451	80	606	220
18	4.49	657	63	375	126	382	62	542	189
19	4.05	592	57	311	115	321	50	484	165
20	3.54	516	50	242	103	252	35	417	140
21	3.01	447	45	179	92	190	27	352	119
22	2.52	370	47	115	88	127	24	281	105
23	1.99	282	63	60	100	75	27	236	91
24	1.48	196	58	13	90	26	20	182	72
25	1.04	113	50	-20	78	-11	15	131	53
26	0.55	5	51	-39	78	-34	23	74	47
27	0.02	-150	67	-13	96	-11	44	21	60
28	0.02	-154	71	-16	100	-12	47	20	64

Strain Gage Measurements

	Pressure	Chan 56	Chan 57	Chan 58	Chan 59	Chan 60	Chan 61	Chan 62	Chan 63
1	0.02	-1	3	-4	-2	-5	-9	1	-8
2	1.04	138	9	20	-40	187	8	148	-10
3	1.57	205	22	19	-47	258	20	225	-7
4	2.01	267	38	13	-50	321	36	296	-1
5	2.52	327	59	6	-40	379	56	366	12
6	3.03	389	86	-7	-30	442	76	443	24
7	3.54	452	102	-19	-29	508	100	512	41
8	4.05	511	126	-33	-20	570	113	585	47
9	4.56	569	144	-44	-13	632	130	652	61
10	5.00	628	157	-52	-12	696	143	718	66
11	5.52	687	174	-63	-8	761	160	785	74
12	6.04	747	192	-73	-1	827	176	854	82
13	6.53	808	219	-89	11	896	189	928	88
14	6.53	810	220	-90	12	899	191	930	90
15	6.02	752	202	-82	0	827	171	856	80
16	5.52	697	187	-74	-2	758	164	784	82
17	5.00	637	167	-62	-12	687	151	713	87
18	4.49	576	144	-48	-20	616	149	641	96
19	4.05	518	125	-36	-24	551	143	571	96
20	3.54	453	104	-22	-32	480	128	494	90
21	3.01	389	87	-12	-35	410	113	420	83
22	2.52	318	69	3	-28	331	101	344	82
23	1.99	272	62	15	-23	257	90	273	80
24	1.48	210	43	26	-31	187	78	201	78
25	1.04	148	23	29	-36	119	64	133	73
26	0.55	73	14	21	-28	35	42	60	60
27	0.02	-3	22	3	-5	-73	29	-15	55
28	0.02	-5	25	2	-1	-76	28	-15	54

	Pressure	Chan 64	Chan 65	Chan 66	Chan 67	Chan 68	Chan 69	Chan 70	Chan 71
1	0.02	-1	-2	-1	-4	-2	-18	16	-1
2	1.04	120	4	124	28	-44	-25	174	-19
3	1.57	193	20	184	52	-58	-20	250	-20
4	2.01	266	36	243	74	-67	-16	322	-22
5	2.52	339	54	300	100	-74	-18	396	-33
6	3.03	420	73	366	124	-83	-2	475	-22
7	3.54	496	91	424	150	-89	7	544	-15
8	4.05	576	110	486	172	-100	26	607	-2
9	4.56	647	127	543	192	-108	44	664	11
10	5.00	721	140	597	210	-117	86	713	33
11	5.52	795	153	655	227	-126	100	772	44
12	6.04	873	164	715	242	-132	140	825	76
13	6.53	953	180	778	262	-142	144	895	86
14	6.53	956	182	780	263	-142	143	898	86
15	6.02	875	168	720	247	-141	118	834	76
16	5.52	797	164	661	247	-140	93	782	56
17	5.00	715	163	610	247	-140	76	715	43
18	4.49	629	158	556	236	-137	60	646	30
19	4.05	551	150	504	225	-131	47	579	20
20	3.54	462	137	441	208	-126	36	505	7
21	3.01	383	124	380	191	-118	19	444	-2
22	2.52	298	113	316	175	-109	-7	387	-20
23	1.99	222	104	256	158	-100	-27	331	-35
24	1.48	144	92	197	139	-87	-48	272	-52
25	1.04	73	76	143	116	-69	-67	216	-67
26	0.55	8	59	83	86	-43	-84	148	-79
27	0.02	-45	47	17	57	-6	-83	82	-82
28	0.02	-45	47	17	56	-6	-87	83	-85

	Pressure	Chan 72	Chan 73	Chan 74	Chan 75	Chan 76	Chan 77	Chan 78	Chan 79
1	0.02	7	7	-7	2	-1	2	1	5
2	1.04	256	-1	157	39	86	18	244	39
3	1.57	353	-1	233	60	146	39	339	58
4	2.01	436	-3	302	82	205	60	420	70
5	2.52	521	-9	370	114	263	83	492	83
6	3.03	603	-5	444	135	327	109	568	97
7	3.54	673	1	513	152	393	124	643	102
8	4.05	739	12	580	163	461	142	713	112
9	4.56	797	20	639	180	523	159	779	117
10	5.00	847	25	691	186	587	166	845	116
11	5.52	904	42	747	197	651	175	912	117
12	6.04	957	62	801	216	716	184	978	116
13	6.53	1021	87	862	229	783	202	1045	125
14	6.53	1024	87	865	230	786	204	1047	126
15	6.02	961	84	800	213	719	190	980	123
16	5.52	908	65	747	206	656	180	914	125
17	5.00	843	53	684	186	589	166	845	122
18	4.49	774	42	617	174	519	151	771	118
19	4.05	709	33	554	163	456	140	704	118
20	3.54	634	22	485	151	385	128	626	117
21	3.01	568	17	419	138	318	119	550	118
22	2.52	505	0	355	132	242	113	462	127
23	1.99	440	-14	294	153	185	127	395	147
24	1.48	365	-28	226	149	140	117	312	140
25	1.04	281	-44	156	127	92	100	220	127
26	0.55	168	-55	78	112	47	90	95	113
27	0.02	14	-68	-18	106	36	96	-81	105
28	0.02	15	-70	-19	111	33	101	-85	109

Strain Gage Measurements

	Pressure	Chan 80	Chan 81	Chan 82	Chan 83	Chan 84	Chan 85	Chan 86	Chan 87
1	0.02	1	0	0	-14	1	-7	6	-5
2	1.04	132	36	166	41	197	21	145	51
3	1.57	195	64	238	52	284	29	219	72
4	2.01	258	88	302	82	353	33	290	82
5	2.52	314	115	359	65	438	31	368	89
6	3.03	384	140	420	69	520	36	443	106
7	3.54	455	166	473	81	594	53	516	128
8	4.05	526	190	529	93	663	68	580	150
9	4.56	593	210	580	143	710	104	633	176
10	5.00	662	230	629	181	766	141	688	207
11	5.52	734	247	678	215	821	174	748	238
12	6.04	807	260	731	246	883	205	811	270
13	6.53	882	282	784	266	946	224	873	292
14	6.53	885	283	785	265	950	226	875	293
15	6.02	809	266	732	246	882	209	807	272
16	5.52	738	266	679	215	828	183	749	242
17	5.00	661	266	628	192	761	163	681	218
18	4.49	582	253	572	176	687	146	607	193
19	4.05	510	240	520	173	612	138	535	179
20	3.54	429	222	460	152	540	118	464	154
21	3.01	353	204	400	131	473	101	395	134
22	2.52	267	189	335	103	406	78	331	108
23	1.99	191	175	273	74	343	55	273	82
24	1.48	115	157	203	42	276	13	214	46
25	1.04	49	135	133	7	207	-14	153	13
26	0.55	-19	103	50	-28	120	-40	88	-19
27	0.02	-88	77	-49	-68	7	-60	29	-46
28	0.02	-91	77	-49	-69	8	-61	30	-47

	Pressure	Chan 88	Chan 89	Chan 90	Chan 91	Chan 92	Chan 93	Chan 94	Chan 95
1	0.02	5	-8	2	-4	2	0	-1	3
2	1.04	159	33	186	41	189	-4	55	14
3	1.57	243	42	266	59	273	-2	99	23
4	2.01	318	30	345	92	339	7	144	29
5	2.52	405	43	420	107	411	-10	202	29
6	3.03	480	60	490	131	484	24	251	59
7	3.54	546	73	557	142	558	25	312	77
8	4.05	606	89	619	166	625	53	362	101
9	4.56	662	113	672	171	691	55	420	115
10	5.00	721	142	727	196	753	73	477	131
11	5.52	779	173	783	195	821	70	540	144
12	6.04	841	209	843	222	889	88	608	159
13	6.53	900	232	902	224	959	87	670	176
14	6.53	903	233	905	225	962	93	672	179
15	6.02	841	211	838	202	894	76	607	159
16	5.52	792	185	784	188	832	68	545	143
17	5.00	726	162	719	180	758	60	478	125
18	4.49	653	143	649	154	688	44	414	108
19	4.05	580	140	582	140	622	37	355	94
20	3.54	508	124	512	125	546	27	291	81
21	3.01	441	105	447	111	475	21	233	68
22	2.52	375	79	386	104	401	21	176	58
23	1.99	314	60	324	101	327	21	127	47
24	1.48	245	28	262	87	249	24	77	38
25	1.04	177	0	198	86	166	19	43	24
26	0.55	110	-20	120	73	70	24	11	16
27	0.02	27	-41	17	46	-36	42	-10	26
28	0.02	29	-41	19	54	-42	47	-12	31

	Pressure	Chan 96	Chan 97	Chan 98	Chan 99	Chan 101	Chan 102
1	0.02	-5	0	-3	-2	-8.14E-04	0.00E+00
2	1.04	193	39	178	-11	-3.26E-03	4.07E-04
3	1.57	292	58	250	-8	-5.49E-03	4.07E-04
4	2.01	385	62	316	-7	-7.93E-03	4.07E-04
5	2.52	458	76	373	-8	-1.12E-02	-6.10E-04
6	3.03	543	110	432	-9	-1.44E-02	-2.03E-03
7	3.54	611	134	484	-13	-1.73E-02	-3.87E-03
8	4.05	690	155	540	-10	-2.01E-02	-7.32E-03
9	4.56	758	171	593	-7	-2.38E-02	-9.56E-03
10	5.00	827	180	647	-7	-2.75E-02	-1.22E-02
11	5.52	889	198	700	-7	-3.13E-02	-1.46E-02
12	6.04	967	212	760	-14	-3.44E-02	-1.69E-02
13	6.53	1023	229	814	-9	-3.70E-02	-1.85E-02
14	6.53	1026	230	816	-10	-3.72E-02	-1.89E-02
15	6.02	955	217	755	-7	-3.74E-02	-1.93E-02
16	5.52	888	202	701	-8	-3.64E-02	-1.93E-02
17	5.00	812	180	644	-15	-3.40E-02	-1.93E-02
18	4.49	735	171	582	-18	-3.09E-02	-1.91E-02
19	4.05	668	161	530	-20	-2.81E-02	-1.85E-02
20	3.54	582	150	467	-22	-2.44E-02	-1.73E-02
21	3.01	504	130	410	-23	-2.16E-02	-1.53E-02
22	2.52	425	114	353	-23	-1.73E-02	-1.14E-02
23	1.99	350	96	297	-26	-1.30E-02	-9.36E-03
24	1.48	271	81	235	-25	-1.04E-02	-8.14E-03
25	1.04	188	62	172	-29	-6.31E-03	-5.09E-03
26	0.55	92	42	93	-31	-4.07E-03	-2.64E-03
27	0.02	-15	48	-23	-28	2.03E-04	-8.14E-04
28	0.02	-18	45	-20	-27	4.07E-04	-8.14E-04